Quantum reflection of a cold antihydrogen wave packet

Pierre-Philippe Crépin

To cite this version:

Pierre-Philippe Crépin. Quantum reflection of a cold antihydrogen wave packet. Quantum Physics [quant-ph]. Sorbonne Université, 2019. English. NNT : 2019SORUS054 . tel-03141367v2

HAL Id: tel-03141367

https://theses.hal.science/tel-03141367v2

Submitted on 15 Feb 2021

École doctorale : "Physique en Île-de-France"

Doctorat de Sorbonne Universités

THÈSE

pour obtenir le grade de docteur délivré par

Sorbonne Universités

réalisée au Laboratoire Kastler-Brossel

présentée et soutenue publiquement par

Pierre-Philippe Crépin

le 3 juin 2019

Réflexion quantique d'un paquet d'onde d'antihydrogène refroidi

---

Quantum reflection of a cold antihydrogen wave packet

devant le jury composé de

M	**Daniel Bloch**	Rapporteur
M	**David Guéry-Odelin**	Rapporteur
M^{me}	**Marie-Christine Angonin**	Examinatrice
M^{me}	**Mathilde Fouché**	Examinatrice
M	**Valery Nesvizhevsky**	Examinateur
M	**Serge Reynaud**	Directeur de thèse
M	**Michael Benzaquen**	Invité

« *Dans notre connaissance des choses de l'Univers (qu'elles soient mathématiques ou autres), le pouvoir rénovateur en nous n'est autre que l'innocence. C'est l'innocence originelle que nous avons tous reçue en partage à notre naissance et qui repose en chacun de nous, objet souvent de notre mépris, et de nos peurs les plus secrètes. Elle seule unit l'humilité et la hardiesse qui nous font pénétrer au coeur des choses, et qui nous permettent de laisser les choses pénétrer en nous et de nous en imprégner.*
[...] *Ce ne sont pas ces dons-là, pourtant, ni l'ambition même la plus ardente, servie par une volonté sans failles, qui font franchir ces "cercles invisibles et impérieux" qui enferment notre Univers. Seule l'innocence les franchit, sans le savoir ni s'en soucier, en les instants où nous nous retrouvons seul à l'écoute des choses, intensément absorbé dans un jeu d'enfant...* »

Alexandre Grothendieck
Récoltes et semailles

À la recherche d'un stage en dernière année de master, le nom de l'équipe "Fluctuations quantiques et relativité" du laboratoire Kastler-Brossel retint mon attention. Quelques mois plus tard, Astrid Lambrecht et Serge Reynaud m'ont fait l'immense plaisir de m'accueillir dans leur équipe, m'accompagnant dans ma découverte des fluctuations quantiques du vide et de l'effet Casimir. Romain Guérout et Nicolas Cherroret m'ont également beaucoup appris et et aidé, notamment à affronter les longs calculs de comportements asymptotiques de fluctuations de potentiel ... Je les en remercie.

Je souhaite particulièrement remercier Serge Reynaud, qui a accepté de devenir mon directeur de thèse. Sa bienveillance, sa disponibilité, ses encouragements, la liberté qu'il m'a accordée, les discussions théoriques que nous avons pu avoir aux pauses de midi et son savoir encyclopédique ont grandement contribué à la réussite et aux bons souvenirs que j'aurai de cette aventure.

Pendant ces trois annés au laboratoire, j'ai eu la chance de croiser la route de Marie-Pascale Gorza, Antoine Canaguier-Durand, Manuel Donaire, Axel Maury, Victoria Esteso et Charles Christen. Je leur souhaite une bonne continuation dans leur parcours et leurs projets. J'ai également eu la chance de participer à la collaboration GBAR au CERN, de capter un signal d'antiprotons la nuit et de rencontrer les chercheurs de cette expérience ambitieuse, en particulier Alexeï Voronin et Valery Nesvizhevsky. Je me souviendrai de leurs intuitions fulgurantes et des fameuses discussions tard le soir à Moriond.

Valery me fait également l'honneur de participer à mon jury de thèse, aux côtés de Daniel Bloch, David Guéry-Odelin, Marie-Christine Angonin, Mathilde Fouché. Je les remercie vivement pour l'intérêt dont ils témoignent pour ma thèse et suis particulièrement reconnaissant à Daniel Bloch et David Guéry-Odelin d'avoir accepté d'en être les rapporteurs. Je me réjouis également de la présence de Michael Benzaquen, avec qui je continuerai à côtoyer le monde de la recherche en tant que post-doc.

Cet appétit et ce goût pour la science ont été nourris par de nombreux enseignants, envers qui je suis pleinement reconnaissant. Je pense notamment aux premiers cours de physique quantique de Jean Dalibard à l'X, qui m'a fait découvrir l'univers de l'infiniment petit avec une grande élégance, puis ceux de Manuel Joffre, avec qui j'ai eu la chance de participer à l'élaboration d'un MOOC. Je souhaite également remercier Frédéric Chevy qui a accepté de m'accompagner lors d'un premier stage de recherche, à la découverte des atomes froids.

Cette aventure a aussi été marquée par des rencontres personnelles. J'aimerais remercier chaleureusement mes amis Sébastien et Guillaume pour leur présence, le voyage surprise à Bruxelles et Amsterdam et tant d'autres moments incroyables ! Je salue également mes anciens coloc', Thibault et Lucie, Gaspard, mes amis de Granville, d'école

… Tous ceux qui se sont libérés le 3 juin pour venir assister à ma soutenance et sont venus la fêter après : Côme, Louis, Cathou, Léo, Kraj, Alexandre, Matthieu, Paul, Cédric, Marie, Marc, Aude, Maxence… Les cadeaux sont géniaux, surtout le paquet d'ondes. Merci à la petite graine jumelle pour ces moments heureux et créatifs, pour cette belle rencontre. Merci à Chipi qui était présente aux manettes derrière les coulisses. Enfin, merci à mes parents et ma sœur pour le soutien indéfectible dont ils ont su faire preuve lors de ce périple, ainsi qu'aux membres de ma famille qui m'ont fait le grand plaisir de venir, parfois de Pologne, pour assister à la soutenance.

Contents

Introduction

Antimatter has remained a topic of great interest for physicists since Dirac published his famous equation [1] in 1928, describing a spin 1/2 particle in the frame of quantum mechanics and relativity. The Dirac equation predicts the existence of antiparticles, having the same mass as particles but with an opposite charge. This theoretical prediction was confirmed in 1932 by Anderson [2] with a first observation of the positron, the antiparticle of electron. A fruitful dialogue between experiment and theory led progressively to the development of the Standard Model in the 1970's, giving a theoretical framework describing three of the four known fundamental forces governing the universe. The antiparticle is now defined as the symmetric of a particle after charge (C), parity (P) and time reversal (T) – the so called CPT symmetry.

Despite many successes and observations, the Standard Model still fails to understand the apparent asymmetry between particles and antiparticles in the visible universe [3–6]. A natural way to progress in this question is to explore gravity for antimatter, that does not fit in the framework of Standard Model. The simple question

"How does antimatter fall ?"

is still debated. Experimental knowledge on this question is much less precise than for gravitational properties of ordinary matter [7, 8]. For example, the aim of measuring the free fall acceleration $\overline{g}$ of antihydrogen ($\overline{H}$) in Earth's gravitational field has been approached only recently [9] with the sign of $\overline{g}$ not even known yet:

$$-65 \leq \overline{g}/g \leq 110$$

Several collaborations are working with antihydrogen atoms produced at CERN to improve the accuracy of $\overline{g}$-measurement in dedicated experiments [10–12].

The GBAR collaboration is installing an experiment at CERN, using the techniques of ultracold atom physics to cool down antihydrogen atoms to microKelvin temperatures [13]. This makes feasible the aim of measuring $\overline{g}$ with an accuracy of the order of 1% by timing the classical free fall of antiatoms on a well defined free fall height [14, 15].

In this thesis we will explore the effect of the gravitational field on a cold antihydrogen matter wave. More precisely we will focus on the last instants of the anti-atom's fall. At small energy and small distances, another potential comes into play, the Casimir-Polder interaction between the atom and the surface of the detector. The Casimir effect constitutes a paradigmatic example of dispersion force between neutral bodies, induced by quantum fluctuations of the electromagnetic field. Since their discovery [16], Casimir and Casimir-Polder forces have had a large impact in the fields of physics, chemistry, biology and nanotechnology [17–19].

While a matter wave is reflected on the gravitational potential much like a classical particle reverses its direction upon reaching the apex of its trajectory, the behavior of a matter wave scattering off the Casimir-Polder potential is very different from that of a classical particle. The Casimir-Polder force is attractive, so that one would expect classically an incoming antihydrogen atom to be accelerated towards the surface and eventually annihilated. For atoms, quantum bounces produced by the Casimir-Polder interaction above the surface where precisely predicted and observed [20–32]. The mechanism is expected to work with antihydrogen atoms, thus preventing their annihilation at the matter surface [33–36]. The study of quantum reflection from the Casimir-Polder potential will be the main object of this thesis, thus continuing the work started by Gabriel Dufour [36]. The combined action of quantum reflection and gravity [37, 38] leads to *quantum levitation states*. We will show that antihydrogen atoms can stay in quantum levitation states for long times which can exceed one second over an helium surface [39]. We will then prove that the accuracy of the $\overline{g}$-measurement can be improved by using quantum interference techniques on these states.

Testing the equivalence principle for antimatter

The recognition that the motion of objects in a gravitational field is independent of their mass and composition was central to the birth of modern science in the 17th century. The universality of free fall or *weak equivalence principle* is a cornerstone of Einstein's General Relativity. Today, the fact that all bodies undergo the same acceleration g at a given point on the surface of the Earth is verified with ever increasing precision both for macroscopic test masses [40] and atoms [41, 42]. The space mission MICROSCOPE tests the weak equivalence principle with a relative precision of 10^{-15} by comparing the free fall of a macroscopic platinum and titanium masses. A preliminary result confirms the weak equivalence principle [43] up to a relative precision of $2 \cdot 10^{-14}$.

However gray areas remain. The mysteries surrounding dark matter and energy remind us that our knowledge of gravitational forces is still incomplete. Our ignorance of how gravity and other interactions are articulated at a fundamental level leaves some room for alternative proposals which include violations of the weak equivalence principle. In particular, the possibility of an asymmetry in the gravitational behavior of matter and antimatter has been raised [4, 44–47]. Although theoretical arguments and experimental observations have been put forward against "antigravity" [5, 7, 48], a direct, model-independent test of the universality of free fall for antimatter is still lacking. A direct measurement of the acceleration $\overline{g}$ of an antimatter particle in the Earth's gravity field is a longtime objective of physicists. Early experiments with charged antiparticles were thwarted by the preponderance of electromagnetic forces over gravity [49]. Current experimental endeavors are thus concentrating on neutral particles, especially the antihydrogen atom. The antihydrogen atom ($\overline{\mathrm{H}}$) is the bound state of an antiproton ($\bar{\mathrm{p}}$) and a positron (e^+); it was first produced at high energies in CERN in 1995 [50]. Since then, much progress has been made towards lower temperatures and longer lifetimes in several experiments based around CERN's Antiproton Decelerator [51, 52].

At CERN, the new deceleration ring ELENA [53] provides cooler antiprotons to a new generation of antimatter experiments. Antiprotons are produced by collisions of 26 GeV protons with a target and cooled down to approximately 100 keV by the AD and ELENA rings. Antiprotons are then used in different experiments. AEGIS aims to measure the deflection of a produced beam of antihydrogen atoms using a Moiré deflectometer [54]. There is also a proposal to build an interferometric gravimeter in the ALPHA experiment [55].

In particular, the GBAR experiment will consist in cooling antihydrogen to the ground state of a harmonic ion trap before releasing it in the Earth's gravity field and timing its free fall [56, 57]. For doing that, antiprotons coming from the ELENA ring are slowed down electrostatically to approximately 1 keV before reaching the reaction chamber. As explained in [36], the specificity of GBAR is that it will produce the antihydrogen ion $\overline{\mathrm{H}}^+$, two positrons orbiting an antiproton, in order to take advantage of ion trapping and cooling techniques [13]. Once the ion is cold, a laser will be used to photodetach the excess positron, letting the neutral antihydrogen atom fall freely towards a detection plate.

The $\overline{\mathrm{H}}^+$ ion will be produced by the successive reaction of an antiproton with two positroniums (the bound state of electron and positron):

$$\bar{\mathrm{p}} + \mathrm{Ps} \rightarrow \overline{\mathrm{H}} + \mathrm{e}^- \ ,$$
$$\overline{\mathrm{H}} + \mathrm{Ps} \rightarrow \overline{\mathrm{H}}^+ + \mathrm{e}^- \ .$$

Producing these reactants and bringing them together in the right conditions will constitute an impressive experimental feat.

Positronium is formed by implanting positrons in a porous silica sample. The positron captures an electron and the resulting positronium diffuses in the network of nanometric pores until it is expelled back into the vacuum with a well defined energy [58]. The positrons themselves are obtained in the collision of 10 MeV electrons from a linear accelerator (LINAC) with a target. They must then be moderated, accumulated in a Penning trap and sympathetically cooled by a cloud of electrons before being sent on the porous silica sample. The positronium will be excited by laser to a higher energy state in order to maximize the cross-section of the reactions [59].

At the output of the reaction chamber, the $\overline{\mathrm{H}}^+$ ions are separated from the neutral $\overline{\mathrm{H}}$ and the negatively charged $\bar{\mathrm{p}}$ and collide with a Coulomb crystal of laser-cooled Be^+ and HD^+ ions. Their energy is efficiently transferred to the ions of the crystal thanks to the small mass ratios between these three species. One $\overline{\mathrm{H}}^+$-Be^+ pair is then transfered to a Paul trap. Raman sideband cooling is performed on the beryllium ion, which has the effect of sympathetically cooling the antihydrogen ion to the ground state of the harmonic trap [60]. A laser pulse is then used to photodetach the extra positron, defining the starting time of the free fall of the neutral antihydrogen atom. The fall ends by the annihilation of the anti-atom on a detection plate some 10 cm below. The annihilation products (pions and gamma photons) are detected by Micromegas detectors [61] and scintillation counters placed outside the vacuum vessel. The acceleration $\overline{g}$ of antihydrogen is deduced from the free fall time. A 1% precision on $\overline{g}$ is expected in this scheme.

Quantum reflection

The classical description of an antihydrogen atom as a point particle is not sufficient at low temperature. In the formalism of the quantum mechanics, cold antihydrogen atom is described by a wavefunction obeying the Schrödinger equation. The atoms live in a gravitational potential described classically (relativistic effects are negligible), and the Casimir-Polder potential.

The confinement of a cold atom trapped above a perfectly reflecting surface in the gravity field leads to gravitationally bound states. These gravitationally bound states have first been observed with ultracold neutrons at the Institut Laue-Langevin [62–64]. Though atomic mirrors have been realized using inhomogeneous electric or magnetic fields [65–72], gravitationally bound quantum states of atoms remain to be observed.

The presence of the attractive Casimir-Polder potential induces quantum reflection phenomena: antihydrogen atoms have a probability to bounce above the surface, preventing their annihilation. Observation of the phenomenon has only been achieved relatively recently for atoms, because very low temperatures are required to reach sufficiently large wavelengths. The first experiments where carried out in the 1980s with helium and hydrogen atoms scattering off a liquid helium surface [23, 73, 74]. It took several more years before reflection from solid surfaces was observed, first with beams of atoms incident on a surface at grazing incidence [26, 27] and later with Bose-Einstein condensates falling towards the surface at normal incidence [28]. Since, a number of experiments have been carried out with rough or nanostructured surfaces [31, 32, 75–80].

In this thesis, we compute precisely the Casimir-Polder potential, taking also into account the heterogeneities in the particular case of metallic surfaces and see how it modifies the potential and eventually the quantum reflection. Despite the progresses in the understanding of the Casimir effect, there still exists a disagreement between experiment and theory in the Casimir community, called the "Drude vs plasma puzzle". Some experiments [81–83] fit better with a theoretical model where the finite conductivity of the metallic medium (Drude model) is supposed infinite (plasma model). With the present work, we thus give now a perspective to probe the model of dissipation in the Casimir-Polder formula, testing the "Drude vs plasma puzzle".

The name "quantum reflection” emphasizes the contrast between the classical and quantum dynamics. In fact, this phenomenon is a general feature of wave propagation in inhomogeneous media [84]. It is met for atmospheric and oceanic waves for example, or electromagnetic waves in dielectrics and transmission lines. Roughly speaking, quantum reflection occurs in regions where the wavelength varies rapidly. In this thesis, we use frequently the *Liouville transformations* that give an intuitive picture of the quantum reflection by transforming the reflection on a well into a reflection on a wall.

If we consider the gravity acting identically for atoms and antiatoms, the antihydrogen atoms are trapped between gravity pulling them downwards and quantum reflection balancing their free fall [37, 38]. It leads to the existence of *quantum levitation states* for ultracold matter waves. We perform for the first time a full quantum treatment of gravity and Casimir-Polder interaction. We compute precisely the Casimir-Polder shifts on gravitationally bound quantum states induced by the Casimir-Polder interaction. A precise knowledge of this phenomenon leads to a new proposition to measure the free fall acceleration for antihydrogen by quantum measurement techniques [85–87].

In this thesis, we use the phenomenon of quantum reflection to propose a new experimental setup keeping almost all antihydrogen atoms, consisting of adding a reflecting surface to generate interferences between quantum states, before the free fall of the antihydrogen on the detector, thus producing interference pattern containing much more information on $\overline{g}$ that the classical free fall time. The quantum nature of the quantum levitation states are thus fully involved, producing beautiful interference figures. Doing that, we prove that the accuracy of the initial GBAR design by three orders of magnitude.

Outline of the thesis

Chapter I of this thesis is devoted to the theoretical study of quantum reflection on a Casimir-Polder potential. We precisely calculate the quantum reflection on a liquid helium bulk, that leads to the highest reflectivity of an antihydrogen atom above a surface and to a surprising manifestation of a shape resonance when varying the thickness of liquid helium film. We also introduce the Liouville transformations, an important tool to understand the quantum reflection and make quantitative calculations.

In chapter II we perform a full quantum treatment of gravity and Casimir-Polder potential. We introduce the Liouville-Langer coordinates to study the quantum levitation states, in a new physical picture corresponding to a cavity built up with two mirrors, a partly reflective one associated with quantum reflection and a perfectly reflecting one due to gravity. We develop also a new effective range theory improving the expansion of the scattering length at low energy. We finally calculate the properties of the quasi-stationary states of the quantum bouncer with a high accuracy.

In chapter III we propose a new measurement technique of the antihydrogen free fall acceleration making interfering quantum levitation states. We describe the experimental setup, that could be implemented in the GBAR experiment, and derive the evolution of the atomic wave packet from the photodetachment to the detection. We also present statistical methods to extract an estimation of $\overline{g}$ and give the standard deviation that is much smaller than the one achieved with the free fall timing experiment.

Chapter IV is focused on the details of the Casimir-Polder interaction. We describe the fluctuations of the Casimir-Polder potential due to the heterogeneities of the medium and see if it could affect the quantum reflection. We also make a more general discussion on the model used for describing the dissipation in metal in the "Drude vs plasma" puzzle, by finding a different asymptotic behavior for the two models.

A list of publications and an index of notations are given at the end of the manuscript.

Chapter I

Quantum reflection on the Casimir-Polder potential

> “ *Mieux vaut regarder là où on ne va pas, parce que, là où on va, on saura ce qu'il y a quand on y sera; et, de toute façon, ce sera jamais que de l'eau.* ”
>
> **Les Shadocks**

The first chapter introduces the phenomenon of quantum reflection. Quantum reflection has been studied theoretically for the attractive van der Waals potential since the early days of quantum mechanics [20, 21]. Theoretical treatments of the effect are reviewed for example in [22, 88]. It was first observed experimentally for H and He atoms [23, 73, 74] and then for ultracold atoms or molecules on solid surfaces [26–28, 31].

The interest of studying quantum reflection also for antimatter has been noticed more than ten years ago [85, 89, 90] and it should play a key role in experiments with antihydrogen atoms [85, 90–93]. The precise knowledge of this phenomenon is in particular crucial for spectroscopic studies of the quantum levitation states [62, 94] of antihydrogen atoms trapped by quantum reflection and gravity [37, 38].

We start by a brief introduction to the quantum reflection of matter waves in section I.1. We also present the scattering length, an important quantity in the scattering theory that encodes the reflection. We introduce the Liouville transformation of the Schrödinger equation in section I.2, an elegant tool that helps us to intuitively and quantitatively appreciate the counter-intuitive phenomenon of quantum reflection by changing the potential landscape while preserving the reflection amplitudes. Then, we discuss the case of an atom interacting with a surface, through the attractive Casimir-Polder potential. We compute the quantum reflection for a liquid helium bulk in section I.3, that offers a very high reflectivity. We finish by taking into account the finite thickness of the liquid helium film in section I.4. We also compute the Casimir-Polder potential and the quantum reflection for different film thicknesses and highlight scattering length oscillations that are explained by an adapted Liouville transformation.

I.1 Quantum reflection

I.1.a Definition

We consider a particle of mass m of total energy E, evolving in a one-dimensional potential landscape $V(z)$. In classical point-particle mechanics, change in the direction of propagation can only occur at turning points $E = V(z)$. If $E > V(z)$, the particle continues straights, its momentum $p(z)$ being related to the kinetic energy:

$$p(z) = \sqrt{2m(E - V(z))}. \tag{I.1}$$

In the wave mechanics description in contrast, a wave packet in inhomogeneous media may very well split into both propagating and counter-propagating components. This phenomenon, when occurring for matter waves, may therefore predict non-zero reflection probability for particles even in classically admissible regions $E > V(z)$, and even when the potential is attractive. It is this stark departure from the classical particle picture which we call *quantum reflection*.

I.1.b Helmholtz and Schrödinger equations

Let us first remark that this phenomenon not only occurs in quantum mechanics but is a general property observable in wave propagation in inhomogeneous media. For a wavefunction $u(z,t)$, the Helmholtz equation is written:

$$\left[\frac{\partial^2}{\partial t^2} - c(z)^2 \frac{\partial^2}{\partial z^2}\right] u(z,t) = 0. \tag{I.2}$$

By assuming that the space and time variable are separable, $u(z,t) = f(z)g(t)$, the spatial component obeys the stationary equation:

$$f''(z) + F(z)f(z) = 0 \tag{I.3}$$

with

$$\begin{aligned} F(z) &= -\frac{1}{c(z)^2 g(t)} \frac{d^2 g(t)}{dt^2} \\ &= k^2(z). \end{aligned} \tag{I.4}$$

In general, solutions of the equation (I.3) asymptotically behave as a sum of propagating and counter-propagating waves with a wavevector k.

In quantum mechanics, the evolution of a massive particle represented by the wavefunction $\psi(z,t)$ is dictated by the Schrödinger equation:

$$i\hbar\frac{\partial\psi(z,t)}{\partial t}+\left[\frac{\hbar^2}{2m}\frac{\partial^2}{\partial z^2}-V(z)\right]\psi(z,t)=0. \tag{I.5}$$

The corresponding stationary equation takes the same form as (I.3):

$$\psi''(z)+F(z)\psi(z)=0 \tag{I.6}$$

with

$$\begin{aligned} F(z) &\equiv \frac{2m(E-V)}{\hbar^2} \\ &= \frac{p^2(z)}{\hbar^2}. \end{aligned} \tag{I.7}$$

In the following of this section, unless otherwise mentioned, we place ourselves in a classically allowed region, where $F(z)>0$. We can also define the associated de Broglie wavelength and wavevector as

$$\lambda_{dB}(z)\equiv\frac{2\pi}{\sqrt{F(z)}}, \quad k_{dB}(z)\equiv\sqrt{F(z)}=\frac{2\pi}{\lambda_{dB}}. \tag{I.8}$$

I.1.c The WKB approximation

In the rest of the thesis, we treat the quantum reflection of an antihydrogen atom interacting with a surface. We have seen that quantum reflection is an emerging phenomenon of the wave description of the particle. One might however wonder if there are regions where the classical description of a point particle evolving in space holds. Or more subtly, even if the classical description fails, is the notion of propagating and counter-propagating wave well defined ?

In order to answer these questions, we introduce the Wentzel-Kramers-Brillouin (WKB) approximation that is a semiclassical approximations to the Schrödinger equation[1]. This approximation scheme has been introduced in the context of quantum mechanics by Wentzel [97], Kramers [98] and Brillouin [99], who complemented it by connection formulas allowing to relate wavefunctions in classically allowed and forbidden areas. The contribution of Jeffreys [100] to the mathematical theory is sometimes acknowledged by appending his initial to the name.

---

[1] A detailed derivation is done in the thesis [36] and historical notes on the development of the WKB approximation can be found in [95, 96]

The most common derivation of the WKB approximation uses an expansion in powers of the reduced Planck constant $\hbar$ (see [22, 97] for example), which emphasizes its semiclassical nature. In this approximation the phase of the wavefunction solution of (I.6) is a primitive of the de Broglie wavevector:

$$\phi_{\mathrm{dB}}(z) \equiv \int_{z_\phi}^{z} k_{\mathrm{dB}}(\zeta)\,\mathrm{d}\zeta\ . \tag{I.9}$$

We call this primitive the WKB phase and leave its dependence on the energy E and the reference point z_ϕ implicit. Within the WKB approximation, a basis of solutions of the Schrödinger equation is

$$\psi^{\pm}_{\mathrm{WKB}}(z) \equiv \frac{1}{\sqrt{\phi'_{\mathrm{dB}}(z)}}\exp(\pm i\phi_{\mathrm{dB}}(z)) = \frac{1}{\sqrt{k_{\mathrm{dB}}(z)}}\exp(\pm i\phi_{\mathrm{dB}}(z))\ . \tag{I.10}$$

In regions where the WKB approximation is applicable, wavepackets follow the classical trajectory corresponding to their energy [36]. In contrast to this semiclassical expectation, the exact wavefunction undergoes quantum reflection. Quantum reflection can be seen as a departure of the exact solution of the Schrödinger equation from its WKB approximation. In particular, it is instructive to write an exact solution to the Schrödinger equation as a linear combination of WKB waves with space-dependent coefficients $a_+(z)$ and $a_-(z)$ [22, 36]:

$$\psi(z) \equiv a_+(z)\psi^{+}_{\mathrm{WKB}}(z) + a_-(z)\psi^{-}_{\mathrm{WKB}}(z)\ . \tag{I.11}$$

The idea is that $a_\pm$ should be constant in regions where the WKB approximation is accurate but may vary elsewhere, allowing for the conversion of an incident wave into a reflected one. Moreover, we expect any fast variations of the wavefunction to be absorbed in the WKB basis functions, so that the coefficients $a_\pm$ vary slowly.

I.1.d Badlands

In fact, although the WKB wavefunctions (I.10) are not exact solutions of the original Schrödinger equation (I.6), they are exact solutions of a modified Schrödinger equation:

$$\psi''^{\pm}_{\mathrm{WKB}}(z) + F(z)(1+Q(z))\psi^{\pm}_{\mathrm{WKB}}(z) = 0 \tag{I.12}$$

where the function $Q(z)$ is:

$$\begin{align} Q(z) &\equiv \frac{1}{2F(z)}\{\phi_{\mathrm{dB}}, z\} \tag{I.13}\\ &= -\frac{1}{4\pi^2}\left(\sqrt{\lambda_{\mathrm{dB}}(z)}\right)^3 \frac{\mathrm{d}^2}{\mathrm{d}z^2}\sqrt{\lambda_{\mathrm{dB}}(z)}. \tag{I.14}\end{align}$$

The symbol $\{\cdot,\cdot\}$ represents the *Schwarzian derivative* and is defined for a three-times differentiable function as:

$$\{f, x\} \equiv \frac{f'''(x)}{f'(x)} - \frac{3}{2}\left(\frac{f''(x)}{f'(x)}\right)^2 . \tag{I.15}$$

From equation (I.12), WKB wavefunctions obey essentially the exact Schrödinger equation (I.6) in regions where $Q(z)$ is small compared to one. This is obviously the case in regions of constant potential, but $Q(z)$ can also be negligible in regions where $F(z) = E - V(z)$ is large, even if $V(z)$ varies rapidly. In these regions the direction of propagation of matter waves can be defined unambiguously, so that no quantum reflection can occur. It follows that quantum reflection can happen only in regions where $Q(z)$ has significant values. These regions are typically associated to small values of $F(z)$ and/or fast variations of the de Broglie wavelength, as it is suggested by (I.13) and (I.14). We expect the WKB approximation to break down in these regions, which are known as the *badlands* [22, 29]. We will use this property more quantitatively, when defining the Liouville transformations in section I.2.

I.1.e Reflection amplitude

Let us now derive a general method to compute the amplitude reflection for a given potential landscape. We introduce a general object used in second order differential equations, the *Wronskian*. Given two differentiable functions ψ_1 and ψ_2, the Wronskian $\mathcal{W}$ is defined as following:

$$\mathcal{W}(\psi_1, \psi_2) \equiv \psi_1(z)\psi_2'(z) - \psi_1'(z)\psi_2(z) \ . \tag{I.16}$$

If ψ_1 and ψ_2 are solutions of (I.6), $\mathcal{W}(\psi_1, \psi_2)$ is independent of z since $\frac{\mathrm{d}}{\mathrm{d}z}\mathcal{W}(\psi_1, \psi_2) = \psi_1(z)\psi_2''(z) - \psi_1''(z)\psi_2(z) = 0$, so that the Wronskian is a bilinear skew-symmetric form on the space of solutions.

The useful property of the Wronskian is the fact that we can explicitly express the amplitudes $a_\pm(z)$ in expression (I.11), even if the amplitudes are not constant [101, 102]:

$$a_\pm(z) = \pm\frac{1}{2i}\mathcal{W}(\psi^\mp_{\mathrm{WKB}}(z), \psi(z)). \tag{I.17}$$

Considering now an atom of mass m and energy E evolving in a potential $V(z)$, as is illustrated for instance in figure I.1. We consider the WKB approximation to be valid on both regions $z \to L$ and $z \to R$ of the potential:

We consider the case of an incident wave arriving from the right which is reflected and transmitted by the potential. Then we can write asymptotically:

$$\psi(z) \underset{z\to L}{\simeq} t\ \psi^-_{\mathrm{WKB}}(z) \tag{I.18}$$

In the right side of the potential, the wavefunction behaves asymptotically as a superposition of incoming and outgoing plane waves:

$$\psi(z) \underset{z\to R}{\simeq} \psi^-_{\mathrm{WKB}}(z) + r\ \psi^+_{\mathrm{WKB}}(z) \tag{I.19}$$

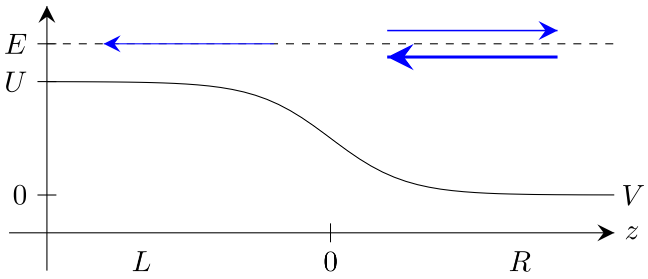

Figure I.1: Example of rounded step potential which causes quantum reflection. Blue arrows show image amplitudes of propagating and counter-propagating waves.

with r and t given by (from (I.17)):

$$r = -\frac{\mathcal{W}(\psi^-_{\rm WKB}(z), \psi(z))|_{z\to R}}{\mathcal{W}(\psi^+_{\rm WKB}(z), \psi(z))|_{z\to R}} \tag{I.20}$$

$$t = \frac{\mathcal{W}(\psi^+_{\rm WKB}(z), \psi(z))|_{z\to L}}{\mathcal{W}(\psi^+_{\rm WKB}(z), \psi(z))|_{z\to R}}. \tag{I.21}$$

r is called the reflection amplitude, while t is the transmission amplitude.

I.1.f Scattering matrix

To treat a scattering process in a general way, we introduce the *scattering matrix* formalism. Let us consider a wavefunction, solution of the stationary Schrödinger equation (I.6). We suppose that on the both left and right sides of the potential, $a_\pm(z)$ converge to constant values:

$$a^L_+ \equiv a^{\rm in}_+ \equiv \lim_{z\to L} a_+(z)\ , \qquad a^R_+ \equiv a^{\rm out}_+ \equiv \lim_{z\to R} a_+(z)\ , \tag{I.22}$$

$$a^L_- \equiv a^{\rm out}_- \equiv \lim_{z\to L} a_-(z)\ , \qquad a^R_- \equiv a^{\rm in}_- \equiv \lim_{z\to R} a_-(z)\ . \tag{I.23}$$

Figure I.2 illustrates these amplitudes, by naming it also differently, in terms of *in* and *out* wave amplitudes.

By definition, the *scattering matrix* S connects the amplitudes of waves propagating *out* and *in*:

$$\begin{pmatrix} a^{\rm out}_+ \\ a^{\rm out}_- \end{pmatrix} = \mathcal{S} \begin{pmatrix} a^{\rm in}_+ \\ a^{\rm in}_- \end{pmatrix} . \tag{I.24}$$

The general form of a one-channel scattering matrix is:

$$\mathcal{S} = \begin{pmatrix} \bar{t} & r \\ \bar{r} & t \end{pmatrix} \tag{I.25}$$

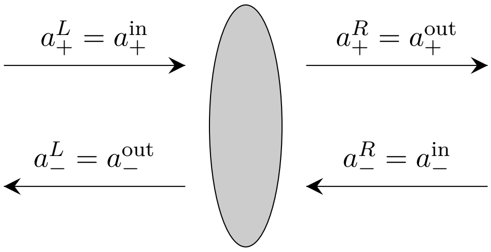

Figure I.2: Diagram showing the amplitudes of leftward and rightward traveling waves on both sides of the scattering region.

r and t correspond to the reflection and transmission amplitudes defined in the previous example. $\bar{r}$ and $\bar{t}$ are the reflection and transmission amplitudes corresponding to an incoming particle from the left, as it is illustrated in figure I.3. Their expression is:

$$\bar{r} = -\frac{\mathcal{W}(\psi^+_{\rm WKB}(z), \psi(z))|_{z\to L}}{\mathcal{W}(\psi^-_{\rm WKB}(z), \psi(z))|_{z\to L}} \tag{I.26}$$

$$\bar{t} = \frac{\mathcal{W}(\psi^-_{\rm WKB}(z), \psi(z))|_{z\to R}}{\mathcal{W}(\psi^-_{\rm WKB}(z), \psi(z))|_{z\to L}}. \tag{I.27}$$

We can also define the *transfer matrix* that relies left and right waves:

$$\begin{pmatrix} a_+^{\rm in} \\ a_-^{\rm out} \end{pmatrix} = \mathcal{T} \begin{pmatrix} a_+^{\rm out} \\ a_-^{\rm in} \end{pmatrix}. \tag{I.28}$$

The link between S and T matrices is given by the following operation :

$$\Pi : \begin{pmatrix} m_{11} & m_{12} \\ m_{21} & m_{22} \end{pmatrix} \mapsto \frac{1}{m_{11}} \begin{pmatrix} 1 & -m_{12} \\ m_{21} & \det(M) \end{pmatrix} \tag{I.29}$$

which is defined for all matrices with a non-zero coefficient $m_{1,1}$. Then, we can check that this operation is an involution transforming $\mathcal{S}$ into $\mathcal{T}$ as well as $\mathcal{T}$ into $\mathcal{S}$:

$$\mathcal{I} = \Pi \circ \Pi \tag{I.30}$$

$$\mathcal{T} = \Pi(\mathcal{S}) \tag{I.31}$$

$$\mathcal{S} = \Pi(\mathcal{T}). \tag{I.32}$$

To describe two successive scattering processes, we also define the $\star$ law for $\mathcal{S}$ matrices from the product law for $\mathcal{T}$ matrices as following [101] :

$$\star : (\mathcal{S}_a, \mathcal{S}_b) \mapsto \mathcal{S}_a \star \mathcal{S}_b \equiv \Pi[\Pi(\mathcal{S}_a) \times \Pi(\mathcal{S}_b)]. \tag{I.33}$$

In the rest of the thesis, we consider no losses in the scattering process, in such a way that the $\mathcal{S}$ matrix is *unitary*:

$$\mathcal{S}^\dagger \mathcal{S} = \mathcal{I}. \tag{I.34}$$

Unitarity is a direct consequence of the current conservation:

$$\begin{aligned} j &= \frac{\hbar}{m}\left(|a_+^L(z)|^2 + |a_-^L(z)|^2\right) && \text{(I.35)} \\ &= \frac{\hbar}{m}\left(|a_+^R(z)|^2 + |a_-^R(z)|^2\right). && \text{(I.36)} \end{aligned}$$

In particular, during the scattering process, the probability is conserved:

$$|r|^2 + |t|^2 = 1. \tag{I.37}$$

I.1.g Reciprocity theorem

The quantum reflection described for an atom approaching a step as shown in figure I.1 holds in fact for an attractive potential. It is in fact a remarkably general property of quantum reflection that it is *reciprocal*, namely that the reflection probability when coming in from a certain direction is the same as for the reverse movement. This remarkable and general result is proven for example by Landau and Lifshitz [103] in the case where $F(z)$ admits finite, positive limits in both $z \to L$ and $z \to R$.

Let us demonstrate this theorem in a modern way, using the scattering formalism [36, 101]. The main idea consists in noticing that if $\psi(z)$ is a solution of the stationary Schrödinger equation, its complex conjugate $\psi^*(z)$ is also a solution, since coefficients in the differential equation are real. Complex conjugation switches the direction of the incoming and outgoing waves. The $\mathcal{S}$ matrix relation (I.24) remains the same under the substitutions $a_+^{\text{in}} \leftrightarrow (a_-^{\text{out}})^*$ and $a_-^{\text{in}} \leftrightarrow (a_+^{\text{out}})^*$:

$$\begin{pmatrix} (a_-^{\text{in}})^* \\ (a_+^{\text{in}})^* \end{pmatrix} = \mathcal{S} \begin{pmatrix} (a_-^{\text{out}})^* \\ (a_+^{\text{out}})^* \end{pmatrix} \tag{I.38}$$

If we introduce the matrix

$$M = \begin{pmatrix} 0 & 1 \\ 1 & 0 \end{pmatrix} \tag{I.39}$$

which exchanges the top and bottom elements of a vector, we find that

$$\mathcal{S}^* = M\mathcal{S}^{-1}M. \tag{I.40}$$

From (I.40), we deduce that

$$|\det \mathcal{S}|^2 = |r\bar{r} + t\bar{t}|^2 = 1 \ , \qquad\qquad \bar{r} = -tr^*/t^* \ . \tag{I.41}$$

Finally, if we add the unitarity property (I.34), we find that

$$t = \bar{t} \ , \quad |r| = |\bar{r}|. \tag{I.42}$$

It means in particular that r and $\bar{r}$ only differ by a phase factor.

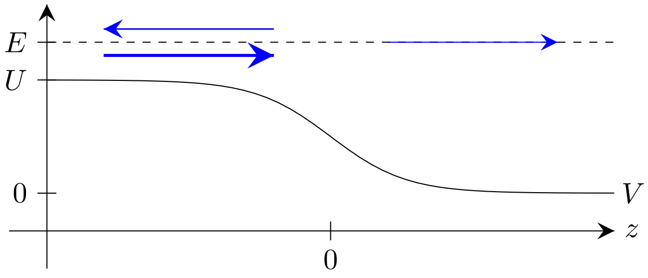

Figure I.3: The same step potential as in figure I.1 illustrating the quantum reflection of an incoming wave from the left.

Thus, quantum reflection occurs with the same probability for a particle approaching an attractive valley than the symmetric case of a particle with a same energy approaching a repulsive step.

I.1.h Scattering length

From the reflection amplitude r, we can extract the complex length $\mathcal{A}(k)$ depending on the wavevector k equivalent to the energy $E = \hbar^2 k^2/(2m)$

$$\mathcal{A}(k) \equiv -\frac{i}{k}\frac{1+r(k)}{1-r(k)}. \tag{I.43}$$

While its energy dependence is treated in II.2, we focus here on the low energy limit $k \to 0$:

$$a \equiv \lim_{k\to 0} \mathcal{A}(k). \tag{I.44}$$

The *scattering length* a so defined is a well-known quantity in the scattering study of ultracold particles. The scattering near the threshold $E = 0$ is universal, in the sense that is only depends on the single parameter a, as was first noted by Wigner [104]. In particular, the interaction between ultracold particles can be replaced by an effective contact potential which depends on a single parameter, the scattering length [103]. For example, this result is used to model interacting Bose-Einstein condensates with the Gross-Pitaevskii equation [105, 106]. In fact, this property applies also to particle-surface collisions, as we use it in this thesis.

In the low energy limit, the reflection amplitude $r(k)$ can be simply expressed in terms of the scattering length a [91]:

$$r(k) \underset{k\to 0}{\simeq} -e^{-2ika}. \tag{I.45}$$

In general the phase choice for r is arbitrary and we fix it to be 0 in the limit $k \to 0$ in the above expression (I.45). The real part of a also determines the phase at reflection (in comparison to the phase origin fixed previously in the limit $k \to 0$) while its imaginary part, denoted by $b \equiv -\mathrm{Im}(a)$, determines the quantum reflection probability:

$$|r(k)|^2 \underset{k\to 0}{\simeq} e^{-4kb}. \tag{I.46}$$

I.2 Liouville transformation of the Schrödinger equation

We introduce now an elegant tool that helps to better understand quantum reflection: *Liouville transformation*. Initially, this transformation was introduced by Liouville in 1837 [107] to derive the approximation to the solutions of the heat equation that would later be known as the WKB approximation. Subsequently, Liouville transformations were mostly used in the same spirit, as a starting point for various approximation schemes, as shows a rich literature in recent decades [108–115]. The Liouville transformation can also be employed to obtain exact mathematical results, for example to relate various exactly solvable Schrödinger equations [116, 117].

Our use of Liouville transformations differs from all these previous works because it is neither used to perform an approximation, nor to obtain analytical results. Our goal here is to perform exact calculations for realistic potentials, precisely in regimes where the comparison equation approximation is not valid [39, 118–120].

I.2.a Liouville transformation group

A Liouville transformation of the Schrödinger equation (I.6) consists in a smooth change of coordinate and an associated rescaling of the wavefunction:

$$\begin{aligned} &z \to \boldsymbol{z}\ , \quad \boldsymbol{z}'(z) > 0 \\ &\boldsymbol{\psi}(\boldsymbol{z}) = \sqrt{\boldsymbol{z}'(z)}\psi(z). \end{aligned} \tag{I.47}$$

The stationary Schrödinger equation (I.6) for ψ is thereby transformed into an equivalent equation for $\boldsymbol{\psi}$ [96, 107]:

$$\begin{aligned} \boldsymbol{\psi}''(\boldsymbol{z}) + \boldsymbol{F}(\boldsymbol{z})\boldsymbol{\psi}(\boldsymbol{z}) &= 0 \\ \boldsymbol{F}(\boldsymbol{z}) &= \frac{F(z) - \frac{1}{2}\{\boldsymbol{z}, z\}}{\boldsymbol{z}'(z)^2} \\ &= z'(\boldsymbol{z})^2 F(z) + \frac{1}{2}\{z, \boldsymbol{z}\}. \end{aligned} \tag{I.48}$$

The curly braces denote the Schwarzian derivative (I.15) of the coordinate transformation $\boldsymbol{z}(z)$.

Liouville transformations form a group for the composition law, denoted by $\circ$. This result is based on the Cayley's identity for the Schwarzian derivatives, involving a third coordinate $\tilde{z}$:

$$\{\boldsymbol{z}, z\} = \left(\tilde{z}'(z)\right)^2 \{\boldsymbol{z}, \tilde{z}\} + \{\tilde{z}, z\}\,. \tag{I.49}$$

Then we check the group properties:

- the identity element is simply given by the transformation $z \to z$
- the Cayley's identity (I.49) ensures that the composition of two transformations $z \to \tilde{z}$ and $\tilde{z} \to \boldsymbol{z}$ is also a transformation $z \to \boldsymbol{z}$: $(\tilde{z} \to \boldsymbol{z}) \circ (z \to \tilde{z}) = (z \to \boldsymbol{z})$
- for each transformation $z \to \tilde{z}$, there is an inverse transformation $\tilde{z} \to z$ obtained by applying (I.49) to the case $\boldsymbol{z} = z$
- the associativity is also satisfied:

$$\begin{aligned}
(\boldsymbol{z} \to \hat{z}) \circ ((\tilde{z} \to \boldsymbol{z}) \circ (z \to \tilde{z})) &= (\boldsymbol{z} \to \hat{z}) \circ (z \to \boldsymbol{z}) \\
&= (z \to \hat{z}) \\
&= (\tilde{z} \to \hat{z}) \circ (z \to \tilde{z}) \\
&= ((\boldsymbol{z} \to \hat{z}) \circ (\tilde{z} \to \boldsymbol{z})) \circ (z \to \tilde{z}).
\end{aligned}$$

The group of Liouville transformations with the normalization choice of the wavefunction (I.47) has the remarkable property of preserving the Wronskian of two solutions ψ_1, ψ_2 of the Schrödinger equation:

$$\begin{aligned}
\mathcal{W}\left(\psi_1, \psi_2\right) &= \psi_1(z)\psi_2'(z) - \psi_1'(z)\psi_2(z) \qquad &\text{(I.50)}\\
&= \boldsymbol{\psi}_1(\boldsymbol{z})\boldsymbol{\psi}_2'(z) - \boldsymbol{\psi}_1'(\boldsymbol{z})\boldsymbol{\psi}_2(\boldsymbol{z}) \qquad &\text{(I.51)}\\
&= \mathcal{W}\left(\boldsymbol{\psi}_1, \boldsymbol{\psi}_2\right). \qquad &\text{(I.52)}
\end{aligned}$$

It follows that the reflection and transmission amplitudes r and t are invariant under the transformation. The probability density current is also preserved as it can be expressed in terms of a Wronskian

$$j = \frac{\hbar}{2im}\mathcal{W}(\psi^*, \psi). \tag{I.53}$$

I.2.b Liouville transformations for the V_4 potential

We study now in details the case of the V_4 potential:

$$V_4(z) \equiv -\frac{C_4}{z^4}. \tag{I.54}$$

This potential corresponds to the long-range part of the Casimir-Polder potential, and its simple form leads to explicit Liouville transformations and interesting related symmetries. The typical length scale related to this potential is ℓ_4, defined as follows:

$$\ell_4 \equiv \frac{\sqrt{2mC_4}}{\hbar}. \tag{I.55}$$

For the V_4 model, the WKB wave-vector has the simple form:

$$k_{\mathrm{dB}}(z) = \sqrt{k^2 + \frac{\ell_4^2}{z^4}}\ . \tag{I.56}$$

This leads to a non trivial symmetry property for the Liouville transformation corresponding to inversion:

$$\hat{z} = -\frac{\zeta^2}{z}\ , \tag{I.57}$$

which maps the physical domain $z \in [0, \infty]$ into an inverted domain $\hat{z} \in [-\infty, 0]$, while exchanging the roles of the cliff-side and far-end.

The inversion (I.57) is an homographic function, so that its Schwarzian derivative $\{z, \hat{z}\}$ vanishes. If $\boldsymbol{z}$ is another map, chosen arbitrarily, Cayley's identity (I.49) leads to:

$$\{\boldsymbol{z}, z\} = \left(\hat{z}'(z)\right)^2 \{\boldsymbol{z}, \hat{z}\}\,. \tag{I.58}$$

In particular, by choosing $\boldsymbol{z} \propto \phi_{dB}$ in (I.58), one finds from (I.14) that the badlands function is invariant under the Liouville transformation $z \to \hat{z}$:

$$Q(z) = \hat{Q}(\hat{z}). \tag{I.59}$$

We consider also two different Liouville transformations adapted to the V_4 potential. The first one, presented in I.2.c, leads to an analytical solution of the Schrödinger equation. The second one, derived in I.2.d, makes appear badlands functions. The two Liouville transformations are represented in the diagram (I.60). The group property of these transformations, which manifests itself by the commutativity of the diagram (I.60), allows to stroll from a representation to another.

$$\begin{tikzcd}
& (z,\psi) \arrow[dl, "\text{Badlands functions}"'] \arrow[dr, "\text{Mathieu functions}"] & \\
(\boldsymbol{z},\boldsymbol{\psi}) & & (\tilde{z},\tilde{\psi}) \arrow[ll]
\end{tikzcd} \tag{I.60}$$

I.2.c Analytical solution with Mathieu coordinates

We derive explicitly an analytical method which is used to solve the Schrödinger equation for the V_4 model [121, 122]. The derivation is based on the work of [123] and uses results from [124, 125]. This change of coordinates is presented as a Liouville transformation [119]:

$$\tilde{z}(z) = \ln\frac{z}{\zeta} \tag{I.61}$$

$$\tilde{\psi}(\tilde{z}) = \frac{\psi(z)}{\sqrt{z}} \tag{I.62}$$

where ζ is defined by :

$$\zeta \equiv \sqrt{\frac{\ell_4}{k}} = \sqrt[4]{\frac{C_4}{E}}. \tag{I.63}$$

The Schrödinger equation (I.6) becomes a modified Mathieu equation:

$$\tilde{\psi}''(\tilde{z}) + (-1/4 + 2q\cosh(2\tilde{z}))\tilde{\psi}(\tilde{z}) = 0 \tag{I.64}$$

with $q \equiv k\ell_4$. A pair of solutions to this equation can be written as series involving products of Bessel functions:

$$\tilde{\psi}^{(\pm)}(\tilde{z}) = \sum_{n=-\infty}^{\infty} (-1)^n A_n^{(\tau)} J_{\pm(n+\tau)}(\sqrt{q}e^{\tilde{z}}) J_{\pm n}(\sqrt{q}e^{-\tilde{z}}). \tag{I.65}$$

τ is the Mathieu characteristic exponent and $A_n^{(\tau)}$ obeys the following recurrence relation:

$$((\tau+2n)^2 - 1/4)A_n^{(\tau)} + q(A_{n+1}^{(\tau)} + A_{n-1}^{(\tau)}) = 0. \tag{I.66}$$

As a result of the invariance of equation (I.64) under parity $\tilde{z} \to -\tilde{z}$, which is the symmetry discussed in (I.57), $\tilde{\psi}^{(\pm)}(-\tilde{z})$ are also solutions, and one can show that:

$$\tilde{\psi}^{(\pm)}(\tilde{z}) = e^{\mp\sigma}\tilde{\psi}^{(\mp)}(-\tilde{z}), \quad \sigma = \ln\frac{\tilde{\psi}^{(-)}(0)}{\tilde{\psi}^{(+)}(0)}. \tag{I.67}$$

From previous equalities and from known asymptotic behaviors of Bessel functions, we deduce reflection and transmission amplitudes for a V_4 potential:

$$r_4 = -i\frac{\sinh(\sigma)}{\sinh(\sigma + i\pi\tau)} \tag{I.68}$$

$$t_4 = \frac{\sin(\pi\tau)}{\sinh(\sigma + i\pi\tau)}. \tag{I.69}$$

The reflection probability $R_4 \equiv |r_4|^2$ is plotted in figure I.4. This reflection probability only depends on the product $k\ell_4$. It means that for a given incident energy E, and also k, the reflection probability increases when ℓ_4, and also the amplitude of the potential given by C_4, decreases.

I.2.d WKB phase: badlands

We specify now a Liouville transformation that is relevant to highlight quantum reflection in the case of a V_4 potential. We choose the new coordinate as a multiple of the WKB phase [118, 119]:

$$\begin{aligned} \boldsymbol{z} &= \frac{\phi_{dB}(z)}{\sqrt{k\ell_4}} \\ \boldsymbol{\psi}(\boldsymbol{z}) &= \sqrt{\boldsymbol{z}'(z)}\psi(z) \end{aligned} \tag{I.70}$$

with ℓ_4 the typical range of the Casimir-Polder potential (I.55).

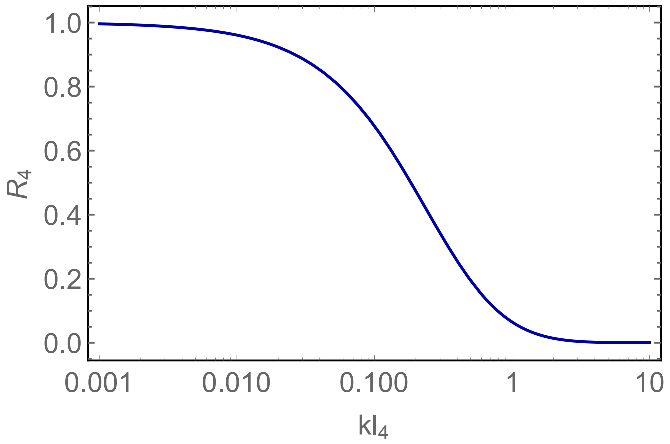

Figure I.4: Reflection probability R_4 obtained for a V_4 potential.

Notice that the WKB phase is defined up to a reference point z_ϕ that has to be fixed. It comes down to choosing a phase origin for the wavefunction ϕ at $z \to +\infty$ where the WKB phase is linear (plane wave):

$$\lim_{z\to+\infty} (\phi_{dB}(z) - kz) = \phi \tag{I.71}$$

$$\boldsymbol{z}_\phi \equiv \int_{z_\phi}^{z_0} \sqrt{F(z')}dz'/\sqrt{k\ell_4}. \tag{I.72}$$

The phase ϕ corresponds actually to some translation length $\boldsymbol{z}_\phi$ in the new coordinates that will be adjusted later on by considerations on symmetries.

We can now rewrite the Schrödinger equation in the transformed coordinates:

$$\begin{gathered} \boldsymbol{\psi}''(\boldsymbol{z}) + \boldsymbol{F}(\boldsymbol{z})\boldsymbol{\psi}(\boldsymbol{z}) = 0 \\ \boldsymbol{F}(\boldsymbol{z}) = \boldsymbol{E} - \boldsymbol{V}_4(\boldsymbol{z}). \end{gathered} \tag{I.73}$$

The new energy, potential and wave-vector are also given by:

$$\begin{gathered} \boldsymbol{E} = k\ell_4 \\ \boldsymbol{V}_4(\boldsymbol{z}) = k\ell_4\, Q(z) \\ \boldsymbol{k} = \sqrt{k\ell_4}. \end{gathered} \tag{I.74}$$

In particular, the potential $\boldsymbol{V}_4(\boldsymbol{z})$ is proportional to the badlands function $Q(z)$ discussed in I.1.d. $\boldsymbol{V}_4$ can also be written explicitly:

$$\boldsymbol{V}_4(\boldsymbol{z}) = \frac{5}{\left(\frac{z^2}{\zeta^2} + \frac{\zeta^2}{z^2}\right)^3}. \tag{I.75}$$

This potential reaches a maximum for $z = \zeta$, corresponding to $\boldsymbol{z}_M \equiv \boldsymbol{z}(z = \zeta)$:

$$\begin{aligned} \boldsymbol{z}_M &= 2\left[{}_2F_1\left(\frac{1}{2}, -\frac{1}{4}, \frac{3}{4}, -1\right) - \frac{1}{\sqrt{2}}\right] + \boldsymbol{z}_\phi \\ &= \boldsymbol{z}_* + \boldsymbol{z}_\phi \end{aligned} \tag{I.76}$$

where ${}_2F_1$ is the hypergeometric function that relates $\boldsymbol{z}$ and z for a perfect C_n potential [36]. We can write $\boldsymbol{z}_*$ in a nicer way:

$$\boldsymbol{z}_* = \frac{1}{\sqrt{\pi}}\Gamma\left(\frac{3}{4}\right)^2. \tag{I.77}$$

In order to make the potential symmetrical, we impose $\boldsymbol{z}_M = 0$, and also $\boldsymbol{z}_\phi = -\boldsymbol{z}_*$. This choice fixes ϕ in the definition (I.71). This choice differs from the phase choice in [119] where $\boldsymbol{z}_\phi = 0$. It implies a translation of the potential in Liouville coordinates and a translation of the reference point at $+\infty$ for calculating reflection and transmission amplitudes, while the reference point at $-\infty$ remains unchanged. As a consequence, the reflection amplitude r_4 (I.68) is unchanged while the transmission amplitude t_4 (I.69) differs by a phase factor $\exp(2ik\ell_4\boldsymbol{z}_*)$ in comparison to [119].

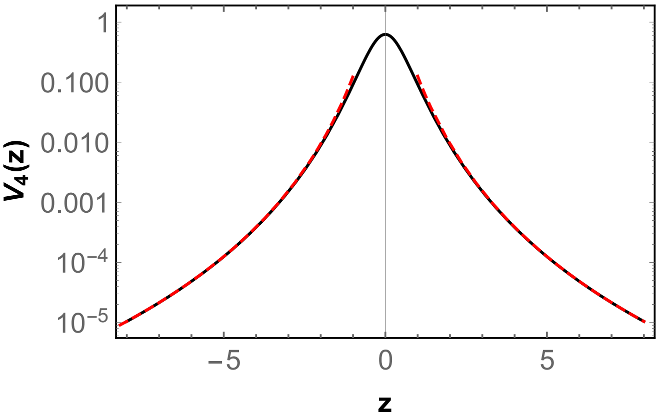

Figure I.5: Black line represents the potential $\boldsymbol{V}_4(\boldsymbol{z})$ and the dashed red lines correspond to the asymptotic behavior: $5/\boldsymbol{z}^6$.

The new potential landscape is plotted in figure I.5. $\boldsymbol{V}_4$ is a peaked function which vanishes far from the surface where the potential goes to zero but also at the surface, where the classical momentum becomes very large. The original problem of quantum reflection on a potential well which diverges at one end of the domain $z \in]0, \infty[$ is therefore mapped onto an equivalent problem where a particle scatters on a potential barrier which vanishes at both ends of the transformed domain $\boldsymbol{z} \in]-\infty, \infty[$. Quantum reflection on an *attractive well* is now intuitively understood as reflection on a *repulsive wall*, with the same scattering properties. The transformed problem is thus a well-defined scattering problem with no interaction in the asymptotic input and output states. Moreover the transformed problem can have classical turning points where $\boldsymbol{F} = 0$ or $\boldsymbol{E} = \boldsymbol{V}$, in which case it corresponds to a semiclassical picture radically different from the original one.

Let's investigate some universal properties of $\boldsymbol{V}_4$ that does not depend on the amplitude of the original V_4 potential since the change of coordinates was done as in (I.70). For doing that, we establish a link with Mathieu coordinates defined in I.2.c.

$$\begin{aligned} \boldsymbol{V}_4(\boldsymbol{z}) &= \frac{5}{8\cosh^3(2\tilde{z})} \\ \boldsymbol{z} &= \int_0^{\tilde{z}} \sqrt{2\cosh(2x)}\mathrm{d}x. \end{aligned} \tag{I.78}$$

From thus expressions, we obtain

$$\boldsymbol{z} \underset{\tilde{z}\to\infty}{\simeq} e^{\tilde{z}}. \tag{I.79}$$

We then find the asymptotic behavior of $\boldsymbol{V}_4$:

$$\boldsymbol{V}_4(\boldsymbol{z}) \underset{\boldsymbol{z}\to\pm\infty}{\simeq} \frac{5}{\boldsymbol{z}^6}. \tag{I.80}$$

If we apply a change of coordinates in (I.78), we find that $\boldsymbol{V}_4$ is an even function of $\boldsymbol{z}$. This is another manifestation of the inversion symmetry (I.57).

We finally remark that the maximum of the $\boldsymbol{V}_4$ peak, that is $\frac{5}{8}$, is independent on the potential amplitude C_4. However, the energy $\boldsymbol{E}$ of the particle in the new coordinates is proportional to ℓ_4. When C_4 decreases, and also ℓ_4, the energy in the new coordinates also decreases while the potential is unchanged. It follows that the reflection probability increases. Thus, we have shown in the case of a V_4 potential that quantum reflection is higher for weaker potentials. This counter intuitive property holds more generally for Casimir-Polder potentials.

I.3 Quantum reflection on liquid helium bulk

I.3.a Casimir interaction

We consider two objects at rest in vacuum, whose interaction with the electromagnetic field is described by the reflection operator $\mathcal{R}$ which gives the field $\vec{\mathcal{E}}_{\text{refl}}$ reflected by the object for a given incident field $\vec{\mathcal{E}}_{\text{in}}$:

$$\vec{\mathcal{E}}_{\text{refl}} = \mathcal{R}\vec{\mathcal{E}}_{\text{in}}. \tag{I.81}$$

The presence of the two objects induces a shift in the energy of the electromagnetic field compared with the situation where they are infinitely far apart. This energy difference induces itself a force, that is called the *Casimir force*.

The Casimir force and the Casimir energy can be computed in general at all temperatures [126, 127]. At temperature T, the number of photons involved in each mode of the electromagnetic field obeys the Plank's law:

$$N(\omega) = \frac{1}{2} + \frac{1}{\exp(\hbar\omega/k_B T) - 1}. \tag{I.82}$$

In the rest of the thesis, we restrict ourself to the zero-temperature expression, that involves only the zero-point contribution of the electromagnetic field. The zero-temperature approximation remains valid since the separation distance z between the two objects is smaller than the thermal wavelength $\lambda_T \equiv \hbar c/k_b T$ (~ 10 µm at 300 K).

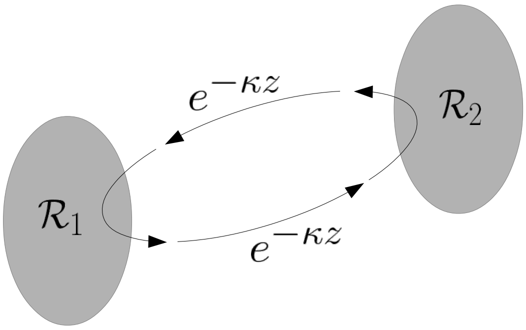

Figure I.6: Schematic representation of a round trip of the field between two objects separated by a distance z and described by reflection operators $\mathcal{R}_1$ and $\mathcal{R}_2$.

In that regime, the Casimir potential can be given a general expression in the scattering formalism [126]:

$$V(z) = \hbar \int_0^\infty \frac{\mathrm{d}\xi}{2\pi} \mathrm{Tr} \log\left(1 - \mathcal{R}_1 e^{-\kappa_z z} \mathcal{R}_2 e^{-\kappa_z z}\right) \tag{I.83}$$

$$\kappa_z = \sqrt{\boldsymbol{q}^2 + \xi^2/c^2}\ , \quad \boldsymbol{k} = \boldsymbol{q} \pm k_z \mathbf{e}_z. \tag{I.84}$$

This formula is obtained after a Wick rotation to imaginary frequencies $\omega = i\xi$, which transforms the oscillating terms $e^{ik_z z}$ describing translation from one object to the other into decaying exponentials $e^{-\kappa_z z}$ In these formulas, $\boldsymbol{k}$ is the wavevector of the electromagnetic radiation. The trace represents a summation over the transverse wavevector $\boldsymbol{q}$ and the polarizations TE, TM of the electromagnetic field.

The product $\mathcal{R}_1 e^{-\kappa_z z} \mathcal{R}_2 e^{-\kappa_z z}$ in the expression (I.83) represents a round trip of the field between the two objets, as it is illustrated in figure I.6. Meanwhile the log represents the sum over the number of roundtrips, since:

$$\log\left(1 - \mathcal{R}_1 e^{-\kappa_z z} \mathcal{R}_2 e^{-\kappa_z z}\right) = -\sum_{n=1}^{\infty} \frac{1}{n} \left(\mathcal{R}_1 e^{-\kappa_z z} \mathcal{R}_2 e^{-\kappa_z z}\right)^n. \tag{I.85}$$

Let us now specify it in the case of an atom above a surface, where we will consider only the dominant term $n = 1$ in this sum.

I.3.b Casimir-Polder interaction

We consider now the case where the first object is an antihydrogen atom in the ground state and the second object is a plane matter surface. We note $\mathbf{e}_z$ the axis perpendicular to the surface, and z the height of the atom above it, as it is represented in figure I.7.

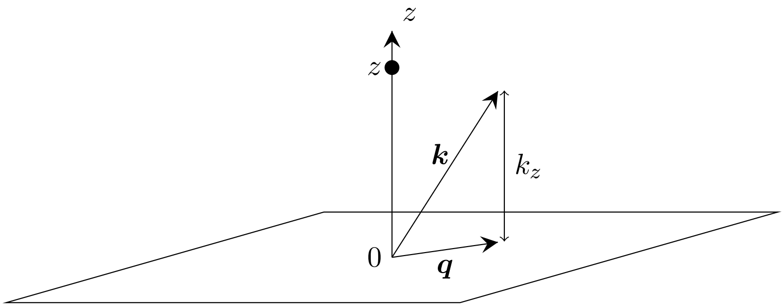

Figure I.7: Schematic representation of an atom at height z above a plane surface. The wavevector $\boldsymbol{k}$ is decomposed along its transverse $\boldsymbol{q}$ and longitudinal k_z components.

In that configuration, the reflection of the electromagnetic field on the two objects is modeled by:

- the dynamic polarizability of the antihydrogen $\alpha(i\xi)$, which is the same as that of hydrogen at the level of approximation needed for our calculations, as confirmed at CERN in the ALPHA experiment [128, 129]. Possible differences between the two cases would be too small to have an influence at the level of precision aimed in the present study. The static polarizability at zero frequency is well known:

$$\frac{\alpha(0)}{4\pi\epsilon_0} = \frac{9}{2}\mathrm{a}_0^3 \tag{I.86}$$

  where a_0 is the Bohr radius. The frequency dependence can be obtained from [130].

- the reflection operator on the plane is diagonal in the plane wave basis where it is given by the Fresnel reflection amplitudes r_{TE}, r_{TM}. These reflection coefficients depend on the material properties of the medium through its relative dielectric function $\varepsilon(i\xi)$. A more detailed treatment taking into account the statistical disorder of the medium and its consequence to the reflection amplitudes and the potential fluctuations is achieved in chapter IV.

As the term corresponding to a roundtrip is small, we neglect multiple reflections on the atom by only keeping the first order of the log expansion (I.85) and find [91, 131]:

$$V(z) = \frac{\hbar}{c^2} \int_0^\infty \frac{d\xi}{2\pi} \xi^2 \alpha(i\xi) \int \frac{d^2\mathbf{q}}{(2\pi)^2} \frac{e^{-2\kappa_z z}}{2\kappa_z} \sum_p s_p r_p \tag{I.87}$$

where $p \in \{\mathrm{TE}, \mathrm{TM}\}$ indices the field polarization, and

$$s_p = \begin{cases} 1 & \text{for } p = \mathrm{TE} \\ -\frac{\xi^2 + 2c^2\mathbf{q}^2}{\xi^2} & \text{for } p = \mathrm{TM} \end{cases} . \tag{I.88}$$

Thanks to the formula (D.1), we can easily compute the Casimir-Polder potential for surfaces for which we know the optical response at all frequencies. Before focusing the calculation on a liquid helium surface, let us expose the asymptotic universal behavior of Casimir-Polder potentials. These potentials, attractive at all distances, behave as non retarded *van der Waals* potentials at short distances and as *retarded* potentials at large distances since it takes into account the finiteness of the speed of light [132, 133], with the two domains separated by the wavelength $\lambda_A \simeq 121\text{nm}$ of the first atomic transition 1S→2P of antihydrogen:

$$V(z) \simeq -\frac{C_3}{z^3} \equiv V_3(z) , \quad z \ll \lambda_A, \tag{I.89}$$

$$V(z) \simeq -\frac{C_4}{z^4} = V_4(z) , \quad z \gg \lambda_A. \tag{I.90}$$

The typical range of the Casimir-Polder potential is related to the retarded regime constant C_4 thanks to (I.55) relation and is of the order of tens or hundreds of nanometers depending on the surface.

medium	C_3 $[\mathrm{E_h a_0^3}]$	C_4 $[\mathrm{E_h a_0^4}]$
ideal mirror	0.25	73.6
gold	0.085	73.4
silicon	0.101	50.3
silica	0.053	28.1
liquid ^{3}He	0.0034	1.19
liquid ^{4}He	0.0045	1.55

Table I.1: Constants C_3 and C_4 for the ideal mirror and for bulks of liquid helium and substrates made of silica, silicon or gold, expressed in atomic units ($\mathrm{E_h}$ and $\mathrm{a_0}$ are the Hartree energy and Bohr radius).

For a perfectly reflecting mirror (for electromagnetic field), the retarded regime corresponds to:

$$V_*(z) = -\frac{C_4^*}{z^4} , \quad C_4^* = \frac{3\alpha(0)\hbar c}{32\pi^2\epsilon_0} \tag{I.91}$$

while constants C_3 and C_4 for liquid helium bulk, and substrates as silica, silicon or gold are calculated numerically and are given in table I.1. Some of these calculations come from [91], while results for liquid helium are presented in I.3.c. The less reflective for the electromagnetic field a material is, the weaker the Casimir-Polder potential, from perfectly reflective to liquid helium mirrors.

I.3.c Casimir-Polder potential for a liquid helium bulk

We are now able to derive the Casimir-Polder potential on a liquid helium surface. The motivations for choosing this surface are the following:

- since liquid helium is almost transparent for electromagnetic fields, the resulting Casimir-Polder potential is very weak. Thanks to the Liouville transformations defined in section I.2, we understand now the counter intuitive property of a high reflectivity for such weak potentials. This implies a large lifetime of the antihydrogen atom on the mirror.
- at low temperatures (below 100 mK) [134], liquid helium offers a well defined surface and perfectly described by an effective dielectric constant in such a way that we disregard the role played by excitations in the helium film.
- the interaction of a hydrogen atom with a liquid helium surface arouses interest. While in this thesis we only consider the Casimir-Polder interaction between the atom and the surface, the potential of interaction for a hydrogen atom leads to the existence of a single bound state with an adsorption energy of the order of 1K on ^{4}He bulk [24, 135, 136]. These differences are not studied in the thesis but the following work is a necessary step to better understand the physics of hydrogen-helium interaction, that could be experimentally tested in the future [137].

We consider an antihydrogen atom above a liquid helium film of thickness d supported by a substrate (see Fig. I.8). We begin with the limiting cases of $d \to \infty$ where we obtain the Casimir-Polder potential of liquid helium bulk (that is liquid helium film with a large thickness). The thickness dependence is studied in I.4.

The reflection amplitudes r_p in expression (D.1) are calculated for polarizations p by combining the Fresnel amplitudes at interfaces and propagation in the helium film. Let us remind its expressions[2]:

$$\begin{aligned} r_{\mathrm{TE}}^{V\to He} &= \frac{\kappa_z - \tilde{\kappa}_z}{\kappa_z + \tilde{\kappa}_z} \\ r_{\mathrm{TM}}^{V\to He} &= \frac{\epsilon(i\xi)\kappa_z - \tilde{\kappa}_z}{\epsilon(i\xi)\kappa_z + \tilde{\kappa}_z} \\ \kappa_z = \sqrt{\boldsymbol{q}^2 + \xi^2/c^2}\ , &\quad \tilde{\kappa}_z = \sqrt{\boldsymbol{q}^2 + \epsilon(i\xi)\xi^2/c^2} \end{aligned} \tag{I.92}$$

---

[2] r_{TE} and r_{TM} are reflection amplitudes for the electromagnetic field, do *not* confuse with reflection amplitude for matter waves.

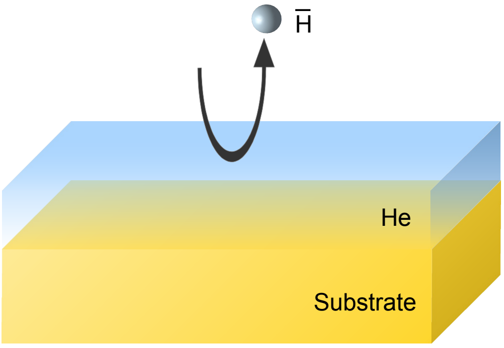

Figure I.8: Representation of the quantum reflection process for an antihydrogen atom falling onto a helium film supported by a substrate. We study the limiting case of a bulk of helium (very large thickness of the film) as well as the general case of a film of finite thickness d supported by a substrate.

where κ_z and $\tilde{\kappa}_z$ are the longitudinal components of the wavevector respectively in vacuum and in the liquid helium bulk expressed after a Wick rotation.

The optical properties of ^{4}He are described with a sufficient accuracy by a model dielectric constant with three resonances [138]

$$\begin{aligned} &\epsilon(i\xi) \simeq 1 + \sum_{k=1,2,3} \frac{a_k}{1+(\xi/\omega_k)^2} \ , \\ &(\omega_1,\omega_2,\omega_3) = (3.22, 3.74, 12) \times 10^{16} \ \text{rad.s}^{-1} \ , \\ &(a_1,a_2,a_3) = (0.016, 0.036, 0.0047) \ . \end{aligned} \tag{I.93}$$

This model corresponds to a dielectric constant close to unity at the static limit ($\epsilon(0) - 1 \simeq 0.0567$) as well as at all frequencies. We also use the optical model (I.93) for ^{3}He, with the same resonance frequencies ω_k, and the resonance amplitudes a_k multiplied by the same factor calculated to reproduce the static dielectric constant $\epsilon(0) - 1 \simeq 0.043$ known from experiments [139]. In both cases we use an effective dielectric constant and disregard the role played by excitations in the helium film. The latter is well justified at temperatures below 100 mK [134], the temperature range where results obtained in the following are accurate.

These numbers lead to a poor reflectance of the film for electromagnetic waves and weak values for the Casimir-Polder potential with values even weaker for ^{3}He than for ^{4}He. It follows that quantum reflection occurs closer to the material surface where the Casimir-Polder potential is much steeper, which explains the large quantum reflection probability found below, with reflection even larger for ^{3}He than for ^{4}He. This result is enhanced by the study of badlands in the frame of Liouville transformations in I.2.

The ratios $V(z)/V_*(z)$ obtained for liquid ^{3}He and ^{4}He bulks as well as silica, silicon and gold bulks are plotted as full lines in Fig. I.9.

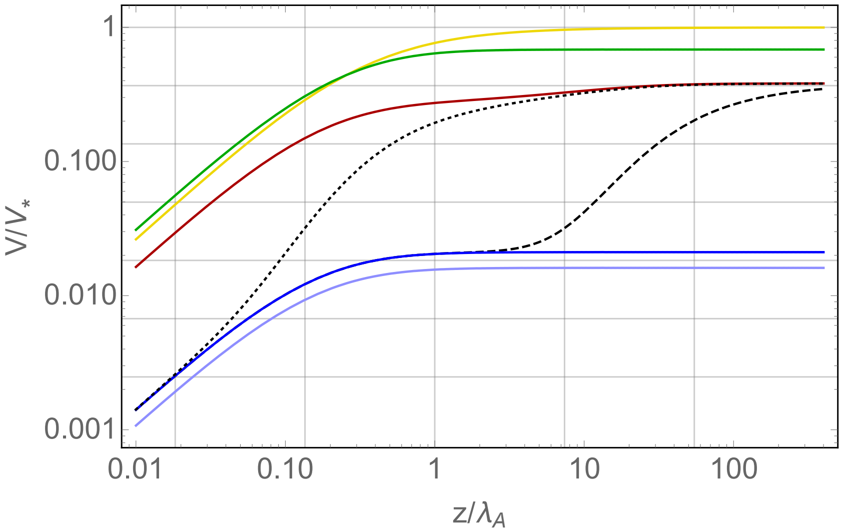

Figure I.9: Casimir-Polder potentials $V(z)$ normalized by the potential $V_*(z)$ calculated for a perfect mirror at large distances. Distances z are normalized by the wavelength $\lambda_A \simeq 121$nm of the 1S→2P antihydrogen transition. The full lines correspond, from bottom to top, to bulks of ^{3}He (light blue), ^{4}He (dark blue), silica (red), silicon (green) and gold (yellow). The other lines correspond to liquid helium films of thickness $d = 10\lambda_A$ (dashed line) and $d = 0.1\lambda_A$ (dotted line) on a silica bulk.

I.3.d Quantum reflection on liquid helium bulk

The previous calculations show a very low value of the Casimir-Polder potential for thick enough liquid helium films, and a large height of the peak for the corresponding badlands. We now discuss quantitatively the consequence of this fact in terms of large quantum reflection from a liquid helium bulk.

To this aim, we solve the Schrödinger equation for the antihydrogen falling into the Casimir-Polder potential above the liquid helium film. We then obtain the reflection amplitude r as the ratio of the outgoing wave to the incoming one far from the film (see (A.14)). The quantum reflection probability is the squared modulus of this amplitude $R = |r|^2$. The results are shown in figure I.10 with larger and larger probability obtained for the weaker and weaker potentials of Fig. I.9. In particular, quantum reflection for atoms falling from a height h and thus having a given energy $E = mgh$ is much larger on a liquid helium bulk than on the other materials studied here [39].

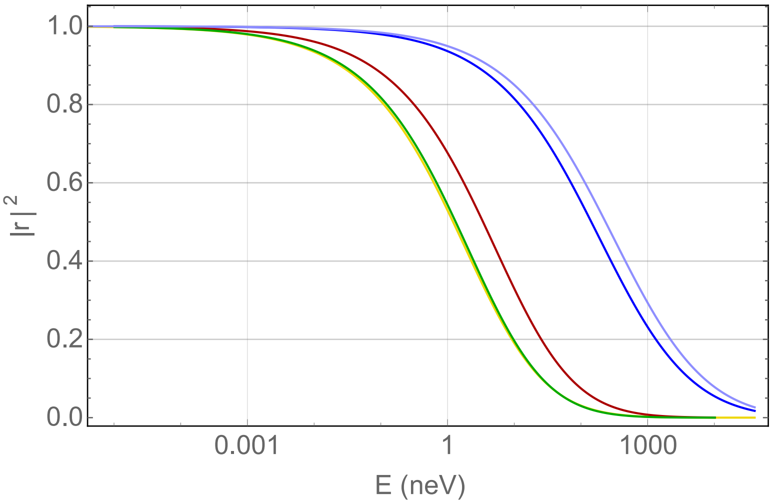

Figure I.10: Quantum reflection probability as a function of the free fall height of the atom h, that is also of its energy $E = mgh$. The full lines correspond, from top to bottom, to bulks of ^{3}He (light blue), ^{4}He (dark blue), silica (red), silicon (green) and gold (yellow).

Scattering lengths obtained for different bulks are summarized in table I.2. In agreement with figure I.10, the smallest values of b corresponding to the better reflectivity are obtained for liquid helium bulks.

material	a [a$_0$]
perfectly reflective	$-53.5 - 544i$
silicon	$-97.8 - 436i$
silica	$-77.8 - 273i$
gold	$-150.9 - 459.9i$
liquid ^4He	$-35.0 - 44.8i$
liquid ^3He	$-30.1 - 35.4i$

Table I.2: Scattering length a in atomic units corresponding to the scattering of antihydrogen atom above different bulks.

The imaginary part b of the scattering length also determines the mean lifetime τ for atoms bouncing above the bulk [120]:

$$\tau = \frac{\hbar}{2mgb}. \tag{I.94}$$

In table I.3, we compare the values obtained for τ from the quantum reflection probabilities drawn on figure I.10. In a classical picture, the bouncing period for an atom prepared at height h is

$$T_1 \equiv 2\sqrt{\frac{2h}{g}}. \tag{I.95}$$

We also give the values for the number $N_1 = \tau/T_1$ of bounces for an atom in the first quantum levitation state ($\sim$ peV, quantum levitation states will be defined in chapter II). The numbers show that liquid helium is a much better reflector for antihydrogen matter waves than the other materials which have been studied up to now [39]. The comparison with porous materials studied in [92] shows also a larger lifetime for liquid helium bulk than for porous silicon or silica with reasonable porosity. The much larger lifetime, that is also the much larger number of bounces before annihilation, implies that it should be possible to trap antimatter for long enough to improve significantly the spectroscopy measurements discussed in [120], or to produce interferences between quantum gravitational states, as detailed in chapter III.

material	τ [s]	N_1
perfectly reflective	0.11	33
silicon	0.14	42
silica	0.22	66
gold	0.13	39
liquid ^4He bulk	1.35	405
liquid ^3He bulk	1.71	514

Table I.3: Lifetime τ of antihydrogen in seconds above various material surfaces and number N_1 of bounces for an atom in the first quantum gravitational state for different bulk materials.

We plotted in figure I.11 different potentials $\boldsymbol{V}(\boldsymbol{z})$ corresponding to the same Casimir-Polder potential between an antihydrogen atom and a liquid helium bulk, but with three different incident energies E: 0.1, 1 and 10 neV. We remark that the right part of these transformed potentials are very close to the $\boldsymbol{V}_4$ potential, while the left part changes with energy and has a large tail, corresponding to the short-range part of the Casimir-Polder potential. We treat this phenomenon in a more quantitative way in II.2.d. In the same way as for the V_4 potential described in I.2.d it is also clear that the reflection probability increases when the energy of the incident particle decreases, the latter having to cross a similar wall with less energy.

Let us finally compare new potential landscapes coming from different Casimir-Polder potentials at the same energy. In fact, it is wiser to compare directly badlands $Q(\boldsymbol{z}) = \boldsymbol{V}(\boldsymbol{z})/k\ell_4$ instead of $\boldsymbol{V}(\boldsymbol{z})$, because the range ℓ_4 changes from a Casimir-Polder potential to another. Badlands for silicon, silica and liquid helium bulks at the same energy $E =$ 1 neV are plotted in figure I.12. The counter intuitive property of a better quantum reflection for a weaker potential is once again emphasized: the weaker the potential is,

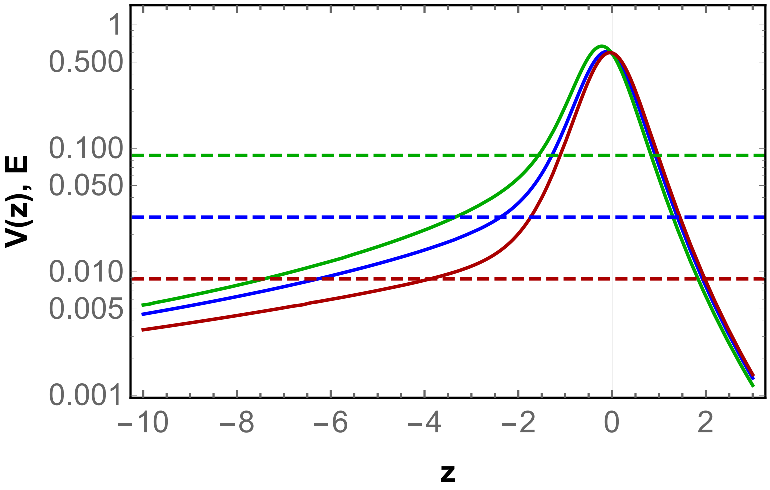

Figure I.11: The plots represent the constants $\boldsymbol{E}$ (horizontal dashed lines) and the potentials $\boldsymbol{V(z)}$ (curves) calculated for different scattering problems, corresponding to the same Casimir-Polder potential between an antihydrogen atom and a liquid helium bulk at energies E equal to 0.1, 1 and 10 neV, respectively in red, blue, and green lines from the lowest to the highest value of E, or from the lowest to the highest value of $\boldsymbol{V}$ in the left-hand part of the plot.

the higher the badlands. In particular, we see in figure I.12 a much higher peak for the badlands coming from the Casimir-Polder potential for liquid helium than for other bulks, which leads to a much better quantum reflection.

I.4 Quantum reflection on liquid helium film

I.4.a Casimir-Polder potential dependence on film thicknesses

The previous calculation supposed an infinite thickness of liquid helium. A more realistic situation corresponds to a liquid helium thin film of thickness d deposited on a substrate.

We also need to compute the Fresnel reflection amplitude r_{TE} and r_{TM} for the full scattering problem. The scattering matrix formalism defined in I.1.f is in fact well adapted to decompose the full reflection process in elementary reflection processes for each field polarization p. Let us denote $\mathcal{S}_p^{V\to He}$ the scattering matrix describing the reflection of the p polarization of the field at the interface between vacuum and liquid helium and in the same way $\mathcal{S}_p^{He\to S}$ the reflection at the interface between liquid helium and the substrate. Let $\mathcal{T}^{prop}$ be matrix corresponding to the propagation of the field in the liquid

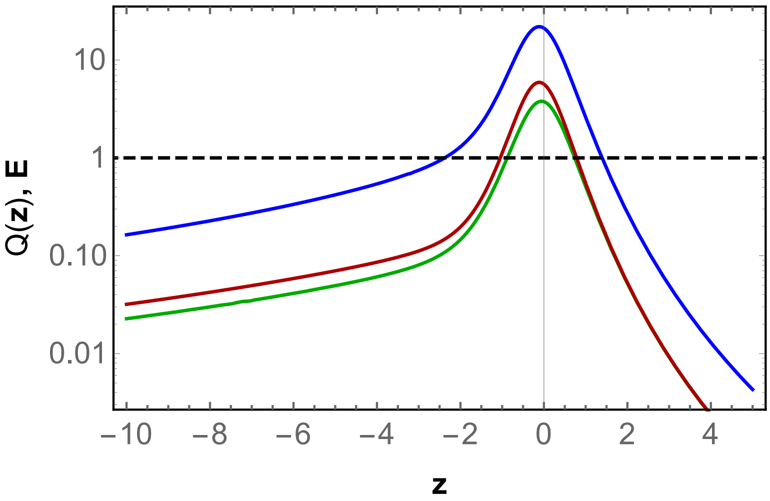

Figure I.12: The plots represent the constant $\boldsymbol{E} = 1$ (horizontal black dashed line) and the badlands $Q(\boldsymbol{z})$ (curves) calculated for different scattering problems, corresponding to different Casimir-Polder potentials between an antihydrogen atom and silicon, silica and liquid helium bulks, respectively in green, red, blue, from the lowest to the highest value of Q in the left-hand part of the plot. The three badlands $Q(\boldsymbol{z})$ are calculated at the same energy $E = 1$ neV.

helium film:

$$\mathcal{T}^{prop} = \begin{pmatrix} e^{-\tilde{\kappa}_z d} & 0 \\ 0 & e^{\tilde{\kappa}_z d} \end{pmatrix}. \tag{I.96}$$

Then, the global transfer matrix of the full reflection problem is simply given by the product of the successive transfer matrices, as it is suggested by the scattering matrices composition law (I.33):

$$\mathcal{T}_p = \Pi\left(\mathcal{S}_p^{He\to S}\right) \cdot \mathcal{T}^{prop} \cdot \Pi\left(\mathcal{S}_p^{V\to He}\right). \tag{I.97}$$

At the end the reflection amplitudes r_p is extracted from the global scattering matrix $\mathcal{S}_p = \Pi\left(\mathcal{T}_p\right)$, using the operator Π discussed in (I.29).

Let us present the calculation of $\mathcal{S}_p^{V\to He}$ and $\mathcal{S}_p^{He\to S}$. Reflection amplitudes $r_p^{V\to He}$ are given by (I.92), while $r_p^{He\to S}$ are defined in a similar way:

$$\begin{aligned} r_{\text{TE}}^{He\to S} &= \frac{\tilde{\kappa}_z - \tilde{\kappa}_z^s}{\tilde{\kappa}_z + \tilde{\kappa}_z^s} \\ r_{\text{TM}}^{He\to S} &= \frac{\epsilon^s(i\xi)\tilde{\kappa}_z - \tilde{\kappa}_z^s}{\epsilon^s(i\xi)\tilde{\kappa}_z + \tilde{\kappa}_z^s} \\ \tilde{\kappa}_z^s &= \sqrt{\boldsymbol{q}^2 + \epsilon^s(i\xi)\xi^2/c^2} \end{aligned} \tag{I.98}$$

with $\tilde{\kappa}_z^s$ the longitudinal component of the wavevector in the substrate and $\epsilon^s(i\xi)$ the dielectric function of the substrate. The other coefficients of the $\mathcal{S}_p^{a\to b}$ matrices are related to (I.92) and (I.98) through:

$$\begin{aligned} \overline{r_p}^{a\to b} &= r_p^{b\to a} = -r_p^{a\to b} \\ t_p^{a\to b} &= 1 + r_p^{a\to b} \\ \overline{t_p}^{a\to b} &= t_p^{b\to a} = 1 + \overline{r_p}^{a\to b}. \end{aligned} \tag{I.99}$$

By injecting (I.99) in (I.97), we finally get:

$$r_p = \frac{r_p^{V\to He} + e^{-2\tilde{\kappa}_z d} \cdot r_p^{He\to S}}{1 + e^{-2\tilde{\kappa}_z d} \cdot r_p^{V\to He} \cdot r_p^{He\to S}}. \tag{I.100}$$

The ratios obtained for liquid ^{4}He films with finite thickness d on silica are plotted in Fig. I.9 as dashed lines. They go smoothly from the one obtained for a liquid helium bulk for $z \ll d$ to that for a silica bulk for $z \gg d$.

I.4.b Scattering length oscillations

We now investigate the effect on quantum reflection of the finite thickness of a liquid ^{4}He film supported by a substrate. We present the results of the calculations in terms of the scattering length a which now depends on the thickness d of the film as well as on the optical properties of the substrate.

Results are presented in figure I.13 for films supported by silica, silicon and gold substrates. The important effect of the thickness is clearly seen on this plot. For thicknesses larger than a few tens of nanometers, the scattering length reaches asymptotically the value found above for a liquid ^{4}He bulk. The curves give the thickness of the film to be chosen sufficient for recovering the large lifetimes predicted at the limit of the bulk. This property is also illustrated in terms of variation of the lifetime in figure I.14. As could be expected, the substrate which leads to the larger lifetime for a given thickness of the liquid helium film is the one which would have the best reflectivity without the film (silica in our case).

For small thicknesses, of the order of a few nanometers, real and imaginary parts of the scattering length are found to oscillate in phase quadrature in figures I.13-I.14. This property is confirmed by the variation of a in the complex plane, shown in figure I.15 in the case of a gold substrate. It looks like a consequence of an interference phenomenon that we discuss now.

I.4.c Shape resonance

The shape of the Casimir-Polder potential for the film of thickness $10\lambda_A$ in figure I.9 suggests that the atom falling onto the film sees two zones of rapid variation of the

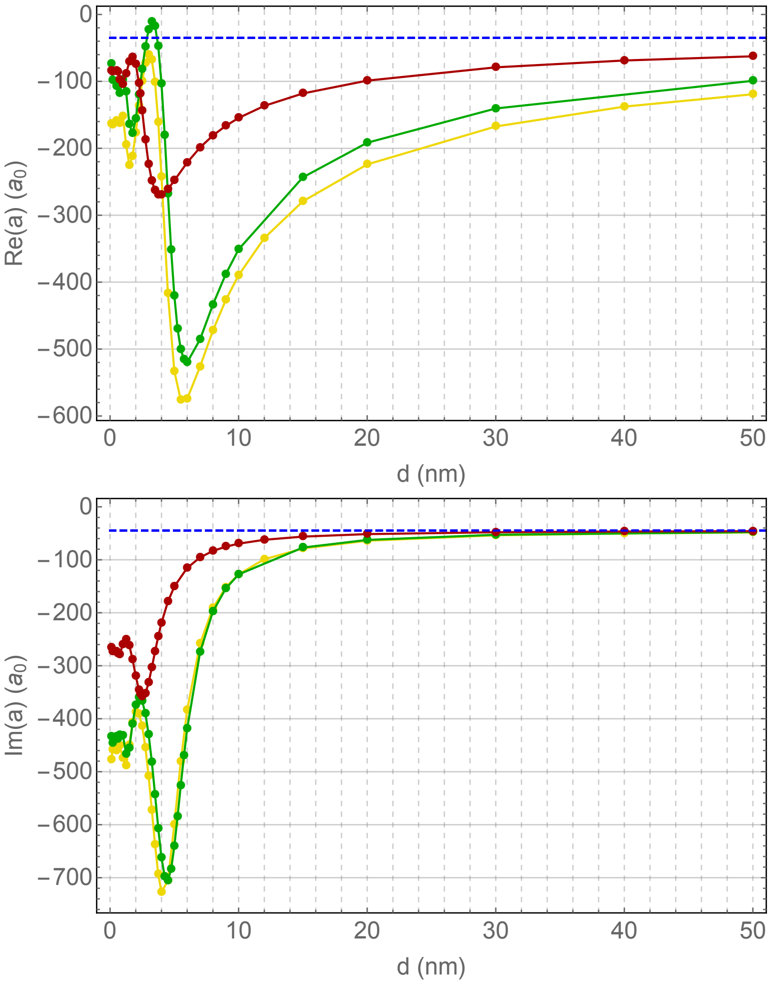

Figure I.13: Real (upper plot) and imaginary (lower plot) parts of the scattering length depending on the thickness d of the liquid ^{4}He film, drawn from the top to the bottom for a silica substrate (red curve), a silicon substrate (green) and a gold substrate (yellow). For comparison, the dashed (blue) line corresponds to real and imaginary parts of the scattering length for a liquid ^{4}He bulk.

potential, the first one at the transition from the potential which would be seen for the naked substrate to that of a helium bulk, and the second one at the approach to the liquid helium film.

Using the Liouville transformation defined in I.2.d, we now interpret the oscillations of the scattering length seen in figure I.15 as an interference between reflections on the two walls. We draw in figure I.16 the badlands function $Q(z)$ for four different thicknesses of the film supported by a gold substrate. Three thicknesses correspond to the colored points emphasized in figure I.13 for d =1 nm (green), 5 nm (red) and 20 nm (blue). For

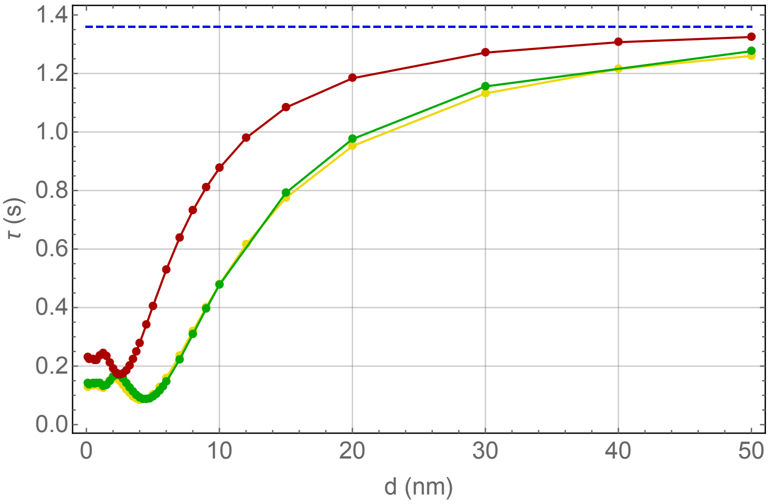

Figure I.14: Lifetime τ depending on the thickness d of the liquid ^{4}He film, drawn from the top to the bottom for a silica substrate (red curve), a silicon substrate (green) and a gold substrate (yellow). For comparison, the dashed (blue) line is the lifetime corresponding to the liquid ^{4}He bulk.

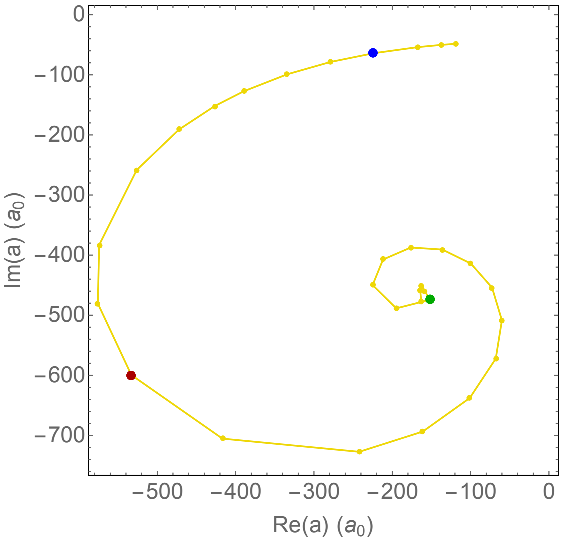

Figure I.15: Scattering length a represented in the complex plane, depending on the thickness d of the liquid helium film above a gold substrate. The thickness ranges from 0.1nm (center of the spiral) to 50nm (outer part of the spiral). Green point corresponds to $d = 1$ nm, red to $d = 5$ nm and blue to $d = 20$ nm.

the purpose of comparison with the case of a naked substrate, a fourth plot is drawn for $d =$ nm (dashed yellow curve). The plots for non null thicknesses show two peaks while only one peak appears for the plot of the naked substrate as well as for the plot of a liquid helium bulk. The peak lying far from the surface is roughly the same for all curves, and it is the same as for the naked substrate. The other one corresponds to the approach to the helium film and its position depends on the thickness of the film.

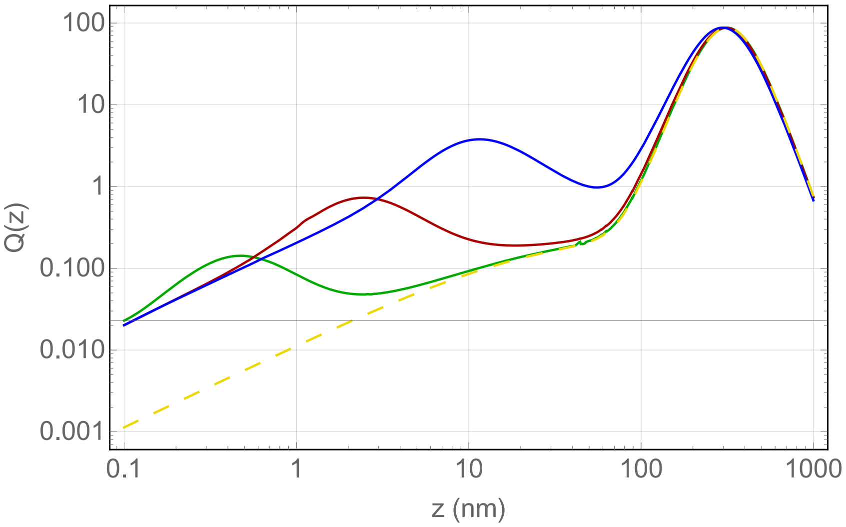

Figure I.16: Badlands functions $Q(z)$ (z in nm) calculated for an antihydrogen atom falling from the energy of the first quantum gravitational state onto a liquid helium film above a gold substrate. The three full lines correspond to three thicknesses of the film, with the same color code as for the points emphasized in figure I.15 : From bottom to top, the thickness of the film is 1 nm (green), 5 nm (red) and 20 nm (blue). The dashed (yellow) curve corresponds to the naked substrate.

For films with non null thicknesses, the two peaks form a cavity where the matter wave can be stored. In the case studied here, the mirror closer to the material surface has a poorer reflectivity than the mirror farther from the material surface. The presence of the cavity leads to a faster annihilation when atoms are trapped, which degrades the lifetime of the antihydrogen atom, as observed in figures I.13-I.14. The interferences taking place in the cavity explain the oscillation patterns highlighted in figure I.13 and I.15. This phenomenon is called *shape resonance* [140]. The associated phase is related to the round-trip dephasing in the cavity, which is determined by the displacement to the left of the weaker peak and the change of the shape of the potential inside the cavity.

Chapter II

Casimir-Polder shifts on quantum levitation states

> “ *J’aime mieux tomber d’en-haut que voler bas.* ”
>
> **Pierre de Ronsard**

Gravitational confinement of particles above a horizontal reflective surface is a common classical process. In quantum physics, this process leads to the existence of quantum levitation states for ultracold matter waves. Such gravitationally bound quantum states have been observed with ultracold neutrons [62–64]. Though atomic mirrors have been realized using inhomogeneous electric or magnetic fields [65–72], gravitationally bound quantum states of atoms remain to be observed.

At the low energies required to reach the quantum regime, quantum levitation states can be built up on quantum reflection above the Casimir-Polder tail created by the surface. It should therefore be possible to trap atoms in quantum levitation states above a horizontal mirror, with gravity pulling them downwards and quantum reflection balancing their free fall [37, 38].

We analyze this system by using a Liouville transformation of the Schrödinger equation and a Langer coordinate adapted to problems with a classical turning point. Reflection on the Casimir-Polder attractive well is replaced by reflection on a repulsive wall and the problem is then viewed as an ultracold atom trapped inside a cavity with gravity and Casimir-Polder potentials acting respectively as top and bottom mirrors. We calculate numerically Casimir-Polder shifts of the energies of the cavity resonances and propose a new approximate treatment which is precise enough to discuss spectroscopy experiments aiming at tests of the weak equivalence principle on antihydrogen.

These quantum levitation states can play a useful role in the emerging investigation of gravitational properties of antimatter. It has recently been proposed to test the weak equivalence principle with antihydrogen by timing its free fall from a height prescribed by a trapping device [11, 14, 141, 142]. The precision of this test, of the order of 1% for the timing experiment, could be improved by using the gravitational quantum states of antihydrogen above a material surface [33, 89].

The basic idea is that the properties of these states are essentially determined by gravity so that spectroscopic techniques can measure accurately the free fall acceleration for antihydrogen [85–87]. As these properties are affected by the proximity of the surface, an accurate determination of the acceleration requires a precise evaluation of Casimir-Polder shifts on quantum levitation states.

In this chapter, we start by presenting separately the effect of gravity on quantum states and a precise description of its quantum reflection on the surface. In section II.1, we recall results for a quantum particle bouncing on an infinitely high and steep potential step, which will be useful as a reference for our discussions, and propose to go a step further than the scattering length to describe the reflection amplitude by proposing an improved effective range theory [143] in section II.2.

We then perform a full quantum treatment of gravity and Casimir-Polder potential. We introduce Liouville-Langer coordinates in section II.3, that will transform the potential landscape while preserving the reflection amplitudes and energies. We calculate the properties of the quasi-stationary states of the quantum bouncer in section II.4, with the transformed physical picture corresponding to a cavity built up with two mirrors, a partly reflective one associated with quantum reflection and a perfectly reflecting one due to gravity. The high accuracy thus achieved should be sufficient for the proposed spectroscopic tests of the weak equivalence principle with antihydrogen, reaching a relative precision of the order of a few 10^{-6} [85–87].

II.1 Gravitational quantum states

II.1.a Quantum bouncers

We consider a particle of mass m and energy E in the Earth gravity field g above a perfectly plane and horizontal mirror, so that the potential V depends only on the altitude z of the particle above the mirror. The wavefunction $\psi(z)$ obeys also the one-dimensional stationary Schrödinger equation

$$-\frac{\hbar^2}{2m}\frac{\mathrm{d}^2\psi}{\mathrm{d}z^2}(z) + V(z)\psi(z) = E\psi(z) \ . \tag{II.1}$$

We start by approximate the mirror as perfectly reflecting. In this ideal *quantum bouncer model*, the particle is perfectly reflected by an infinite repulsive step

$$V(z) = \begin{cases} mgz & \text{if } z > 0 \ , \\ +\infty & \text{otherwise} \ . \end{cases} \tag{II.2}$$

This is a suitable model for neutrons which bounce off the repulsive Fermi pseudo-potential step resulting from the strong interaction of the wavepacket with nuclei in the mirror [144].

We define the length and energy scales associated with quantum effects in the Earth gravity field

$$\ell_g = \left(\frac{\hbar^2}{2m^2 g}\right)^{1/3} \approx 5.87 \ \mu\text{m} \ , \tag{II.3}$$

$$\epsilon_g = \left(\frac{\hbar^2 m g^2}{2}\right)^{1/3} \approx 0.602 \ \text{peV} \ . \tag{II.4}$$

The numerical values correspond to a hydrogen (or antihydrogen) atom and $g \approx 9.81$ m.s^{-2}. They would have to be changed if the acceleration were different for antihydrogen.

II.1.b Airy functions

When written in terms of the dimensionless variables,

$$x \equiv z/\ell_g - E/\epsilon_g \ , \qquad\qquad y(x) \equiv \psi(z), \tag{II.5}$$

the Schrödinger equation (II.1) becomes the Airy equation:

$$y''(x) - xy(x) = 0. \tag{II.6}$$

The general solution of the Schrödinger equation is given by a linear combination of independent solutions of the Airy functions Ai and Bi [125, 145], so that :

$$\psi(z) = A \,\text{Ai}\left(\frac{z}{\ell_g} - \frac{E}{\epsilon_g}\right) + B \,\text{Bi}\left(\frac{z}{\ell_g} - \frac{E}{\epsilon_g}\right) . \tag{II.7}$$

The Airy functions are plotted in figure II.1. They exhibit oscillatory behavior on the negative real line, which corresponds to the classically allowed region:

$$\text{Ai}(-x) \underset{x\to\infty}{\simeq} \frac{1}{\sqrt{\pi}x^{1/4}} \cos\left(\frac{2}{3}x^{3/2} - \frac{\pi}{4}\right) \ , \tag{II.8}$$

$$\text{Bi}(-x) \underset{x\to\infty}{\simeq} \frac{-1}{\sqrt{\pi}x^{1/4}} \sin\left(\frac{2}{3}x^{3/2} - \frac{\pi}{4}\right) \ . \tag{II.9}$$

For positive x, Ai tends exponentially to zero whereas Bi diverges:

$$\text{Ai}(x) \underset{x\to\infty}{\simeq} \frac{\exp\left(-\frac{2}{3}x^{3/2}\right)}{2\sqrt{\pi}x^{1/4}} \ , \qquad\qquad \text{Bi}(x) \underset{x\to\infty}{\simeq} \frac{\exp\left(\frac{2}{3}x^{3/2}\right)}{\sqrt{\pi}x^{1/4}} \ . \tag{II.10}$$

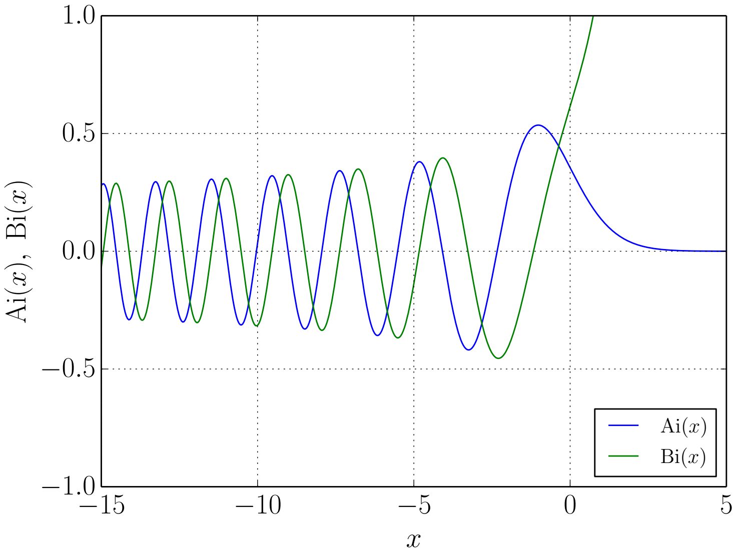

Figure II.1: The Airy functions Ai and Bi.

More properties of the Airy functions can be found in the extensive work of Vallée and Soares [145] and in the NIST Handbook of Mathematical Functions [125].

II.1.c Quantization of gravitational bound states

Notice that equation (II.1) contains one classical turning point z_t:

$$z_t \equiv \frac{E}{mg}. \tag{II.11}$$

The asymptotic behavior of the function Bi above the classical turning point z_t, corresponds to an unphysical exponentially growing wave, which leads to set $B = 0$ in equation (II.7).

The infinite potential step in $z = 0$ enforces the boundary condition $\psi(0) = 0$, which gives the energy levels E_n^0 of the ideal quantum bouncer in terms of the zeros $(-\lambda_n)$ of the function Ai [146–148]

$$E_n^0 = \lambda_n \epsilon_g \ , \qquad \mathrm{Ai}(-\lambda_n) = 0 \ , \qquad n = 1, 2, \ldots \tag{II.12}$$

The Airy function has a countable infinity of zeros, with the numerical values of the first ones given in table II.1. Following values can be found in table 9.9.1 of the Digital Library of Mathematical Functions (see [125]). From the asymptotic form of the Airy function at negative infinity (II.9), we deduce an asymptotic expression for the zeros for large n:

$$\lambda_n \underset{n\to\infty}{\simeq} \left(\frac{3\pi}{2}\left(n-\frac{1}{4}\right)\right)^{2/3}. \tag{II.13}$$

n	1	2	3	4	5	6	7	8
λ_n	2.338	4.088	5.521	6.787	7.944	9.023	10.040	11.008
$\left(\frac{3\pi}{2}\left(n-\frac{1}{4}\right)\right)^{2/3}$	2.320	4.082	5.517	6.784	7.942	9.021	10.039	11.008

Table II.1: First zeros of the Airy functions $\mathrm{Ai}(-\lambda_n) = 0$, compared with their asymptotic expression (II.13).

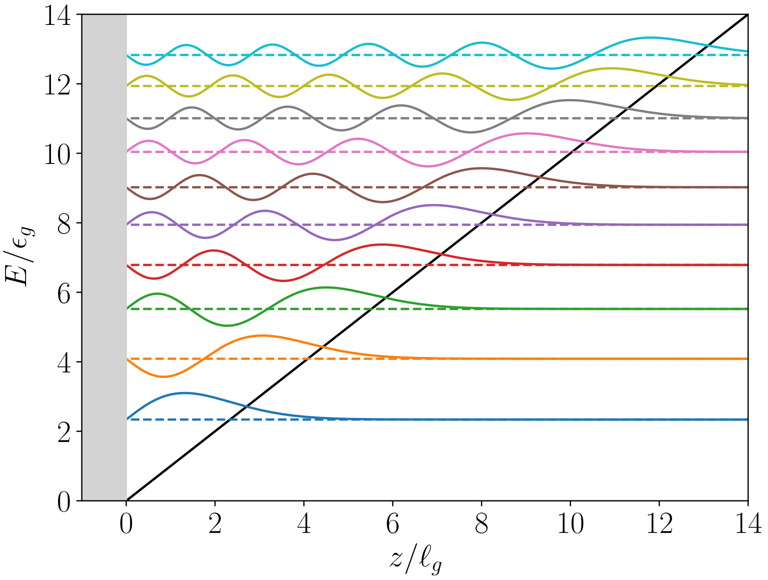

Figure II.2: Wavefunctions of the first ten gravitationally bound states.

Finally, the wavefunctions of the gravitationally bound states are

$$\psi_n(z) \equiv \frac{\Theta(z)}{\sqrt{\ell_g}\,\mathrm{Ai}'(-\lambda_n)}\,\mathrm{Ai}\left(\frac{z}{\ell_g}-\lambda_n\right) \tag{II.14}$$

where $\Theta(z)$ is the Heaviside step function. The wavefunctions of the first states are plotted in figure II.2. We have chosen the normalization such that the wavefunctions satisfy the orthogonality relation

$$\int_{-\infty}^{+\infty} \psi_m(z)\psi_n(z)\ \mathrm{d}z = \delta_{m,n}. \tag{II.15}$$

A list of interesting properties of these eigenstates are presented in [36, 149]. We summarized here the mean values and dispersions. The mean average position is proportional to the n-th Airy zero in the dimensionless coordinates (II.5):

$$\langle\psi_n|\hat{Z}|\psi_n\rangle = \frac{2\lambda_n}{3}\ell_g \tag{II.16}$$

and its average momentum is zero:

$$\langle\psi_n|\hat{P}|\psi_n\rangle = 0. \tag{II.17}$$

Its position dispersion is also proportional to the n-th Airy zero:

$$\Delta z_n = \sqrt{\langle\psi_n|\hat{Z}^2|\psi_n\rangle - \langle\psi_n|\hat{Z}|\psi_n\rangle^2} = \frac{2\lambda_n}{3\sqrt{5}}\ell_g \tag{II.18}$$

while its momentum dispersion scales as the square root of the n-th Airy zero:

$$\Delta p_n = \sqrt{\langle\psi_n|\hat{P}^2|\psi_n\rangle} = \sqrt{\frac{\lambda_n}{3}}p_g. \tag{II.19}$$

Note that both Δz_n and Δp_n increase with n and that the product

$$\Delta z_n \Delta p_n = \frac{4\,\lambda_n^{3/2}}{3\sqrt{15}} \times \frac{\hbar}{2} \tag{II.20}$$

does not reach the minimum of Heisenberg's uncertainty principle.

II.1.d Scattering length approximation

After having built quantum bouncers on a perfectly reflecting surface for matter wave, let us discuss the lengths scales associated to the full quantum problem.

Quantum bouncers defined by (II.14) spread out over a length of the order of $\ell_g \sim 6$ µm while the quantum reflection occurs in the range of the Casimir-Polder potential $\ell_4 \sim 10$ nm. Since

$$\ell_4 \ll \ell_g \tag{II.21}$$

the effect of gravity can be decoupled of the effect of the Casimir-Polder interaction in a first approximation for most distances involved in the phenomenon.

We present here a first approximation of the full quantum problem taking into account the effect of the Casimir-Polder interaction on the gravitational quantum states. We still suppose that atoms are absorbed when touching the surface, which corresponds to the physical boundary condition for antihydrogen annihilated when reaching contact with matter. The Schrödinger equation is written

$$-\frac{\hbar^2}{2m}\frac{\mathrm{d}^2\psi}{\mathrm{d}z^2}(z) + V(z)\psi(z) = E\psi(z), \tag{II.22}$$

with the potential $V(z)$ being the sum of the gravitational potential mgz and the Casimir-Polder potential denoted $V_{CP}(z)$

$$V(z) = mgz + V_{CP}(z), \tag{II.23}$$

The solutions of the Schrödinger equation (II.22) are given by the unconstrained solution (II.7) when the atom is far away from the surface, whereas the scattering on the Casimir-Polder potential modifies the boundary condition at z of the order of ℓ_4.

For the lowest quantum states with not too large values of n ($\lambda_n\epsilon_\mathrm{g} \ll \epsilon_\mathrm{CP}$), the scattering amplitudes are mainly given by the scattering length a. In this approximation, we disregard the energy dependance studied in II.2. It follows that the energies are shifted by a quantity mga resulting from the complex phase shift experienced by the atom upon reflection on the Casimir-Polder tail [33, 89] (the calligraphic $\mathcal{E}$ signals that those energies are complex while the superscript 1 indicates that CP shifts are calculated in a first approximation, to be improved in the following)

$$\mathcal{E}_n^1 = \lambda_n\epsilon_\mathrm{g} + mga. \tag{II.24}$$

The imaginary part of the complex shift is related to the lifetime of the quasi-stationary states (more detailed discussions in II.4.d).

Within the approximation (II.24), called the *scattering length approximation* in the following, the transition frequencies [150–152] between quantum states are independent of the atom-surface interaction

$$\omega_{mn}^1 = \frac{\mathcal{E}_n^1 - \mathcal{E}_m^1}{\hbar} = \frac{E_n^0 - E_m^0}{\hbar} = \omega_{mn}^0 \ . \tag{II.25}$$

Therefore spectroscopy experiments on transitions between quantum states give access to the value of ϵ_g, that is also g, while being unaffected by the details of the interaction with the surface. This is the key idea opening perspectives for testing the free fall on antihydrogen through accurate frequency measurements. In the following, we perform an exact treatment of the full potential including the effects of gravity and Casimir-Polder interaction, which will allow us to assess the accuracy of the approximation (II.24). We also give improved numerical and analytical results sufficient for discussing the proposed spectroscopic tests of free fall [85–87].

II.2 Improved effective range theory

Since the typical length associated with the Casimir-Polder potential ℓ_4 is much smaller than the typical size of gravitational quantum states ℓ_g ($\ell_4 \ll \ell_g$), we can now focus only in the region close to the surface, where quantum reflection occurs. We also study the energy dependance of the reflection amplitude, by making one step more than the constant scattering length approximation. This energy dependance is crucial for computing the quantum levitation state with an accuracy sufficient for spectroscopic tests.

The *effective range theory* was developed in the early age of quantum mechanics [153–158]. It consists of expanding the quantity $\mathcal{A}(k)$ in terms of the wavevector k for a given potential $V(z)$. In fact, it is more convenient to consider the dimensionless quantity

$$\tilde{\mathcal{A}}(k) \equiv k\mathcal{A}(k) \tag{II.26}$$

in such a way that its link to the reflection amplitude is given by:

$$\tilde{\mathcal{A}}(k) = -i\frac{1+r(k)}{1-r(k)} \tag{II.27}$$

or reciprocally:

$$r(k) = \frac{i\tilde{\mathcal{A}}(k)-1}{i\tilde{\mathcal{A}}(k)+1}. \tag{II.28}$$

II.2.a Effective range theory for the V_4 potential

We first present this energy expansion in the case of a V_4 potential. A derivation is done in details in [121, 159]. This derivation uses implicitly the Liouville transformation that maps the Schrödinger equation (I.6) to the Mathieu equation (I.64). Since we have obtained analytical reflection and transmission amplitudes (I.68) and (I.69), we can directly find the expansion of $r_4(k)$ and also the corresponding $\tilde{\mathcal{A}}_4(k)$. For doing so, we use properties of Mathieu functions that may be found in [160]. In particular, the Mathieu characteristic exponent τ can be expanded at low values of k:

$$\tau = \frac{1}{2} + \frac{2}{3}(k\ell_4)^2 + \mathcal{O}(k\ell_4)^4 \tag{II.29}$$

This can be done also for σ defined in (I.67):

$$\begin{aligned} e^{-\sigma} &= \frac{\tilde{\psi}^{(+)}(0)}{\tilde{\psi}^{(-)}(0)} \\ &= \sqrt{k\ell_4}\left(1 + \frac{2}{3}(k\ell_4)^2\ln(k\ell_4) - (k\ell_4)^2\left(\frac{4}{3}\ln(2) + \frac{4}{3}\psi(3/2) - \frac{10}{9}\right)\right) \\ &\quad + \mathcal{O}(k\ell_4)^3. \end{aligned} \tag{II.30}$$

By injecting (II.29) and (II.30) in the expression of the reflection amplitude $r_4(k)$ (I.68), we retrieve the expansion of $\tilde{\mathcal{A}}_4(k)$ known as an universal function of k [122, 161], with the following expansion suggested in [121, 159, 162, 163]:

$$\tilde{\mathcal{A}}_4(k) = -ik\ell_4\left(\alpha_0 + \alpha_1 k\ell_4 + \alpha_2 (k\ell_4)^2 + \alpha_2^{'}(k\ell_4)^2 \ln k\ell_4\right) + \mathcal{O}(k\ell_4)^4 \tag{II.31}$$

with

$$\begin{aligned}\alpha_0 &= 1\\ \alpha_1 &= \frac{\pi}{3}i\\ \alpha_2 &= \frac{8}{3}(\gamma + \ln 2) - \frac{28}{9} - \frac{2\pi}{3}i\\ \alpha_2^{'} &= \frac{4}{3}\end{aligned} \tag{II.32}$$

where γ is the Euler-Mascheroni constant[1].

II.2.b Effective range theory for a potential with a V_4 tail

We consider now the case of a potential $V(z)$ that decreases as $1/z^4$ in the long-range regime. Its difference to the $V_4(z)$ potential is denoted $\Delta V(z)$:

$$\Delta V(z) \equiv V(z) - V_4(z). \tag{II.33}$$

In the case where $\Delta V(z)$ is short-range, by decreasing faster than any power of $1/z$ for $z \to \infty$, the *modified* effective range theory [121] generalizes the expansion (II.31).

We present here the main result, while a complete derivation is detailed in appendix A. We start from the Schrödinger equation where the potential is decomposed on the V_4 potential and the short-range ΔV part:

$$\psi''(z) + \frac{2m}{\hbar^2}\left(E - [V_4(z) + \Delta V(z)]\right)\psi(z) = 0. \tag{II.34}$$

The main idea is to compare solutions obtained for the considered potential $V(z)$ with solutions obtained for the V_4 potential, that are locally designed by φ – corresponding to $\Delta V(z) = 0$. We then introduce the *effective range* $\mathcal{R}_0$ built from both solutions ψ and φ in the limit of energy E going to 0 in (II.34):

$$\frac{1}{2}\mathcal{R}_0 \equiv \lim_{E\to 0}\int_0^\infty dz\ (\varphi^2(z) - \psi^2(z)). \tag{II.35}$$

We also introduce the length ℓ corresponding to the scattering length a through:

$$a = -i\ell. \tag{II.36}$$

---

[1] $\gamma \equiv \lim_{n\to\infty}\left(-\ln n + \sum_{k=1}^{\infty}\frac{1}{k}\right) \simeq 0.577$

It follows that the expansion of $\tilde{\mathcal{A}}(k)$ is similar to the expansion of $\tilde{\mathcal{A}}_4(k)$ (II.31):

$$\tilde{\mathcal{A}}(k) = -ik\ell\left(\tilde{\alpha}_0 + \tilde{\alpha}_1 k\ell_4 + \tilde{\alpha}_2 (k\ell_4)^2 + \tilde{\alpha}_2^{'}(k\ell_4)^2 \ln k\ell_4\right) + \mathcal{O}(k\ell_4)^4 \tag{II.37}$$

with modified coefficients:

$$\begin{aligned}
\tilde{\alpha}_0 &= \alpha_0 \\
\tilde{\alpha}_1 &= \alpha_1 \cdot \ell_4/\ell \\
\tilde{\alpha}_2 &= \alpha_2 + \pi(\ell-\ell_4)^2/\ell\ell_4 - i\mathcal{R}_0\ell/2\ell_4^2 \\
\tilde{\alpha}_2^{'} &= \alpha_2^{'}
\end{aligned} \tag{II.38}$$

II.2.c Necessity of a new effective range theory

The previous derivation of the effective range theory for a potential that behaves asymptotically as the $V_4(z)$ potential holds only for a short range $\Delta V(z)$. Unfortunately, the Casimir-Polder potential does not respect this criterium. The two regimes $V_3(z)$ and $V_4(z)$ coexist and lead for instance to a non-zero coefficient for the $1/z^5$ term in the $\Delta V(z)$ expansion. The previous mathematical development is therefore not valid.

We define the short-range length scale for the Casimir-Polder potential as:

$$\ell_3 = \frac{2mC_3}{\hbar^2}. \tag{II.39}$$

Typical values for these different lengths calculated for helium and silica surfaces are summarized in table II.2.

	ℓ_4	ℓ_3	ℓ
He	75.5	16.5	$44.8 - 35.0i$
SiO_2	321.3	194.7	$273 - 77.8i$

Table II.2: Different length scales for helium and silica surfaces in atomic units.

It is obvious that $\ell \neq \ell_4$ and that the short-range part $V_3(z)$ in the Casimir-Polder potential radically changes the expansion of $\tilde{\mathcal{A}}$. Thus it is necessary to build a new effective range theory, by considering a new point of view suggested by Liouville transformations.

II.2.d V_3 tail

The new effective range theory we build now is based on a change of coordinates through the Liouville transformation presented in I.2. Since Liouville transformation preserves reflection amplitude $r(k)$, $\tilde{\mathcal{A}}(k)$ is also preserved:

$$\begin{aligned}\tilde{\mathcal{A}}(k) &= -i\frac{1+r(k)}{1-r(k)} \\ &= -i\frac{1+\mathbf{r}(\boldsymbol{k})}{1-\mathbf{r}(\boldsymbol{k})} \\ &= \tilde{\mathcal{A}}(\boldsymbol{k}).\end{aligned} \tag{II.40}$$

In this new potential landscape, the $\boldsymbol{V}_4$ potential studied in I.2.b is symmetric. However, the asymptotic behavior of a real Casimir-Polder potential for $z \to 0$ is $-C_3/z^3$. If we note $\boldsymbol{V}_3(\boldsymbol{z})$ the potential in the Liouville coordinates corresponding to $V_3(z)$, we then have the asymptotic behavior:

$$\boldsymbol{V}(\boldsymbol{z}) \underset{\boldsymbol{z}\to-\infty}{\simeq} \boldsymbol{V}_3(\boldsymbol{z}). \tag{II.41}$$

This new contribution to the potential breaks the symmetry that exists for a perfect V_4 potential and it significantly modifies the left part of the potential in Liouville coordinates, as we can see in figure II.3.

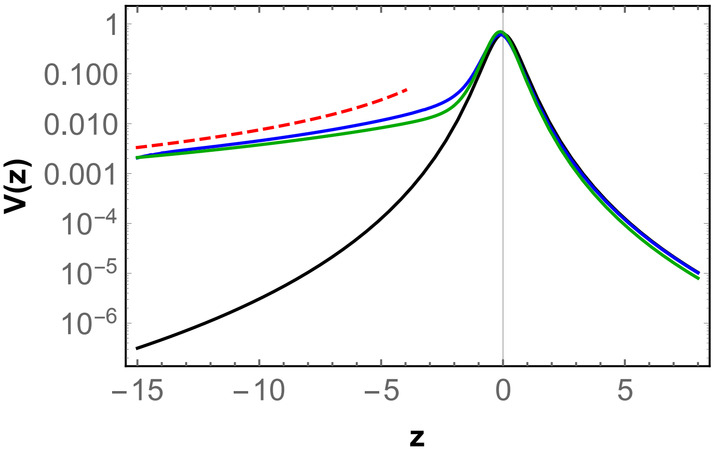

Figure II.3: Different Casimir-Polder potentials plotted in Liouville coordinates (blue line for He and green line for SiO$_2$), calculated at energy $E = 1$ neV. The black line still represents the $\boldsymbol{V}_4$ potential while the red dashed line is the asymptotic behavior of the $\boldsymbol{V}_3$ tail: $3/4\boldsymbol{z}^2$.

The expression of $\boldsymbol{V}_3$ is known [36]:

$$\begin{aligned}\boldsymbol{V}_3(x) &= 3x\frac{1+16x^3}{16(1+x^3)^3} \\ \boldsymbol{z} &= 3x\left[{}_2F_1\left(\frac{1}{2},-\frac{1}{3},\frac{2}{3},-\frac{1}{x^3}\right)-\frac{2}{3}\sqrt{1+\frac{1}{x^3}}\right]\end{aligned} \tag{II.42}$$

From (II.42), we deduce that $\boldsymbol{z} \underset{x\to 0}{\simeq} -2/\sqrt{x}$ and also obtain :

$$\boldsymbol{V}(\boldsymbol{z}) \underset{z\to-\infty}{\simeq} \boldsymbol{V}_3(\boldsymbol{z}) \underset{z\to-\infty}{\simeq} \frac{3}{4\boldsymbol{z}^2}. \tag{II.43}$$

II.2.e Scattering matrix composition

The Liouville transformation we use, leads to a potential landscape that is smoother than the original one and where we can decompose the scattering process into two successive processes. The first one is the reflection on the $\boldsymbol{V}_4$ wall, and the second one is the reflection on the $\boldsymbol{V}_3$ tail in the case where the atom has been transmitted trough the first universal barrier. We also use the convenient formalism of the scattering matrices presented in I.1.f for studying this problem.

In our case, we deal with two successive scattering processes: the reflection above the $\boldsymbol{V}_4$ potential, described by the S_4 matrix, and the reflection above the tail of the potential, described by the S_ρ matrix – ρ being the reflection amplitude on the $\boldsymbol{V}_3$ potential – as it is represented in figure II.4.

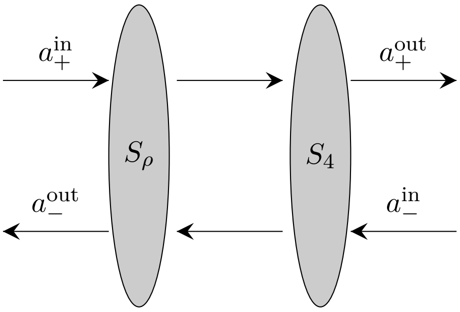

Figure II.4: Scattering process is decomposed in two successive processes.

The whole process is also described by the S matrix:

$$S = S_\rho \star S_4 \equiv \begin{pmatrix} \bar{t} & r \\ \bar{r} & t \end{pmatrix} \tag{II.44}$$

where $\star$ is the composition law for $\mathcal{S}$ matrices defined in (I.33).

The decomposition of the whole scattering process into two successive processes might appear as artificial, in particular if the two processes take place in the same space region.

However, knowing S and S_4, we can always define correctly the S_ρ matrix as:

$$S_\rho = S \star S_4^{-1} \tag{II.45}$$

where S_4^{-1} is the inverse matrix of S_4 for the $\star$ law:

$$S_4^{-1} = \Pi([\Pi(S_4)]^{-1}) \tag{II.46}$$

while $[\Pi(S_4)]^{-1}$ represents the inverse of the $\Pi(S_4)$ matrix for the usual product law of matrices. We can also check that S_ρ is formally well defined and we can keep our guess of two scattering processes as a helpful physical intuition.

Let us first focus on the $\mathcal{S}_4$ matrix and on its symmetries. The scattering process is still lossless in such a way that the unitarity defined in I.1.f is satisfied:

$$|r_4|^2 + |t_4|^2 = 1 \tag{II.47}$$

$$|\overline{r_4}|^2 + |\overline{t_4}|^2 = 1 \tag{II.48}$$

$$\overline{t_4}^* r_4 + \overline{r_4}^* t_4 = 0. \tag{II.49}$$

The reciprocity defined in I.1.g is also satisfied:

$$|\mathrm{det}\mathcal{S}_4|^2 = |t_4\overline{t_4} - r_4\overline{r_4}|^2 = 1 \tag{II.50}$$

$$\overline{r_4}t_4^* + t_4 r_4^* = 0. \tag{II.51}$$

The interesting property here is the *parity* of the $\boldsymbol{V}_4(\boldsymbol{z})$ potential. Indeed, the $\boldsymbol{V}_4$ potential obtained is even in Liouville coordinates $\boldsymbol{z}$. It means that the reflection and transmission amplitudes are the same if we consider a scattered wave coming from the left or from the right. It follows:

$$\overline{r_4} = r_4 \tag{II.52}$$

$$\overline{t_4} = t_4. \tag{II.53}$$

The $\mathcal{S}_4$ matrix is also very simple:

$$\mathcal{S}_4 = \begin{pmatrix} t_4 & r_4 \\ r_4 & t_4 \end{pmatrix}. \tag{II.54}$$

Its characteristic polynomial factorizes:

$$\chi_{\mathcal{S}_4}(X) = (t_4 - X)^2 - r_4^2 \tag{II.55}$$

$$= (X - (t_4 + r_4))(X - (t_4 - r_4)). \tag{II.56}$$

Thus, the eigenvalues are simply written:

$$s_1 = t_4 + r_4 \tag{II.57}$$

$$s_2 = t_4 - r_4. \tag{II.58}$$

The unitarity imposes the eigenvalues to be of modulus 1:

$$|s_1|^2 = |s_2|^2 = 1. \tag{II.59}$$

We can also write:

$$\begin{aligned} t_4 + r_4 &= e^{i\delta_+} \\ t_4 - r_4 &= e^{i\delta_-} \end{aligned} \tag{II.60}$$

with δ_+, $\delta_- \in \mathbb{R}$.

All theses nice properties are checked out from the explicit expression of the reflection and transmission amplitudes found in I.2.c:

$$r_4 = -i\frac{\sinh(\sigma)}{\sinh(\sigma + i\pi\tau)} \tag{II.61}$$

$$t_4 = \frac{\sin(\pi\tau)}{\sinh(\sigma + i\pi\tau)} \tag{II.62}$$

Thanks to the previous relations, we can now write the reflection amplitude on the complete potential. If we denote by ρ the reflection amplitude of the S_ρ matrix, the general form of r, using (II.44), (II.52) and (II.53), is given by:

$$r = \frac{r_4 - \rho r_4^2 + \rho t_4^2}{1 - \rho r_4}. \tag{II.63}$$

Thanks to (II.47), (II.51), (II.52) and (II.53), we obtain the following relation:

$$r_4^2 - t_4^2 = \frac{r_4}{r_4^*}. \tag{II.64}$$

By injecting (II.64) into (II.63), we also deduce the final expression of r:

$$r = r_4 \frac{1 - \rho/r_4^*}{1 - \rho r_4} \tag{II.65}$$

We can reverse the problem and write ρ depending on r and r_4:

$$\rho = \frac{r_4^*}{r_4}\frac{r_4 - r}{1 - r_4^* r} \tag{II.66}$$

II.2.f Derivation of $\tilde{\mathcal{A}}$

We start from the expression of $\tilde{\mathcal{A}}_4$ in Liouville coordinates. Since $\tilde{\mathcal{A}}_4(k) = \tilde{\mathcal{A}}_4(\boldsymbol{k})$ and $\boldsymbol{k} = \sqrt{k\ell_4}$, we can write:

$$\tilde{\mathcal{A}}_4(\boldsymbol{k}) = -i\boldsymbol{k}^2[\alpha_0 + \alpha_1\boldsymbol{k}^2 + \alpha_2\boldsymbol{k}^4 + 2\alpha_2'\boldsymbol{k}^4 \ln \boldsymbol{k}] + \mathcal{O}(\boldsymbol{k}^8) \tag{II.67}$$

with α_i coefficients written in (II.32). In particular we see that if we want an expansion of $\tilde{\mathcal{A}}(k)$ up to the order 3 in k, we need an expansion of $\tilde{\mathcal{A}}(\boldsymbol{k})$ up to the order 6 in $\boldsymbol{k}$.

By expressing $r(\boldsymbol{k})$ in terms of $\tilde{\mathcal{A}}(\boldsymbol{k})$ (II.28), we deduce from (II.65):

$$\tilde{\mathcal{A}} = \tilde{\mathcal{A}}_4 + \frac{\rho(1 - i\tilde{\mathcal{A}}_4)(\tilde{\mathcal{A}}_4^* - \tilde{\mathcal{A}}_4)}{1 + i\tilde{\mathcal{A}}_4^* + \rho(1 - i\tilde{\mathcal{A}}_4)}. \tag{II.68}$$

It is interesting to note that if $\tilde{\mathcal{A}}_4 \in \mathbb{R}$ for some values of k, $\tilde{\mathcal{A}} = \tilde{\mathcal{A}}_4$ independently of ρ. From equation (II.68), it remains to know an expansion of ρ in order to write an expansion of $\tilde{\mathcal{A}}$. Since $\tilde{\mathcal{A}}_4^* - \tilde{\mathcal{A}}_4 \sim \boldsymbol{k}^2$, we only need an expansion of $\rho(\boldsymbol{k})$ up to the order 4, in order to obtain an expansion of $\tilde{\mathcal{A}}(\boldsymbol{k})$ up to the order 6.

A natural way is to guess the shape of the ρ expansion and to fit numerically the coefficients. Once the shape is fixed, the fit can be achieved numerically since we have an exact expression for $\mathbf{r}_4(\boldsymbol{k})$ and a numerical knowledge of $\mathbf{r}(\boldsymbol{k})$ for different surfaces. The preliminary work with Liouville transformation leads us to postulate the following guess: the expansion of ρ is *polynomial* in $\boldsymbol{k}$ coordinates. The potential $\boldsymbol{V}_3$ is indeed regular and decreases asymptotically fast enough to apply Lippmann-Schwinger equations in scattering theory:

$$\rho(\boldsymbol{k}) = \rho_0 + \rho_1\boldsymbol{k} + \rho_2\boldsymbol{k}^2 + \rho_3\boldsymbol{k}^3 + \rho_4\boldsymbol{k}^4 \tag{II.69}$$

with ρ_i coefficients to be numerically determined with a fit.

The fits are tested in a range $k\ell_4 \in [2 \cdot 10^{-3}, 10^{-1}]$. For $k\ell_4 < 2 \cdot 10^{-3}$, the numerical noise is too large, and for $k\ell_4 > 10^{-1}$, the truncated expansion starts to be non valid. We take uniformly 1000 points in the interval to build the discrete set of points which are fitted. Numerical results are presented in table II.3.

	He	SiO_2
ρ_0	$0.158 + 0.336i$	$0.064 + 0.138i$
ρ_1	$-0.009 + 0.011i$	$-0.001 - 0.004i$
ρ_2	$0.098 - 0.117i$	$0.026 + 0.034i$
ρ_3	$-0.513 + 0.611i$	$-0.359 + 0.469i$
ρ_4	$-0.083 - 0.487i$	$0.204 - 0.740i$

Table II.3: Coefficients in the expansion of ρ for He and SiO_2 surfaces.

This polynomial expansion introduces square root terms in the original coordinates expansion of ρ and the of $\tilde{\mathcal{A}}$. We compare the quality of the previous fit with a similar fit obtained by keeping only the even powers of $\boldsymbol{k}$ in the expansion (II.69):

$$\rho(\boldsymbol{k}) = \rho_0' + \rho_2'\boldsymbol{k}^2 + \rho_4'\boldsymbol{k}^4, \tag{II.70}$$

that corresponds to a polynomial expansion in the original coordinates. We name it the *square* expansion.

The precision of the two fits are presented in table II.4. For each real and imaginary part of ρ, and each surface (He or SiO$_2$), the estimated standard deviation $\hat{\sigma}$ is calculated. The ratio $\hat{\rho}/\rho$ plotted in figure II.5 illustrates the quality of the two fits.

$10^{-6}\ \hat{\sigma}$	He		SiO$_2$	
	Re(ρ)	Im (ρ)	Re(ρ)	Im (ρ)
Square fit	31	36	41	80
Polynomial fit	2	2.4	1.0	5.5

Table II.4: Estimated standard deviations $\hat{\sigma}$ for real and imaginary parts of the fit of ρ, depending on the fit method and the surface (liquid helium or silica).

The large improvement of the quality of the fit with the polynomial expansion confirms the intuition on which our new method was built. Liouville coordinates has revealed square root terms that could not have been discovered without it.

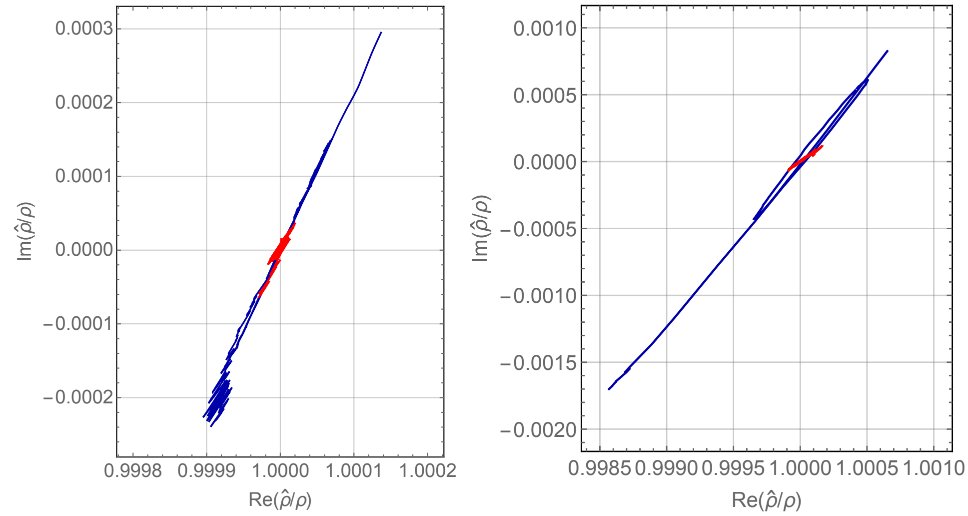

Figure II.5: Ratio $\hat{\rho}/\rho$ of the $\hat{\rho}$ obtained by the fit over the ρ known numerically. The left figure is a plot for He and the right for SiO$_2$. The square fit is plotted in blue, while the polynomial fit is plotted in in red.

We can now derive the expansion of $\tilde{\mathcal{A}}$ knowing the expansions of $\tilde{\mathcal{A}}_4$ and ρ. Using the original coordinates, the general form is :

$$\begin{aligned}\tilde{\mathcal{A}}(k) = -ik\ell[\beta_0 + \beta_{12}(k\ell_4)^{1/2} + \beta_1 k\ell + \beta_{32}(k\ell_4)^{3/2} \\ + \beta_2(k\ell_4)^2 + \beta_2'(k\ell_4)^2 \ln k\ell_4] + \mathcal{O}(k\ell_4)^4.\end{aligned} \tag{II.71}$$

where ℓ can be seen as a renormalization of the long-range length scale of the potential, due to the presence of the tail in $\boldsymbol{V}_3$:

$$\ell = \frac{1-\rho_0}{1+\rho_0}\,\ell_4. \tag{II.72}$$

The constants can be expressed from α_i (equation (II.32)) and ρ_i [143]:

$$\begin{aligned}
\beta_0 &= \alpha_0 \\
\beta_{12} &= -\frac{2\alpha_0\rho_1}{\sqrt{(1+\rho_0)(1-\rho_0)^3}} \\
\beta_1 &= \frac{2\alpha_0(\rho_1^2-(1+\rho_0)\rho_2)-\alpha_1(1+\rho_0)^3}{(1+\rho_0)(1-\rho_0)^2} \\
\beta_{32} &= \frac{2\alpha_0[\rho_1^3-2(1+\rho_0)\rho_1\rho_2+(1+\rho_0)^2\rho_3]}{\sqrt{(1+\rho_0)^3(1-\rho_0)^5}} \\
\beta_2 &= \frac{\alpha_0[2\rho_1^4-6(1+\rho_0)\rho_1^2\rho_2+4(1+\rho_0)^2\rho_1\rho_3]}{(1+\rho_0)^2(1-\rho_0)^3} \\
&\quad + \frac{2\alpha_0\rho_2^2}{(1-\rho_0)^3} - \frac{\alpha_2^{'}(1+\rho_0)^2\ln\left((1-\rho_0)/(1+\rho_0)\right)}{(1-\rho_0)^2} \\
&\quad + \frac{(1+\rho_0)(-2\alpha_0\rho_4+\alpha_2+\rho_0[4\alpha_0\alpha_1+(2+\rho_0)\mathrm{Im}(\alpha_2)i-\rho_0\mathrm{Re}(\alpha_2)])}{(1-\rho_0)^3} \\
\beta_2^{'} &= \alpha_2^{'}\left(\frac{1+\rho_0}{1-\rho_0}\right)^2.
\end{aligned} \tag{II.73}$$

II.2.g Advantages of the new effective range theory

We finish our analysis of the new effective range theory by showing the benefit of this new square terms in the final precision of the estimation of $\tilde{\mathcal{A}}$. In the modified effective range theory discussed in II.2.b, only two parameters have to be fixed in the expansion of $\tilde{\mathcal{A}}$: the scattering length a (or equivalently ℓ) and the effective range $\mathcal{R}_0$ (or equivalently $\tilde{\alpha}_2$). Other coefficients (II.38) are universal and derived from the theory. We summarized the values of the scattering length $a = -i\ell$ and $\tilde{\alpha}_2$ for helium and silica in table II.5.

	He	SiO$_2$
a	$-35.0 - 44.8i$	$-77.8 - 273i$
$\tilde{\alpha}_2$	$2.54 - 2.51i$	$1.73 - 3.67i$

Table II.5: Maximum of the relative error defined as (II.74) for the modified effective range theory and the new effective range theory for helium and silica surfaces.

In the new effective range theory we propose, in contrast, five parameters remain to be determined: ρ_i, $i \in [\![0,4]\!]$, some of them leading to new terms in the expansion of $\tilde{\mathcal{A}}$. We calculate the error due to the two expansions by comparing the values of the expansions to the precise numerical one.

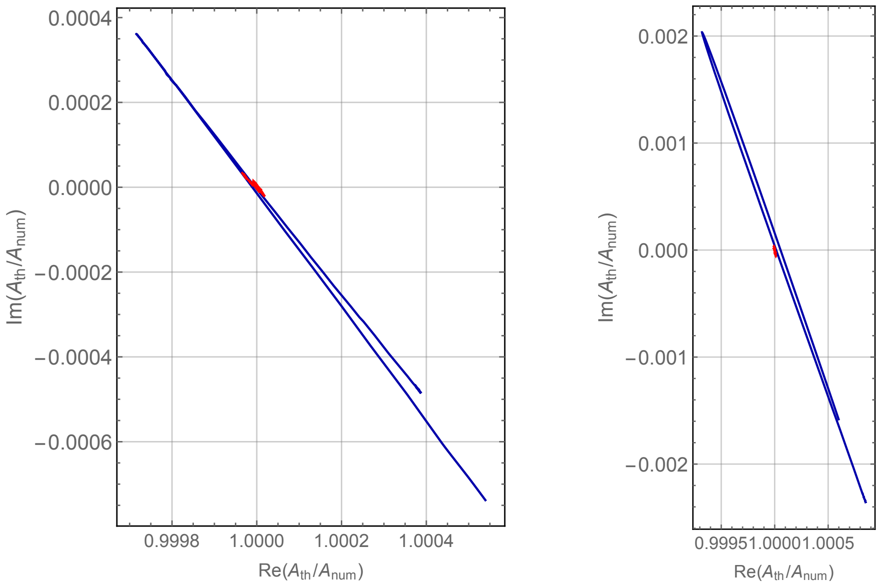

Figure II.6: Ratio $\tilde{\mathcal{A}}_{th}/\tilde{\mathcal{A}}_{num}$ of $\tilde{\mathcal{A}}_{th}$ obtained theoretically over $\tilde{\mathcal{A}}_{num}$ known numerically. The modified effective range theory appears in blue while the new effective range theory appears in red. The left figure is a plot for He and the right for SiO$_2$.

We plotted in figure II.6 the ratio $\tilde{\mathcal{A}}_{th}/\tilde{\mathcal{A}}_{num}$ of $\tilde{\mathcal{A}}_{th}$ in the complex plan obtained theoretically for both effective range theory and new effective range theory, over $\tilde{\mathcal{A}}_{num}$ known numerically. It is clear that the new effective range theory reproduces much better the energy dependance of $\tilde{\mathcal{A}}$ than the original effective range theory. To be more quantitative, we compute the maximum of the relative distance between $\tilde{\mathcal{A}}_{th}$ and $\tilde{\mathcal{A}}_{num}$ for both theories we compare:

$$\left\| \frac{\tilde{\mathcal{A}}_{th} - \tilde{\mathcal{A}}_{num}}{\tilde{\mathcal{A}}_{num}} \right\|_{\infty} \equiv \max_{k\ell_4 \in [2\cdot 10^{-3}, 10^{-1}]} \left| \frac{\tilde{\mathcal{A}}_{th}(k) - \tilde{\mathcal{A}}_{num}(k)}{\tilde{\mathcal{A}}_{num}(k)} \right| . \tag{II.74}$$

Results are summarized in table II.6. They confirm what is visible in the figure II.6: the expansion suggested by new effective range theory is more than 10 times more accurate than the expansion derived from the original effective range theory.

	He	SiO$_2$
Modified ERT	$9.1 \cdot 10^{-4}$	$2.5 \cdot 10^{-3}$
New ERT	$4.8 \cdot 10^{-5}$	$4.3 \cdot 10^{-5}$

Table II.6: Maximum of the relative error defined as (II.74) for the modified effective range theory and the new effective range theory for helium and silica surfaces.

Of course, since the new effective range theory allows new degrees of freedom (5 instead of 2), the quality of the fit is necessary better. This is true but we are convinced than the new terms that appear in the expansion (A.24) represent a better physical understanding of the scattering process. They come from a well defined scattering problem in Liouville coordinates. The coefficients ρ_i obtained with the new fit are sufficient to compute the expansion of $\tilde{\mathcal{A}}$ with a very high accuracy, that will be sufficient to precisely determined the Casimir-Polder shifts in the following.

II.3 Liouville-Langer transformation

In that section we present the Liouville-Langer transformation that helps us to perform a full quantum treatment of gravity and Casimir-Polder interaction. We apply a new change of coordinates, that gives us a well adapted frame to study the quantum levitation states.

II.3.a Turning point

We want to study the Schrödinger equation (II.22) with the potential built as a sum of gravitational and Casimir-Polder potentials:

$$V(z) = mgz + V_{CP}(z). \tag{II.75}$$

In I.2.d, we defined a Liouville transformation from the WKB phase

$$\boldsymbol{z}(z) = \phi_{\mathrm{dB}}(z) = \int_{z_\phi}^{z} \sqrt{F(\zeta)}\mathrm{d}\zeta \tag{II.76}$$

$$F(z) = \frac{2m(E - V(z))}{\hbar^2}. \tag{II.77}$$

It led to a new potential landscape that was well adapted to the study of the scattering length oscillations I.4.c or the derivation of the new effective range theory II.2.

From the integral form of the WKB phase (II.76), we deduce that the new coordinate is well defined only when $F(z)$ is positive. While this property remains true everywhere for the case of the attractive Casimir-Polder potential, the contribution of gravity in (II.75) leads to a presence of a turning point z_t defined as the solution of:

$$F(z_t) = 0. \tag{II.78}$$

This turning point corresponds to the maximum altitude reached classically. It is illustrated in figure II.7, at the intersection between the energy level and the potential. The coordinate (II.76) can also only be used below the classical turning point but it cannot help to study the connection with the region above this point [97–99].

II.3.b Langer coordinates

We now introduce a coordinate proposed by Langer [164, 165] which is well adapted to this problem, as it leads to a wavefunction regular at the crossing of the turning point. The turning point z_t corresponding to $F(z_t) = 0$ satisfies $F'(z_t) < 0$, with $F(z)$ nearly linear in its neighborhood:

$$F(z) \underset{z \to z_t}{\simeq} -F'(z_t)(z_t - z). \tag{II.79}$$

The Langer coordinate $\boldsymbol{z}$ is defined so that $\boldsymbol{F}(\boldsymbol{z})$ shows the same linear behavior in the vicinity of $\boldsymbol{z}_t = \boldsymbol{z}(z_t)$ (boldfaces denote now all quantities related to the Langer coordinate system)

$$\boldsymbol{F}(\boldsymbol{z}) \underset{\boldsymbol{z} \to \boldsymbol{z}_t}{\simeq} \boldsymbol{z}_t - \boldsymbol{z} \;, \quad \boldsymbol{z}_t = \frac{E}{\epsilon_{\mathrm{g}}} \;. \tag{II.80}$$

We have partly used the freedom in the definition of the Langer coordinate $\boldsymbol{z}$, by fixing $\boldsymbol{z}_t$ and $\boldsymbol{F}'(\boldsymbol{z}_t) = -1$.

The change of coordinate $\boldsymbol{z}(z)$ reduces to a linear function near the turning point

$$\boldsymbol{z}(z) \underset{z \to z_t}{\simeq} \boldsymbol{z}_t + \left(-F'(z_t)\right)^{1/3}(z - z_t), \tag{II.81}$$

and the Schwarzian derivative $\{\boldsymbol{z}, z\}$ vanishes around the turning point, with equation (I.48) reducing to

$$\boldsymbol{F}(\boldsymbol{z}) \underset{z \to z_t}{\simeq} \frac{F(z)}{\boldsymbol{z}'(z)^2}. \tag{II.82}$$

We now fix the definition by requiring the right hand sides of equations (II.80) and (II.82) to be equal for all z

$$\boldsymbol{z}'(z) = \sqrt{\frac{F(z)}{\boldsymbol{z}_t - \boldsymbol{z}}} \;, \quad \text{for} \quad z \neq z_t, \tag{II.83}$$

$$\boldsymbol{z}'(z_t) = \left(-F'(z_t)\right)^{1/3}. \tag{II.84}$$

Evaluating equation (I.48) for the Langer coordinate yields:

$$\boldsymbol{F}(\boldsymbol{z}) = \boldsymbol{z}_t - \boldsymbol{z} - \frac{5}{16(\boldsymbol{z} - \boldsymbol{z}_t)^2} + (\boldsymbol{z} - \boldsymbol{z}_t)Q(z), \tag{II.85}$$

where $Q(z)$ is the badlands function (I.13) written with the initial coordinate z.

Note that the two last terms in equation (II.85) diverge at the turning point while their sum does not. In regions where $\boldsymbol{F}(\boldsymbol{z}) \simeq (\boldsymbol{z}_t - \boldsymbol{z})$, in particular around the turning point, the Schrödinger equation reduces to an Airy equation, and the connection problem at the turning point is solved as in (II.7) by the Airy function Ai

$$\boldsymbol{\psi}(\boldsymbol{z}) \simeq a \,\mathrm{Ai}(\boldsymbol{z} - \boldsymbol{z}_t). \tag{II.86}$$

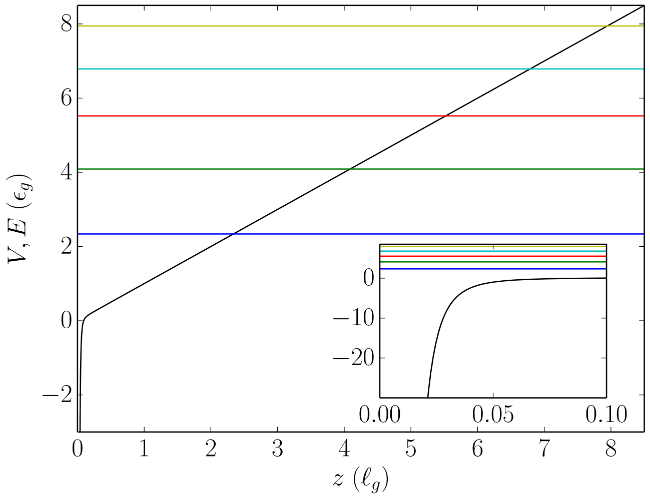

Figure II.7: The original problem for antihydrogen atom in the combined gravity and CP potentials $V(z) = mgz + V_{\mathrm{CP}}(z)$ (black curve) above a silica bulk. Horizontal lines correspond to energies chosen for the illustration as $E_n^0 = \lambda_n \epsilon_{\mathrm{g}},\ n = 1, ..., 5$ (blue, green, red, cyan and yellow lines, respectively from bottom to top line). A zoom on the potential well near the surface is shown in the inset.

II.3.c Transformed potential landscape

In the following, we give a complete solution of the Schrödinger equation (II.22), keeping all terms in the expression (II.85) of $\boldsymbol{F}$. The solution is therefore fully equivalent to the exact solution of the original Schrödinger equation (II.22), illustrated on figure II.7 for antihydrogen atom above a silica bulk [91]. The horizontal lines are drawn for energies (II.12) matching the states $n = 1, ..., 5$ (blue, green, red, cyan and yellow lines, from bottom to top line) of an ideal quantum bouncer. The exact energies, shifted with respect to (II.12) due to the effect of the CP interaction, are calculated in the following.

Figure II.8 shows the same problem as on Figure II.7 now treated in the Langer coordinate system, with the coordinate $\boldsymbol{z}$ spanning the whole real axis and the transformed $\boldsymbol{F}$−function (II.85) written in terms of a transformed energy $\boldsymbol{E}$ and a transformed potential $\boldsymbol{V}$

$$\boldsymbol{F}(\boldsymbol{z}) = \boldsymbol{E} - \boldsymbol{V}(\boldsymbol{z}), \tag{II.87}$$

$$\boldsymbol{E} = \boldsymbol{z}_t = \frac{E}{\epsilon_{\mathrm{g}}}, \tag{II.88}$$

$$\boldsymbol{V}(\boldsymbol{z}) = \boldsymbol{z} - \boldsymbol{V}_{\mathrm{CP}}(\boldsymbol{z})\ . \tag{II.89}$$

The potential $\boldsymbol{V}$ is the sum of a linear gravity potential and an effective potential $\boldsymbol{V}_{\mathrm{CP}}(\boldsymbol{z})$ producing quantum reflection. In sharp contrast with the CP well on Figure II.7, the transformed potential $\boldsymbol{V}_{\mathrm{CP}}$ now shows a high peak close to the surface. Its height is much larger than the energies of the lowest quantum states illustrated by the horizontal lines on Figure II.8, at $\boldsymbol{E}_n^0 = \lambda_n,\ n = 1, ..., 5$ (same color codes as on Figure II.7).

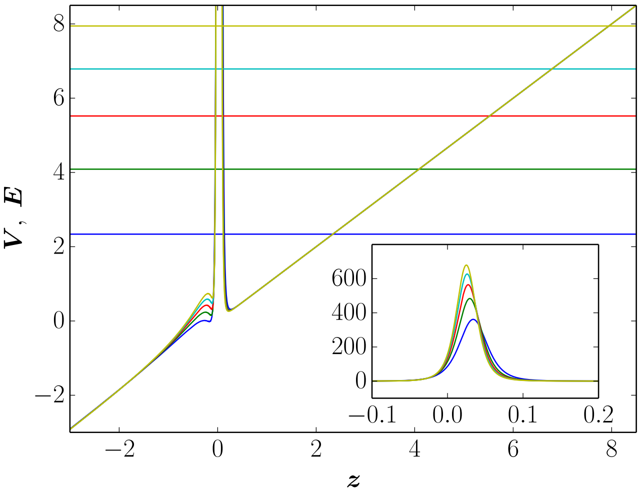

Figure II.8: The same problem as on figure II.7 after a Liouville transformation to the Langer coordinate $\boldsymbol{z}$, with energies chosen for the illustration as $\boldsymbol{E}_n^0 = \lambda_n,\ n = 1, ..., 5$ and potential $\boldsymbol{V} = \boldsymbol{z} + \boldsymbol{V}_{\mathrm{CP}}$. The color code is the same as in figure II.7. A zoom on the wall is shown in the inset.

II.4 Quantum levitation states

II.4.a Fabry-Perot cavity

With quantum reflection understood as classically expected reflection on a repulsive wall, we get a new physical picture for quantum levitation states corresponding to matter waves trapped in a Fabry-Perot cavity. The top mirror of the vertical cavity perfectly reflects matter waves due to gravity, while the bottom mirror partially reflects them due to quantum reflection. We interpret the properties of quantum levitation states in terms of cavity resonances, by performing calculations in analogy with the theory of optical Fabry-Perot cavities [126].

Around and above the top mirror, that is also around and above the turning point $\boldsymbol{z}_t$, the solution of the Schrödinger equation is given by the Airy function (II.86), that we rewrite as a linear superposition of upward and downward traveling waves Ci^+ and Ci^-

$$\psi_m(z) = \frac{a_m}{2}\Big(\mathrm{Ci}^+(z-z_t) + \mathrm{Ci}^-(z-z_t)\Big)\,, \tag{II.90}$$

$$\mathrm{Ci}^\pm(z) = \mathrm{Ai}(z) \pm i\,\mathrm{Bi}(z). \tag{II.91}$$

The upward and downward waves have an equal amplitude for the reason already discussed for equation (II.7), that is the absence in (II.90) of the combination Bi corresponding to an exponentially growing wave above the turning point. This amplitude is denoted a_m in (II.90) as it depends on the number m of bounces of the matter wave on the bottom mirror, as explained now.

II.4.b Round-trip factor: numerical analysis

With the ideal quantum bouncer model, the ideal energy levels E_n^0 would be recovered by obtaining the stationary quantum solutions of (II.90). But the more general problem studied here is not unitary since atoms transmitted through the bottom mirror are lost (antihydrogen going through the bottom mirror is annihilated when reaching contact with the matter plate).

As a consequence, the quantum levitation states can only be obtained as quasi-stationary states, with the amplitude a_m decreasing after each bounce, due to the losses. In analogy with the theory of optical Fabry-Perot cavities [126], we introduce a factor describing the modification of the traveling waves after one cavity round trip

$$\rho \equiv \frac{a_{m+1}}{a_m}. \tag{II.92}$$

This round trip factor can be obtained by solving numerically the quantum reflection problem on the bottom mirror of the cavity (that is the peak in the potential drawn on figure II.8). Precisely, the Schrödinger equation (II.22) is solved with appropriate boundary conditions far from this mirror: above the mirror ($z \to \infty$), the downward traveling wave matches the component proportional to $a_m\,\mathrm{Ci}^-$ in (II.90) while the upward traveling wave matches the component proportional to $a_{m+1}\,\mathrm{Ci}^+ = \rho a_m\,\mathrm{Ci}^+$:

$$\psi(z) \underset{z\to+\infty}{\simeq} a_m\,\mathrm{Ci}^-(z) + a_{m+1}\,\mathrm{Ci}^+(z) \tag{II.93}$$

$$\underset{z\to+\infty}{\simeq} a_m\,\mathrm{Ci}^-(z) + \rho a_m\,\mathrm{Ci}^+(z). \tag{II.94}$$

Below the mirror ($z \to -\infty$), the downward traveling wave is proportional to $b_m\,\mathrm{Ci}^-$, with b_m related to a_m by a transmission amplitude, whereas the upward traveling wave vanishes there:

$$\psi(z) \underset{z\to-\infty}{\simeq} b_m\,\mathrm{Ci}^-(z) \tag{II.95}$$

$$\underset{z\to-\infty}{\simeq} t a_m\,\mathrm{Ci}^-(z). \tag{II.96}$$

This procedure produces a complex-valued function $\rho(E)$ of the energy E, that is also of the altitude $\boldsymbol{z}_t$ of the turning point. Stationary quantum states would correspond to the condition $\rho = 1$ which cannot be met in the presence of losses. But we may define energies E_n of quasi-stationary states by requiring $\rho(E_n)$ to be a real number slightly smaller than unity. The value attained for $\rho(E_n)$ is related to the loss at each bounce, that is also the finesse of the cavity resonance. This relation will be discussed in more details below in II.4.d.

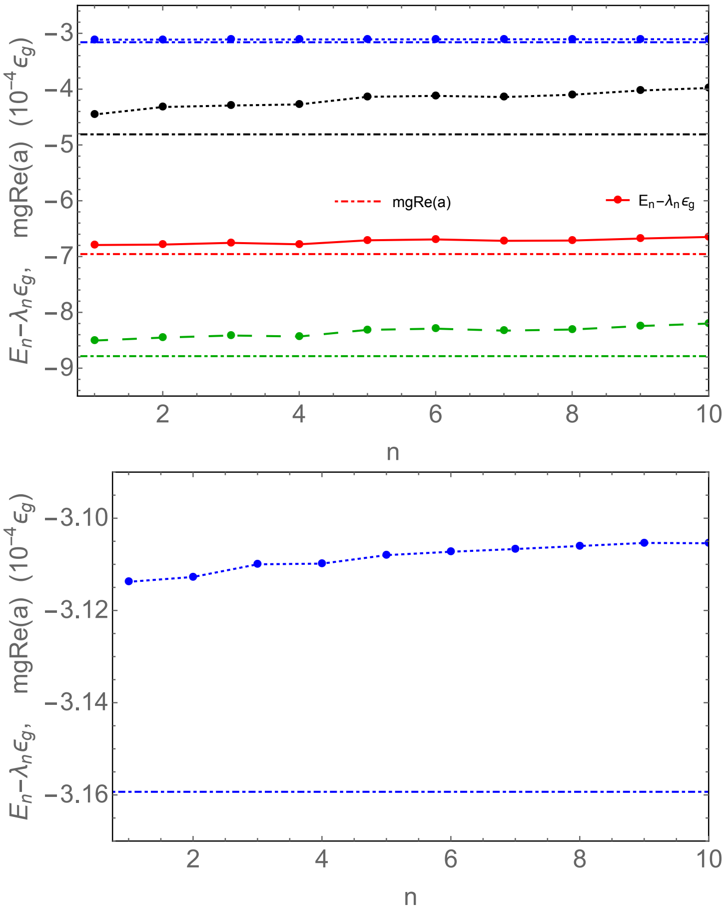

Figure II.9: Energy shift $E_n - E_n^0$ for antihydrogen interacting with a perfect mirror (black, up middle), a silicon bulk (green, bottom lines), a silica bulk (red, bottom middle lines) and a helium bulk (blue, top lines), in units of $10^{-4}\epsilon_\text{g}$. The shift corresponding to the real part of mga is represented by the horizontal lines. The bottom figures is a zoom on helium bulk of the top figure.

The energy shifts due to the CP effect are seen as the non vanishing differences $E_n - E_n^0$ between the numerical values E_n obtained here and the expressions $E_n^0 = \lambda_n \epsilon_\text{g}$ calculated for the ideal quantum bouncer. They are shown on Figure II.9 for the ten first resonances

$n = 1, 2, \ldots, 10$. The shifts for a given mirror are close to the constant value $mg\,\mathrm{Re}(a)$ predicted by the scattering length approximation (II.24) discussed above. The latter is confirmed as a first approximation of the numerical results, with an accuracy of the order of 10^{-4}. We will now use the new effective range theory developed in II.2 to propose a better analytical approximation, corresponding to an improved accuracy for the analysis of spectroscopy tests of free fall.

II.4.c Round-trip factor: analytical expression

The round-trip factor ρ is a scattering amplitude which can be evaluated in terms of Wronskians of solutions and, therefore, can be calculated in the initial or transformed coordinate systems equivalently. We now design an analytical approximation of this factor, built up on the optical analogy discussed above.

The round trip factor ρ is approximated as the product of two factors, the quantum reflection amplitude r on the Casimir-Polder tail, and a propagation phase factor deduced from the phase θ of the Airy functions

$$\rho \simeq -re^{2i\theta(-\boldsymbol{z}_t)}, \tag{II.97}$$

$$\tan\theta(x) = \frac{\mathrm{Ai}(x)}{\mathrm{Bi}(x)}, \quad e^{2i\theta(x)} = -\frac{\mathrm{Ci}^-(x)}{\mathrm{Ci}^+(x)}. \tag{II.98}$$

The determination of the solution in (II.98) is such that $\theta(0) = \pi/6$ with $\theta(x)$ a continuous function [125]. After the discussions in the preceding section, the resonance energies E_n, with $\rho(E_n)$ a real number slightly smaller than unity, are the solutions of the equation

$$2\theta\left(-\boldsymbol{z}_t\right) + \arg\left(-r\right) = 2n\pi. \tag{II.99}$$

θ can be evaluated in the initial or Langer coordinate system, and it depends on the single parameter

$$\boldsymbol{z}_t = \boldsymbol{E} = \frac{E}{\epsilon_\mathrm{g}} = \frac{z_t}{\ell_\mathrm{g}}. \tag{II.100}$$

The argument of the complex amplitude $(-r)$ depends on the energy E or on the equivalent wavevector k.

For a perfect quantum reflection $r = -1$, the equation (II.99) would give the energy levels E_n^0 as the zeros $(-\lambda_n)$ of the Airy function Ai also obey

$$\theta(-\lambda_n) = n\pi. \tag{II.101}$$

With the reflection amplitude replaced by its scattering length approximation:

$$\arg\left(-r\right) = -2k\,\mathrm{Re}(a), \tag{II.102}$$

and the equation (II.99) solved perturbatively in the small parameter ka, the energies E_n are recovered as the real parts of $\mathcal{E}_n^1$ given in (II.24).

In the following, we use the new effective-range approximation developed in II.2 which is much more accurate than the scattering length approximation. The reflection coefficient is thus written as a function of the wavevector k and a complex length $\mathcal{A}(k)$ from (II.28). We recall the expansion form of $\tilde{\mathcal{A}}(k)$:

$$\begin{aligned}\tilde{\mathcal{A}}(k) = -ik\ell[\beta_0 + \beta_{12}(k\ell_4)^{1/2} + \beta_1 k\ell_4 + \beta_{32}(k\ell_4)^{3/2} \\ + \beta_2(k\ell_4)^2 + \beta_2'(k\ell_4)^2 \ln k\ell_4] + \mathcal{O}(k\ell_4)^4.\end{aligned} \tag{II.103}$$

In that expansion, β_0 and β_2' are fixed (II.73):

$$\beta_0 = 1 \tag{II.104}$$

$$\beta_2' = \frac{4}{3}. \tag{II.105}$$

Other constants β_i, are obtained from ρ_i and α_i (II.73) or can be directly fitted from the numerical calculation of $\tilde{\mathcal{A}}(k)$. The fit was achieved in the same interval as in II.2: $k\ell_4 \in [2 \cdot 10^{-3}, 10^{-1}]$. In terms of energy, it corresponds to fit over the few first hundreds Airy states. For instance for a silica bulk, the fit is achieved on the interval corresponding to $E \in [0.5\epsilon_{\mathrm{g}}, 1200\epsilon_g]$. The upper bound of the interval is also small enough for the expansion (II.103) to remain a good approximation of the function and, at the same time, large enough to keep a low numerical noise in the fit. We have checked that the truncated numerical values given in the table are sufficient to reproduce the variation of $r(k)$ for the purpose of our calculations, with errors in the evaluation of energies smaller than a few $10^{-6}\epsilon_{\mathrm{g}}$ for $E < 500\epsilon_{\mathrm{g}}$ independently on the surface material. The coefficients obtained in this manner are given in table II.4.c. Notice that the expansion (II.103) differs from the expansion used in [120]. The latter was based on an improvement "by hand" of the original effective range theory II.2.b.

	Perfect mirror	Silicon bulk	Silica bulk	Liquid helium
ℓ	$544 - 53.5i$	$436 - 97.8i$	$273 - 77.8i$	$44.8 - 35.0i$
β_{12}	$-0.0018 + 0.0016i$	$-0.0028 + 0.0155i$	$-0.0065 + 0.0271i$	$-0.153 + 0.194i$
β_1	$-0.0755 + 0.984i$	$-0.186 + 0.805i$	$-0.265 + 0.838i$	$2.71 - 3.45i$
β_{32}	$-0.105 - 0.0668i$	$-0.168 + 0.727i$	$0.209 + 0.222i$	$-34.0 + 43.2i$
β_2	$0.528 - 1.68i$	$0.799 - 2.93i$	$0.730 - 2.34i$	$116 - 147i$

Table II.7: Coefficients of the expansion of $\tilde{\mathcal{A}}(k)$ obtained from a fit of the numerically calculated values of $r(k)$. ℓ is expressed in atomic units.

Within the new effective-range theory, the resonance energies are given as solutions of the equation

$$\theta\left(-\boldsymbol{E}_n\right) - \mathrm{Re}\left(\arctan\left(i\tilde{\mathcal{A}}(k_n)\right)\right) = n\pi, \tag{II.106}$$

$$\boldsymbol{E}_n \equiv \frac{E_n}{\epsilon_{\mathrm{g}}}, \quad k_n = \frac{\sqrt{2mE_n}}{\hbar}, \tag{II.107}$$

with $\tilde{\mathcal{A}}(k)$ defined by the expansion (II.103) with the coefficients in table II.4.c.

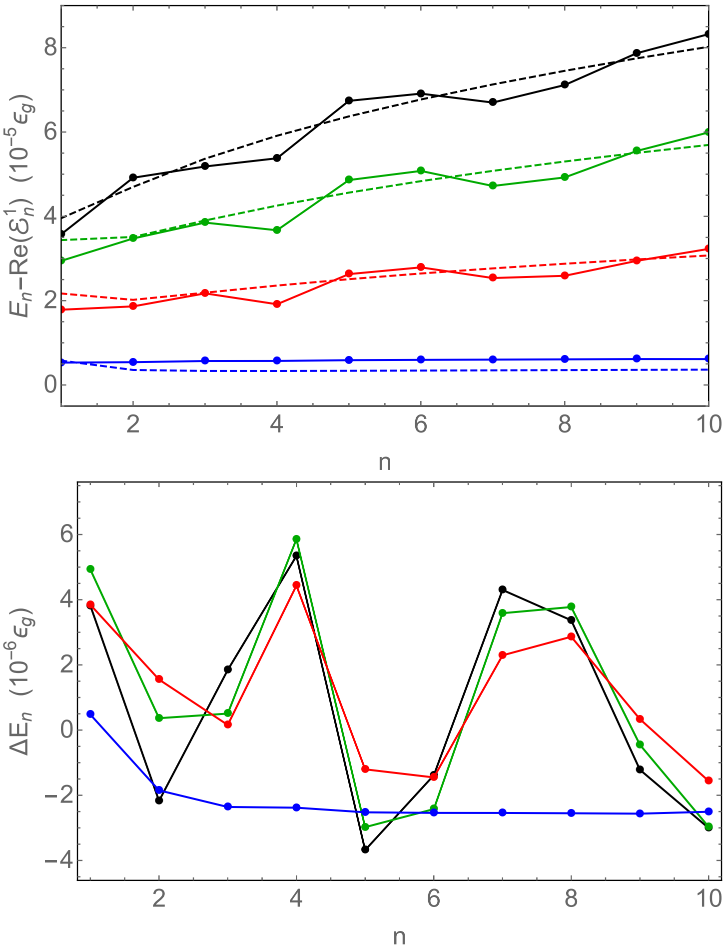

Figure II.10: Upper plot : Variation of $E_n - \mathrm{Re}(\mathcal{E}_n)^1 = E_n - \lambda_n \epsilon_\mathrm{g} - mg\,\mathrm{Re}(a)$ for antihydrogen interacting with a perfect mirror (black lines), a silicon bulk (green lines), silica bulk (red lines) or liquid helium bulk (blue lines), in units of $10^{-5}\epsilon_\mathrm{g}$. Points are obtained from numerical results E_n^{num} in II.4.b and full lines interpolate between these points. Dashed curves correspond to solutions E_n^{ana} of the effective-range equation (II.106). Lower plot : Difference ΔE_n between analytical and numerical energies on the upper plot for a perfect mirror (black dotted line), a silicon bulk (green dashed line), a silica bulk (red full line) and a liquid helium bulk (blue dashed line) in units of $10^{-6}\epsilon_\mathrm{g}$.

In order to assess the precision of the results, we draw on the upper plot of figure II.10 the variation of

$$E_n - \lambda_n \epsilon_{\mathrm{g}} - mg\,\mathrm{Re}(a) = E_n - \mathrm{Re}(\mathcal{E}_n^1) \tag{II.108}$$

for the first quantum states of antihydrogen above a perfect mirror (black lines), a silicon bulk (green lines), a silica bulk (red lines) and a liquid helium bulk (blue lines). Points are obtained from the numerical results E_n^{num} discussed in II.4.b for $n = 1, 2, \ldots, 10$ with full lines interpolating between these points. Dashed lines are obtained from the solutions E_n^{ana} of the analytical effective-range equation (II.106). For completeness, the differences between the analytical and numerical values are also plotted on the lower plot of figure II.10.

$$\Delta E_n = E_n^{\mathrm{ana}} - E_n^{\mathrm{num}} \ . \tag{II.109}$$

Figure II.10 shows small oscillations of the numerical values around the smoother variation obtained from the analytical approximation. These oscillations remain smaller than a few $10^{-6}\epsilon_{\mathrm{g}}$ for the first ten quantum states, which means that the effective-range theory is sufficient to compute the corrections caused by the Casimir-Polder interaction at this accuracy level.

II.4.d Complex Casimir-Polder shifts

The round-trip factor ρ is a causal scattering amplitude, that is also an analytic function of energy E. This function can be continued to the complex plane where the equation $\rho = 1$ can now be solved for complex energies $\mathcal{E}_n$, the imaginary part of which are related to the widths of the cavity resonances.

The complex solutions $\mathcal{E}_n$ of the equation $\rho = 1$ are also the poles of the *cavity response function* f accounting for multiple interference of different numbers of round trips as for optical Fabry-Perot cavities [126]

$$f\left(E\right) \equiv \frac{\rho\left(E\right)}{1-\rho\left(E\right)} = \rho + \rho^2 + \rho^3 + \ldots \ . \tag{II.110}$$

When the reflection amplitude is replaced by its scattering length approximation, and the Casimir-Polder shifts treated perturbatively, these complex energies are obtained as $\mathcal{E}_n^1$ (see eq.(II.24)). The real part $\mathrm{Re}(\mathcal{E}_n)$ is close to the resonance energy E_n discussed in the preceding sections whereas the imaginary part

$$\mathrm{Im}(\mathcal{E}_n) \simeq -mgb \tag{II.111}$$

with $b = -\,\mathrm{Im}(a)$ is directly related to the width of the resonance and consequently to the inverse of the cavity lifetime. In the scattering length approximation, the widths or lifetimes are thus determined by the same quantity mgb for the different quantum states [33, 89].

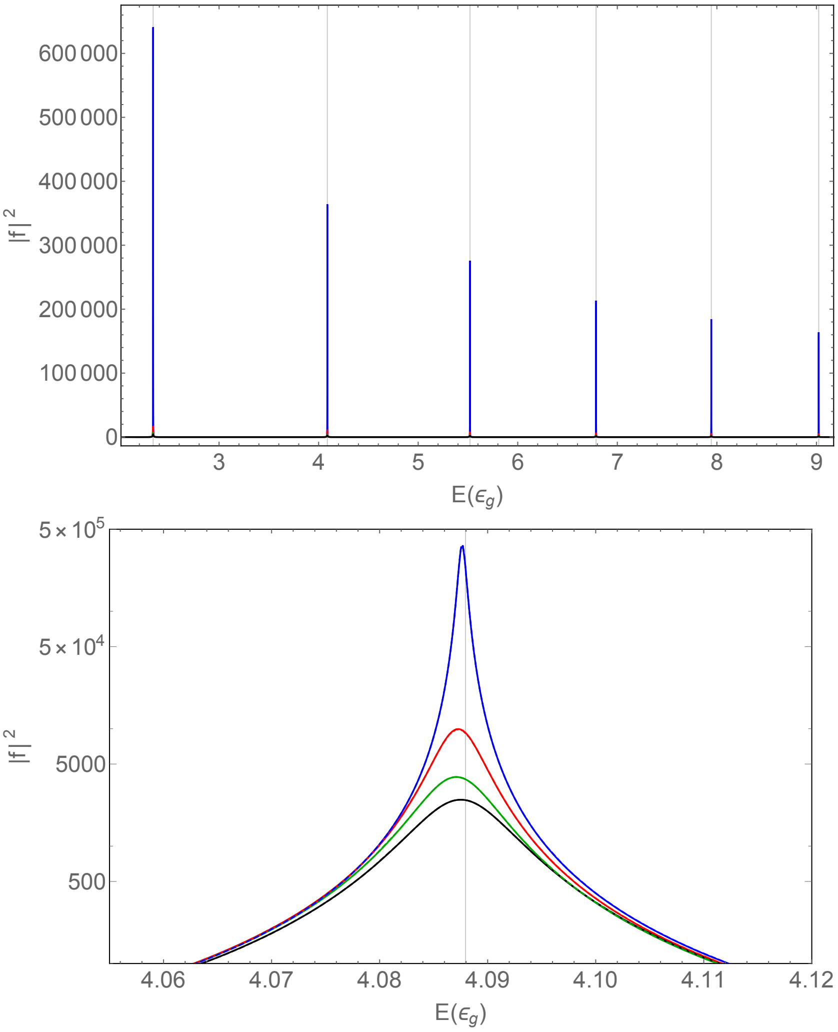

Figure II.11: Upper plot : Squared modulus $|f(E)|^2$ of the cavity response function (II.110) as a function of energy for antihydrogen interacting with a perfect mirror (black lines), a silicon bulk (green lines), a silica bulk (red lines) or liquid helium bulk (blue lines). The closed loop function for liquid helium bulk is much larger than for other bulks. Lower plot : Second peak of the squared modulus $|f(E)|^2$ of the closed loop function for antihydrogen interacting with a perfect mirror (black), a silicon bulk (green), silica bulk (red) or liquid helium bulk (blue), in logarithmic vertical scale. Lorentzians (II.115) are plotted in dashed lines. The vertical grey line indicates the position of the ideal quantum bouncer energy $E_2^0 = \lambda_2 \epsilon_g$.

This is explained by a classical picture of the bounces. For an energy $E = mgH$, the bouncing period is

$$2\sqrt{\frac{2H}{g}} \tag{II.112}$$

while the probability of transmission through the quantum reflection barrier at each bounce is

$$1 - |r|^2 \simeq 4b\frac{\sqrt{2mE}}{\hbar}. \tag{II.113}$$

The lifetime is given by the ratio of these two quantities

$$\tau = \frac{\hbar}{2mgb} \tag{II.114}$$

which does not depend on E. The lower reflection probability at higher energies is compensated by the smaller bouncing frequency, so that the lifetime is independent of energy. This simple property is no longer exact with the more accurate treatment which has been developed here.

In a first stage, we use the numerical results to obtain the complex energies. The upper plot on figure II.11 shows the first resonance peaks of $|f(E)|^2$ for antihydrogen interacting with a perfect mirror, a silicon bulk, a silica bulk or a liquid helium bulk. The plot shows Lorentzian resonances for E close to the complex energies $\mathcal{E}_n$:

$$|f|^2 \simeq \frac{A_n}{|E - \mathcal{E}_n|^2} = \frac{A_n}{(E - \mathrm{Re}(\mathcal{E}_n))^2 + (\mathrm{Im}(\mathcal{E}_n))^2} \tag{II.115}$$

$$A_n = \frac{1}{|\rho'_n|^2} \ , \quad \rho'_n \equiv \frac{\mathrm{d}\rho}{\mathrm{d}\mathcal{E}}\left(\mathcal{E}_n\right). \tag{II.116}$$

As the resonances are well separated, the contributions of other peaks have been disregarded in (II.115). The parameters for one peak can be retrieved by fitting numerical values $|f|^2$ with (II.115). The lower plot on figure II.11 represents a zoom on the second peak which shows an excellent agreement with the fitting functions for the three different mirrors.

We finally use the analytical approximate expressions results presented in II.4.c to obtain the complex energies. As the reflection amplitude and Airy phase function appearing in the expression (II.97) of ρ are analytical functions, this is simply done by solving the equation

$$\rho\left(\mathcal{E}\right) = 1 \tag{II.117}$$

continued to the complex plane. The results of these calculations are shown on figure II.12 as differences between the complex energies $\mathcal{E}_n$ and their scattering length approximations $\mathcal{E}_n^1 = \lambda_n \epsilon_\mathrm{g} + mga$. The upper and lower plots correspond to real and imaginary parts of these differences and show that the differences are at a level of a few $10^{-5}\epsilon_\mathrm{g}$ for the lowest lying quantum levitation states.

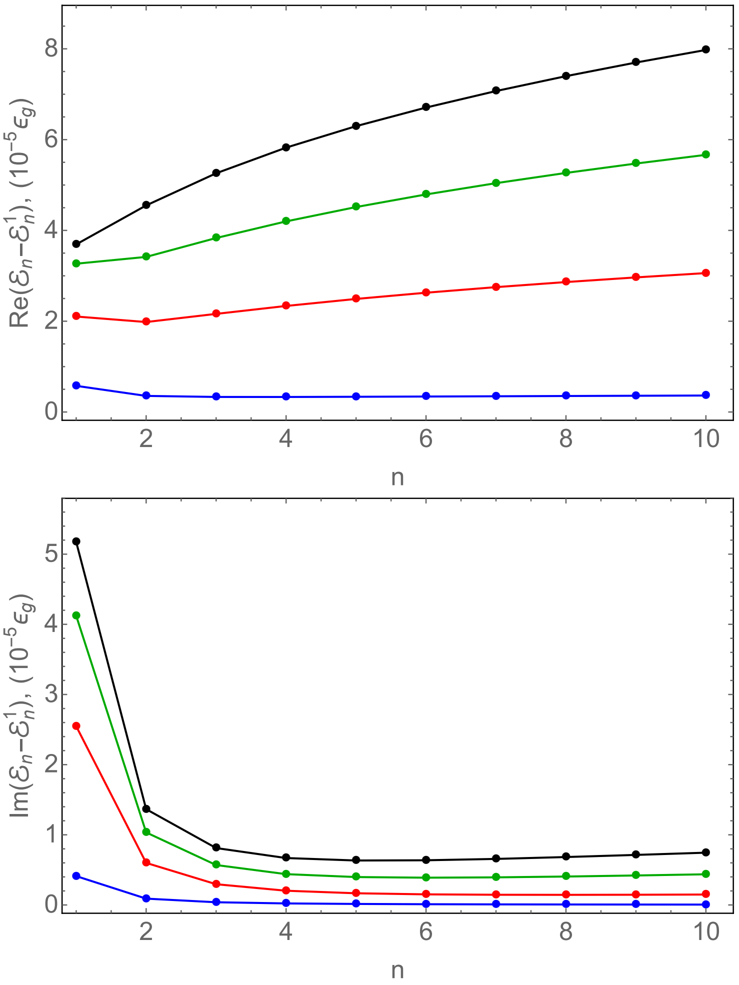

Figure II.12: Differences between the complex energies $\mathcal{E}_n$ and their approximate expressions $\mathcal{E}_n^1 = \lambda_n \epsilon_{\text{g}} + mga$ for a perfect mirror (black line), a silicon bulk (green line), a silica bulk (red line) and a liquid helium bulk (blue line). The upper and lower plots show the real and imaginary parts of these complex differences, both in units of $10^{-5}\epsilon_{\text{g}}$.

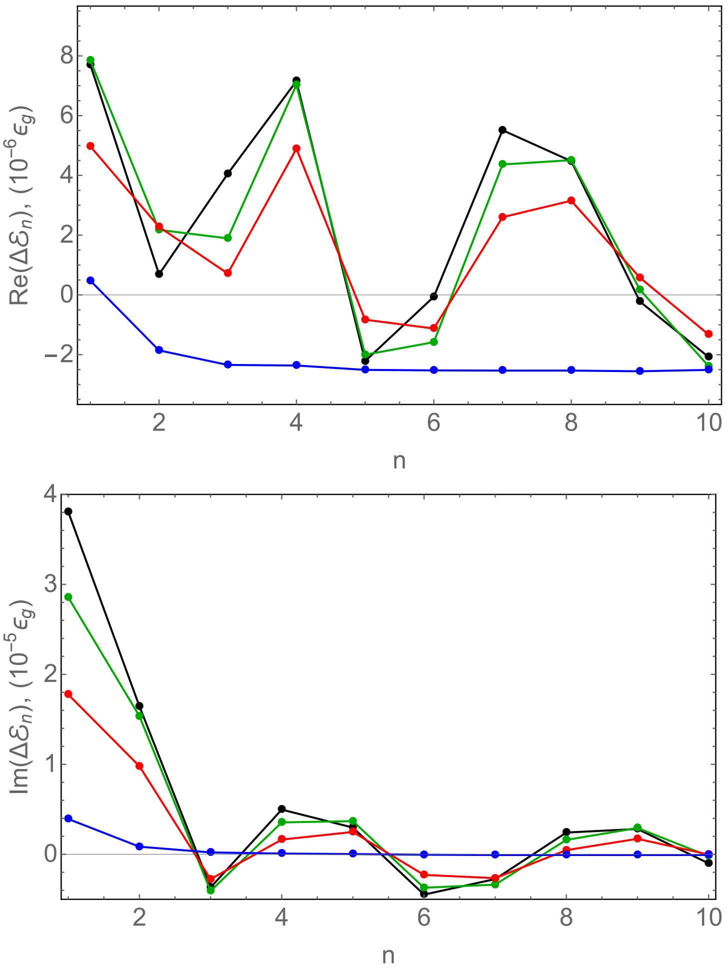

Figure II.13: Differences between the complex energies $\mathcal{E}_n$ calculated in the analytical and numerical methods for a perfect mirror (black line), a silicon bulk (green line), a silica bulk (red line) and a liquid helium bulk (blue line). The upper and lower plots show the real and imaginary parts of these complex differences, in units of $10^{-6}\epsilon_\text{g}$ and in units of $10^{-5}\epsilon_\text{g}$ respectively.

We show on Figure II.13 the differences between the analytical and numerical solutions for complex energies

$$\Delta\mathcal{E}_n = \mathcal{E}_n^\text{ana} - \mathcal{E}_n^\text{num}. \tag{II.118}$$

The upper and lower plots show the real and imaginary parts of $\Delta\mathcal{E}_n$, in units of $10^{-6}\epsilon_\text{g}$ and $10^{-5}\epsilon_\text{g}$ respectively. Both plots show oscillations of the numerical values around the smoother variation obtained from the analytical method. These oscillations remain at a level smaller than $8 \cdot 10^{-6}\epsilon_\text{g}$ for the real part, $4 \cdot 10^{-5}\epsilon_\text{g}$ for the imaginary part. Though the level of agreement is worse by a factor of the order of 5 for the imaginary parts than for the real ones, we note that the precise knowledge of resonance widths is less critical than that of resonance positions when analyzing spectroscopic measurements.

In this chapter, we have given detailed calculations of the Casimir-Polder shifts on quantum levitation states of antihydrogen atoms above a material surface. We have used Liouville transformations and Langer coordinates to build up a physical picture of these states corresponding to resonances of a cavity. The bottom mirror of the cavity is a partly reflective one associated with quantum reflection on the CP potential while the top mirror is a perfectly reflecting one due to gravity. We have presented a full numerical treatment as well as an improved approximate analytical discussion of the properties of the cavity resonances. We have also proposed two different methods for characterizing these properties through the complex energies $\mathcal{E}_n$ defined as poles of the cavity response function or the real resonance energies E_n defined from the cavity round trip phase. We have checked that

$$|\mathrm{Re}(\mathcal{E}_n) - E_n| < 6 \cdot 10^{-6} \epsilon_\mathrm{g} \tag{II.119}$$

for all low-lying quantum states.

The comparison of all these results shows that the analytical treatment built up in the present work on the new effective-range theory is sufficient to compute the corrections caused by the Casimir-Polder interaction at an accuracy level better than $10^{-5}\epsilon_\mathrm{g}$ for the positions of the resonances (a few 10^{-6} for a liquid helium mirror). This should be sufficient for analyzing spectroscopic tests of the weak equivalence principle with antihydrogen [85–87] up to an accuracy of this order.

Chapter III

Quantum interferences of gravitational quantum states

> “ *[...] comme la fluide peinture de certains primitifs, faisait se détacher les détails les plus insignifiants de leur vie, sur un fond d'or. Pour la plupart, les visages mêmes de ces jeunes filles étaient confondus dans cette rougeur confuse de l'aurore d'où les véritables traits n'avaient pas encore jailli.* ”
>
> ---
>
> **Marcel Proust**
> ***À l'ombre des jeunes filles en fleurs***

The experimental knowledge of the behavior of antihydrogen ($\overline{H}$) in a gravitational field remains imprecise with the best measurement [9] not even giving the sign of its free fall acceleration $\overline{g}$. This is why several collaborations have proposed dedicated experiments for improving the accuracy of $\overline{g}$-measurement by using different techniques on antihydrogen atoms produced at CERN [10–12]. In particular, the GBAR collaboration is installing an experiment on ultracold antihydrogen atoms aiming to measure $\overline{g}$ by a classical timing method [14].

In this chapter, we propose to improve the accuracy of the equivalence principle test for antihydrogen by using quantum interference techniques on the gravitationally bound quantum states of ultracold antihydrogen atoms bouncing above a reflecting matter surface. The idea we present here is drawn from experiments performed by inducing transitions between gravitational quantum states of ultracold neutrons [62–64, 148, 166]. For antihydrogen atoms, the mechanism should still work since the quantum reflection is produced by the rapidly varying attractive Casimir-Polder interaction calculated in chapter I [22–26, 28, 29].

Atoms with a low vertical velocity above the surface are trapped by the combined action of quantum reflection and gravity and they stay in quantum levitation states for long times which can exceed one second over an helium surface [39]. The transition frequencies between these states, well known in the case of perfect quantum reflection, are not perturbed here by any mechanism inducing transitions between these states. They are only submitted to shifts due to the Casimir-Polder interaction which have been precisely calculated in chapter II. It follows that the accuracy of the $\overline{g}$-measurement can be improved by using quantum interference techniques on these quantum levitation states [93, 167]. The method we develop in this chapter shows the advantage of using most antiatoms prepared in the experiment and being simple in its principle as interferences between quantum states are read without inducing transitions between them.

We start by presenting the free fall timing experiment in section III.1. We introduce the Wigner function, an adapted tool to treat the classical propagation of the matter wave in the gravitational potential. We also compute the current on the detector, that is the observed experimental signal. In section III.2, we compute the uncertainty on the measurement of $\overline{g}$. First by using analytical expressions of the current obtained for the free fall time experiment, then by presenting statistical tools – Monte Carlo simulation and Cramer-Rao estimation – for extracting the value of the free fall acceleration from the pattern on the detector. Finally, in section III.3 we present a new experimental setup decomposed in two zones. The first one is the interference zone, made of a mirror on which gravitational quantum states interfere. The second one is the free fall zone, that transforms the interference pattern at the end of the mirror to an interference pattern on a the detector. By statistical methods, we show that the accuracy is improved by approximately three orders of magnitude with respect to the classical timing technique planned for the first stage of the [168].

III.1 Free fall of a matter wave

In this section, we describe precisely the free fall of an atomic wave packet from a macroscopic height, corresponding to the initial idea of a free fall timing in the GBAR experiment [11, 14, 141]. In particular we introduce the Wigner function that is an important tool used in our calculations for the new proposed experimental setup.

III.1.a Description of the free fall timing experiment

In the GBAR experiment, an $\overline{H}^+$ ion is prepared in the ground state of an harmonic trap of frequency ω [11, 14]. The ion is then irradiated by a laser photodetachment pulse which releases freely falling $\overline{H}$ atoms. The free fall time measurement starts at this point. The photodetachment process produces also some horizontal kick, with a velocity v_0. The $\overline{H}$ atom freely falls from a height H in the earth gravitational field, until it is annihilated on the detector. The annihilation event is recorded at time T and position X (uppercase letters refer to the detector) by the detector, with a respective sensitivity of 0.1µs and 0.1mm. The signal is the current $J(X,T)$ which depends on the position X and the time T of the annihilation event, and is defined in equation (III.43). The space and time coordinates allow us to measure the current $J(X,T)$ on the detector, which is defined in the following.

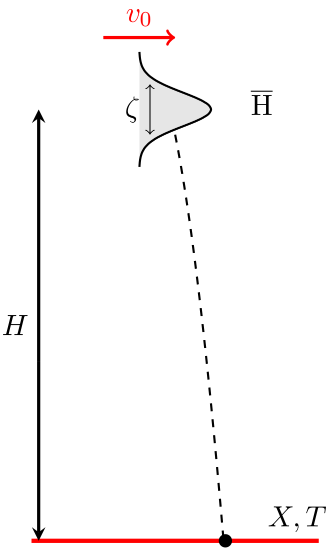

Figure III.1: Schematic representation of the classical timing experiment setup.

The initial state is described by a gaussian wavepacket factorized along x and z axis

$$\Psi_0(x,z) = \phi_0(x)\psi_0(z). \tag{III.1}$$

It minimizes Heisenberg uncertainty relation:

$$\begin{aligned}\psi_0(z) &= \left(\frac{1}{2\pi\zeta^2}\right)^{1/4} \exp\left(-\frac{(z-H)^2}{4\zeta^2}\right), \\ \phi_0(x) &= \left(\frac{1}{2\pi\zeta^2}\right)^{1/4} \exp\left(-\frac{x^2}{4\zeta^2} + i\frac{mv_0}{\hbar}x\right),\end{aligned} \tag{III.2}$$

where v_0 is the horizontal velocity and ζ the dispersion of positions, identical along the 2 axis, that corresponds to a trap frequency

$$\omega = \frac{\hbar}{2m\zeta^2}. \tag{III.3}$$

The parameters corresponding to the GBAR experiment are $0.007\,\mu\text{m} \leq \zeta \leq 0.5\,\mu\text{m}$ and $H = 30$ cm.

III.1.b Time evolution of the wavefunction

The evolution of the wave packet obeys also the time dependent Schrödinger equation in a potential mgz:

$$i\hbar\frac{\partial\Psi}{\partial t} = \left[-\frac{\hbar^2}{2m}\frac{\partial^2}{\partial x^2} - \frac{\hbar^2}{2m}\frac{\partial^2}{\partial z^2} + mgz\right]\Psi. \tag{III.4}$$

Since the Hamiltonian is separable in x and z coordinates, the wavefunction remains factorized:

$$\Psi_t(x,z) = \phi_t(x)\psi_t(z). \tag{III.5}$$

The horizontal evolution leads to a mere spreading of the wave packet:

$$\phi_t(x) = \left(\frac{m\omega}{\pi\hbar(1+i\omega t)^2}\right)^{1/4} \exp\left(-\frac{mv_0^2}{2\hbar\omega}\right) \exp\left(-\frac{m\omega}{2\hbar(1+i\omega t)}(x - iv_0/\omega)^2\right). \tag{III.6}$$

We focus now on the vertical evolution. The solution of the Schrödinger equation in a uniform gravitational field can be obtained from the solution of the free equation after transformation to a uniformly accelerated frame [169, 170]. In this sense, non-relativistic quantum mechanics is compatible with the weak equivalence principle [170–175]. A precise development is done in [36], and we present here the main results. We first place ourselves in an inertial reference frame with coordinate z_0. In this frame the quantum state of the particle is $|\psi^0\rangle$ and it evolves with the free Schrödinger equation:

$$i\hbar\frac{\mathrm{d}}{\mathrm{d}t}|\psi^0\rangle = \hat{H}_0|\psi^0\rangle = \frac{\hat{P}_z^2}{2m}|\psi^0\rangle, \tag{III.7}$$

where the free Hamiltonian $\hat{H}_0$ depends only on the momentum operator $\hat{P}_z$ and not on the position operator $\hat{Z}$. Its evolution operator $\hat{U}_0(t)$ relates the free state $|\psi_t^0\rangle$ to the state at time 0 $|\psi_0^0\rangle$ through:

$$|\psi_t^0\rangle = \hat{U}_0(t)|\psi_0^0\rangle \tag{III.8}$$

$$\hat{U}_0(t) \equiv \exp\left(\frac{-i}{\hbar}\hat{H}_0 t\right) = \exp\left(\frac{-i}{\hbar}\frac{\hat{P}_z^2}{2m}t\right). \tag{III.9}$$

Let us now consider a state $|\psi\rangle$ evolving in a gravitational potential, according to the Schrödinger equation:

$$i\hbar\frac{\mathrm{d}}{\mathrm{d}t}|\psi\rangle = \left(\frac{\hat{P}_z^2}{2m} + mg\hat{Z}\right)|\psi\rangle. \tag{III.10}$$

The solution $|\psi_t\rangle$ to this equation can be expressed in terms of the initial state $|\psi_0\rangle$:

$$|\psi_t\rangle = \hat{U}(t)|\psi_0\rangle \tag{III.11}$$

where $\hat{U}(t)$ is the evolution operator defined in two forms that are identical [36]:

$$\hat{U}(t) = \exp\left(\frac{i}{\hbar}\frac{mg^2t^3}{3}\right)\hat{T}\hat{S}\hat{U}_0 = \exp\left(\frac{-i}{\hbar}\frac{mg^2t^3}{6}\right)\hat{S}\hat{T}\hat{U}_0, \tag{III.12}$$

$$\hat{S} = \exp\left(-\frac{i}{\hbar}mgt\hat{Z}\right), \qquad \hat{T} = \exp\left(\frac{i}{\hbar}\frac{gt^2}{2}\hat{P}_z\right). \tag{III.13}$$

In position space, we write the wavefunction in terms of the solution $\psi_t^0(z)$ of the free equation:

$$\psi_t(z) \equiv \langle z\,|\psi_t\rangle \tag{III.14}$$

$$= \psi_t^0\left(z + \frac{gt^2}{2}\right)\exp\left(\frac{-i}{\hbar}\left(mgtz + \frac{mg^2t^3}{6}\right)\right). \tag{III.15}$$

In momentum space the wavefunction can be written directly in terms of the initial wavefunction:

$$\widetilde{\psi}_t(p_z) \equiv \langle p_z\,|\psi_t\rangle \tag{III.16}$$

$$= \widetilde{\psi}_t^0(p_z + mgt)\exp\left(\frac{-i}{\hbar}\left(\frac{p_z^2t}{2m} + \frac{gt^2p_z}{2} + \frac{mg^2t^3}{6}\right)\right). \tag{III.17}$$

Evaluating it between an initial and a final momentum state gives the propagator in momentum space:

$$K_p(p_z^f, p_z^i, t) \equiv \langle p_z^f|\hat{U}(t)|p_z^i\rangle \tag{III.18}$$

$$= \exp\left(\frac{-i}{\hbar}\left(\frac{(p_z^f)^2t}{2m} + \frac{gt^2p_z^f}{2} + \frac{mg^2t^3}{6}\right)\right)\delta(p_z^f + mgt - p_z^i). \tag{III.19}$$

In coordinate space the propagator is expressed in terms of the free propagator:

$$K(z_f, z_i, t) \equiv \langle z_f|\hat{U}(t)|z_i\rangle \tag{III.20}$$

$$= K_0\left(z_f + \frac{gt^2}{2}, z_i, t\right)\exp\left(\frac{-i}{\hbar}\left(mgtz_f + \frac{mg^2t^3}{6}\right)\right), \tag{III.21}$$

with

$$K_0(z_f, z_i, t) \equiv \langle z_f|\hat{U}_0(t)|z_i\rangle = \int\frac{\mathrm{d}p_z}{2\pi}\,\langle z_f|p_z\rangle\exp\left(\frac{-i}{\hbar}\frac{p_z^2}{2m}t\right)\langle p_z|z_i\rangle \tag{III.22}$$

$$= \sqrt{\frac{m}{2i\pi\hbar t}}\exp\left(\frac{i}{\hbar}\frac{m(z_f - z_i)^2}{2t}\right), \tag{III.23}$$

and

$$K(z_f, z_i, t) = \sqrt{\frac{m}{2i\pi\hbar t}} \exp\left(\frac{i}{\hbar}\left(\frac{m(z_f - z_i)^2}{2t} - \frac{mg(z_f + z_i)t}{2} - \frac{mg^2t^3}{24}\right)\right). \tag{III.24}$$

$$\tag{III.25}$$

We remark that

$$K(z_f, z_i, t) = \sqrt{\frac{m}{2i\pi\hbar t}} \exp\left(\frac{i}{\hbar} S_{\mathrm{cl}}(z_f, z_i, t)\right), \tag{III.26}$$

with $S_{\mathrm{cl}}(z_f, z_i, t)$ Hamilton's principal function associated with the classical trajectory joining points z_i and z_f in time t:

$$S_{\mathrm{cl}}(z_f, z_i, t) = \int_0^t \left(\frac{m}{2}\left(\frac{\mathrm{d}z_{\mathrm{cl}}}{\mathrm{d}\tau}(\tau)\right)^2 - mgz_{\mathrm{cl}}(\tau)\right) \mathrm{d}\tau, \tag{III.27}$$

$$z_{cl}(\tau) = z_i + v_i\tau - \frac{g\tau^2}{2}, \quad v_i = \frac{z_f - z_i}{t} + \frac{gt}{2}. \tag{III.28}$$

The fact that the phase of the quantum propagator is proportional to the action associated with the classical trajectory is a well known property of systems with Hamiltonians that are at most quadratic in position and momentum [176].

III.1.c Wigner function

We have just seen that the propagator (III.26) in a uniform field can be written in terms of the classical action. Quantum states thus propagate classically in a linear potential. However, the state itself can be highly non-classical. This is best seen in the phase space formulation of quantum mechanics introduced by Wigner [177], as discussed in particular in [178].

The Wigner phase space quasi-distribution or *Wigner function* is a mixed position-momentum representation of the density matrix $\hat{\rho}$. It is equivalent to the density matrix, meaning that it can describe both pure states and statistical ensembles [179]. Its proximity to the classical phase space distribution makes the Wigner function an ideal tool to study the classical limit [180], but we stress that it is a fully quantum object.

In a bidimensional space, the Wigner function is a real function of the pairs of conjugate variables x and p_x, and z and p_z defined by:

$$\begin{aligned} W_t(x, z, p_x, p_z) \equiv & \frac{1}{(2\pi\hbar)^2} \int_{\mathbb{R}^2} \mathrm{d}\zeta_x \mathrm{d}\zeta_z \; e^{-i(p_x\zeta_x + p_z\zeta_z)/\hbar} \\ & \times \langle x + \zeta_x/2, z + \zeta_z/2 | \hat{\rho}(t) | x - \zeta_x/2, z - \zeta_z/2 \rangle, \end{aligned} \tag{III.29}$$

which is easily shown to be equivalent to the dual definition

$$\begin{aligned} W_t(x,z,p_x,p_z) \equiv &\frac{1}{(2\pi\hbar)^2}\int_{\mathbb{R}^2}\frac{\mathrm{d}\varpi_x}{2\pi\hbar}\frac{\mathrm{d}\varpi_z}{2\pi\hbar}e^{i(\varpi_x x+\varpi_z z)/\hbar} \\ &\times \langle p_x+\varpi_x/2, p_z+\varpi_z/2|\hat{\rho}(t)|p_x+\varpi_x/2, p_z-\varpi_z/2\rangle\,. \end{aligned} \tag{III.30}$$

For a pure state $\hat{\rho} = |\Psi\rangle\langle\Psi|$, we get in the original space:

$$\begin{aligned} W_t(x,z,p_x,p_z) = &\frac{1}{(2\pi\hbar)^2}\int_{\mathbb{R}^2}\mathrm{d}\zeta_x\mathrm{d}\zeta_z e^{-i(p_x\zeta_x+p_z\zeta_z)/\hbar} \\ &\times \Psi_t(x+\zeta_x/2, z+\zeta/2)\Psi_t^*(x-\zeta_x/2, z-\zeta/2). \end{aligned} \tag{III.31}$$

In the momentum space, the formula is similar:

$$\begin{aligned} W_t(x,z,p_x,p_z) = &\frac{1}{(2\pi\hbar)^2}\int_{\mathbb{R}^2}\frac{\mathrm{d}\varpi_x}{2\pi\hbar}\frac{\mathrm{d}\varpi_z}{2\pi\hbar}e^{i(\varpi_x x+\varpi_z z)/\hbar} \\ &\times \Psi_t(p_x+\varpi_x/2, p_z+\varpi_z/2)\Psi_t^*(p_x-\varpi_x/2, p_z-\varpi_z/2). \end{aligned} \tag{III.32}$$

Unlike the classical phase space distribution function, the Wigner function is not a proper probability density, in particular it can take negative values [181, 182]. Nevertheless, it is known as a quasi-probability distribution since it can be used to write averages of observables on phase space:

$$\langle\hat{A}\rangle \equiv \mathrm{Tr}(\hat{\rho}\hat{A}) \tag{III.33}$$

$$= \int_{\mathbb{R}^4}\mathrm{d}x\mathrm{d}z\mathrm{d}p_x\mathrm{d}p_z\, W(x,z,p_x,p_z,t)A_W(x,z,p_x,p_z,t), \tag{III.34}$$

where $A_W(x,z,p_x,p_z,t)$ is the Weyl transform of the observable:

$$\begin{aligned} A_W(x,z,p_x,p_z,t) \equiv &\int_{\mathbb{R}^2}\mathrm{d}\zeta_x\mathrm{d}\zeta_z e^{-i(p_x\zeta_x+p_z\zeta_z)/\hbar} \\ &\times \langle x+\zeta_x/2, z+\zeta_z/2|\hat{A}(t)|x-\zeta_x/2, z-\zeta_z/2\rangle\,. \end{aligned} \tag{III.35}$$

The marginals of the Wigner function give the probability densities in position and momentum space:

$$\int_{\mathbb{R}^2}\mathrm{d}x\mathrm{d}z\, W_t(x,z,p_x,p_z) = \frac{1}{(2\pi\hbar)^2}\langle p_x,p_z|\hat{\rho}|p_x,p_z\rangle\,, \tag{III.36}$$

$$\int_{\mathbb{R}^2}\mathrm{d}p_x\mathrm{d}p_z\, W_t(x,z,p_x,p_z) = \langle x,z|\hat{\rho}|x,z\rangle\,. \tag{III.37}$$

The vertical probability current density can be expressed as:

$$J(x,z,t) = \int_{\mathbb{R}^2}\mathrm{d}p_x\mathrm{d}p_z\,\frac{p_z}{m}W_t(x,z,p_x,p_z). \tag{III.38}$$

Finally, the Wigner function has the following remarkable property for at most quadratic potentials: it relates *classicaly* two positions in space and time, as it is proven in appendix B:

$$W_t(x,z,p_x,p_z) = W_{t-\tau}\left(x - \frac{p_x}{m}\tau, z - \frac{p_z}{m}\tau - \frac{g\tau^2}{2}, p_x, p_z + mg\tau\right) \tag{III.39}$$

We plot in figure III.2 the Wigner quasi-distribution $W_t(x_{\mathrm{cl}}, z, p_{x,\mathrm{cl}}, p_z)$ in (z, p_z) space while x and p_x coordinates follow the classical trajectory. The initial wave packet is gaussian (III.78), and we take $H = 20\ell_g$ for more visibility in the plot. Marginal distributions are also represented in figure III.2. The classical free fall time of a classical particle dropped with no initial velocity is defined as:

$$T_H \equiv \sqrt{\frac{2H}{g}} \tag{III.40}$$

The Wigner function is plotted at $t = 0$, $t = T_H/2$ and $t = T_H$. We can note that the momentum distribution is centered on the classical momentum $z_{\mathrm{cl}}(t) = -mgt$ and that it keeps its shape. The center of the position distribution also moves along the classical trajectory $z_{\mathrm{cl}}(t) - gt^2/2$ but the wavepacket spreads as it falls.

The fact that the Wigner function propagates like a classical phase space distribution in a linear potential will prove useful in upcoming calculations. However, one must keep in mind that the Wigner function describes a quantum state. For instance, in contrast with a classical distribution, it is constrained by Heisenberg's uncertainty principle.

III.1.d Current on the detector

Based on the results of Wigner formalism, we are now able to compute easily the current on the detector for a Gaussian wave packet freely falling. The initial wavefunction is $\Psi_0(x, z)$ (III.78). The corresponding Wigner function at time $t = 0$ is also computed:

$$W_0(x,z,p_x,p_z) = \frac{1}{(\pi\hbar)^2}\exp\left(-\frac{x^2}{2\xi^2} - \frac{(z-H)^2}{2\xi^2} - \frac{2(p_x - mv_0)^2\xi^2}{\hbar^2} - \frac{2p_z^2\xi^2}{\hbar^2}\right). \tag{III.41}$$

so that after a free fall time t it becomes (by taking $\tau = t$ in (III.39)):

$$\begin{aligned} W_t(x,z,p_x,p_z) = \frac{1}{(\pi\hbar)^2}\exp\Bigg(&-\frac{(x - p_x t/m)^2}{2\xi^2} - \frac{(z - H - p_z t/m - gt^2/2)^2}{2\xi^2} \\ &- \frac{2(p_x - mv_0)^2\xi^2}{\hbar^2} - \frac{2(p_z + mgt)^2\xi^2}{\hbar^2}\Bigg). \end{aligned} \tag{III.42}$$

The current J on the detector (at $Z = 0$) is also obtained by integrating (III.42) (we omit to write the z coordinate for the current since it will be always calculated on the detector at $Z = 0$):

$$J(X,T) = \int_{\mathbb{R}^2} \mathrm{d}p_x \mathrm{d}p_z \, \frac{p_z}{m} W_T(X, 0, p_x, p_z). \tag{III.43}$$

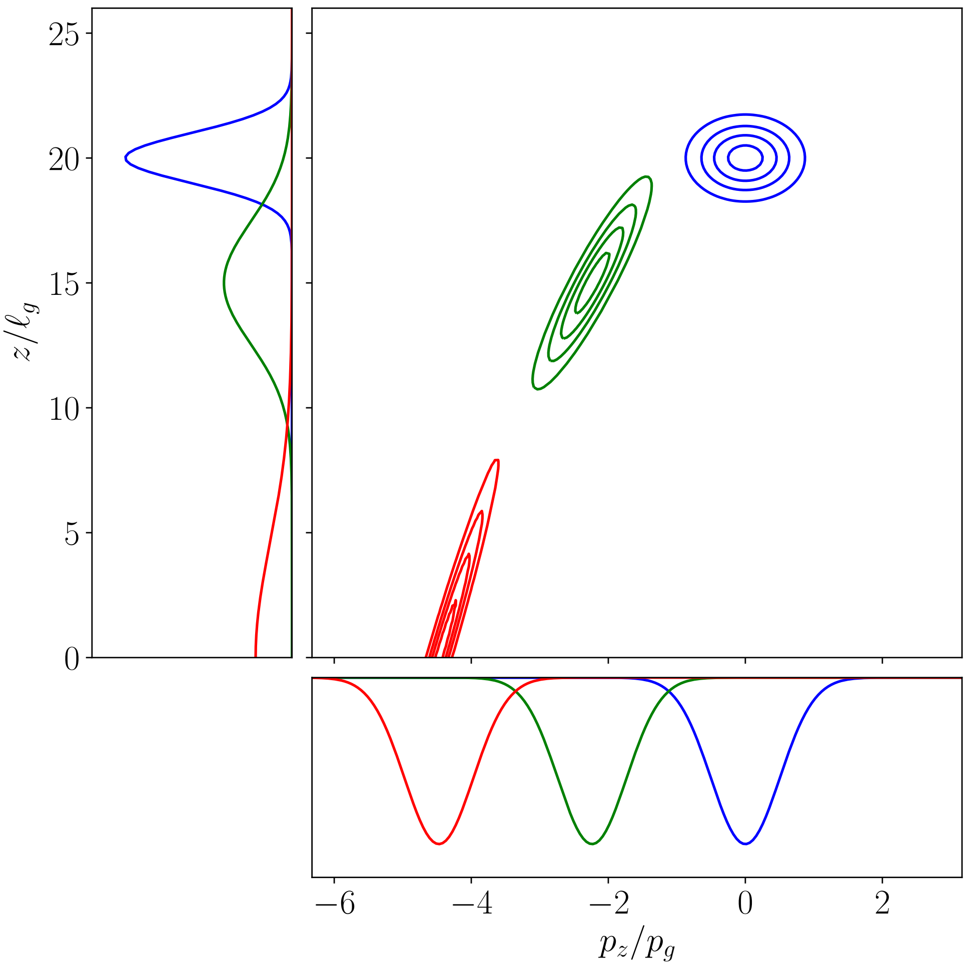

Figure III.2: Freely falling Gaussian wavepacket dropped from height $H = 20\ell_g$ with no average velocity, at times $t = 0$ (blue), $T_H/2$ (green) and T_H (red). Central panel: Wigner function, left panel: probability density in coordinate space, bottom panel: probability density in momentum space.

An explicit calculation leads to the following expression:

$$\begin{aligned} J(X,T) = &-\frac{t}{\pi(1+(\omega T)^2)^2}\sqrt{\frac{m\omega^5}{2\hbar}}\left(H+\frac{gT^2}{2}+\frac{g}{\omega^2}\right) \\ &\times \exp\left(-\frac{m\omega}{\hbar}\left[\frac{\left(H-gT^2/2\right)^2+\left(X-v_0T\right)^2}{1+(\omega T)^2}\right]\right). \end{aligned} \tag{III.44}$$

We remark that $J(X,T)$ is always negative and has a maximal amplitude for the classical free fall time trajectory. The probability current density $|J(X,T)|$ thus obtained is plotted in figure III.3. The oblique shape can be understood intuitively: the first atoms that are annihilated on the detector (corresponding to the upper region of the plot) have less time to move horizontally, that is why the are concentrated on the left region of the plot. On the contrary the vertically slowest falling atoms can reach more distant region in the horizontal axis.

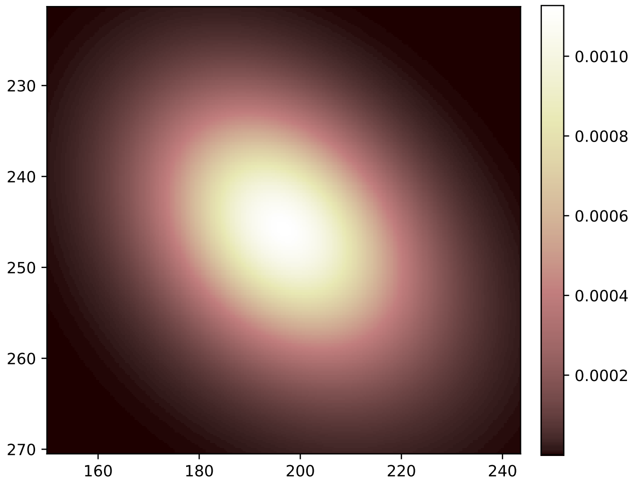

Figure III.3: Probability current density $|J(X,T)|$ on the detection plate for the classical free fall timing experiment for an initial gaussian wavepacket Ψ_0 (III.78) with $\zeta = 0.5\,\mu$m, $H = 30$ cm and $v_0 = 0.8\,\mathrm{m.s}^{-1}$, as a function of X (horizontal axis, in mm) and T (vertical axis, in ms; unit chosen for the distribution so that it is normed).

III.2 Estimation of the uncertainty

Tests of the weak equivalence principle which time the free fall of a test mass are often limited by the control over the initial dropping time, position and velocity. For this reason, the most precise tests of the equivalence principle on macroscopic masses are performed using torsion pendulums [40, 183]. For microscopic test masses this is no longer possible and a precise control of the initial conditions is essential.

Since the antihydrogen atom is cold, quantum uncertainties corresponding to the width of the wavepacket itself limit the final accuracy. They are constrained by Heisenberg's uncertainty principle:

$$\zeta \times \sigma_v \geq \frac{\hbar}{2m} \tag{III.45}$$

III.2.a Classical time uncertainty

In an experiment where an atom is prepared in a trap and then dropped on a detection plate, both types of uncertainties will result in a spread of the arrival time distribution. In this section we will determine this spread supposing that the particle is dropped from a height $\simeq H$ with initial vertical velocity $\simeq 0$ and that it is detected by an ideal detector as it crosses the plane $z = 0$, as it is illustrated in figure III.1. We have shown that the quantum phase space quasi-distribution $W(z, p, t)$ obeys classical equations of motion in a uniform gravity field. It follows that we can do all calculations based on classical trajectories, by treating classical and quantum uncertainties on the same footing [36, 93]. Classically, the horizontal motion is decoupled from the vertical one. It follows that in a classical free fall time measurement, the initial horizontal velocity v_0 does not play an important role.

Classically, a particle with initial position z_i and initial velocity v_i follows the trajectory:

$$z(\tau) = z^i + v_z^i \tau - \frac{g\tau^2}{2} \tag{III.46}$$

Therefore a particle dropped from $z^i = H + \delta z$ with velocity $v_z^i = 0 + \delta v_z$ reaches $z = 0$ at time $T = T_H + \delta t$ with

$$T_H = \sqrt{\frac{2H}{g}} \qquad \text{and} \qquad \delta t \simeq \frac{\delta z + T_H \delta v_z}{g T_H} \tag{III.47}$$

at first order in the small errors δz, δv.

The standard deviation σ_T on the arrival time can be expressed in terms of ζ and σ_v, the standard deviations of δz, δv_z considered as independent and normally distributed:

$$\sigma_T = \left(\frac{\zeta}{g T_H}\right)^2 + \left(\frac{\sigma_v}{g}\right)^2 \tag{III.48}$$

and so the relative uncertainty on the arrival time is:

$$\frac{\sigma_T}{T_H} = \sqrt{\left(\frac{\zeta}{2H}\right)^2 + \left(\frac{\sigma_v}{v_H}\right)^2}\,, \qquad v_H \equiv \sqrt{2gH}. \tag{III.49}$$

For a quantum wavepacket, in the best possible case, σ_z and σ_v are of purely quantum origin and they saturate the Heisenberg inequality (III.45). The uncertainty on the arrival time (III.49) can then be expressed in terms of σ_z only

$$\frac{\sigma_T}{T_H} = \sqrt{\left(\frac{\zeta}{2H}\right)^2 + \left(\frac{\hbar}{2mv_H\zeta}\right)^2}. \tag{III.50}$$

It reaches an optimum for

$$\sigma_z^{\text{opt}} = \sqrt{\frac{\hbar H}{mv_H}}, \qquad \omega^{\text{opt}} = \frac{1}{T_H} = \frac{1}{t_g}\sqrt{\frac{\ell_g}{H}}. \tag{III.51}$$

The corresponding optimum resolution for the free fall measurement is:

$$\left(\frac{\sigma_T}{T_H}\right)_{\text{opt}} = \sqrt{\frac{\hbar}{2mv_H H}}. \tag{III.52}$$

The larger the product $mv_H H$ is with respect to $\hbar/2$, the better this optimal resolution becomes.

The relative uncertainty on g is exactly twice the relative uncertainty on the time arrival [93]:

$$\frac{\sigma_g}{g} = 2\frac{\sigma_T}{T_H}. \tag{III.53}$$

Then, for a number of atoms $N = 1000$ and for a free fall height $H = 30$ cm,

$$\left(\frac{\sigma_g}{g}\right)_{\text{opt}} = \frac{1}{\sqrt{N}}\sqrt{\frac{2\hbar}{mv_H H}} = 1.3\cdot 10^{-5}. \tag{III.54}$$

However, the optimum resolution is not achieved experimentally. The uncertainty on the arrival time is dominated by the standard deviation of the initial vertical velocity Δv_z in (III.50), in such a way that we can write:

$$\frac{\sigma_g}{g} \simeq \frac{1}{\sqrt{N}}\frac{\hbar}{2mv_H\zeta}. \tag{III.55}$$

An efficient way to decrease the relative uncertainty consists also in increasing the vertical position dispersion ζ. We summarize in table III.1 relative uncertainty on g for different values of vertical position dispersion ζ achievable experimentally. We find a relative uncertainty of the order of the % for $\zeta = 0.07$ µm and $\sigma_g/g = 1.6\cdot 10^{-3}$ in the best case for the lowest achievable frequency trap ω.

ζ (µm)	0.07	0.2	0.5
$\omega/2\pi$ (kHz)	1031	126	20
E_c (neV)	2.13	0.26	0.04
σ_g/g (%)	**1.2**	**0.41**	**0.16**

Table III.1: Relative uncertainty depending on ζ and corresponding frequency trap ω and kinetic energy.

III.2.b Uncertainty estimation from the probability current distribution

Without any approximation, we can directly compute the arrival time distribution from the expression of the probability current distribution $J(X,T)$ (III.44). Expanding the argument of the exponential to second order in $\delta T = T - T_H$ and $\delta X = X - X_H$, with $X_H \equiv v_0 T_H$, we find for $\delta T \ll T_H$ and $\delta X \ll X_H$:

$$\frac{m\omega}{\hbar}\left[\frac{\left(H - gT^2/2\right)^2 + \left(X - v_0 T\right)^2}{1 + (\omega T)^2}\right] \simeq \frac{\delta T^2}{2\sigma_T^2} + \frac{\delta X^2}{2\sigma_X^2} - \frac{\delta T \delta X}{2\sigma_{TX}^2}, \tag{III.56}$$

$$\sigma_T^2 = \frac{\hbar}{2m\omega}\left[\frac{1 + (\omega T_H)^2}{(gT_H)^2 + v_0^2}\right] \tag{III.57}$$

$$\sigma_X^2 = \frac{\hbar[1 + (\omega T_H)^2]}{2m\omega} = \zeta^2[1 + (\omega T_H)^2] \tag{III.58}$$

$$\sigma_{TX}^2 = \frac{\hbar[1 + (\omega T_H)^2]}{4m\omega v_0}. \tag{III.59}$$

In these formulas, the horizontal velocity v_0 induces correlations between arrival time and position. In the case of low velocity v_0, (III.57) becomes:

$$\sigma_T^2 = \frac{\hbar}{4m\omega g H} + \frac{\hbar\omega}{2mg^2} \tag{III.60}$$

$$= \left(\frac{\zeta T_H}{2H}\right)^2 + \left(\frac{\hbar T_H}{2m v_H \zeta}\right)^2 \tag{III.61}$$

and we recover the classical calculation (III.50).

On the contrary, when the horizontal velocity v_0 is sufficiently high:

$$v_0 \geq g T_H \simeq 2.4 \text{ m.s}^{-1} \tag{III.62}$$

the horizontal velocity is defined more precisely than in the case of a simple spread around $v_0 = 0$. It follows that the standard deviation σ_T decreases with v_0. For a reasonable horizontal velocity $v_0 = 0.25$ m.s^{-1} in the more favorable case of $\zeta = 0.5$ µm, the final uncertainty remains approximately the same:

$$\frac{\sigma_g}{g} = 1.6 \cdot 10^{-3}. \tag{III.63}$$

III.2.c Monte-Carlo simulation

In a case of a gaussian wave packet freely falling on a detector, we can compute analytically the probability current density and deduce the accuracy of the $\overline{g}$ measurement. However, in the new proposed setup in section III.3, it is no longer possible to treat it analytically. We also use statistical methods to estimate the parameter g and then deduce the variance of this estimation. These methods are presented here to build some intuition in a simple case, and will be very useful and necessary when the interference pattern on the detector will be more complex.

The method we use is a Monte Carlo simulation, based on a maximum likelihood estimator [184, 185]. We assume that we have 1000 prepared $\overline{H}$-atoms, that are annihilated on the detector. We thus draw randomly 1000 detection events in the probability distribution $\mathbb{P}_{g_0}$ corresponding to an *a priori* value of the acceleration, say the standard value $g_0 = 9.81$ m.s^{-2}. We consider that this random draw of detection events $\mathcal{D} = \{(X_i, T_i),\ 1 \leq i \leq N\}$ simulates the output of one experiment.

We then use a maximum likelihood method to get an estimator $\hat{g}$ of the parameter g as would be done in the data analysis of the experiment:

$$\mathbb{L}_{\mathcal{D}}\left(g\right) = \prod_{i=1}^{N} \mathbb{P}_g(X_i, T_i), \tag{III.64}$$

$$\ln \mathbb{L}_{\mathcal{D}}\left(g\right) = \sum_{i=1}^{N} \ln \mathbb{P}_g(X_i, T_i). \tag{III.65}$$

This estimator $\hat{g}$ maximizes the likelihood of the random draw $\mathcal{D}$ to reproduce the distributions $\mathbb{P}_g$ corresponding to different *a posteriori* values of the parameters:

$$\left(\frac{\partial \ln \mathbb{L}_{\mathcal{D}}\left(g\right)}{\partial g}\right)_{\hat{g}} = 0. \tag{III.66}$$

Figure III.4 shows quadratic fits of the log likelihood functions (i.e. gaussian fits of the likelihood functions) around their extrema. These fits correspond to 15 random draws of 1000 events, with each fit yielding an estimator $\hat{g}$ of the parameter g and an estimator $\hat{\sigma}_g$ of the dispersion associated with this estimator :

$$\begin{gathered}\ln \mathbb{L}_{\mathcal{D}}\left(g\right) \approx a_{\mathcal{D}} g^2 + b_{\mathcal{D}} g + c_{\mathcal{D}} \\ \hat{g} = -\frac{b_{\mathcal{D}}}{2a_{\mathcal{D}}}, \quad \hat{\sigma}_g = \frac{1}{\sqrt{2|a_{\mathcal{D}}|}}.\end{gathered} \tag{III.67}$$

We have normalized the gaussians so that the variation of their variance is seen more easily as a variation of their height. In that case, all the log-likelihood have approximately the same width, meaning that $\hat{g}$ does not depend on the log-likelihood function we consider in the sample. The variation of the peaks shows the dispersion of the estimator $\hat{g}$ around g_0 for different random draws. The number of 15 draws has been chosen to illustrate this variance while simultaneously avoiding confusion on the figure.

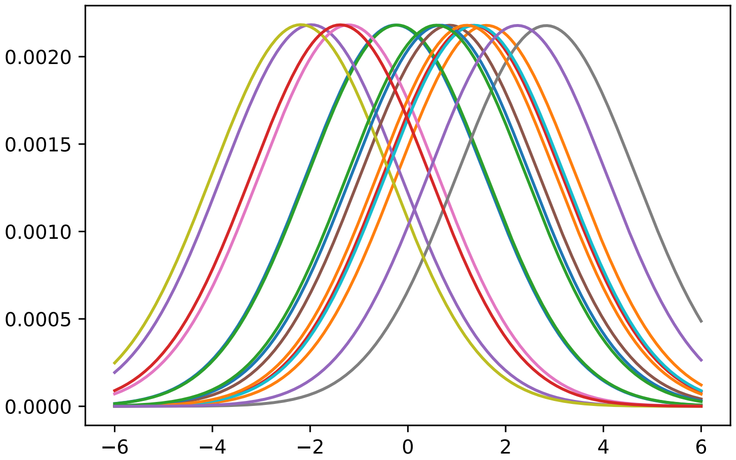

Figure III.4: Fifteen gaussian distributions obtained by a quadratic fit of the log-likelihood function calculated for a random drawing of $N = 1000$ atoms. The colors have no meaning, they only allow one to distinguish the various functions.The horizontal axis scales as $(g - g_0)/g_0 \times 10^3$.

In order to give a robust estimation of the variance, we have finally repeated the full procedure for M different random draws of the N points. The histogram shown in figure III.5 corresponds to $M = 5000$ such draws of the N points, with the parameters ζ corresponding to figure III.9, and a velocity $v_0 = 0.25\,\mathrm{m.s}^{-1}$.

The standard deviation thus obtained is denoted Σ_g and corresponds to the uncertainty on the $\overline{g}$ measurement. For the classical free fall time experiment, with parameters $\zeta = 0.5\ \mu$m and $v_0 = 0.25$ m.s^{-1}, we find:

$$\Sigma_g \simeq 1.7 \cdot 10^{-3}\, g \tag{III.68}$$

This value is consistent with the uncertainty calculated analytically in III.2.a and III.2.b.

III.2.d Cramer-Rao lower bound

Although the Monte-Carlo simulation reproduces the same dispersion as the analytical calculations, we may wonder if there exists another way to extract more information from the probability current density that lead to a lower uncertainty Σ_g. In fact, the information contained on the probability distribution can be quantified by the *Fisher information*:

$$\mathcal{I}(g) = \mathbb{E}\left[-\frac{\partial^2}{\partial g^2}\ln \mathbb{P}_g\right], \tag{III.69}$$

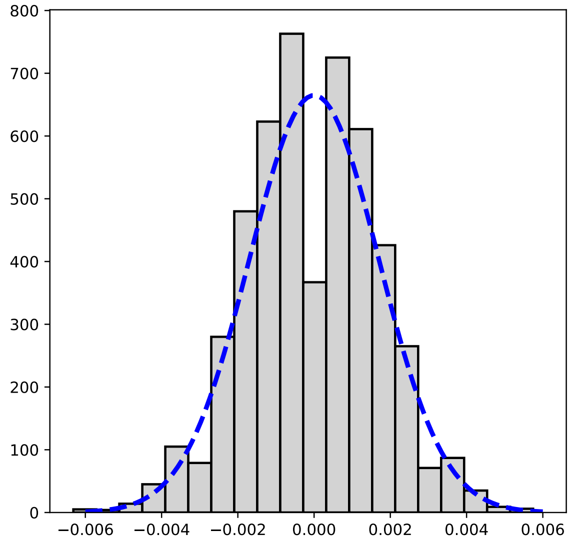

Figure III.5: Histogram of the relative variations $(\hat{g} - g_0)/g_0$ obtained by repeating 5000 times a Monte Carlo simulation on 1000 events, for $\zeta = 0.5$ μm and $v_0 = 0.25$ m.s^{-1}. The vertical axis counts the number of events per channel.

with $\mathbb{E}$ denoting expectation values:

$$\mathbb{E}[f] \equiv \int dXdT\,\mathbb{P}_g(X,T)f(X,T). \tag{III.70}$$

Another way of writing $\mathcal{I}(g)$ can be obtained after an integration by part:

$$\begin{aligned}\mathcal{I}(g) &= -\int dXdT\,\mathbb{P}_g(X,T)\frac{\partial^2}{\partial g^2}\ln\mathbb{P}_g(X,T)\\ &= -\int dXdT\,\mathbb{P}_g(X,T)\left(\frac{\partial^2\,\mathbb{P}_g(X,T)}{\partial g^2}\,\mathbb{P}_g(X,T)-\left(\frac{\partial\,\mathbb{P}_g(X,T)}{\partial g}\right)^2\right)/\,\mathbb{P}_g(X,T)^2\\ &= -\frac{\partial^2}{\partial g^2}\left(\int dXdT\,\mathbb{P}_g(X,T)\right)+\int dXdT\,\mathbb{P}_g(X,T)\left(\frac{\partial}{\partial g}\ln\mathbb{P}_g(X,T)\right)^2\\ &= \mathbb{E}\left[\left(\frac{\partial}{\partial g}\ln\mathbb{P}_g\right)^2\right].\end{aligned} \tag{III.71}$$

The larger the information, the lower the uncertainty is. From the Fisher information, we build the standard deviation $\Sigma_g^{\mathcal{F}}$ defined as following:

$$\Sigma_g^{\mathcal{F}} \equiv \frac{1}{\sqrt{N\mathcal{I}(g)}}. \tag{III.72}$$

It is proven in the general case that for any estimator of the parameter g whose dispersion is Σ_g, the latter dispersion is low bounded [184, 185] by $\Sigma_g^{\mathcal{F}}$:

$$\Sigma_g \geq \Sigma_g^{\mathcal{F}}. \tag{III.73}$$

$\Sigma_g^{\mathcal{F}}$ defines the so-called *Cramer-Rao* lower bound. It means that whatever the estimation method we use, we can never reach a better uncertainty for the considered parameter than (III.72). The proof of the inequality (III.73) is based on Cauchy-Schwarz inequality and becomes an equality for a gaussian probability distribution.

We also define the *statistical efficiency* $\mathfrak{E}$ as [184]:

$$\mathfrak{E} \equiv \left(\frac{\Sigma_g^{\mathcal{F}}}{\Sigma_g}\right)^2. \tag{III.74}$$

$\mathfrak{E}$ always satisfies the inequality:

$$0 \leq \mathfrak{E} \leq 1 \tag{III.75}$$

and an estimator is called efficient if $\mathfrak{E} \simeq 1$, meaning that the Cramer-Rao lower bound is saturated. For the free fall timing experiment, $\Sigma_g^{\mathcal{F}}$ is numerically computed and we finally get:

$$\mathfrak{E} = 94\%. \tag{III.76}$$

The log-likelihood estimator is thus efficient in that case and the dispersion obtained with Monte-Carlo simulation is the best we can achieve for the given probability density distribution $|J(X,T)|$.

We detailed a proof of the asymptotic efficiency of the log-likelihood estimator in appendix C. Detailing the proof has the advantage of showing the condition for the likelihood estimator to be considered as efficient. By assuming the unbiased condition (C.9) converging fast, the efficiency is reach as soon as $B_1 \to -\mathcal{I}(g)$. This is achieved when likelihood functions are gaussian. In that case, the variation of $\hat{g}$ and the expectation value $\mathbb{E}(\hat{\sigma}_g)$ are reliable:

$$\mathbb{E}(\hat{\sigma}_g) \simeq \Sigma_g \simeq \Sigma_g^{\mathcal{F}}. \tag{III.77}$$

In our case, the relative dispersion of $\hat{\sigma}_g / \mathbb{E}(\hat{\sigma}_g) \simeq 0.09\%$. It means that the uncertainty is directly obtain on a single draw corresponding to a single experiment, by fitting the corresponding log likelihood function (III.67).

The second expression of the Fisher information $\mathcal{I}(g)$ given in (III.71) encourage us to propose a new experimental setups that lead to a probability current distribution more sensitive to small variations of g. In simple words, more details act as thin graduations that make it easier to observe small displacement and distortion on the probability current distribution when g is varying, and lead to a larger Fisher information $\mathcal{I}(g)$.

III.3 Interferences of gravitational quantum states

We propose now a new method that consists of measuring the coordinates in space and time of the annihilation of antihydrogen atoms on a detector after a flight above a reflecting surface, thus producing an interference pattern. Similar methods were used in experiments on neutron whispering gallery [186] and we present here a detailed study of the method applied to antihydrogen atoms. In contrast to previous ideas [93], there is not need for a velocity selection, which allows for a large gain in accuracy while effectively using most antihydrogen atoms.

The new method assumes simultaneous measurement of many gravitational quantum states, thus enormously increasing statistics compared to previous proposals [167, 187] which considered one or a few quantum states. A practical implementation of this method is also simple, since it does not need precision optics and mechanics and does not need the selection of a single quantum state. The transition frequencies between these states are also not perturbed by any mechanism inducing transitions.

III.3.a Experimental setup

We give below a precise description of the new quantum interference technique which should lead to a largely improved accuracy for the $\overline{g}$-measurement. Starting from the ultracold antihydrogen $\overline{H}^+$ ions prepared in the GBAR experiment, the method appears as a sequence of steps schematized in figure III.6.

First, the $\overline{H}^+$ wavepacket is prepared as the ground state of an ion trap [11, 14], submitted to a kick giving it a mean horizontal velocity v_0 and irradiated by a laser photodetachment pulse which releases freely falling $\overline{H}$ atoms. The kick can be produced for example by electrostatic means or by the photodetachment process.

The novelty comparing to the free fall timing experiment consists in adding a surface, on which atoms bounce. When considering a liquid helium surface, the atom may bounce hundreds of times before being annihilated, as was calculated in I.3.d, in such a way that the surface is treated here as a perfect quantum reflector. The quantum paths corresponding to different gravitational quantum states interfere. The interference pattern thus produced is detected after a macroscopic free fall down to an horizontal detection plate. The analysis of the distribution in space and time gives access to the estimation of $\overline{g}$. This last part is analogous to the previously studied case III.2 but it leads to an improved accuracy.

This estimation is in principle sensitive to the initial distribution of the atoms after the kick, and this distribution will have to be determined from the envelop of the detection pattern, as discussed below. In the following, we choose a simple model for this distribution, which is sufficient for the purpose of the current work.

In figure III.6 as well as in the text, lowercase letters represent the quantities relative to first stages of preparation and interference above the mirror, while uppercase letters represent quantities associated with free fall and detection stages.

III.3.b Interferences above mirror

The antihydrogen atoms of mass m are released from the fundamental state of an harmonic trap of frequency ω centered at height h above the perfectly reflecting mirror. This state is described by a gaussian wavepacket factorized along x and z axis $\Psi_0(x,z) = \phi_0(x)\psi_0(z)$ which minimizes Heisenberg uncertainty relation:

$$\begin{aligned} \psi_0(z) &= \left(\frac{1}{2\pi\zeta^2}\right)^{1/4} \exp\left(-\frac{(z-h)^2}{4\zeta^2}\right), \qquad \text{(III.78)} \\ \phi_0(x) &= \left(\frac{1}{2\pi\zeta^2}\right)^{1/4} \exp\left(-\frac{x^2}{4\zeta^2} + i\frac{mv_0}{\hbar}x\right), \end{aligned}$$

where v_0 is the velocity kick and ζ the dispersion of positions, identical along the 2 axis, that corresponds to a trap frequency ω (III.3).

The evolution of the wave packet can be decomposed in two parts. Firstly the propagation above the mirror, for $x < d$, treated in this subsection. Then the macroscopic free fall for $x > d$ that is derived in III.3.c. We suppose having no diffraction at the end of the mirror and no horizontal quantum reflection induced by the brutal change of the

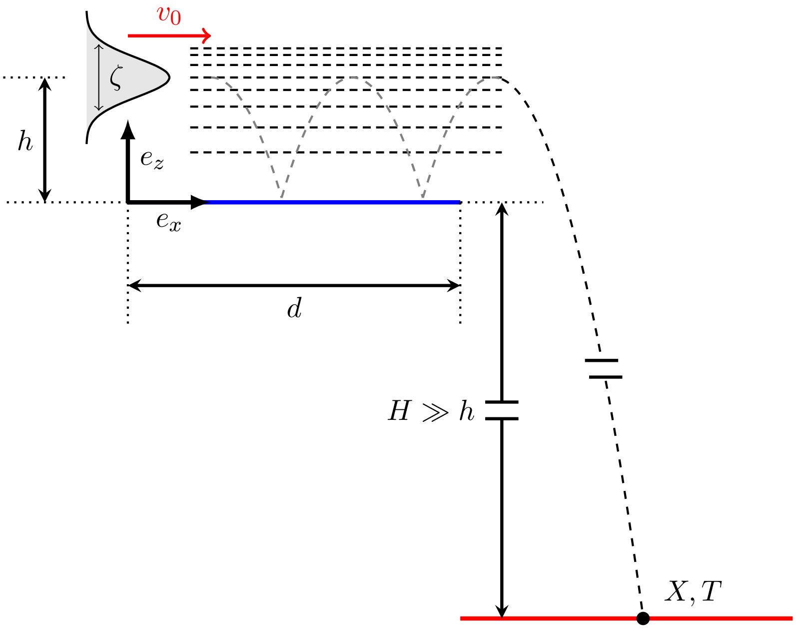

Figure III.6: Schematic representation of the experimental setup. The mirror, of length d, is shown as the blue horizontal line and the detector, a distance H below, as the red horizontal line. X and T are the positions in space and time of the detection events (e_x-axis horizontal, e_z-axis vertical). The wave packet has initially a mean height h above the mirror, a dispersion ζ and an horizontal velocity v_0. The parabolas represent a classical motion with rebounds above the mirror while the horizontal dashed lines represent the paths through different quantum states which interfere in the detection pattern.

potential at $x = d$. These conditions impose the continuity of the wavefunction and its derivative at $x = d$:

$$\Psi(d^-, z) = \Psi(d^+, z) \tag{III.79}$$

$$\frac{\partial \Psi}{\partial x}(d^-, z) = \frac{\partial \Psi}{\partial x}(d^+, z), \tag{III.80}$$

in such a way that we can write without creating confusion $\Psi(d, z)$ and $\frac{\partial \Psi}{\partial x}(d, z)$. Such approximations are made for neutrons and lead to a good agreement between theory and experiment.

The evolution of the wave packet above the surface obeys also the time dependent Schrödinger equation in a potential mgz:

$$i\hbar \frac{\partial \Psi}{\partial t} = \left[-\frac{\hbar^2}{2m} \frac{\partial^2}{\partial x^2} - \frac{\hbar^2}{2m} \frac{\partial^2}{\partial z^2} + mgz \right] \Psi \tag{III.81}$$

with $\Psi(x, 0) = 0$ as a condition of perfect reflectivity of the mirror. We consider the wavefunction remaining factorized in the region $x < d$:

$$\Psi_t(x, z) = \phi_t(x) \psi_t(z), \tag{III.82}$$

as the Hamiltonian is separable in x and z coordinate. This condition imposes severe requirements on the quality of the mirror surface roughness and material homogeneity, but these requirements can be met.

The horizontal evolution leads to a mere spreading of the wave packet:

$$\begin{aligned} \phi_t(z) = {} & \left(\frac{m\omega}{\pi\hbar(1 + i\omega t)^2} \right)^{1/4} \exp\left(-\frac{m v_0^2}{2\hbar\omega} \right) \\ & \times \exp\left(-\frac{m\omega}{2\hbar(1 + i\omega t)} (x - i v_0/\omega)^2 \right). \end{aligned} \tag{III.83}$$

The vertical evolution can be simply described through a decomposition on the orthogonal basis of Airy functions which solve the Schrödinger equation when perfect reflection on the mirror is assumed:

$$\psi_t^n(z) = \Theta(z) \frac{\mathrm{Ai}(z/\ell_g - \lambda_n)}{\sqrt{\ell_g}\mathrm{Ai'}(-\lambda_n)} \exp\left(-i\lambda_n t/t_g\right). \tag{III.84}$$

The Heaviside step function Θ describes perfect reflection at the surface, Ai is the first Airy function and $(-\lambda_n)$ its nth zero; t_g, ℓ_g and p_g are the typical time, length (II.3) and momentum scales determined by $\hbar$, m and g:

$$t_g \equiv \left(\frac{2\hbar}{mg^2} \right)^{1/3} \simeq 1.09 \text{ ms},$$

$$p_g \equiv \frac{\hbar}{\ell_g} \simeq 1.79 \times 10^{-29} \text{ kg.m.s}^{-1}.$$

Using the orthogonality relation (II.15), we can write the decomposition of any wavefunction with support on $\mathbb{R}_+$ on the bound states:

$$\begin{aligned}\psi_t(z) &= \sum_n c_n \psi_t^n(z),\\ c_n &= \int_0^\infty dz \frac{\psi(z)}{\sqrt{l_g}\text{Ai'}(-\lambda_n)} \text{Ai}\left(\frac{z}{l_g} - \lambda_n\right).\end{aligned} \tag{III.85}$$

A Gaussian wavefunction centered around a height h that is much larger than its width ζ has negligible values outside $\mathbb{R}_+$. We can also extend the integral (III.85) to $\mathbb{R}$. We finally find that the expansion coefficients are:

$$\begin{aligned}c_n \simeq \frac{\zeta^{1/2}}{\ell_g^{1/2}} \frac{(8\pi)^{1/4}}{\text{Ai}'(-\lambda_n)} &\text{Ai}\left(\frac{h}{\ell_g} - \lambda_n + \frac{\zeta^4}{\ell_g^4}\right)\\ &\times \exp\left(\frac{\zeta^2}{\ell_g^2}\left(\frac{h}{\ell_g} - \lambda_n + \frac{2}{3}\frac{\zeta^4}{\ell_g^4}\right)\right).\end{aligned} \tag{III.86}$$

After propagating above the mirror, the atom falls freely on the detector. Since the free fall height H is much larger than the height h of the wave packet above the mirror, the free fall can be considered as classical, as it was explained with the Wigner formalism in subsection III.1.c. The free fall thus acts in a similar way as a diffraction process, with the space and time positions of the annihilation event on the detector reading the interaction time and momentum of the atom leaving the interference zone. This implies that the relevant quantity to evaluate at the end of the mirror is the squared wavefunction in momentum representation.

In order to express this relevant quantity, we introduce the Fourier transform $\widetilde{\psi_t}(p_z)$ of the wavefunction $\psi_t(z)$ at a given time t and deduce the expression of the squared wavefunction $\Pi_t(p_z)$ in momentum representation:

$$\begin{aligned}\widetilde{\psi_t}(p_z) &= \frac{1}{\sqrt{2\pi\hbar}} \int_{\mathbb{R}} dz \psi_t(z) e^{-ip_z z/\hbar},\\ \Pi_t(p_z) &= |\widetilde{\psi_t}(p_z)|^2 = \sum_{n,m} c_n c_m^* \pi_{n,m}(p_z) e^{i\omega_{nm}t},\\ \pi_{n,m}(p_z) &\equiv \widetilde{\psi_n}(p_z)\left(\widetilde{\psi_m}(p_z)\right)^*.\end{aligned} \tag{III.87}$$

The first functions $\pi_{n,m}(p_z)$ are represented in figure III.7. The real and imaginary part of $\pi_{n,m}(p_z)$ for $n \neq m$ are respectively plotted in blue and red outside the diagonal, while $\pi_{n,n}(p_z)$ is a modulus squared and is plotted in black in the diagonal. Exchanging the roles of n and m corresponds to complex conjugation.

The main quantity Π_t depends on the frequency ω_{nm}. This quantity remains unchanged when adding the Casimir-Polder shifts in the scattering length approximation

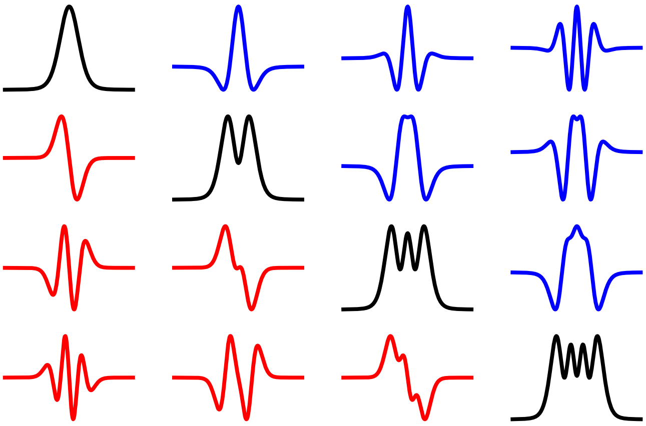

Figure III.7: Behavior of $\pi_{n,m}(p_z)$ for $1 \leq n, m \leq 4$. The diagonal cases $m = n$ are real functions shown as black curves. The non diagonal cases are complex functions, with their real and imaginary parts plotted respectively in blue above the diagonal, and in red below the diagonal.

II.1.d. Although the approximation can be improved by the new effective range theory developed in II.2, we restrain our study in this chapter to this approximation, that is sufficient to have an estimation of the final interference pattern and the corresponding uncertainty, especially in the case of a liquid helium surface.

The final interference pattern depends sensibly on the choice of some parameters that can be tuned for preparing a given initial state: the trap frequency ω, the height of the center h of the initial wavepacket and the horizontal kick velocity v_0. The change of the two first parameters leads to different ways of populating the gravitational quantum state. A smaller frequency trap corresponds to a smaller energy dispersion and tends to decrease the number of states in the gravitational quantum state decomposition. Similarly, a higher h leads to taking into account gravitational quantum state with larger energy, that oscillate more rapidly.

It follows from our calculations that a large number of gravitational quantum states is preferable, as long as the oscillations are resoluble by the detector at the end of the free fall (see discussions below). The interpretation of this result is that a more complex pattern contains more information on the value of the parameter g, so that we can in the end extract a better estimation of g. We also want to focus on a range of parameters that can be experimentally achieved [11, 14]. These considerations have led us to chose a trap frequency $\omega/2\pi = 20$ kHz, for a corresponding position dispersion 0.5 µm and an initial mean height of the Gaussian wave packet $h = 10$ µm above the surface.

The horizontal kick v_0 has also to be selected carefully. The prime criterion is that only a small proportion of antihydrogen atoms be lost for the measurement of g. This implies that v_0 is by far larger than the standard deviation of the velocity distribution in the initial wave packet. As the dispersion of velocities σ_v is the same in both x and z axes, this condition also implies that the atoms are concentrated in a narrow beam along the $x-$axis so that our modelization with only one horizontal propagation direction is sufficient in a good approximation.

Another criterion is that most atoms survive their flight above the reflecting surface in a realistic situation where quantum reflection is not perfect. The surface with a highest reflection probability is liquid helium at a temperature of 0.1 K, on which gravitational quantum state bounce more than a few hundreds times [39]. On the other side, too low a velocity would result in the signal concentrating around the same spot on the detector plate and penalizing precision.

In the end of this discussion, it appears that an initial velocity of about a few tens of cm.s^{-1} satisfies all our requirements. Figures are plotted below for $v_0 = 0.8\,\mathrm{m.s}^{-1}$ for the sake of a good visibility, while Monte Carlo simulations are done with an optimized $v_0 = 0.25\,\mathrm{m.s}^{-1}$. Numerical simulations demand increasing resource as one considers higher energy levels, so that we choose to restrict ourselves here to the first 100 states. With the numbers chosen for ζ and h, this eliminates the 20% most energetic antihydrogen atoms released from the trap, at an absorber placed at height 360 µm above the mirror [93]. The accuracy obtained below will be a conservative value, as an analysis using all antiatoms, even the more energetic ones, would yield finer structures in the interference pattern, leading to a better precision.

After these choices, the probability density in momentum space at the end of the mirror is drawn on figure III.8. Bright oblique lines can be seen, corresponding to constructive interferences. They are aligned along classical motions, with momentum linearly decreasing from a high positive value to the opposite negative value, before abruptly changing sign at the bounce on the mirror. The timing bounds have been chosen to correspond to the time spent above the mirror by the fastest (with horizontal speed $v_0 + 3\sigma_v$) and slowest (with horizontal speed $v_0 - 3\sigma_v$) antiatoms respectively. It will become apparent in the following section that this range of times in fact deliminates exactly the signal transmitted onto the detector plate during the free fall.

III.3.c Interference pattern on the detector

We now present the analytic calculations of the probability density current on the detector plate, assumed to be perfectly absorbing. This is justified by the large velocity acquired by the antiatoms during their free fall on a macroscopic height of 30 cm. The same assumption implies that the description of the free fall can be made in a classical way. This free fall thus acts in a similar way as a diffraction process, with the positions

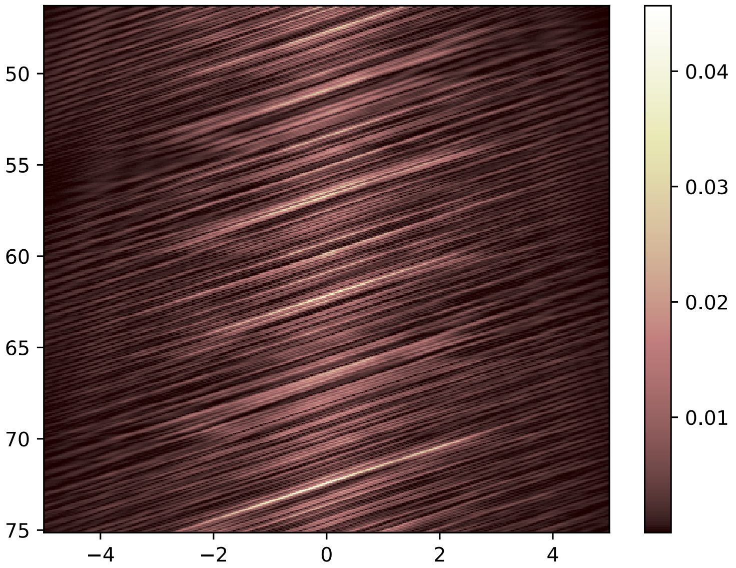

Figure III.8: Probability density in momentum space $\Pi_t(p_z)$ at the end of the interference zone for $\zeta = 0.5\,\mu\mathrm{m}$, $h = 10\,\mu\mathrm{m}$ and $v_0 = 0.8\,\mathrm{m.s}^{-1}$ as a function of p_z (horizontal axis, unit p_g) and t (vertical axis, unit t_g; unit chosen for the distribution so that it is normed).

in space and time of the annihilation event on the detector reading the interaction time and momentum of the atom at the end of the interference zone. This readout procedure is analogous to that used in experimental studies of neutron whispering gallery modes [186, 188].

As in the free fall time experiment, the interference pattern on the detector is the current probability density $J(X,T)$ on the horizontal detection plate where X and T are the positions in space and time of the annihilation event. This current can be expressed from the Wigner quasi-distribution (III.38). It can be calculated by using the fact that the evolution of the latter in the quantum free fall is classical. We are able to relate the Wigner function on the detector to the Wigner function at the end of the interference zone through classical relations (III.39):

$$\begin{aligned} J(X,T) &= \int_{\mathbb{R}^2} \mathrm{d}P_x \mathrm{d}P_z \frac{P_z}{m} W_t(x,z,p_x,p_z), \\ X &= x + \frac{p_x \tau}{m}, \quad Z = z + \frac{p_z \tau}{m} - \frac{g\tau^2}{2}, \\ P_x &= p_x \;, \qquad\quad P_z = p_z - mg\tau, \\ \tau &\equiv T - t. \end{aligned} \tag{III.88}$$

We have denoted τ the time of free fall, that is also the difference between the detection time T and the time t spent in the interference zone. Rigorously speaking, a second degree equation has to be solved to extract the dependence of the free fall time τ on the other parameters.

However the free fall height is large as compared with the microscopic lengths h, ζ, and we can use the following approximations where needed in the calculations:

$$\begin{gathered} X \approx d + \frac{p_x \tau}{m} \ , \quad Z \approx \frac{p_z \tau}{m} - \frac{g\tau^2}{2} , \\ \tau \approx \frac{p_z}{mg} + T_H \approx T_H \ , \quad T_H = \sqrt{\frac{2H}{g}} \ , \quad P_z \approx -mg\tau \ . \end{gathered} \tag{III.89}$$

The large free fall height has the additional effect that virtually all antiatoms have downwards velocities when they reach the detector plate. The current $J(X, T)$ can be assumed to be everywhere negative, and $|J(X, T)|$ is the detection probability density.

We now use the relations written above to change integration variables from the detection plate back to the end of the interference zone, and eliminate the dependence on the non relevant parameters of the Wigner quasi-distribution. We finally use the well-known property that the marginal of the Wigner function integrated over position is the probability distributions in momentum representation that is separable at the end of the mirror:

$$\begin{aligned} |J(X,T)| &= \frac{gm^2}{T_H} \int_{\mathbb{R}^2} \mathrm{d}x \mathrm{d}z W_t(x,z,p_x,p_z), \\ &= \frac{gm^2}{T_H} |\widetilde{\phi_t}(p_x)|^2 \Pi_t(p_z), \\ t =& \frac{T_H d}{X-d} \ , \quad p_x = \frac{m(X-d)}{T_H}, \\ p_z &= mg\left(T - \frac{T_H X}{X-d}\right) . \end{aligned} \tag{III.90}$$

In the end, the detection probability density in X, T is given from the probability density $\Pi_t(p_z)$ in momentum representation at the endside of the mirror through a classical anamorphosis (relations written in the last equation) and a weighing by the probability density of the horizontal momentum $|\widetilde{\phi_t}|^2$. The resulting interference pattern on the detector is shown in figure III.9 for the same parameters as its counterpart III.8. It can be seen that the resolution of the detector designed for GBAR [14], of the order of 0.1 µs in time and 0.1 mm in space, are largely sufficient for resolving the finer details in the interference pattern.

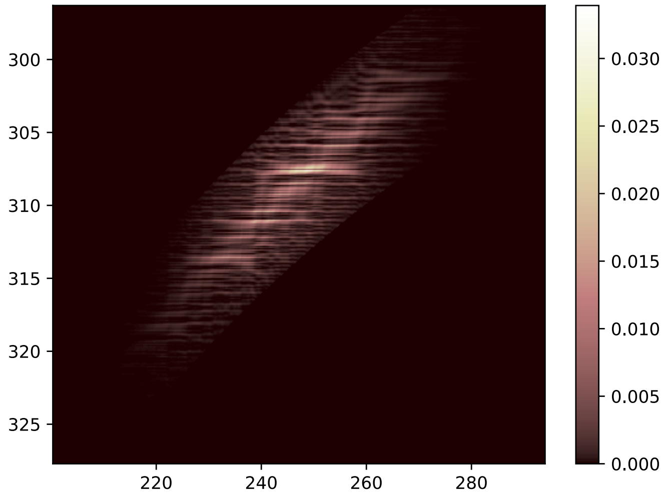

Figure III.9: Probability current density $|J(X,T)|$ on the detection plate for $\zeta = 0.5\,\mu\text{m}$, $h = 10\,\mu\text{m}$ and $v_0 = 0.8\,\text{m.s}^{-1}$ as a function of X (horizontal axis, in mm) and T (vertical axis, in ms; unit chosen for the distribution so that it is normed).

In order to understand the relationship between the two figures III.8 and III.9, it is worth looking at the anamorphosis relations when fixing T or X, and observing the resulting variations of t, p_x or p_z :

$$\begin{aligned} &\delta X = 0 \;\rightarrow\; \delta t = \delta p_x = 0 \;, \quad \delta p_z = mg\delta T \;; \\ &\delta T = 0 \;\rightarrow\; \frac{\delta t}{t} = \frac{\delta p_x}{p_x} = -\frac{\delta X}{X-d} \;, \quad \delta p_z = -mg\,\delta t \;. \end{aligned} \tag{III.91}$$

It follows that the bright oblique lines corresponding to constructive interferences and classical free-fall movement on figure III.8 become the bright horizontal lines on figure III.9 which correspond to constructive interferences and are parallel to the X axis on the detector plate. This discussion is illustrated by the two plots in figure III.10 where orange lines represent constructive interferences transformed into one another by the anamorphosis. Meanwhile white lines, also transformed into one another by the anamorphosis, are vertical on the detector ($\delta X = 0$) and horizontal at the end side of the mirror ($\delta t = 0$).

III.3.d Uncertainty estimation

We now estimate the uncertainty in the estimation of the value of g from the interference pattern registered on the detection plate. As the distance between fringes depends on g, it could be tempting to measure g directly from this distance. This technique is however unpractical here, namely because we have only a small number of annihilation events to sample this probability distribution. We use a much more robust maximum

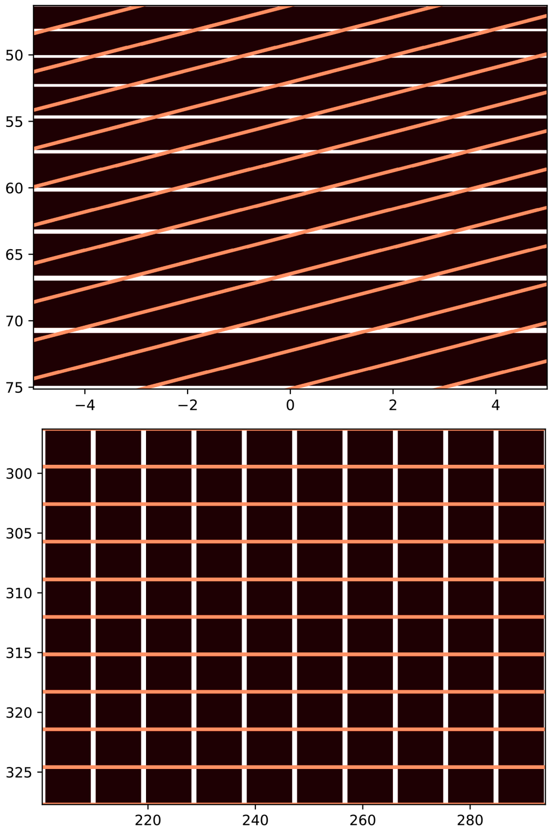

Figure III.10: Grids of lines transformed into one another by the anamorphosis at the end side of the mirror (upper plot) and on the detection plate (lower plot). The orange lines represent the constructive interferences, they correspond to classical free-fall trajectories on the mirror and to horizontal lines on the detector ($\delta T = 0$). The white lines are horizontal on the upper plot ($\delta t = 0$) and vertical on the lower plot ($\delta X = 0$). The bounds for the two plots the same as on figure III.8 and figure III.9 respectively.

likelihood method presented in III.2.c to estimate the parameter g and also deduce a variance for this estimation.

We assume that we have 1000 prepared $\overline{H}$-atoms that is also $N = 800$ detection events after 20% $\overline{H}$-atoms are lost in the absorber. We thus choose randomly 800 detection events in the probability distribution $\mathbb{P}_{g_0}$ corresponding to an *a priori* value g_0 of the acceleration. We consider that the set of detection events $\mathcal{D}$ simulates the output of an experiment and then use a maximum likelihood method to get an estimator $\hat{g}$. As would be done in the data analysis of the experiment, we define the estimator as the $\hat{g}$ maximizing the likelyhood of the N points to reproduce the distributions $\mathbb{P}_g$ corresponding to different *a posteriori* values.

We show in figure III.11 the gaussians fitted for 15 random drawings of the experiment, each with $N = 800$ atoms. We have normalized the gaussians so that the variation of their variance is seen more easily as a variation of their height. The variation of their peak contains the same information as the histogram shown on figure III.12 as the result of a Monte-Carlo simulation (with 2300 drawings in figure III.12 but only 15 in figure III.11 in order to avoid confusion). As in the free fall time experiment, the likelihood functions are well fitted by gaussians, meaning that the efficiency e is close to one. The main difference between figure III.11 and III.4 is the larger dispersion of $\hat{\sigma}_g$ in the case of interferences. We find:

$$\mathbb{E}(\hat{\sigma}_g) = 7.3 \cdot 10^{-6}\, g. \tag{III.92}$$

The relative dispersion of $\hat{\sigma}_g/\mathbb{E}(\hat{\sigma}_g) \simeq 8\%$. It means that the knowledge of a single likelihood function obtained with a single experiment still gives a good estimation of the uncertainty.

In order to check out the statistical efficiency of the method just outlined, we have repeated the full procedure for M different random drawings of the N points. The histogram shown in figure III.12 corresponds to $M = 2200$ drawings of the N events, with the parameters ζ and h corresponding to figure III.9, and a velocity $v_0 = 0.25\,\text{m.s}^{-1}$. The blue dotted line is a gaussian fit of the histogram which gives the following dispersion which is far better than that evaluated for the classical timing method:

$$\Sigma_g \simeq 7.8 \cdot 10^{-6}\, g \tag{III.93}$$

The value (III.93) is obtained from a Monte-Carlo simulation repeating a large number of times a numerical experiment simulating the real experiment which can hardly be repeated due to the small number of available $\overline{H}-$atoms. This value is in fact close to what can be obtained from a single drawing of N events as would be done in the experiment. This shows that $N = 800$ is large enough for a good statistical efficiency, in spite of the fact that this number is not sufficient to accurately sample all the details

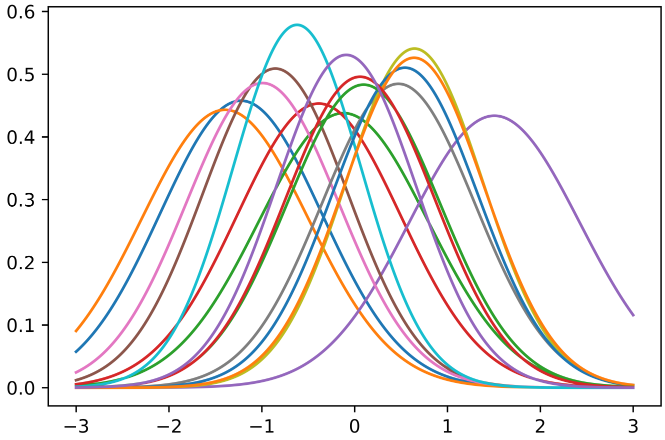

Figure III.11: Fifteen gaussian distributions obtained by a quadratic fit of the log-likelihood function calculated for a random drawing of $N = 800$ atoms. The gaussians are normalized so that the variation of their variance is seen more easily as a variation of their height. The colors have no meaning, they only allow one to distinguish the various functions.The horizontal axis scales as $(g - g_0)/g_0 \times 10^5$.

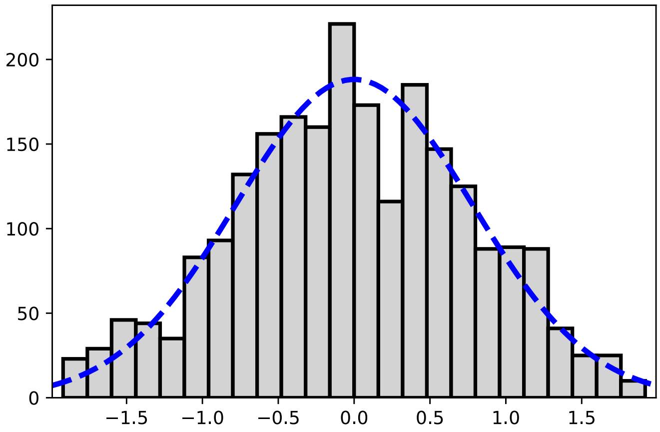

Figure III.12: Histogram of the relative variations $(g-g_0)/g_0 \times 10^5$ obtained by repeating 2300 times a Monte Carlo simulation on 800 events, for $\zeta = 0.5$ µm, $h = 10$ µm and $v_0 = 0.25$ m.s^{-1}. The vertical axis counts the number of events per channel. The blue dashed line is a gaussian fit of the histogram.

of the interference pattern. In fact, even if the pattern is complicated, the statistical efficiency expresses a convergence property of likelihood functions that are much more regular than the interference pattern itself.

We repeat that a smaller kick velocity would enhance the duration of the interference period above the mirror while also increasing the probability for the atom to be annihilated. For a realistic treatment of the uncertainty calculation, we should thus describe the reflection on the surface by adding an energy dependent annihilation probability at each bounce of the atom above the surface [120]. It would also be necessary to take into account quantum reflection on the detection plate [91].

Anyway, the calculations presented here show that a large improvement of the g measurement accuracy may in principle be attained by using quantum interference methods rather than classical timing, which opens attractive perspectives for the equivalence principle test on antihydrogen atoms.

Chapter IV

Casimir-Polder fluctuations

> “ *Si l’ordre est le plaisir de la raison, le désordre est le délice de l’imagination.* ”
>
> **Paul Claudel**
> ***Le soulier de Satin***

In the previous chapters, we studied the quantum reflection of an antihydrogen atom above different surfaces. The quantum reflection is induced by the Casimir-Polder potential, describing the interaction between the atom and the surface treated as an homogeneous medium described by a dielectric constant $\epsilon(i\xi)$. In fact, each surface contains some heterogeneities, and it is interesting to study how they affect the mean Casimir-Polder potential. The effect of a non-planar surface [189], or the fluctuations of the potential above a dielectric surface [190, 191] have already been studied. In this chapter, we focus on the fluctuations of the Casimir-Polder potential for an antihydrogen atom above a metallic surface. While the liquid helium is a dielectric medium described with enough precision by the effective dielectric constant, the detector of antihydrogen is recovered by a surface of gold. It is also important to know if the effect of some heterogeneities could modify the quantum reflection phenomenon.

Furthermore, the basics of the Casimir effect has recently attracted renewed interest, as a result of a large amount of experimental work allowing for precision measurements, and of the observation of disagreements between the results of these experiments and theoretical predictions [192]. Most precise measurements of the Casimir force are performed between large spheres and metallic plates separated in distances ranging from a fraction of micrometer to a few micrometers. The force is dominated by zero-point quantum fluctuations of the electromagnetic field at separations much smaller than the thermal wavelength $\lambda_T = \hbar c/(k_B T)$ (7.6 µm at room temperature), whereas thermal fluctuations also contribute at larger separations. In both cases, the magnitude of the force depends on the reflection properties of the sphere (or atom) and plate, which themselves depend on the complex dielectric function of the materials. In metals, the low-frequency limit of the latter is controlled by the conductivity, that is in practice by the Drude description of electron scattering from the metal impurities.

The most precise measurements performed at submicrometric separations appear to be in good agreement with the so-called plasma model, that is the Drude model with dissipation discarded [193–196]. In contrast, experiments performed at larger distances of a few micrometers (i.e. at separations approaching λ_T) obtain results in good agreement with the dissipative Drude model, after a large contribution of electrostatic effets is substracted [197, 198]. To the best of our knowledge, this intriguing contradiction on the role of dissipation in Casimir experiments has not yet been solved, though a number of potential explanations has already been investigated [127].

In the following, we provide for the first time a detailed description of spatial fluctuations of the Casimir-Polder potential for a metallic plate, which turn out to be richer than the fluctuations arising with dielectric disordered materials [190, 191, 199]. We discover that unlike the mean Casimir-Polder potential, at $T = 0$ and large distances the variation of these fluctuations with the sphere-plate separation distance significantly depends on the amount of dissipation in the metallic bulk. Furthermore, by analyzing δV at finite temperature, we come up with the surprising result that fluctuations decay exponentially with the sphere-plate separation, in strong contrast with the behavior of mean Casimir potentials that decay algebraically.

More precisely, in section IV.1, we pay attention to the average Casimir-Polder potential. We introduce the Green functions – useful tool for studying fluctuations – and give a precise description of Fresnel coefficients. In section IV.2, we compute precisely the fluctuations of the Casimir-Polder potential and we interpret their magnitude. We finally add the role of the temperature in section IV.3, and see how the potential and its fluctuations behave at finite temperature.

IV.1 Mean Casimir-Polder potential

IV.1.a Qualitative description of the interaction between an atom and a metallic medium

We consider an antihydrogen atom of mass m placed above a metallic plate, at height z, as represented in figure IV.1. The metallic medium contains impurities, randomly distributed. These static heterogeneities act as scatterers for conduction electrons of Fermi wavelength λ_F that move in the metal. The Fermi velocity v_F corresponding to the mean velocity of free electrons in metal is defined from the Fermi wavevector k_F as follows:

$$v_F \equiv \frac{\hbar k_F}{m}, \quad k_F \equiv \frac{2\pi}{\lambda_F}. \tag{IV.1}$$

The average distance travelled by a moving electron between successive collisions is the *mean free path*[1] l. The relaxation rate γ is the inverse of the mean time between two electron scatterings:

$$\gamma \equiv \frac{v_F}{l}. \tag{IV.2}$$

The interaction of the electromagnetic field with the electrons probes the disorder in the medium and adds a non-specular contribution to the Casimir-Polder interaction potential.

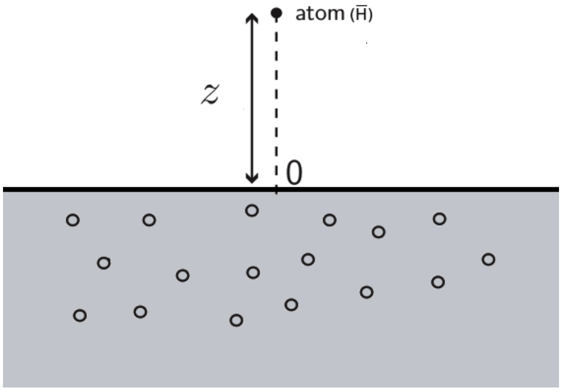

Figure IV.1: Schematic representation of an antihydrogen atom placed above a metallic plate at height z. In the metallic medium, static impurities illustrated by black circles are randomly distributed.

The general form of the Casimir-Polder potential is

$$V(z) = \frac{\hbar}{c^2}\int_0^\infty \frac{d\xi}{2\pi}\xi^2\alpha(i\xi)\int \frac{d^2\mathbf{q}_a}{2\pi}\frac{d^2\mathbf{q}_b}{2\pi}\frac{e^{-2\kappa_z z}}{2\kappa_z}\sum_{a,b=\mathrm{TE,TM}} r_{ab}(\omega)\,\boldsymbol{\epsilon}_a^+(\boldsymbol{q}_a)\cdot\boldsymbol{\epsilon}_b^-(\boldsymbol{q}_b) \tag{IV.3}$$

where $\boldsymbol{\epsilon}_a^+(\boldsymbol{q}_a)$ and $\boldsymbol{\epsilon}_b^-(\boldsymbol{q}_b)$ are polarization vectors.

The reflection amplitudes in the Casimir-Polder potential formula (IV.3) are also decomposed in two terms: a mean term $\overline{r}_{ab}(i\xi)$ corresponding to the reflection of the electromagnetic field over an effective medium and a fluctuating term $\delta r_{ab}(i\xi)$ that manifests the contributions from the heterogeneities of the metallic plate:

$$r_{ab}(i\xi) = \overline{r}_{ab}(i\xi) + \delta r_{ab}(i\xi). \tag{IV.4}$$

---

[1] The mean free path l should not be be confused with the complex length ℓ related to the scattering length $a = -i\ell$.

In practice, the latter contribution manifests itself as a spatial fluctuation δV of the potential around a mean value $\overline{V}$ as the atom is moved above the plate at fixed separation. Alternatively, by virtue of the ergodicity principle, δV can also be seen as a fluctuation from sample to sample of the Casimir-Polder interaction between an atom and macroscopically identical –but microscopically different– metallic plates. Physically, the mean CP potential $\overline{V}$ is mediated by the field fluctuations specularly reflected from the surface of the metal. The space-varying fluctuation δV, on the other hand, stems from the part of the radiation that is re-emitted *non specularly*, as illustrated in figure IV.2, after having penetrated the metal and interacted with electrons scattered in the disordered metallic bulk. Due to this mechanism, the very existence of the fluctuating part of the Casimir force relies on the presence of impurities in the metallic plate, and thus constitutes a natural probe of dissipation.

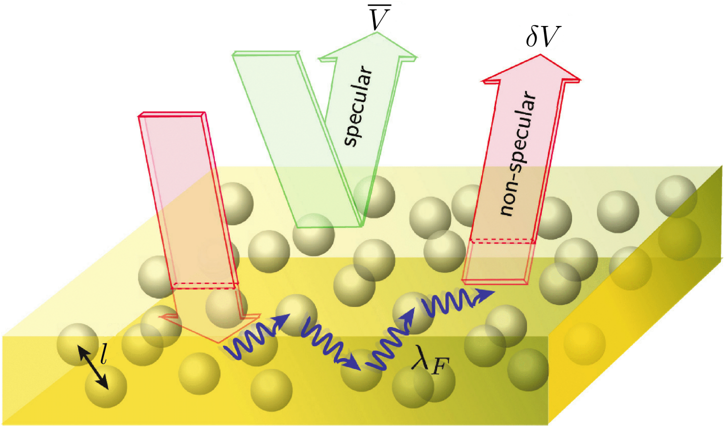

Figure IV.2: The Casimir potential $V = \overline{V} + \delta V$ between an arbitrary object and a metallic plate containing impurities has two contributions. The first is the (main) specular part, $\overline{V}$, controlled by the reflection properties of the flat surface of the metal. The second is a non-specular part, δV, and originates from the spatial heterogeneities (impurities) in the metallic bulk, from which conduction electrons (of Fermi wavelength λ_F) are scattered (with a mean free path l).

In this section, we focus on the average Casimir-Polder interaction $\overline{V}$, treating the metal as an homogeneous effective medium. We pay attention with more details on the Casimir-Polder potential formula (D.1), presenting first the Casimir-Polder potential at finite temperature, then developing a Green function formalism which will be very useful for treating the potential fluctuations in section IV.2.

IV.1.b Green tensor of the Helmholtz equation

We consider the metallic plate as an effective medium described by a dielectric constant $\epsilon(i\xi)$. We study the electromagnetic field both in vacuum and in the homogeneous metallic plate. If we first disregard the effects of polarization, the electromagnetic field obeys also the free Helmholtz equation:

$$\left[-\frac{1}{k_i^2}\boldsymbol{\nabla}\times\boldsymbol{\nabla}+\mathbf{I}\right]\mathbf{E}(\mathbf{r})=\mathbf{0}. \tag{IV.5}$$

The index i denotes the medium where the field propagates: the vacuum ($i=1$) or the metal ($i=2$). $k_1\equiv k$ is also the wavevector in vacuum while $k_2\equiv\tilde{k}=\sqrt{\epsilon(i\xi)}k$ is the wavevector in the metal.

We calculate now the Green tensor $\overline{\boldsymbol{G}}_i^{(0)}(\mathbf{r},\mathbf{r}')$ solution of the corresponding equation (IV.5) encoding the propagation of the field between two points $\mathbf{r}$ and $\mathbf{r}'$:

$$\left[-\frac{1}{k_i^2}\boldsymbol{\nabla}\times\boldsymbol{\nabla}+\mathbf{I}\right]\overline{\boldsymbol{G}}_i^{(0)}(\mathbf{r},\mathbf{r}')=\delta(\mathbf{r}-\mathbf{r}')\mathbf{I}. \tag{IV.6}$$

Thus, it follows:

$$\begin{aligned}\overline{\boldsymbol{G}}_i^{(0)}(\mathbf{r},\mathbf{r}')&=\left[\frac{1}{k_i^2}\boldsymbol{\nabla}\times\boldsymbol{\nabla}+\mathbf{I}\right]\overline{\mathcal{G}}_i(\mathbf{r},\mathbf{r}'),\\ \overline{\mathcal{G}}_i(\mathbf{r},\mathbf{r}')&\equiv-\frac{e^{i\mathbf{k_i}\cdot(\mathbf{r}-\mathbf{r}')}}{4\pi|\mathbf{r}-\mathbf{r}'|}.\end{aligned} \tag{IV.7}$$

We decompose vectors $\mathbf{r}$ and wavevectors $\mathbf{k_i}$ over transverse and longitudinal components:

$$\begin{aligned}\mathbf{r}&=(\mathbf{r}_\perp,z)\\ \mathbf{k_i}&=(\mathbf{q},k_{iz}).\end{aligned} \tag{IV.8}$$

By applying the Fourier transform in expression (IV.7), we obtain:

$$\overline{\boldsymbol{G}}_i^{(0)}(\mathbf{r},\mathbf{r}')=-\frac{i}{8\pi^2}\int\frac{d^2\boldsymbol{q}}{k_{iz}}e^{i\boldsymbol{q}\cdot(\mathbf{r}_\perp-\mathbf{r}'_\perp)+ik_{iz}(z-z')}\left[\mathbf{I}-\mathbf{k_i}\otimes\mathbf{k_i}\right]. \tag{IV.9}$$

We finally use the orthogonality of the basis

$$\mathbf{I}=\boldsymbol{\epsilon}_{TE}^{+}\otimes\boldsymbol{\epsilon}_{TE}^{+}+\boldsymbol{\epsilon}_{TM}^{+}\otimes\boldsymbol{\epsilon}_{TM}^{+}+\mathbf{k_i}\otimes\mathbf{k_i}, \tag{IV.10}$$

where indices i for polarization vectors are implicit, to write:

$$\overline{\boldsymbol{G}}_i^{(0)}(\mathbf{r},\mathbf{r}')=-\frac{i}{8\pi^2}\int\frac{d^2\boldsymbol{q}}{k_{iz}}e^{i\boldsymbol{q}\cdot(\mathbf{r}_\perp-\mathbf{r}'_\perp)+ik_{iz}(z-z')}\sum_{p=TE,TM}\boldsymbol{\epsilon}_p^{+}\otimes\boldsymbol{\epsilon}_p^{+}. \tag{IV.11}$$

By analogy, we make an Ansatz for Green tensors $\overline{\boldsymbol{G}}_i^{(r)}$ and $\overline{\boldsymbol{G}}_i^{(t)}$, corresponding to the propagators of the field that is respectively reflected and transmitted through the interface:

$$\overline{\boldsymbol{G}}_i^{(r)}(\mathbf{r},\mathbf{r}') \equiv -\frac{i}{8\pi^2}\int \frac{d^2\boldsymbol{q}}{k_{iz}} e^{i\boldsymbol{q}\cdot(\mathbf{r}_\perp-\mathbf{r}'_\perp)+ik_{iz}(z-z')} \sum_{p=TE,TM} \overline{r}_p \boldsymbol{\epsilon}_p^- \otimes \boldsymbol{\epsilon}_p^+ \tag{IV.12}$$

$$\overline{\boldsymbol{G}}_i^{(t)}(\mathbf{r},\mathbf{r}') \equiv -\frac{i}{8\pi^2}\int \frac{d^2\boldsymbol{q}}{k_{iz}} e^{i\boldsymbol{q}\cdot(\mathbf{r}_\perp-\mathbf{r}'_\perp)+ik_{iz}(z-z')} \sum_{p=TE,TM} \overline{t}_p \boldsymbol{\epsilon}_p^+ \otimes \boldsymbol{\epsilon}_p^+ \tag{IV.13}$$

with $\overline{r}_p$ and $\overline{t}_p$ the reflection et transmission amplitudes for the effective medium. For a point $\mathbf{r}'$ source in vacuum, the global Green tensor in space writes:

$$\overline{\boldsymbol{G}}(\mathbf{r},\mathbf{r}') = \begin{cases} \overline{\boldsymbol{G}}_1^{(0)}(\mathbf{r},\mathbf{r}') + \overline{\boldsymbol{G}}_1^{(r)}(\mathbf{r},\mathbf{r}') & \text{if } z>0 \\ \overline{\boldsymbol{G}}_2^{(t)}(\mathbf{r},\mathbf{r}') & \text{if } z<0. \end{cases} \tag{IV.14}$$

We suppose a translation invariance in the transverse plane in the medium on average, in such a way that Green tensors depends only on $\mathbf{r}_\perp - \mathbf{r}'_\perp$:

$$\overline{\boldsymbol{G}}_i(\mathbf{r}_\perp,\mathbf{r}'_\perp,z,z') = \overline{\boldsymbol{G}}_i(\mathbf{r}_\perp-\mathbf{r}'_\perp,z,z'). \tag{IV.15}$$

By taking the Fourier transform over the transverse coordinate and taking $z\to 0$, $z'\to 0$, we get:

$$\overline{\boldsymbol{G}}_i^{(0)}(\boldsymbol{q},0,0) = -\frac{i}{2k_{iz}} \sum_{p=TE,TM} \boldsymbol{\epsilon}_p^+ \otimes \boldsymbol{\epsilon}_p^+ \tag{IV.16}$$

$$\overline{\boldsymbol{G}}_i^{(r)}(\boldsymbol{q},0,0) = -\frac{i}{2k_{iz}} \sum_{p=TE,TM} \overline{r}_p\boldsymbol{\epsilon}_p^- \otimes \boldsymbol{\epsilon}_p^+ \tag{IV.17}$$

$$\overline{\boldsymbol{G}}_i^{(t)}(\boldsymbol{q},0,0) = -\frac{i}{2k_{iz}} \sum_{p=TE,TM} \overline{t}_p\boldsymbol{\epsilon}_p^+ \otimes \boldsymbol{\epsilon}_p^+ \tag{IV.18}$$

IV.1.c Fresnel coefficients

We derive now the reflection and transmission coefficients $\overline{r}_{ab}$, $\overline{t}_{ab}$:

$$\overline{r}_{ab} \equiv 2ik_{iz}\langle \boldsymbol{q}_b, p_b|\overline{\boldsymbol{G}}_i^{(r)}(\boldsymbol{q}_a,\boldsymbol{q}_b,0^+,0^+)|\boldsymbol{q}_a,p_a\rangle \tag{IV.19}$$

$$\overline{t}_{ab} \equiv 2ik_{iz}\langle \boldsymbol{q}_b, p_b|\overline{\boldsymbol{G}}_i^{(t)}(\boldsymbol{q}_a,\boldsymbol{q}_b,0^+,0^-)|\boldsymbol{q}_a,p_a\rangle. \tag{IV.20}$$

By injecting (IV.17) and (IV.18) in the previous definitions, we finally obtain the diagonal expressions:

$$\overline{r}_{ab} = (2\pi)^2\delta(\boldsymbol{q}_a-\boldsymbol{q}_b)\delta_{p_a,p_b}\overline{r}_{p_a} \tag{IV.21}$$

$$\overline{t}_{ab} = (2\pi)^2\delta(\boldsymbol{q}_a-\boldsymbol{q}_b)\delta_{p_a,p_b}\overline{t}_{p_a}. \tag{IV.22}$$

The continuity of the electric and magnetic field at the interface between vacuum and metal implies continuity relations for the Green function (IV.14) from either side of the interface. We recover the well-known Fresnel coefficients:

$$\overline{r}_{TE}^{1\to 1} = \frac{\kappa_z - \tilde{\kappa}_z}{\kappa_z + \tilde{\kappa}_z} \qquad \overline{r}_{TM}^{1\to 1} = \frac{\epsilon(i\xi)\kappa_z - \tilde{\kappa}_z}{\epsilon(i\xi)\kappa_z + \tilde{\kappa}_z} \tag{IV.23}$$

$$\overline{t}_{TE}^{1\to 2} = \frac{2\kappa_z}{\kappa_z + \tilde{\kappa}_z} \qquad \overline{t}_{TM}^{1\to 2} = \frac{2\sqrt{\epsilon(i\xi)}\kappa_z}{\epsilon(i\xi)\kappa_z + \tilde{\kappa}_z} \tag{IV.24}$$

where $\kappa_z = \sqrt{\boldsymbol{q}^2 + \xi^2/c^2}$ and $\tilde{\kappa}_z = \sqrt{\boldsymbol{q}^2 + \epsilon(i\xi)\xi^2/c^2}$ are the longitudinal wavevectors written in terms of complex frequency ξ.

When injecting (IV.21) and (IV.23) in the average Casimir-Polder potential

$$\overline{V}(z) = \frac{\hbar}{c^2}\int_0^\infty \frac{d\xi}{2\pi}\xi^2\alpha(i\xi)\int \frac{d^2\mathbf{q}_a}{2\pi}\frac{d^2\mathbf{q}_b}{2\pi}\frac{e^{-2\kappa_z z}}{2\kappa_z}\sum_{a,b=\mathrm{TE,TM}} \overline{r}_{ab}(i\xi)\,\boldsymbol{\epsilon}_a^+(\boldsymbol{q}_a)\cdot\boldsymbol{\epsilon}_b^-(\boldsymbol{q}_b), \tag{IV.25}$$

we recover the expression (D.1) given in chapter I.

The Fresnel coefficients from metal to vacuum are written in a similar way:

$$\overline{r}_{TE}^{2\to 2} = \frac{\tilde{\kappa}_z - \kappa_z}{\kappa_z + \tilde{\kappa}_z} = -\overline{r}_{TE}^{1\to 1} \qquad \overline{r}_{TM}^{2\to 2} = \frac{\tilde{\kappa}_z - \epsilon(i\xi)\kappa_z}{\tilde{\kappa}_z + \epsilon(i\xi)\kappa_z} = -\overline{r}_{TM}^{1\to 1} \tag{IV.26}$$

$$\overline{t}_{TE}^{2\to 1} = \frac{2\tilde{\kappa}_z}{\kappa_z + \tilde{\kappa}_z} \qquad \overline{t}_{TM}^{2\to 1} = \frac{2\sqrt{\epsilon(i\xi)}\tilde{\kappa}_z}{\tilde{\kappa}_z + \epsilon(i\xi)\kappa_z}. \tag{IV.27}$$

IV.1.d Drude vs plasma puzzle

In order to compute the mean Casimir-Polder potential (IV.25), we need to know the reflection coefficient and also the permittivity $\epsilon(i\xi)$ at all frequencies. The permittivity is a sum of contributions corresponding to bound and conduction electrons. By normalizing the expression by ϵ_0, the permittivity due to conduction is written:

$$\epsilon(i\xi) = 1 + \frac{\sigma(i\xi)}{\xi} \tag{IV.28}$$

where σ is the effective conductivity of the metal. Optical data [200, 201] provide the value of ϵ in a certain range of frequencies, but they have to be extrapolated, especially at low frequency in order to compute the Casimir-Polder potential.

The *Drude model* is an effective model considering an electron relaxation rate in the metal γ and a plasma frequency ω_p:

$$\sigma(i\xi) = \frac{\omega_p^2}{\gamma + \xi}. \tag{IV.29}$$

At low frequency, $\sigma(i\xi)$ tends to the finite static conductivity of the metal:

$$\sigma_0 = \frac{\omega_p^2}{\gamma}. \tag{IV.30}$$

A simplest model considering a lossless plasma of conduction electron ($\gamma \to 0$) is often considered. It is called the *plasma model* with a conductivity then given by:

$$\sigma(i\xi) = \frac{\omega_p^2}{\xi}. \tag{IV.31}$$

This model is non physical since the conductivity diverges in the limit of low frequency. It leads also to a poorer fit of tabulated optical data than the Drude model (IV.29). However, the plasma model seems to better reproduce the Casimir-Polder potential when comparing with experimental measurements, as in the experiment done by Decca et al [81–83] for instance.

The reasons of that disagreement between theory and experience are still debated. A first consequence for us of the different behavior of the conductivity at low frequency is a change of the asymptotic behavior of Fresnel coefficients.

By playing with the asymptotical behavior of reflection amplitudes and of the polarizability $\alpha(i\xi)$ of the atom, we retrieve the asymptotical regimes of the mean Casimir-Polder potential studied in chapter I: the van der Waals and the retarded regimes, for the Drude and plasma model. We will see in the following that this is no longer the case for the Casimir-Polder potential fluctuations.

IV.2 Fluctuations of the Casimir-Polder potential

We study now the spatial fluctuations of the Casimir-Polder force experienced by an atom moved above a metallic plate at fixed separation distance. We demonstrate that unlike the mean force, the magnitude of these fluctuations crucially relies on the relaxation of conduction electron in the metallic bulk, and even achieves values that differ by orders of magnitude depending on the amount of dissipation. We also discover that fluctuations suffer a spectacular decrease at large distances in the case of nonzero temperature.

IV.2.a General expression of fluctuations

We follow the same scheme as in [190] where fluctuations where derived for a dielectric material. The presence of impurities in the metal makes the CP potential

$$V(z) = \overline{V}(z) + \delta V(z) \tag{IV.32}$$

fluctuate spatially around its mean value $\overline{V}$. The fluctuating contribution δV stems from electromagnetic fields that enter the metallic bulk and are reflected through their interaction with conduction electrons scattered from impurities. We describe δV by adding a non-specular contribution δr_{ab} to the reflection coefficient:

$$r_{ab} = \overline{r}_{ab} + \delta r_{ab}, \tag{IV.33}$$

which we calculate by making use of a statistical approach where the metallic plate is taken from a random ensemble of plates with different microscopic configurations of the impurity positions. The magnitude of potential fluctuations is then given by the variance

$$\overline{\delta^2 V} \equiv \overline{V^2} - \overline{V}^2, \tag{IV.34}$$

where the overbar denotes averaging over the random ensemble.

To evaluate $\overline{\delta^2 V}$, we square the equation(D.1), subtract $\overline{V}^2$ (IV.3) and apply the configuration average. We obtain:

$$\begin{aligned}\overline{\delta V^2}(z) = \frac{\hbar^2}{c^4} \int_0^\infty \frac{d\xi_1}{2\pi}\frac{d\xi_2}{2\pi} \xi_1^2 \xi_2^2 \alpha(i\xi_1)\alpha(i\xi_2) \prod_{i=a,b,c,d} \int \frac{d^2\boldsymbol{q}_i}{(2\pi)^2} \\ \times \sum_{a,b,c,d} \overline{\delta r_{ab}(i\xi_1)\delta r_{cd}(i\xi_2)} \frac{e^{-(\kappa_z^a+\kappa_z^b+\kappa_z^c+\kappa_z^d)z}}{4\kappa_z^a\kappa_z^c} \boldsymbol{\epsilon}_a^+(\boldsymbol{q}_a)\cdot\boldsymbol{\epsilon}_b^-(\boldsymbol{q}_b)\, \boldsymbol{\epsilon}_c^+(\boldsymbol{q}_c)\cdot\boldsymbol{\epsilon}_d^-(\boldsymbol{q}_d).\end{aligned} \tag{IV.35}$$

Scalar products $\boldsymbol{\epsilon}_a^+(\boldsymbol{q}_a)\cdot\boldsymbol{\epsilon}_b^-(\boldsymbol{q}_b)$ and $\boldsymbol{\epsilon}_c^+(\boldsymbol{q}_c)\cdot\boldsymbol{\epsilon}_d^-(\boldsymbol{q}_d)$ are summarized in table IV.1.

$\boldsymbol{\epsilon}_a^+(\boldsymbol{q}_a)\cdot\boldsymbol{\epsilon}_b^-(\boldsymbol{q}_b)$	$b = \mathrm{TE}$	$b = \mathrm{TM}$
$a = \mathrm{TE}$	$\cos(\phi' - \phi)$	$\frac{c\kappa_z^b \sin(\phi'-\phi)}{\xi_1}$
$a = \mathrm{TM}$	$\frac{c\kappa_z^a \sin(\phi'-\phi)}{\xi_1}$	$-c^2 \frac{q_a q_b + \kappa_z^a \kappa_z^b \cos(\phi'-\phi)}{\xi_1^2}$

$\boldsymbol{\epsilon}_c^+(\boldsymbol{q}_c)\cdot\boldsymbol{\epsilon}_d^-(\boldsymbol{q}_d)$	$d = \mathrm{TE}$	$d = \mathrm{TM}$
$c = \mathrm{TE}$	$\frac{q_d - q_b\cos\phi + q_a\cos\phi'}{q_c}$	$\frac{c\kappa_d}{\xi_2}\frac{q_a\sin\phi' - q_b\sin\phi}{q_c}$
$c = \mathrm{TM}$	$\frac{c\kappa_c}{\xi_2}\frac{q_a\sin\phi' - q_b\sin\phi}{q_c}$	$-\frac{c^2}{\xi_2^2}\left[\kappa_c\kappa_d \frac{q_d - q_b\cos\phi + q_a\cos\phi'}{q_c} + q_c q_d\right]$

Table IV.1: Values $\boldsymbol{\epsilon}_a^+(\boldsymbol{q}_a)\cdot\boldsymbol{\epsilon}_b^-(\boldsymbol{q}_b)$ and $\boldsymbol{\epsilon}_c^+(\boldsymbol{q}_c)\cdot\boldsymbol{\epsilon}_d^-(\boldsymbol{q}_d)$ for the various combinations of polarizations. $q_i \equiv |\boldsymbol{q}_i|$ and ϕ is the angle between $\boldsymbol{q}_b$ and $\boldsymbol{q}_d$, while ϕ' is the angle between $\boldsymbol{q}_a$ and $\boldsymbol{q}_d$.

IV.2.b Correlations in metal

The expression (IV.35) involves the correlator $\overline{\delta r_{ab}(i\xi_1)\delta r_{cd}(i\xi_2)}$ of reflection coefficients. The correlator $\overline{\delta r_{ab}(i\xi_1)\delta r_{cd}(i\xi_2)}$ stems from the fact that the two electron scattering trajectories from $\mathbf{r}$ to $\mathbf{r}_1$ and from $\mathbf{r}'$ to $\mathbf{r}'_1$ can share one or several metal impurities, as it is diagrammatically represented in figure IV.3a.

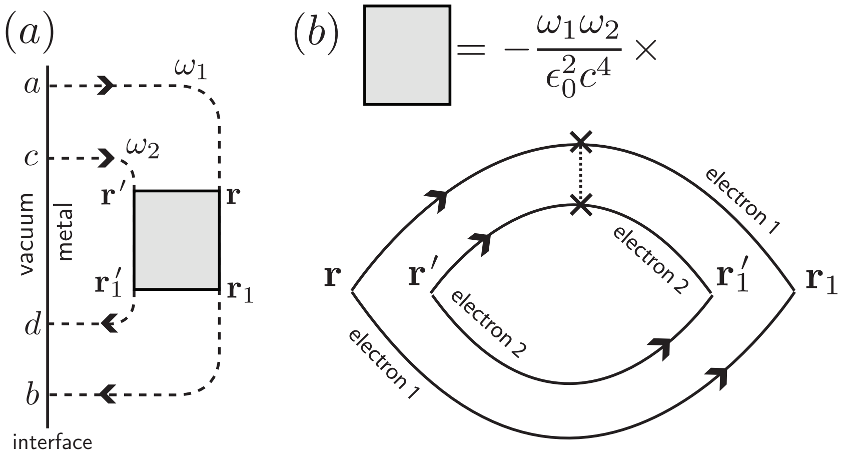

Figure IV.3: (a) Diagram representing the correlator $\overline{\delta r_{ab}(i\xi_1)\delta r_{cd}(i\xi_2)}$. Dashed lines symbolize propagation of the electromagnetic field inside the metal. a and c are the incoming modes, and b and d the outgoing modes. The field in the outer (inner) branch accelerates an electron at point $\mathbf{r}$ ($\mathbf{r}'$), which later re-emits a radiation at point $\mathbf{r}_1$ ($\mathbf{r}_1'$). (b) The conductivity correlator $\overline{\delta\sigma_{ab}(i\xi_1,\mathbf{r},\mathbf{r}_1)\delta\sigma_{cd}(i\xi_2,\mathbf{r}',\mathbf{r}_1')}$ encodes the correlation of the two electron scattering trajectories. For a good metal ($k_F l \gg 1$), the leading-order contribution to this correlator involves only one scattering event on an impurity of the metal (cross symbol).

The outer branch of the diagram describes the following physical mechanism: an electromagnetic field fluctuation of frequency $\omega_1 = i\xi_1$ penetrates the metal, then accelerates an electron at some point $\mathbf{r}$. This electron propagates through the metal up to a final point $\mathbf{r}_1$ where it re-emits a radiation that eventually leaves the metal. The inner branch of the diagram describes a similar process at frequency $\omega_2 = i\xi_2$. While the correlator has already been calculated for a dielectric medium [190], we present here the calculation for a metallic plate [202].

From the definition of r_{ab} (IV.19) in terms of Green function, it follows that the contribution δr comes from an additional term $\overline{\delta\mathbf{G}}$ in the Green tensor when considering the impurities in the metal. These impurities are encoded in the *local conductivity tensor* $\sigma_{\alpha,\beta}$ that is written as:

$$\sigma_{\alpha,\beta}(i\xi,\mathbf{r},\mathbf{r}_1) = \sigma(i\xi)\delta(\mathbf{r}-\mathbf{r}_1)\delta_{\alpha,\beta} + \delta\sigma_{\alpha,\beta}(i\xi,\mathbf{r},\mathbf{r}_1) \tag{IV.36}$$

where $\sigma(i\xi)$ is the global Drude conductivity (the plasma model is reached by taking $\gamma \to 0$) and α, $\beta \in \{x,y,z\}$ encode the three space directions.

The Helmholtz equation (IV.5) in each direction α inside the metal becomes:

$$(\boldsymbol{\nabla}\times\boldsymbol{\nabla}\times\mathbf{E}(\mathbf{r}))_\alpha - k^2 \sum_{\beta=x,y,z} \int d\mathbf{r}_1 \frac{\sigma_{\alpha,\beta}(i\xi,\mathbf{r},\mathbf{r}_1)}{\xi} E_\beta(\mathbf{r}_1) = k^2 E_\alpha(\mathbf{r}). \tag{IV.37}$$

By making an analogy with the Schrödinger equation – the electromagnetic field $\mathbf{E}$ playing the role of a wavefunction – we can read equation (IV.37) as:

$$(\hat{H}^{\text{eff}} + \hat{V})\mathbf{E} = \mathcal{E}\mathbf{E} \tag{IV.38}$$

with $\hat{H}^{\text{eff}}$ corresponding to the field in the effective medium and $\hat{V}$ being the perturbative potential due to impurities in the metal:

$$\begin{aligned} \mathcal{E} &\equiv k^2 && \text{(IV.39)}\\ \hat{H}^{\text{eff}}\,\mathbf{E} &\equiv \boldsymbol{\nabla}\times\boldsymbol{\nabla}\times\mathbf{E}(\mathbf{r}) - k^2\frac{\sigma(i\xi)}{\xi}\mathbf{E}(\mathbf{r}) && \text{(IV.40)}\\ \hat{V}\,\mathbf{E} &\equiv -k^2\int d\mathbf{r}_1\frac{\delta\boldsymbol{\sigma}(i\xi,\mathbf{r},\mathbf{r}_1)\cdot\mathbf{E}_\beta(\mathbf{r}_1)}{\xi} && \text{(IV.41)} \end{aligned}$$

The Green tensor $\mathbf{G}$ of the total Hamiltonian $\hat{H} \equiv \hat{H}^{\text{eff}} + \hat{V}$ can be written in terms of the Green tensor for the effective medium $\overline{\boldsymbol{G}}$ and the perturbative potential $\hat{V}$:

$$\begin{aligned} \mathbf{G} &= (\mathcal{E} - \hat{H})^{-1}\\ &= (\mathcal{E} - \hat{H}^{\text{eff}} - \hat{V})^{-1}\\ &= ((\mathcal{E} - \hat{H}^{\text{eff}})(\mathbf{I} - (\mathcal{E} - \hat{H}^{\text{eff}})^{-1}\hat{V})^{-1}\\ &= (\mathbf{I} - \overline{\boldsymbol{G}}\hat{V})^{-1}\overline{\boldsymbol{G}}\\ &= \sum_{n=0}^{\infty}(\overline{\boldsymbol{G}}\hat{V})^n\overline{\boldsymbol{G}} \end{aligned} \tag{IV.42}$$

By only keeping the first perturbative term, we obtain:

$$\mathbf{G} \simeq \overline{\boldsymbol{G}} + \delta\mathbf{G}, \quad \delta\mathbf{G} \equiv \overline{\boldsymbol{G}}\hat{V}\overline{\boldsymbol{G}}. \tag{IV.43}$$

The effective Green tensor $\overline{\boldsymbol{G}}$ is the propagator of the field inside the effective medium. The field with polarizability a coming from the vacuum penetrates first inside the metal, with some probability encode by the Fresnel transmission coefficient $\overline{t}_a^{1\to 2}$. Then, the field on the other side of the interface, inside the metal, has two possibilities to reach the point $\mathbf{r}$: directly or by being first internally reflected from the surface with some probability encoded by the Fresnel reflection coefficient $\overline{r}_a^{2\to 2}$. At the end, the Green tensor $\overline{\boldsymbol{G}}$ is written:

$$\begin{aligned} \overline{G}_a(\boldsymbol{q}_a,\mathbf{r}) &= \overline{t}_a^{1\to 2}[\overline{\boldsymbol{G}}_2^{(0)}(\boldsymbol{q}_a,\mathbf{r}) + \overline{\boldsymbol{G}}_2^{(r)}(\boldsymbol{q}_a,\mathbf{r})] && \text{(IV.44)}\\ &= \frac{\overline{t}_a^{1\to 2}(1+\overline{r}_a^{2\to 2})}{-2\tilde{\kappa}_z^a}\cdot e^{i\boldsymbol{q}_a\cdot\mathbf{r}_\perp - \tilde{\kappa}_z^a z}\,\boldsymbol{\epsilon}_a^+. && \text{(IV.45)} \end{aligned}$$

Finally, the correlator $\overline{\delta r_{ab}(i\xi_1)\delta r_{cd}(i\xi_2)}$ involves the correlator $\overline{\delta\mathbf{G}\delta\mathbf{G}}$ (IV.43), itself involving the conductivity correlator through $\hat{V}$:

$$\begin{aligned}\overline{\delta r_{ab}(i\xi_1)\delta r_{cd}(i\xi_2)} =& 4\kappa_z^a\kappa_z^c\int d^3\mathbf{r}\, d^3\mathbf{r}_1 d^3\mathbf{r}' d^3\mathbf{r}'_1 \\ &\times \overline{G}_a(\boldsymbol{q}_a,\mathbf{r})\overline{G}_b(\boldsymbol{q}_b,\mathbf{r}_1)\overline{G}_c(\boldsymbol{q}_c,\mathbf{r}')\overline{G}_d(\boldsymbol{q}_d,\mathbf{r}'_1) \\ &\times \frac{\xi_1\xi_2}{c^4}\overline{\delta\sigma_{ab}(i\xi_1,\mathbf{r},\mathbf{r}_1)\delta\sigma_{cd}(i\xi_2,\mathbf{r}',\mathbf{r}'_1)}.\end{aligned} \tag{IV.46}$$

The diagrammatic representation of the correlator $\overline{\delta\sigma_{ab}(i\xi_1,\mathbf{r},\mathbf{r}_1)\delta\sigma_{cd}(i\xi_2,\mathbf{r}',\mathbf{r}'_1)}$ is represented in figure IV.3. To evaluate it, we assume that the material is weakly disordered, i.e. that $k_F l \gg 1$, which is an excellent approximation for good metals such as gold. The main contribution of the conductivity correlator to δV is then due to electron trajectories correlated via a *single* impurity [190], as diagrammatically shown in figure IV.3b. Evaluation of this diagram leads to (see [203] for a more general discussion of conductivity correlations in metals):

$$\overline{\delta\sigma_{ab}(i\xi_1,\mathbf{r},\mathbf{r}_1)\delta\sigma_{cd}(i\xi_2,\mathbf{r}',\mathbf{r}'_1)} = \frac{\lambda_F^2 l}{2\pi}\frac{\delta_{ab}\delta_{cd}\,\sigma_0^2}{(1+\xi_1/\gamma)^2(1+\xi_2/\gamma)^2}\delta(\mathbf{r}-\mathbf{r}')\delta(\mathbf{r}_1-\mathbf{r}'_1)\delta(\mathbf{r}-\mathbf{r}_1). \tag{IV.47}$$

where l is the electron mean free path ($l = v_F/\gamma$ with v_F the Fermi velocity), λ_F the Fermi wavelength and σ_0 the static Drude conductivity (IV.30).

We note that this important property was not fulfilled in a recent work by Allocca et al. [204], who used a diffusion approximation to describe electronic motion in a metal. Such an approximation is inadequate in the context of the Casimir effect because it underestimates the weight of short electron scattering trajectories, which turn out to be the dominant ones [190].

To derive equation (IV.47), we have neglected the finite range and anisotropic structure of the conductivity correlator [203]. Taking into account this structure is not necessary here, as it would eventually give rise to relative corrections to $\overline{\delta^2 V}$ smaller by a factor $\sim 1/(k_F l) \ll 1$. By reporting equation (IV.47) into (IV.46), we obtain:

$$\begin{aligned}\overline{\delta r_{ab}(i\xi_1)\delta r_{cd}(i\xi_2)} =& \frac{\pi\lambda_F^2 l\omega_p^4}{2c^4\gamma^2}\frac{\xi_1\xi_2}{(1+\xi_1/\gamma)^2(1+\xi_2/\gamma)^2}\frac{\kappa_z^a\kappa_z^c(\boldsymbol{\epsilon}_a^+\cdot\boldsymbol{\epsilon}_b^-)(\boldsymbol{\epsilon}_c^+\cdot\boldsymbol{\epsilon}_d^-)}{\tilde{\kappa}_z^a\tilde{\kappa}_z^c\tilde{\kappa}_z^b\tilde{\kappa}_z^d(\tilde{\kappa}_z^a+\tilde{\kappa}_z^b+\tilde{\kappa}_z^c+\tilde{\kappa}_z^d)} \\ &\times \overline{t}_a^{1\to2}\overline{t}_c^{1\to2}\overline{t}_b^{2\to1}\overline{t}_d^{2\to1}\prod_{i=a,b,c,d}(1+\overline{r}_i^{2\to2})\,\delta(\boldsymbol{q}_a-\boldsymbol{q}_b-\boldsymbol{q}_c+\boldsymbol{q}_d),\end{aligned} \tag{IV.48}$$

where $\overline{t}_b^{2\to1}$, $\overline{t}_d^{2\to1}$ are the Fresnel transmission coefficients from the metal to the vacuum. The Dirac delta function that appears in the expression (IV.48) indicates momentum conservation of the total scattering process.

IV.2.c Magnitude of the fluctuations

By computing $\overline{\delta^2 V}$ using equations (IV.35) and (IV.48), we write the final expression in the following form:

$$\frac{\overline{\delta^2 V}}{\overline{V}^2} = \frac{(2\pi\lambda_F)^2 l}{\lambda_\gamma^2 \lambda_p} \mathcal{F}(z). \tag{IV.49}$$

λ_γ is the length scale associated with the dissipation rate γ:

$$\lambda_\gamma = \frac{2\pi c}{\gamma}. \tag{IV.50}$$

We discuss now intuitively and quantitatively this result.

The prefactor $(2\pi\lambda_F)^2 l/(\lambda_\gamma^2\lambda_p)$ in expression (IV.49) describes the interaction of the electromagnetic field with conduction electrons in the metal, and quantifies the strength of relative fluctuations. Over a time span t, one can associate to an electron trajectory in the metal an effective, classical tube of length $v_F t$ and cross-section λ_F^2, as it is illustrated in figure IV.4. This tube has a volume

$$V_e = v_F t \lambda_F^2. \tag{IV.51}$$

Since a finite variance $\overline{\delta^2 V}$ arises due to correlations between electron scattering trajectories, as it is represented in figure IV.3, we have to estimate the probability for a crossing between two such tubes to take place. This probability is given by the ratio of

$$\text{(proba of crossing after t)} \sim \frac{V_e}{V} \tag{IV.52}$$

where V is the effective volume of the metal accessible to the electromagnetic field. Over the same time span t, the field can transversally propagate over a surface $(ct)^2$ and it can penetrate the metal up to a distance $\sim \lambda_p$ (the typical skin depth), giving:

$$V = \lambda_p (ct)^2. \tag{IV.53}$$

The probability of crossing after a time t is thus

$$\frac{V_e}{V} = \frac{v_F t \lambda_F^2}{\lambda_p (ct)^2}. \tag{IV.54}$$

If we finally note that the typical time scale for electron relaxation is $t = \gamma^{-1}$, that $v_F/\gamma = l$ and $c/\gamma = \lambda_\gamma/(2\pi)$, we recover the prefactor in equation (IV.49):

$$\frac{V_e}{V} = \frac{2\pi\lambda_F^2 l}{\lambda_\gamma^2 \lambda_p}. \tag{IV.55}$$

At this stage, let us mention that the function $\mathcal{F}(z)$ remains finite when $\gamma \to 0$ (see below). Therefore, since $(2\pi\lambda_F)^2 l/(\lambda_\gamma^2\lambda_p) \propto \gamma$, the fluctuating part of the Casimir-Polder potential vanishes when $\gamma \to 0$. This is required since the spatial fluctuations of V find their origin in the metal heterogeneities, encoded in γ.

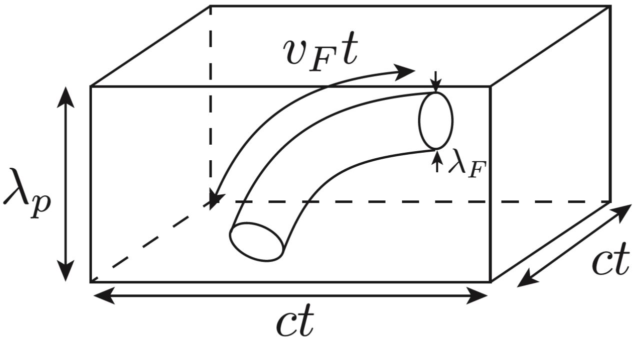

Figure IV.4: Classical electron trajectory inside the volume effectively accessible to the electromagnetic field.

IV.2.d Asymptotic behavior of fluctuations

The function $\mathcal{F}(z)$ in equation (IV.49) is displayed in figure IV.5 (blue dots). For comparison, we also show the same function in the limit where $\gamma \to 0$ (red dots), calculated using the plasma limit for the mean permittivity $\epsilon(i\xi)$. For simplicity we here set $\lambda_p = \lambda_A$, so that only two characteristic length scales remain in the problem, the plasma wavelength λ_p and the relaxation wavelength $\lambda_\gamma = 2\pi c/\gamma$. Overall, $\mathcal{F}(z)$ is a decaying function of z, which confirms the intuition that the sphere tends to average out the metal heterogeneities at large separations.

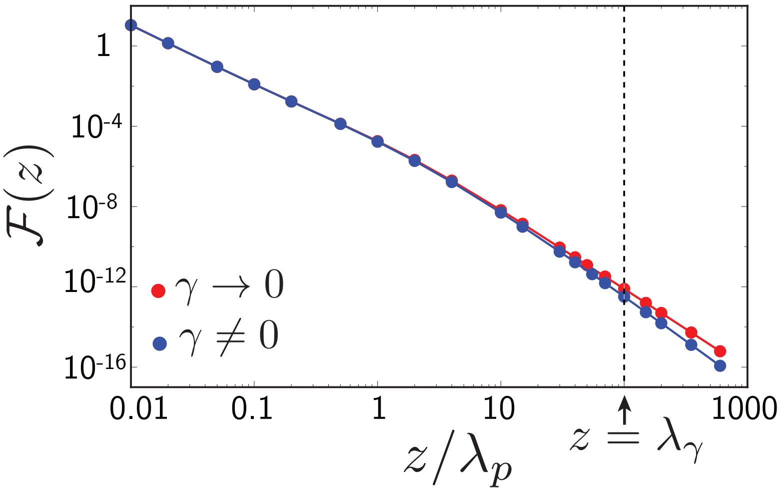

Figure IV.5: Function $\mathcal{F}(z)$ versus z/λ_p, at $T = 0$ and for $\lambda_p = \lambda_A$ (blue dots). We have set $\lambda_\gamma = 2\pi c/\gamma = 10^2 \lambda_A$. Red dots show the same function in the limit $\gamma \to 0$. Lines joining the points are guides to the eye.

At small separations, we find:

$$\mathcal{F}(z) \underset{z\ll\lambda_p}{\sim} \left(\frac{\lambda_p}{z}\right)^3. \tag{IV.56}$$

This characteristic scaling is not surprising, as it is reminiscent of what has been found for spatial fluctuations of Casimir-Polder forces above dielectric disordered plates [190, 199]. Indeed, small separations are described by large frequencies where the electromagnetic field penetrates easily the metal, which thus behaves similarly to a dielectric material. In that case, the Casimir potential at distance z from the medium is controlled by the interaction of radiation with the matter contained in a volume $\propto z^3$. It follows that the relative fluctuations are of the order of $1/\sqrt{N_A}$, where $N_A = nz^3$ is the number of scatterers in that volume and n the density of scatterers [190].

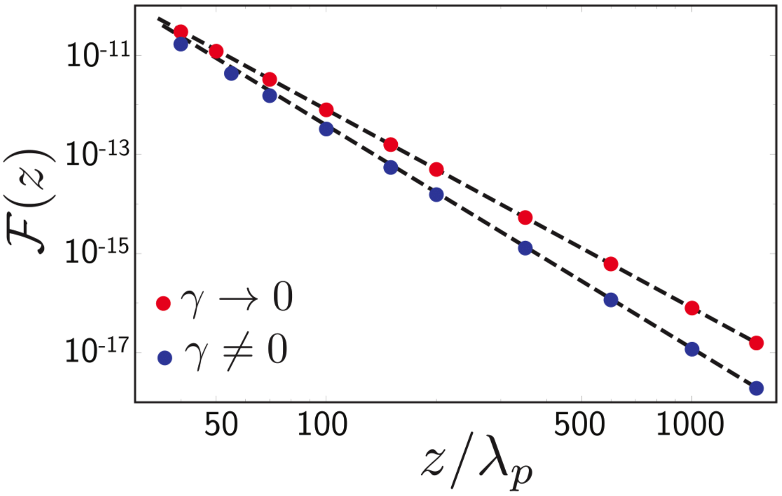

Figure IV.6: Zoom of figure IV.5 in the range $z \gg \lambda_p$. The dashed lines are the asymptotes (IV.58a) in red and (IV.58b) in blue.

A quick look at the two curves in figure IV.5 also indicates that the function $\mathcal{F}(z)$ does not depend much on γ at small separations $z \ll \lambda_p$. This can be qualitatively understood from the coincidence of the plasma and the Drude models for the mean permittivity at large frequencies:

$$\epsilon(i\xi) \underset{\xi\gg\gamma}{\simeq} 1 + \frac{\omega_p^2}{\xi^2}. \tag{IV.57}$$

In strong contrast, a very interesting behavior shows up at large separations where the z variation of $\mathcal{F}(z)$ starts to qualitatively depend on γ. This is well visible in figure IV.6, which focuses on the range $z \gg \lambda_p$. This observation is also confirmed by an asymptotic analysis of $\mathcal{F}(z)$ at large separations (the analysis for the Drude model is detailed in appendix (D)), which yields:

$$\mathcal{F}(z) = \begin{cases} c_1 \left(\frac{\lambda_p}{z}\right)^4 & \lambda_p \ll z \ll \lambda_\gamma \qquad \text{(IV.58a)} \\ c_2 \left(\frac{\lambda_p}{\lambda_\gamma}\right)^4 \left(\frac{\lambda_\gamma}{z}\right)^{9/2} & z \gg \lambda_\gamma \qquad \text{(IV.58b)} \end{cases}$$

where $c_1 \simeq 8.0 \times 10^{-5}$ and $c_2 \simeq 3.9 \times 10^{-5}$ are numerical constants. These asymptotic limits are shown in Fig. IV.6 as dashed lines, and describe very well the exact numerical results.

Equations (IV.58a) and (IV.58b) constitute an important result of the chapter. They indicate that at large separations, the variance of the Casimir-Polder potential has a different scaling with z depending on γ. In other words, the fluctuations achieve values that differ by orders of magnitude depending on the amount of dissipation in the metal. This behavior can be traced back to the low-frequency asymptotics of the mean permittivity

$$\epsilon(i\xi) = 1 + \frac{\omega_p^2}{\xi(\gamma + \xi)}, \qquad \text{(IV.59)}$$

which is crucially affected by γ. Eq. (IV.48) depends on $\epsilon(i\xi)$ through the wave numbers and Fresnel coefficients. At low frequencies, they behave differently for Drude and plasma models. This shows again that the spatial fluctuations of Casimir-Polder forces could be used as an efficient probe to unambiguously assess the effect of dissipation in the Casimir effect in metals.

IV.2.e Possibility of an experimental test

We have described for the first time the spatial fluctuations of Casimir-Polder forces above metals. As these fluctuations are triggered by electron scattering, their observation would constitute a natural probe of dissipation in the Casimir effect. Furthermore, we have shown that their dependence on the atom-plate separation depends significantly on the low-frequency description of the metal permittivity. For gold, a free electron density $n = 6 \times 10^{28}/\text{m}^3$ [205] and an elastic mean free path $l = 37.7$ nm [206] lead to

$$\left(\frac{(2\pi\lambda_F)^2 l}{\lambda_\gamma^2 \lambda_p}\right)^{1/2} \sim 3.4 \times 10^{-5} \qquad \text{(IV.60)}$$

for the magnitude of spatial fluctuations, which are thus typically small. Thus, quantum reflection between an antihydrogen atom and a metallic plate is not significantly affected by the heterogeneities of the medium. Our previous calculations based on the average Casimir-Polder potential are then sufficient.

However, conditions more favorable for the observation of these spatial fluctuations can be achieved by lowering the mean free path. For instance, nichrome is a nickel-chromium alloy used in resistive wires. It has $l = 4$ nm [207] at room temperature and $n = 9 \times 10^{28}/\mathrm{m}^3$. This leads to spatial fluctuations that are an order of magnitude larger than for gold. Alternatively, disordered thick films traditionally used in mesoscopic physics could be promising candidates for experimentally unveiling these fluctuations [208].

IV.3 Effect of the temperature

So far we have discussed only zero temperature. It is also interesting to study the effect of the temperature on the mean Casimir-Polder potential and its fluctuations.

IV.3.a Casimir-Polder potential at finite temperature

The average Casimir-Polder potential at zero temperature is given by the formula (IV.25). Let us now briefly describe the regime of finite temperature T. From the Planck's law (I.82), the number of photon per mode is an increasing function of the temperature T. In fact, for a given T, the integral over all frequencies in formula (IV.3) can be written as a sum over Matsubara frequencies ξ_n:

$$\xi_n = n\frac{2\pi k_B T}{\hbar}. \tag{IV.61}$$

The mean potential is also written [127]:

$$\overline{V}(z) = \frac{k_B T}{c^2}\sum_n{}^{'}\, \xi_n^2 \alpha(i\xi_n)\int \frac{d^2\mathbf{q}_a}{2\pi}\frac{d^2\mathbf{q}_b}{2\pi}\frac{e^{-2\kappa_z z}}{2\kappa_z}\sum_{a,b=\mathrm{TE,TM}} r_{ab}(i\xi)\,\boldsymbol{\epsilon}_a^+(\boldsymbol{q}_a)\cdot\boldsymbol{\epsilon}_b^-(\boldsymbol{q}_b). \tag{IV.62}$$

The primed over the sum symbol indicates that the contribution of the first Matsubara frequency ($n = 0$) is counted for only one half:

$$\sum_n{}^{'}\,\Phi(n) = \frac{1}{2}\Phi(0) + \sum_{n=1}^{\infty}\Phi(n). \tag{IV.63}$$

We define the thermal wavelength:

$$\lambda_T \equiv \frac{\hbar c}{k_B T}. \tag{IV.64}$$

For $z \ll \lambda_T$, the potential (IV.62) behaves as the potential at zero temperature (IV.3). However, for $z \gg \lambda_T$, the asymptotic behavior of the potential changes [209], as we show now.

We start by introducing the dimensionless transverse wavevector $\mathbf{Q}$:

$$\mathbf{Q} = \mathbf{q}z. \tag{IV.65}$$

Then the exponential decay terms $\kappa_z z$ becomes :

$$\kappa_z z = \sqrt{\frac{n^2 z^2}{\lambda_T^2} + \mathbf{Q}^2}. \tag{IV.66}$$

For $z \gg \lambda_T$, the term corresponding to the first Matsubara frequency $n = 0$ is dominant in the exponential decay $e^{-\kappa_z z}$. By keeping only the term for $n = 0$ in the sum, and computing the reflection coefficients, we find:

$$\overline{V}(z) \underset{z \gg \lambda_T}{\simeq} -\frac{\alpha(0) k_B T}{2} \frac{1}{z^3} \int \frac{d^2\mathbf{Q}}{(2\pi)^2} |\mathbf{Q}| e^{-2|\mathbf{Q}|} \tag{IV.67}$$

$$\underset{z \gg \lambda_T}{\simeq} -\frac{\alpha(0) k_B T}{16\pi z^3}. \tag{IV.68}$$

At room temperature, $T = 300$ K, the thermal wavelength is $\lambda_T = 7.6$ µm. We distinguish also three regimes for the Casimir-Polder potential, as is illustrated in IV.7:

- for $z \ll \lambda_A$, $V(z) \sim 1/z^3$: the van der Waals regime,
- for $\lambda_A \ll z \ll \lambda_T$, $V(z) \sim 1/z^4$: the retarded regime,
- for $\lambda_T \ll z$, $V(z) \sim 1/z^3$: the thermal regime.

Note that these three regimes does not depend on the description of the metallic medium. They only depend on the static polarizability, the temperature and physical constants.

IV.3.b Fluctuations of the potential at finite temperature

The calculation of the variance $\overline{\delta^2 V}$ at $T \neq 0$ follows the same lines as at $T = 0$, except that it involves a double sum over Matsubara frequencies $2\pi k_B T n/\hbar$ and $2\pi k_B T m/\hbar$, where n, m are integers running from 0 to ∞. At finite temperature, we find that the general form (IV.49) still holds, with the function $\mathcal{F}(z)$ now modified at separations $z \gtrsim \lambda_T$ as compared to the results of figure IV.5.

$\mathcal{F}(z)$ is shown in the main panel of figure IV.8 at $T \neq 0$ (blue dots). For definiteness we set $\lambda_T = 10^3 \lambda_A > \lambda_\gamma = 10^2 \lambda_A$. Points such that $z \ll \lambda_T$ are identical to those in figure IV.5. At large separations however, temperature gives rise to a collapse of spatial fluctuations. A plot of $\mathcal{F}(z)$ in log scale (inset of figure IV.8) suggests that this decay is close to *exponential.* Finite temperatures thus turn out to average out the spatial fluctuations of the Casimir force.

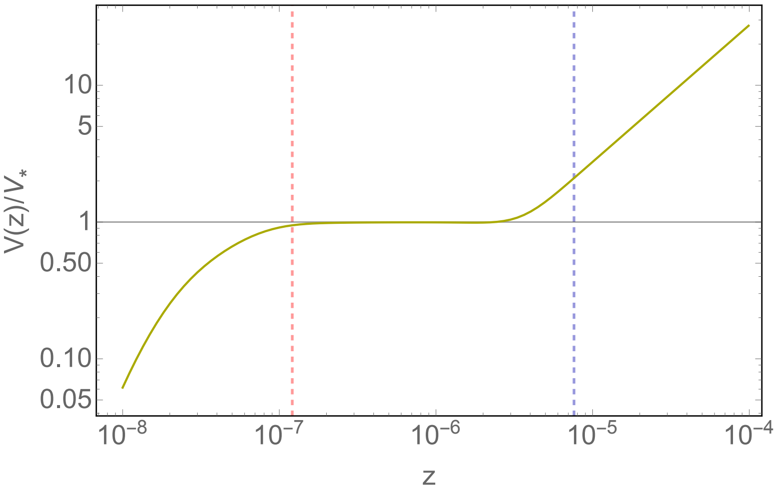

Figure IV.7: The average Casimir-Polder potential for an antihydrogen atom above a gold surface, calculated at room temperature $T = 300$ K. The horizontal axis is the distance between the atom and the surface, in nanometers. The vertical red dashed line is positioned at λ_A, while the blue dashed line is at λ_T.

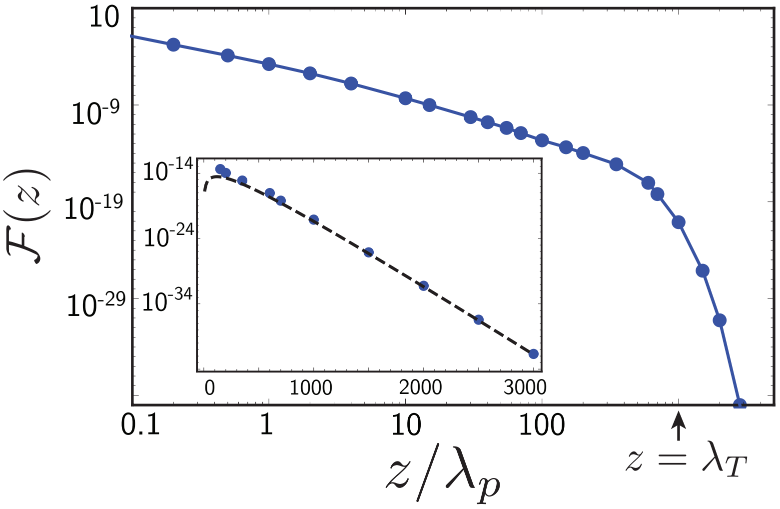

Figure IV.8: Main panel: function $\mathcal{F}(z)$ at finite temperature, for $\lambda_0 = \lambda_p$, $\lambda_\gamma = 2\pi c/\gamma = 10^2 \lambda_A$ and $\lambda_T = 10^3 \lambda_A$ (blue dots). The fluctuations collapse exponentially at $z \gg \lambda_T$. Inset: same curve in log scale, together with the asymptotic law (IV.69).

To better understand this intriguing result, we have also investigated the regime $z \gg \lambda_T$ analytically. As we have already shown, for the mean potential $\overline{V}$ this limit is controlled by the zeroth-order Matsubara frequency term in the sum, which turns out to be nonzero and reduces to equation (IV.68). The situation is very different for the variance $\overline{\delta^2 V}$, for which we find that the contributions involving zero-order Matsubara frequencies ($n = 0$ or $m = 0$) identically vanish. One can already guess this result from the expression of the correlator of reflection coefficients, equation (IV.48), which falls to zero when ξ_1 or $\xi_2 \to 0$. Because the term ($n = 0$ or $m = 0$) is identically zero, the large-separation asymptotics of $\overline{\delta^2 V}$ is naturally governed by the first-order contribution $(n, m) = (1, 1)$. This term can be explicitly calculated by means of a saddle-point approximation, leading to

$$\mathcal{F}(z) \simeq c_3 \left(\frac{\lambda_p}{\lambda_T}\right)^4 \left(1 + \frac{\lambda_T}{\lambda_\gamma}\right)^{-1/2} \left(\frac{z}{\lambda_T}\right)^3 e^{-8\pi z/\lambda_T}, \tag{IV.69}$$

where $c_3 \simeq 115.7$.

This asymptote is shown in the inset of figure IV.8 as a dashed line, and matches well the exact numerical calculation. Note that the exponential decay of fluctuations is controlled by the thermal wavelength, the dissipation γ appearing only through the prefactor $(1 + \lambda_T/\lambda\gamma)^{-1/2}$. The result (IV.69) is remarkably different from the algebraic decay of $\overline{V}$ (IV.25). At a very qualitative level, it can be understood by the argument that in the strict limit of zero frequency, the electromagnetic field (of infinite wavelength) cannot resolve the spatial heterogeneities (impurities) of the metal. The contribution of zeroth-order Matsubara frequency to the fluctuation $\overline{\delta^2 V}$ must therefore be zero. We expect this argument to be universal, independent of the details of the material like the type of impurities or the value of the mean free path. It does of course not hold for the mean Casimir potential $\overline{V}$, which finds its origin in the reflection of the electromagnetic field from the purely homogeneous surface of the metal, so that even a field of infinite wavelength can contribute to $\overline{V}$.

Conclusion and perspectives

The exploration of a system as simple as a single cold (anti)-hydrogen atom placed above a surface offers surprisingly beautiful and interesting physics to study. In this thesis, we have focused our attention on the quantum reflection phenomenon, whose understanding is crucial for the GBAR experiment.

We presented the Casimir-Polder interaction between the atom and different surfaces using the scattering formalism. We developed a very precise description of the interaction of the atom with a metallic medium. This description is not only useful to better understand the probable deviations from the average Casimir-Polder interaction between the antihydrogen atom and the detector for instance, but it also fits the more general frame of the dissipation description in metallic media. With the help of Nicolas Cherroret, we were able to compute the statistical fluctuations of the potential, due to the heterogeneities of the metal. We described the path of the electromagnetic field in the Green function formalism, that allowed us to relate the statistical fluctuations of the potential to the conductivity correlators in the metal. We proposed an intuitive picture for interpreting the magnitude of the fluctuations. A relevant fact we discovered in this study is a different power law for the fluctuations of the Casimir-Polder potential, depending on the Drude or plasma model used for the description of the conductivity. A precise measurement of the Casimir-Polder potential of an atom or a small sphere placed above a high disordered metal could help to discriminate between these two models, and also to progress in the "Drude vs plasma" puzzle still unsolved in the Casimir community. Hopefully, the weak amplitude we found ensures that the mean-field potential used in other parts of this manuscript is sufficient to treat precisely the quantum reflection.

We also discussed the phenomenon of quantum reflection on this attractive mean potential by using Liouville transformations. The group of transformations mapping a reflection on a well into a reflection on a wall – the badlands – guided us in our search for a high reflectivity for matter waves, which paradoxically corresponds to a high transparency for electromagnetic waves. We studied the Casimir-Polder potential between an antihydrogen atom and a liquid helium film, offering the highest quantum reflection. Thanks to the scattering formalism, we computed Casimir-Polder potentials for different thicknesses of the liquid helium film. For thicknesses larger than 50 nm, the film is considered as a bulk and we found a very high reflectivity. The lifetime of the antihydrogen on such a bulk excesses one second, that is better than lifetimes achieved for different materials already studied, such as silica or even nano-porous materials ! For thicknesses of the order of a few nanometers, we discovered oscillations of the scattering length – length that encodes the quantum reflection in the limit of low energy. We explained this phenomenon once again thanks to the Liouville transformations producing a "cavity" in the transformed potential made of two bumps corresponding to the quantum reflection on the thin liquid helium film and the substrate. By this analogy, we found a non trivial manifestation of a shape resonance.

We continued our exploration by adding the gravitational potential. We thus performed for the first time a full quantum treatment of an atom coupled to the gravity and the Casimir-Polder potential. We used an adapted Liouville transformation for the one turning point problems that led to a new potential landscape. With these Langer coordinates, the atom levitates between two mirrors: an upper perfectly reflecting mirror due to the gravity and a bottom partially reflecting mirror due to the quantum reflection on the Casimir-Polder potential. By using the analogy with a Fabry-Perot cavity, we not only offered an intuitive understanding of these quantum levitation states, but also were able to precisely quantize the energies of the states, improving the scattering length approximation – used until now – by two orders of magnitude. For doing that, we had to develop a new effective range theory taking into account the energy dependance on the scattering length. While the numerical tests confirm the new shape of the energy expansion of the scattering length, it would be interesting to obtain an analytical development, in the spirit of the Lippmann-Schwinger derivation in the Liouville coordinates and see if the development is generalizable for a larger class of potentials.

The precise description of the quantum levitation states offers new perspectives for a measurement of the free fall acceleration using quantum spectroscopic techniques. While in previous proposals such as the velocity selector a large fraction of antiatoms where lost due to the annihilation, we proposed a new technique relatively easy to implement in the GBAR experiment, that keeps almost all antihydrogen atoms. We described precisely the evolution of the matter wave in this new experimental setup made of two parts. The first part consisting of letting the atom bounce on a high reflecting surface such as liquid helium film, thus building quantum interferences between gravitational quantum states. The second part consisting in a macroscopic free fall revealing the interferences on the detector. For doing the latter calculation, we introduced the Wigner function that relates classically the variables at the end of the interference zone to the variables in position and time on the detector. The numerical calculation was done for a superposition of hundred states, but depending on the initial state preparation, a calculation with more states – that would be time consuming – should be achieved. We then proposed a method to estimate $\overline{g}$ by a Monte Carlo simulation and a Cramer-Rao lower bound estimation. We checked that a good statistical efficiency was reached with this method. This is quite surprising regarding the complexity of the interference pattern and the relative low number of atoms probing this pattern. A more mathematical study would be interesting, in order to understand convergence properties of statistical method, and to better understand the dependance on initial parameters of the final accuracy calculation. The physics of the photo-detachment should also be scrutinized. However, with the set of parameters known today, we reached a relative accuracy better than 10^{-5} improving the initial GBAR uncertainty estimation by almost three orders of magnitude !

During this thesis, we explored theoretically subtle effects of quantum reflection for an antihydrogen atom above different surfaces, especially liquid helium that offers the best reflectivity. The physical effects could be first tested experimentally for an hydrogen atom interacting with a liquid helium surface, as proposed in [137]. One of the difficulties remains in the detection of the hydrogen atom. A promising way could be to test the quantum reflection for helium atoms, as was already achieved on gratings [27, 210–212], or metastable helium [30, 213] that is easily detectable. We hope that these projects with atoms will reveal beautiful physics and bring further new ideas.

Appendices

A Effective range theory

We present here the derivation of the effective range theory for a potential that decreases asymptotically as $-C_4/z^4$, with a difference with the $V_4(z)$ potential that is short-range. We follow the detailed derivation presented in [159]. The ideas used in that derivation are quite general and could give some insights to perform an analytical treatment of the new effective range theory we propose in section II.2.

A.1 Schrödinger equations

Let us denote by $\varphi(z)$ solutions of the Schrödinger equation for energy $E = \hbar^2 k^2/2m$ and a $V_4(z)$ potential:

$$\varphi''(z) + \frac{2m}{\hbar^2} \left(E - V_4(z)\right) \varphi(z) = 0. \tag{A.1}$$

We consider now a potential $V(z)$ that behaves asymptotically for $z \to \infty$ as $V_4(z)$. We also introduce the difference $\Delta V(z)$:

$$\Delta V(z) \equiv V(z) - V_4(z) \tag{A.2}$$

that vanishes as $z \to \infty$ more rapidly that any power of $1/z$. In that sense, $\Delta V(z)$ is considered as a short-range potential. A wave function $\psi(z)$ obeys also the Schrödinger equation:

$$\psi''(z) + \frac{2m}{\hbar^2} \left(E - [V_4(z) + \Delta V(z)]\right) \psi(z) = 0. \tag{A.3}$$

Because of the quick cancellation of ΔV at large distances, solutions of the equation (A.3) are also asymptotically solutions of the equation (A.1):

$$\psi(z) \underset{z\to\infty}{\sim} \varphi^s(z) + B\varphi^c(z) \equiv \tilde{\varphi}(z) \tag{A.4}$$

with φ^s and φ^s two independent and convenient solutions of (A.1) built from Mathieu functions $\tilde{\psi}^{(+)}$ and $\tilde{\psi}^{(-)}$:

$$\varphi^s(z) \propto e^{-\sigma} \cos(\delta)\tilde{\psi}^{(-)}(\tilde{z}) + e^{\sigma} \sin(\delta)\tilde{\psi}^{(+)}(\tilde{z}) \tag{A.5}$$

$$\varphi^c(z) \propto e^{-\sigma} \sin(\delta)\tilde{\psi}^{(-)}(\tilde{z}) + e^{\sigma} \cos(\delta)\tilde{\psi}^{(+)}(\tilde{z}) \tag{A.6}$$

where

$$\delta \equiv \frac{\pi}{2}\left(\tau - \frac{1}{2}\right). \tag{A.7}$$

The constant B that appears in the equation (A.4) can be extracted from the solutions $\psi(z)$ and $\tilde{\varphi}(z)$ of the Schrödinger equation, as we explained below.

A.2 Effective range

Let ψ_1 and ψ_2 be solutions of (A.3) with for energies E_1 and E_2 respectively, and $\tilde{\varphi}_1$ and $\tilde{\varphi}_2$ solutions of (A.1) for the same energies. Integrating the quantity $\psi_1(z)\psi_2''(z) - \psi_2(z)\psi_1''(z)$ (and doing the same with $\tilde{\varphi}_{1,2}$) and using the fact that ψ and $\tilde{\varphi}$ are solutions of the Schrödinger equation, we obtain for any given z_m and z_M:

$$[\psi_1(z)\psi_2'(z) - \psi_2(z)\psi_1'(z)]_{z_m}^{z_M} = (k_1^2 - k_2^2)\int_{z_m}^{z_M} \psi_1(z)\psi_2(z)dz \tag{A.8}$$

$$[\tilde{\varphi}_1(z)\tilde{\varphi}_2'(z) - \tilde{\varphi}_2(z)\tilde{\varphi}_1'(z)]_{z_m}^{z_M} = (k_1^2 - k_2^2)\int_{z_m}^{z_M} \tilde{\varphi}_1(z)\tilde{\varphi}_2(z)dz. \tag{A.9}$$

We subtract the two equations :

$$\begin{split}[\psi_1(z)\psi_2'(z) - \psi_2(z)\psi_1'(z)]_{z_m}^{z_M} - [\tilde{\varphi}_1(z)\tilde{\varphi}_2'(z) - \tilde{\varphi}_2(z)\tilde{\varphi}_1'(z)]_{z_m}^{z_M} \\ = (k_2^2 - k_1^2)\int_{z_m}^{z_M} \tilde{\varphi}_1(z)\tilde{\varphi}_2(z) - \psi_1(z)\psi_2(z)dz.\end{split} \tag{A.10}$$

We now take $z_M \to \infty$. ψ and $\tilde{\varphi}$ being asymptotically equal, the left term of (A.10) evaluated at z_M is zero. We choose in the same way $z_m \to 0$. In the left term of (A.10), the bracket for ψ vanishes [159], while the bracket for $\tilde{\varphi}$ is $B_2/\ell_4 - B_1/\ell_4$. We thus obtain the equality:

$$\frac{B_2}{\ell_4} - \frac{B_1}{\ell_4} = (k_2^2 - k_1^2)\int_0^\infty \tilde{\varphi}_1(z)\tilde{\varphi}_2(z) - \psi_1(z)\psi_2(z)dz \tag{A.11}$$

that can be evaluated at $k_1 = 0$ and becomes

$$\frac{B}{\ell_4} = \frac{B_0}{\ell_4} + \frac{1}{2}\rho(k)k^2 \tag{A.12}$$

with

$$\frac{1}{2}\rho(k) = \int_0^\infty \tilde{\varphi}_0(z)\tilde{\varphi}_k(z) - \psi_0(z)\psi_k(z)dz. \tag{A.13}$$

The approximation consists in taking $\rho(0) \equiv \mathcal{R}_0$ instead of $\rho(k)$ to get :

$$\frac{B}{\ell_4} \simeq \frac{B_0}{\ell_4} + \frac{1}{2}\mathcal{R}_0 k^2 \tag{A.14}$$

with

$$\frac{1}{2}\mathcal{R}_0 = \int_0^\infty \tilde{\varphi}_0^2(z) - \psi_0^2(z)dz. \tag{A.15}$$

The error due to this approximation involves a term of the order $\mathcal{O}(k^4)$.

A.3 Expansion of $\mathcal{A}$

We would like to calculate the phase shift η, obtained when we introduce the potential V, in order to get the length $\mathcal{A}$. We use the fact that asymptotically:

$$\psi(z) \underset{z\to\infty}{\sim} \tilde{\varphi}(z) \underset{z\to\infty}{\simeq} \sin(kz+\eta). \tag{A.16}$$

It follows that the reflection amplitude can be expressed in terms of η:

$$r(k) = -e^{2i\eta}. \tag{A.17}$$

By matching (A.5) and (A.6) with the asymptotic form $\sin(kz+\eta)$, we obtain:

$$\tan(\eta) = \frac{e^{-2\sigma} - \tan^2(\delta) + B\tan(\delta)(e^{-2\sigma}-1)}{\tan(\delta)(1-e^{-2\sigma}) + B(1-e^{-2\sigma}\tan^2(\delta))}. \tag{A.18}$$

We are now going to calculate step by step the expansion of $\tan(\eta)$ up to order $k^2\ln(k)$. We use expansions of τ and σ, as general properties of Mathieu equation that can be found in [160]. Keeping only terms of a relevant order, we obtain

$$\begin{aligned}\tan(\eta) =& \frac{k\ell_4\left[1-\frac{\pi B_0}{3}k\ell_4+\frac{4}{3}(k\ell_4)^2\ln(k\ell_4)-(k\ell_4)^2\left(\frac{8}{3}\ln(2)+\frac{8}{3}\psi(3/2)-\frac{20}{9}-\frac{\pi B_0}{3}\right)\right]}{B_0\left[1+(k\ell_4)^2\left(\frac{\pi}{3B_0}+\frac{\mathcal{R}_0}{2\ell_4 B_0}\right)\right]}\\ &+\mathcal{O}(k\ell_4)^4.\end{aligned} \tag{A.19}$$

After some algebra, we find:

$$\begin{aligned}\tan(\eta) = \frac{k\ell_4}{B_0}\Bigg[1-\frac{\pi B_0}{3}k\ell_4+\frac{4}{3}(k\ell_4)^2\ln(k\ell_4)-\\ \left(\frac{8}{3}\ln(2)+\frac{8}{3}\psi(3/2)-\frac{20}{9}-\frac{\pi B_0}{3}+\frac{\pi}{3B_0}+\frac{\mathcal{R}_0}{2\ell_4 B_0}\right)(k\ell_4)^2\Bigg]+\mathcal{O}(k\ell_4)^4.\end{aligned} \tag{A.20}$$

Let us now make the link with $\mathcal{A}(k)$. From (A.17) and the link between $r(k)$ and $\mathcal{A}(k)$

$$\mathcal{A}(k) = -\frac{i}{k}\frac{1+r(k)}{1-r(k)} \tag{A.21}$$

we find that:

$$\mathcal{A}(k) = -\frac{\tan(\eta)}{k}. \tag{A.22}$$

In the limit of zero energy $k \to 0$, by injecting equation (A.20) in (A.22), we find

$$\mathcal{A}(0) = -\frac{\ell_4}{B_0} \equiv a. \tag{A.23}$$

The next terms of the expansion (computed with Mathematica and consistent with the expression given in [163]) are given by:

$$\begin{aligned}\mathcal{A}(k) \simeq a \Bigg[& 1 + \frac{\pi \ell_4}{3a} k\ell_4 + \frac{4}{3}(k\ell_4)^2 \ln(k\ell_4/4) \\ & + \left(\frac{20}{9} - \frac{8}{3}\psi(3/2) - \frac{\pi\ell_4}{3a} + \frac{\pi a}{3\ell_4} + \frac{\mathcal{R}_0 a}{2\ell_4^2} \right) (k\ell_4)^2 \\ & - \left(\frac{\pi a}{3\ell_4} + \frac{\pi \ell_4}{135a} \right) (k\ell_4)^3 + \frac{8}{9}(k\ell_4)^4 \log^2(k\ell_4/4) \\ & + \left(\frac{4\pi a}{9\ell_4} + \frac{44}{15} - \frac{4\pi\ell_4}{9a} + \frac{2\mathcal{R}_0 a}{3\ell_4^2} - \frac{32}{9}\psi(3/2) \right) (k\ell_4)^4 \log(k\ell_4/4) \Bigg] \\ & + \mathcal{O}(k\ell_4)^5 . \end{aligned} \tag{A.24}$$

B Time evolution of the Wigner function in gravitational field

We derive the time evolution of the Wigner function in gravitational field, in a similar way as in [36]. For more commodity in the notations, we only consider the one-dimensional case of a wave function $\psi(z)$ evolving in the gravitational potential mgz. This derivation can easily be generalized in 2 or 3 dimensions.

B.1 Von Neumann equation

To obtain the evolution equation of the Wigner function, we start with the von Neumann equation for the density matrix:

$$i\hbar \frac{\mathrm{d}\hat{\rho}}{\mathrm{d}t} = [\hat{H}, \hat{\rho}] = \left(\frac{\hat{P}^2}{2m} + V(\hat{Z}) \right) \hat{\rho} - \hat{\rho} \left(\frac{\hat{P}^2}{2m} + V(\hat{Z}) \right). \tag{B.1}$$

Using the momentum and position representations to treat the kinetic and potential terms respectively, one shows that the Wigner function obeys an equation known as the quantum Liouville or Wigner equation:

$$\frac{\partial W_t}{\partial t}(z,p) = -\frac{p}{m}\frac{\partial W}{\partial z}(z,p,t) + \Theta[V]W_t(z,p), \tag{B.2}$$

where we used the shorthand notation

$$\begin{aligned}\Theta[V]W_t(z,p) \equiv -\frac{i}{2\pi\hbar^2} \int_{\mathbb{R}} & \mathrm{d}\zeta \, [V(z+\zeta/2) - V(z-\zeta/2)] \\ & \times \langle z+\zeta/2 | \hat{\rho} | z - \zeta/2 \rangle \, e^{-ip\zeta/\hbar}. \end{aligned} \tag{B.3}$$

If V is infinitely differentiable, $\Theta[V]$ can be written as a pseudo-differential operator:

$$\Theta[V] = \frac{i}{\hbar} \left[V\left(z - \frac{i\hbar}{2}\frac{\partial}{\partial p} \right) - V\left(z + \frac{i\hbar}{2}\frac{\partial}{\partial p} \right) \right] \tag{B.4}$$

$$= \sum_{n=0}^{\infty} \frac{(-\hbar^2/4)^n}{(2n+1)!} \frac{\partial^{2n+1} V}{\partial z^{2n+1}}(z) \left(\frac{\partial}{\partial p} \right)^{2n+1} . \tag{B.5}$$

Another possible representation is

$$\Theta[V]W_t(z,p) = \int \mathrm{d}\varpi \; W(z, p+\varpi, t)\mathcal{J}(z,\varpi) \;, \tag{B.6}$$

with

$$\mathcal{J}(z,\varpi) = \frac{1}{2\pi\hbar^2}\int \mathrm{d}\zeta \, [V(z+\zeta/2) - V(z-\zeta/2)]\sin(\varpi\zeta/\hbar) \;, \tag{B.7}$$

provided this last integral is defined.

B.2 Quadratic potential: from quantum to classical

If the potential $V(z)$ is at most quadratic, the pseudo-differential operator reduces to its zeroth order term and the *quantum* Liouville equation reduces to the *classical* Liouville equation which describes the evolution of a classical phase space density in a potential $V(z)$:

$$\frac{\partial}{\partial t}W_t(z,p) = -\frac{p}{m}\frac{\partial W_t}{\partial z}(z,p) + \frac{\mathrm{d}V}{\mathrm{d}z}(z)\frac{\partial W_t}{\partial p}(z,p). \tag{B.8}$$

In this case the exact quantum evolution can be expressed in terms of classical trajectories. Indeed, if the functions $z_{\mathrm{cl}}(t), p_{\mathrm{cl}}(t)$ (III.28) obey the classical equations of motion

$$\frac{\mathrm{d}z_{\mathrm{cl}}}{\mathrm{d}t} = \frac{p_{\mathrm{cl}}}{m} \tag{B.9}$$

$$\frac{\mathrm{d}p_{\mathrm{cl}}}{\mathrm{d}t} = -\frac{\mathrm{d}V}{\mathrm{d}z}(z_{\mathrm{cl}}), \tag{B.10}$$

then

$$\frac{\mathrm{d}W_t}{\mathrm{d}t}(z_{\mathrm{cl}}(t), p_{\mathrm{cl}}(t)) = \frac{\partial W_t}{\partial t} + \frac{\mathrm{d}z_{\mathrm{cl}}}{\mathrm{d}t}\frac{\partial W_t}{\partial z} + \frac{\mathrm{d}p_{\mathrm{cl}}}{\mathrm{d}t}\frac{\partial W_t}{\partial p} \tag{B.11}$$

$$= 0. \tag{B.12}$$

We also deduce that:

$$W_t(z_{\mathrm{cl}}(t), p_{\mathrm{cl}}(t)) = W_{t-\tau}(z_{\mathrm{cl}}(t-\tau), p_{\mathrm{cl}}(t-\tau)). \tag{B.13}$$

In particular, for a linear gravitational potential $V(z) = mgz$, the equation is

$$\frac{\partial W_t}{\partial t}(z,p) = -\frac{p}{m}\frac{\partial W_t}{\partial z}(z,p) + mg\frac{\partial W_t}{\partial p}(z,p) \tag{B.14}$$

and

$$z_{\mathrm{cl}}(t-\tau) = z_{\mathrm{cl}}(t) - \frac{p_{\mathrm{cl}}(t)}{m}\tau - \frac{1}{2}g\tau^2 \tag{B.15}$$

$$p_{\mathrm{cl}}(t-\tau) = p_{\mathrm{cl}}(t) + mg\tau, \tag{B.16}$$

so that (replacing $z_{\mathrm{cl}}(t), p_{\mathrm{cl}}(t)$ by z, p)

$$W_t(z,p) = W_{t-\tau}\left(z - \frac{p\tau}{m} - \frac{g\tau^2}{2}, \; p + mg\tau\right) \;. \tag{B.17}$$

Moreover, this evolution is easily generalized to three dimensions ($\vec{g} \equiv -g\vec{e}_z$):

$$W_t(\vec{r}, \vec{p}) = W_{t-\tau}\left(\vec{r} - \frac{\vec{p}\tau}{m} + \frac{\vec{g}\tau^2}{2},\ \vec{p} - m\vec{g}\tau\right). \tag{B.18}$$

C Asymptotic efficiency of the log-likelihood estimator

We present a proof of the asymptotic efficiency of the log-likelihood estimator, for sufficiently regular probability distributions, in the sense that $\mathfrak{E} \to 1$ for $N \to \infty$. The proof is presented in the same spirit as done in [184].

Proof. We start by expanding the derivative of the log likelihood function $\ln \mathbb{L}_{\mathcal{D}}$ (III.64) around g_0 using the Taylor-Lagrange formula up to the order 2:

$$\frac{1}{N}\frac{\partial}{\partial g} \ln \mathbb{L}_{\mathcal{D}}(g) = B_0 + B_1(g - g_0) + \frac{1}{2}B_2(g - g_0)^2, \tag{C.1}$$

where B_0, B_1 and B_2 are functions of the sample distribution $\mathcal{D}$:

$$B_0 = \frac{1}{N}\left(\sum_{i=1}^{N} \frac{\partial}{\partial g} \ln \mathbb{P}_g(X_i, T_i)\right)_{g_0} \tag{C.2}$$

$$B_1 = \frac{1}{N}\left(\sum_{i=1}^{N} \frac{\partial^2}{\partial g^2} \ln \mathbb{P}_g(X_i, T_i)\right)_{g_0} \tag{C.3}$$

$$||B_2||_\infty < \infty. \tag{C.4}$$

The expectations of B_0 and B_1 are known:

$$\mathbb{E}(B_0) = \frac{1}{N}\sum_{i=1}^{N} \mathbb{E}\left(\frac{\partial}{\partial g} \ln \mathbb{P}_g(X_i, T_i)\right) = 0 \tag{C.5}$$

$$\mathbb{E}(B_1) = \frac{1}{N}\sum_{i=1}^{N} \mathbb{E}\left(\frac{\partial^2}{\partial g^2} \ln \mathbb{P}_g(X_i, T_i)\right) = -\mathcal{I}(g) \tag{C.6}$$

$$\tag{C.7}$$

We evaluate now (C.1) for the estimator $\hat{g}$, that satisfies by definition:

$$\frac{1}{N}\left(\frac{\partial}{\partial g} \ln \mathbb{L}_{\mathcal{D}}(g)\right)_{\hat{g}} = 0. \tag{C.8}$$

From this equality, we can prove that $\hat{g}$ is an unbiased estimator:

$$\hat{g} \underset{N\to\infty}{\to} g_0. \tag{C.9}$$

We then rewrite the Taylor expansion (C.1) as:

$$\sqrt{N\mathcal{I}(g)}(\hat{g}-g_0) = \frac{1/\sqrt{N\mathcal{I}(g)} \cdot \sum_{i=1}^{N} \frac{\partial}{\partial g} \ln \mathbb{P}_g(X_i, T_i)}{-B_1/\mathcal{I}(g) - \frac{1}{2} B_2(\hat{g}-g_0)/\mathcal{I}(g)} \tag{C.10}$$

The upper term of the ratio (C.10) converges in probability:

$$\frac{1}{\sqrt{N\mathcal{I}(g)}} \sum_{i=1}^{N} \frac{\partial}{\partial g} \ln \mathbb{P}_g(X_i, T_i) \underset{N\to\infty}{\to} \mathcal{N}(0,1). \tag{C.11}$$

The lower term of (C.10) obeys:

$$-\frac{B_1}{\mathcal{I}(g)} \underset{N\to\infty}{\to} 1 \tag{C.12}$$

by the law of large numbers, and

$$-\frac{1}{2\mathcal{I}(g)} B_2(\hat{g}-g_0) \underset{N\to\infty}{\to} 0 \tag{C.13}$$

because $\hat{g}$ is an unbiased estimator (C.9). The expression (C.10) finally leads to the convergence in probability:

$$\hat{g} \underset{N\to\infty}{\to} \mathcal{N}\left(g_0, \Sigma_g^{\mathcal{F}}\right). \tag{C.14}$$

□

D Asymptotic behavior of $\overline{\delta V^2}/\overline{V}^2$ at large distance

We derive explicitly the asymptotic behavior of $\overline{\delta V}^2(z)/\overline{V}^2(z)$ in the retarded regime $z \gg \lambda_A$ at zero temperature (or at finite temperature in such a way that $z \ll \lambda_T$).

D.1 Average Casimir-Polder potential in the retarded regime

We start by retrieving the asymptotic behavior of the average Casimir-Polder potential in the retarded regime. The mean potential is given by:

$$\overline{V}(z) = \frac{\hbar}{c^2} \int_0^\infty \frac{d\xi}{2\pi} \xi^2 \alpha(i\xi) \int \frac{d^2\mathbf{q}}{(2\pi)^2} \frac{e^{-2\kappa_z z}}{2\kappa_z} \sum_{p=\mathrm{TE,TM}} \overline{r}_p(i\xi)\, \boldsymbol{\epsilon}_p^+(\boldsymbol{q}) \cdot \boldsymbol{\epsilon}_p^-(\boldsymbol{q}) \tag{D.1}$$

with

$$\boldsymbol{\epsilon}_p^+(\boldsymbol{q}) \cdot \boldsymbol{\epsilon}_p^-(\boldsymbol{q}) = \begin{cases} 1 & \text{for } p = \mathrm{TE} \\ -\frac{\xi^2+2c^2\mathbf{q}^2}{\xi^2} & \text{for } p = \mathrm{TM} \end{cases}. \tag{D.2}$$

In order to find the asymptotic regime and to take out of the integral the z dependance, we apply the following change of variable:

$$\mathbf{Q} = \mathbf{q}z, \quad x = \frac{\xi z}{c}. \tag{D.3}$$

Using this notation, the wavevector κ_z and $\tilde{\kappa}_z$ are transformed:

$$\kappa_z = \frac{\sqrt{\mathbf{Q}^2 + x^2}}{z} \equiv \frac{K}{z}, \tag{D.4}$$

$$\tilde{\kappa}_z = \frac{\sqrt{\mathbf{Q}^2 + \epsilon(ixc/z)x^2}}{z} \equiv \frac{\tilde{K}_z}{z}. \tag{D.5}$$

The dielectric function ϵ becomes:

$$\epsilon(ixc/z) = 1 + \frac{\omega_p^2 z}{xc(\gamma + xc/z)}. \tag{D.6}$$

At large distances, we also find the following behaviors:

$$\epsilon(ixc/z) \simeq \frac{\omega_p^2 z}{\gamma xc}, \tag{D.7}$$

$$\tilde{K}_z \simeq \omega_p \sqrt{\frac{x}{\gamma cz}}. \tag{D.8}$$

The polarizability of the antihydrogen atom can be approximated by its static polarizability $\alpha(0)$.

We are now able to compute the asymptotical behavior of the average Casimir-Polder potential:

$$\begin{aligned}
\overline{V}(z) &\simeq -\frac{\alpha(0)\hbar c}{z^4}\int_0^\infty \frac{dx}{2\pi}\int \frac{d^2\mathbf{Q}}{(2\pi)^2}\frac{e^{-2\sqrt{x^2+\mathbf{Q}^2}}}{2\sqrt{x^2+\mathbf{Q}^2}}\left(2x^2 + 2\mathbf{Q}^2\right) \\
&\simeq -\frac{\alpha(0)\hbar c}{z^4}\int_0^\infty \frac{dx}{2\pi}\int_x^\infty \frac{2\pi K dK}{(2\pi)^2}\frac{e^{-2K}}{K}K^2 \\
&\simeq -\frac{\alpha(0)\hbar c}{(2\pi)^2 z^4}\int_0^\infty dx \int_x^\infty dK K^2 e^{-2K} \\
&\simeq -\frac{3\alpha(0)\hbar c}{32\pi^2 z^4}.
\end{aligned} \tag{D.9}$$

While the intermediate calculations depend on the dissipation rate γ, it is interested to notice that the asymptotical behavior of the Casimir-Polder potential does *not* depend on γ. It means that at large distance, the atom does not "see" the details of the metal, the Drude or the plasma model lead in particular to the same expression (D.9).

D.2 Asymptotical behavior of the Casimir-Polder fluctuations

Let us now look at the fluctuations of the Casimir-Polder potential. The general expression of the fluctuations is written:

$$\begin{aligned}\overline{\delta V^2}(z) = \frac{\hbar^2}{c^4}\int_0^\infty \frac{d\xi_1}{2\pi}\frac{d\xi_2}{2\pi}\xi_1^2\xi_2^2\alpha(i\xi_1)\alpha(i\xi_2)\prod_{i=a,b,c,d}\int\frac{d^2\boldsymbol{q}_i}{(2\pi)^2} \\ \times\sum_{a,b,c,d}\overline{\delta r_{ab}(i\xi_1)\delta r_{cd}(i\xi_2)}\frac{e^{-(\kappa_z^a+\kappa_z^b+\kappa_z^c+\kappa_z^d)z}}{4\kappa_z^a\kappa_z^c}\boldsymbol{\epsilon}_a^+(\boldsymbol{q}_a)\cdot\boldsymbol{\epsilon}_b^-(\boldsymbol{q}_b)\,\boldsymbol{\epsilon}_c^+(\boldsymbol{q}_c)\cdot\boldsymbol{\epsilon}_d^-(\boldsymbol{q}_d).\end{aligned} \tag{D.10}$$

with scalar products $\boldsymbol{\epsilon}_a^+(\boldsymbol{q}_a)\cdot\boldsymbol{\epsilon}_b^-(\boldsymbol{q}_b)$ and $\boldsymbol{\epsilon}_c^+(\boldsymbol{q}_c)\cdot\boldsymbol{\epsilon}_d^-(\boldsymbol{q}_d)$ summarized in table IV.1. The correlator $\overline{\delta r_{ab}(i\xi_1)\delta r_{cd}(i\xi_2)}$ is given by:

$$\begin{aligned}\overline{\delta r_{ab}(i\xi_1)\delta r_{cd}(i\xi_2)} =& \frac{\pi\lambda_F^2 l\omega_p^4}{2c^4\gamma^2}\frac{\xi_1\xi_2}{(1+\xi_1/\gamma)^2(1+\xi_2/\gamma)^2}\frac{\kappa_z^a\kappa_z^c}{\tilde{\kappa}_z^a\tilde{\kappa}_z^c\tilde{\kappa}_z^b\tilde{\kappa}_z^d(\tilde{\kappa}_z^a+\tilde{\kappa}_z^b+\tilde{\kappa}_z^c+\tilde{\kappa}_z^d)} \\ &\times\bar{t}_a^{1\to2}\bar{t}_c^{1\to2}\bar{t}_b^{2\to1}\bar{t}_d^{2\to1}\prod_{i=a,b,c,d}(1+\bar{r}_i^{2\to2})\,\delta(\boldsymbol{q}_a-\boldsymbol{q}_b-\boldsymbol{q}_c+\boldsymbol{q}_d),\end{aligned} \tag{D.11}$$

By inserting (D.11) into (D.13), we obtain:

$$\begin{aligned}\overline{\delta V^2}(z) =& \frac{\hbar^2\pi\lambda_F^2 l\omega_p^4}{8c^8\gamma^2}\int_0^\infty\frac{d\xi_1}{2\pi}\frac{d\xi_2}{2\pi}\frac{\xi_1^3\xi_2^3\alpha(i\xi_1)\alpha(i\xi_2)}{(1+\xi_1/\gamma)^2(1+\xi_2/\gamma)^2}\prod_{i=a,b,d}\int\frac{d^2\boldsymbol{q}_i}{(2\pi)^2} \\ &\times\sum_{a,b,c,d}\frac{e^{-(\kappa_z^a+\kappa_z^b+\kappa_z^c+\kappa_z^d)z}}{\tilde{\kappa}_z^a\tilde{\kappa}_z^c\tilde{\kappa}_z^b\tilde{\kappa}_z^d(\tilde{\kappa}_z^a+\tilde{\kappa}_z^b+\tilde{\kappa}_z^c+\tilde{\kappa}_z^d)}\bar{t}_a^{1\to2}\bar{t}_c^{1\to2}\bar{t}_b^{2\to1}\bar{t}_d^{2\to1} \\ &\times\prod_{i=a,b,c,d}(1+\bar{r}_i^{2\to2})\boldsymbol{\epsilon}_a^+(\boldsymbol{q}_a)\cdot\boldsymbol{\epsilon}_b^-(\boldsymbol{q}_b)\,\boldsymbol{\epsilon}_c^+(\boldsymbol{q}_c)\cdot\boldsymbol{\epsilon}_d^-(\boldsymbol{q}_d).\end{aligned} \tag{D.12}$$

with $\boldsymbol{q}_c = \boldsymbol{q}_a - \boldsymbol{q}_b + \boldsymbol{q}_d$ due to momentum conservation.

We then apply the change of variable (D.3) in (D.12):

$$\begin{aligned}\overline{\delta V^2}(z) =& \frac{\hbar^2\pi\lambda_F^2 l\omega_p^4}{8\gamma^2}\cdot\frac{1}{z^{14}}\int_0^\infty\frac{dx_1}{2\pi}\frac{dx_2}{2\pi}\frac{x_1^3x_2^3\alpha(ix_1c/z)\alpha(ix_2c/z)}{(1+x_1c/\gamma z)^2(1+x_2c/\gamma z)^2}\prod_{i=a,b,d}\int\frac{d^2\mathbf{Q}_i}{(2\pi)^2} \\ &\times\sum_{a,b,c,d}\frac{e^{-(K^a+K^b+K^c+K^d)}}{\tilde{\kappa}_z^a\tilde{\kappa}_z^c\tilde{\kappa}_z^b\tilde{\kappa}_z^d(\tilde{\kappa}_z^a+\tilde{\kappa}_z^b+\tilde{\kappa}_z^c+\tilde{\kappa}_z^d)}\bar{t}_a^{1\to2}\bar{t}_c^{1\to2}\bar{t}_b^{2\to1}\bar{t}_d^{2\to1} \\ &\times\prod_{i=a,b,c,d}(1+\bar{r}_i^{2\to2})\boldsymbol{\epsilon}_a^+(\boldsymbol{q}_a)\cdot\boldsymbol{\epsilon}_b^-(\boldsymbol{q}_b)\,\boldsymbol{\epsilon}_c^+(\boldsymbol{q}_c)\cdot\boldsymbol{\epsilon}_d^-(\boldsymbol{q}_d).\end{aligned} \tag{D.13}$$

We use now some approximations in the frame of the Drude model. We let the interested reader to apply the same gait to find the asymptotical behavior in the case of plasma model. First, at large distance, the polarizability can be approximated by the static polarizability $\alpha(0)$. Then the wavevectors $\tilde{\kappa}_z$ are replaced by their equivalent (D.8). We also show that the leading contribution in the sum over all polarizations is obtained for the TE mode:

$$\bar{t}_a^{1\to2}\bar{t}_c^{1\to2}\bar{t}_b^{2\to1}\bar{t}_d^{2\to1}\prod_{i=a,b,c,d}(1+\bar{r}_i^{2\to2}) \simeq 4\left(2\sqrt{\frac{\gamma x_1 c}{\omega_p^2 z}}\right)\left(2\sqrt{\frac{\gamma x_2 c}{\omega_p^2 z}}\right) \tag{D.14}$$

$$\simeq 16\frac{\gamma\sqrt{x_1 x_2}c}{\omega_p^2 z}. \tag{D.15}$$

Thus, fluctuations expression becomes:

$$\begin{aligned}\overline{\delta V^2}(z) \simeq & \frac{\hbar^2\pi\lambda_F^2 l\omega_p^4\alpha(0)^2}{8\gamma^2}\cdot\frac{1}{z^{14}}\int_0^\infty\frac{dx_1}{2\pi}\frac{dx_2}{2\pi}x_1^3x_2^3\prod_{i=a,b,d}\int\frac{d^2\mathbf{Q}_i}{(2\pi)^2}\\ &\times\frac{(\gamma cz)^{5/2}e^{-(K^a+K^b+K^c+K^d)}}{\omega_p^5x_1^2x_2^2(2\sqrt{x_1}+2\sqrt{x_2})}\cdot 16\frac{\gamma\sqrt{x_1x_2}c}{\omega_p^2 z}\\ &\times\boldsymbol{\epsilon}_{TE}^{+}(\boldsymbol{q}_a)\cdot\boldsymbol{\epsilon}_{TE}^{-}(\boldsymbol{q}_b)\,\boldsymbol{\epsilon}_{TE}^{+}(\boldsymbol{q}_c)\cdot\boldsymbol{\epsilon}_{TE}^{-}(\boldsymbol{q}_d).\end{aligned} \tag{D.16}$$

By rearranging terms, we find:

$$\begin{aligned}\overline{\delta V^2}(z) \simeq & \frac{16\hbar^2\pi\lambda_F^2 l\alpha(0)^2\gamma^{3/2}c^{7/2}}{\omega_p^3}\cdot\frac{\sqrt{z}}{z^{13}}\int_0^\infty\frac{dx_1}{2\pi}\frac{dx_2}{2\pi}\frac{x_1^{3/2}x_2^{3/2}}{\sqrt{x_1}+\sqrt{x_2}}\prod_{i=a,b,d}\int\frac{d^2\mathbf{Q}_i}{(2\pi)^2}\\ &\times e^{-(K^a+K^b+K^c+K^d)}\cdot\boldsymbol{\epsilon}_{TE}^{+}(\boldsymbol{q}_a)\cdot\boldsymbol{\epsilon}_{TE}^{-}(\boldsymbol{q}_b)\,\boldsymbol{\epsilon}_{TE}^{+}(\boldsymbol{q}_c)\cdot\boldsymbol{\epsilon}_{TE}^{-}(\boldsymbol{q}_d).\end{aligned} \tag{D.17}$$

The integrals are now just a number denoted c_2:

$$\begin{aligned}c_2 \equiv & \frac{32}{9}\cdot(2\pi)^{3/2}\int_0^\infty\frac{dx_1}{2\pi}\frac{dx_2}{2\pi}\frac{x_1^{3/2}x_2^{3/2}}{\sqrt{x_1}+\sqrt{x_2}}\prod_{i=a,b,d}\int\frac{d^2\mathbf{Q}_i}{(2\pi)^2}\\ &\times e^{-(K^a+K^b+K^c+K^d)}\cdot\boldsymbol{\epsilon}_{TE}^{+}(\boldsymbol{q}_a)\cdot\boldsymbol{\epsilon}_{TE}^{-}(\boldsymbol{q}_b)\,\boldsymbol{\epsilon}_{TE}^{+}(\boldsymbol{q}_c)\cdot\boldsymbol{\epsilon}_{TE}^{-}(\boldsymbol{q}_d).\end{aligned} \tag{D.18}$$

D.3 Derivation of the ratio $\overline{\delta V^2}/\overline{V}^2$

The last step consists in taking the ratio of $\overline{\delta V^2}$ (D.17) by the square of $\overline{V}$ (D.9):

$$\frac{\overline{\delta V^2}(z)}{\overline{V}^2(z)} \simeq \frac{32\pi^5\lambda_F^2 l\gamma^{3/2}c^{3/2}}{(2\pi)^{3/2}\omega_p^3}\cdot c_2\cdot\frac{1}{z^{9/2}} \tag{D.19}$$

Finally, we express the previous expression in terms of characteristic lengths

$$\lambda_F=\frac{2\pi}{k_F},\qquad \lambda_\gamma=\frac{2\pi c}{\gamma},\qquad \lambda_p=\frac{2\pi c}{\omega_p} \tag{D.20}$$

to obtain:

$$\frac{\overline{\delta V^2}(z)}{\overline{V}^2(z)} \simeq \frac{(2\pi\lambda_F)^2 l}{\lambda_\gamma^2\lambda_p}\cdot c_2\cdot\left(\frac{\lambda_p}{\lambda_\gamma}\right)^4\cdot\left(\frac{\lambda_\gamma}{z}\right)^{9/2}. \tag{D.21}$$

Index of notations

General

- $\mathbf{r}$, $\boldsymbol{q}$ and other bold letters represent vectors exept for $\mathbf{G}$, the Green tensor of rank 2, and $\mathbf{z}$, a Liouville coordinate.
- The Schwarzian derivative $\{\hat{z}, z\}$ is defined by

$$\{\hat{z}, z\} = \frac{\hat{z}'''(z)}{\hat{z}'(z)} - \frac{3}{2}\left(\frac{\hat{z}''(z)}{\hat{z}'(z)}\right)^2.$$

- The Wronskian of two functions $\psi_1(z)$ and $\psi_2(z)$ is

$$\mathcal{W}(\psi_1, \psi_2) = \psi_1(z)\psi_2'(z) - \psi_1'(z)\psi_2(z).$$

- Stars and daggers denote complex and hermitian conjugation, respectively.

Constants

Constants are given in the new SI [214]:

Plank constant	$h = 6.62607015 \cdot 10^{-34}$ J.s
Reduced Plank constant	$\hbar \approx 1.05457182 \cdot 10^{-34}$ J.s
Speed of light	$c = 2.99792458 \cdot 10^{8}$ m.s^{-1}
Boltzmann constant	$k_B = 1.380649 \cdot 10^{-23}$ J.K^{-1}

Units

Atomic units (a.u.) are well adapted to express most physical quantities at the atomic range. In atomic units, $\hbar = 1$ and the other units are:

Length	$\mathrm{a_0} \approx 5.29177 \cdot 10^{-11}$ m (Bohr radius)
Energy	$\mathrm{E_h} \approx 4.35974 \cdot 10^{-18}$ J (Hartree)
Momentum	$\mathrm{p_{au}} \approx 1,05457 \cdot 10^{-34}$ J.s
Time	$\mathrm{t_{au}} \approx 2.41888 \cdot 10^{-18}$ s

Quantum effects in a gravitational field involve the following scales:

- Gravity field on Earth: $g \simeq 9.81$ m.s^{-2}
- Length $\quad \ell_g = \left(\frac{\hbar^2}{2m^2 g}\right)^{1/3} \approx 5.87 \cdot 10^{-6}$ m
- Energy $\quad \epsilon_g = \left(\frac{\hbar^2 m g^2}{2}\right)^{1/3} \approx 9.64 \cdot 10^{-32}$ J $\approx 6.02 \cdot 10^{-4}$ neV
- Momentum $\quad p_g = (2\hbar m^2 g)^{1/3} \approx 1.80 \cdot 10^{-29}$ kg.m.s^{-1}
- Time $\quad t_g = \left(\frac{2\hbar}{m g^2}\right)^{1/3} \approx 1.09 \cdot 10^{-3}$ s

Special functions

We follow the definitions and notations of the NIST Handbook of Mathematical Functions [125]:

$\mathrm{Ai}(x)$, $\mathrm{Bi}(x)$	Airy functions
$Ai(-\lambda_n) = 0$	zeros of the Airy function
$J_n(x)$	Bessel function
${}_2F_1(a, b, c; x)$	Gauss hypergeometric function
$\tilde{\psi}^{\pm}(\tilde{z})$	Mathieu functions
τ	Mathieu characteristic exponent

Gravitation and GBAR experiment

- m inertial mass of antihydrogen atom
- M gravitational mass of antihydrogen atom
- g gravity field on Earth
- $\overline{g} = Mg/m$
- For all numerical applications, we suppose $\overline{g} = g$, in such a way that $M = m \approx 1.67353 \cdot 10^{-27}$ kg
- ω trap frequency
- ζ dispersion of positions
- T fall time

- H fall height
- $T_H = \sqrt{2H/g}$
- $v_H = \sqrt{2gH}$

Electromagnetism

- ω angular frequency
- $\xi = -i\omega$ angular frequency after a Wick rotation
- $\mathbf{k} = \boldsymbol{q} + k_z \mathbf{e}_z$ wave vector decomposed in transverse and longitudinal mode
- $\kappa_z = -ik_z$
- $\alpha(\omega)$ dynamic polarizability
- λ_A first atomic transition of the (anti)hydrogen atom
- $\varepsilon(\omega)$ dynamic relative permittivity of a medium
- $\sigma(\omega)$ effective dynamic conductivity of the metal
- ω_p plasma frequency
- λ_p plasma wavelength
- λ_F Fermi wavelength
- v_F Fermi velocity
- l mean free path
- γ relaxation rate
- λ_γ associated wavelength

Casimir interaction

- homogeneous potentials $V(z) = -\dfrac{C_n}{z^n}$
- $\ell_n = \left(\frac{2mC_n}{\hbar^2}\right)^{\frac{1}{n-2}}$

Schrödinger equation

- $\Psi_t(x,z) = \phi_t(x)\psi_t(z)$ time-dependent wavefunction
- $\tilde{\psi}_t(p_z),\ \tilde{\phi}_t(p_x)$ wavefunctions in momentum space
- $F(z) = \dfrac{\hbar^2}{2m}\,(E - V(z))$
- De Broglie wavevector $k_{\mathrm{dB}}(z) = \sqrt{F(z)}$
- De Broglie wavelength $\lambda_{\mathrm{dB}}(z) = \dfrac{2\pi}{k_{\mathrm{dB}}(z)}$
- WKB phase $\phi_{\mathrm{dB}} = \int^z k_{\mathrm{dB}}(z)\mathrm{d}z$
- $Q(z)$ WKB badlands function
- $\boldsymbol{z},\ \tilde{z}$ are one-dimensional transformed coordinates in Liouville transformation
- $J(x,z,t)$ probability density current
- $W_t(x,z,p_x,p_z)$ Wigner function

Scattering

- $\mathcal{S} = \begin{pmatrix} \bar{t} & r \\ \bar{r} & t \end{pmatrix}$ scattering matrix
- $\mathcal{T}$ transfer matrix
- Π involution transforming $\mathcal{S}$ to $\mathcal{T}$ and conversely
- $\star$ composition law for S matrices
- $a = -i\ell$ scattering length
- $b = -\operatorname{Im}(a)$
- $a_\pm$ wave amplitudes

Statistics

- $\mathbb{P}$ probability density
- $\mathbb{E}$ expected value
- $\mathcal{I}$ Fisher information
- $\mathfrak{E}$ statistical efficiency

- $\mathbb{L}$ likelihood function
- $\hat{\sigma}$ estimator of the standard deviation – more generally quantities with a hat are estimators

List of publications

Articles in peer-reviewed journals

- N. Cherroret, P.-P. Crepin, R. Guerout, A. Lambrecht, and S. Reynaud, “Casimir-Polder force fluctuations as spatial probes of dissipation in metals”, EPL (Europhysics Letters) **117**, 63001 (2017)
- P.-P. Crépin, G. Dufour, R. Guérout, A. Lambrecht, and S. Reynaud, “Casimir-Polder shifts on quantum levitation states”, Physical Review A **95**, 032501 (2017)
- P.-P. Crépin, E. Kupriyanova, R. Guérout, A. Lambrecht, V. Nesvizhevsky, S. Reynaud, S. Vasilyev, and A. Voronin, “Quantum reflection of antihydrogen from a liquid helium film”, EPL (Europhysics Letters) **119**, 33001 (2017)
- P.-P. Crépin, C. Christen, R. Guérout, V. Nesvizhevsky, A. Voronin, and S. Reynaud, “Quantum interference test of the equivalence principle on antihydrogen”, Physical Review A (2019)
- P.-P. Crépin, R. Guérout, and S. Reynaud, “Improved Effective Range Expansion for Casimir-Polder potential”, submitted to European Physical Journal D (2019)

Articles in peer-reviewed conference proceedings

- P.-P. Crépin, G. Dufour, R. Guérout, A. Lambrecht, and S. Reynaud, “Casimir-Polder shifts on quantum levitation states”, Gravitation, E. Augé, J. Dumarchez, J. Trân Thanh Vân, ed. ARISF, 179-184 (2017)
- V. Nesvizhevsky, A. Voronin, P.-P. Crépin, and S. Reynaud, “Interference of several gravitational quantum states of antihydrogen in GBAR experiment”, Hyperfine Interactions **240** (2019)
- P.-P. Crepin, E. A. Kupriyanova, R. Guerout, A. Lambrecht, V. V. Nesvizhevsky, S. Reynaud, S. Vasiliev, and A. Y. Voronin, “Quantum reflection of antihydrogen from a liquid helium bulk”, Hyperfine Interactions **240** (2019)

Bibliography

[1] P. A. M. Dirac, "The quantum theory of the electron", Proceedings of the Royal Society of London A: Mathematical, Physical and Engineering Sciences **117**, 610 (1928) (cited on p. 1).

[2] C. D. Anderson, "The apparent existence of easily deflectable positives", Science **76**, 238 (1932) (cited on p. 1).

[3] H. Bondi, "Negative mass in General Relativity", Reviews of Modern Physics **29**, 423 (1957) (cited on p. 1).

[4] J. Scherk, "Antigravity: A crazy idea?", Physics Letters B **88**, 265 (1979) (cited on pp. 1, 3).

[5] M. M. Nieto, and T. Goldman, "The arguments against "antigravity" and the gravitational acceleration of antimatter", Physics Reports **205**, 221 (1991) (cited on pp. 1, 3).

[6] G. Chardin, and G. Manfredi, "Gravity, antimatter and the Dirac-Milne universe", Hyperfine Interactions **239**, 45 (2018) (cited on p. 1).

[7] E. G. Adelberger, B. R. Heckel, C. W. Stubbs, and Y. Su, "Does antimatter fall with the same acceleration as ordinary matter?", Physical Review Letters **66**, 850 (1991) (cited on pp. 1, 3).

[8] T. W. Darling, F. Rossi, G. I. Opat, and G. F. Moorhead, "The fall of charged particles under gravity: a study of experimental problems", Reviews of Modern Physics **64**, 237 (1992) (cited on p. 1).

[9] The ALPHA Collaboration, and A. E. Charman, "Description and first application of a new technique to measure the gravitational mass of antihydrogen", Nature Communications **4**, 1785 (2013) (cited on pp. 1, 70).

[10] A. Kellerbauer, et al., "Proposed antimatter gravity measurement with an antihydrogen beam", Nuclear Instruments and Methods in Physics Research B **266**, 351 (2008) (cited on pp. 1, 70).

[11] P. Indelicato, et al., "The GBAR project, or how does antimatter fall?", Hyperfine Interactions **228**, 141 (2014) (cited on pp. 1, 38, 70, 71, 88, 92).

[12] W. A. Bertsche, "Prospects for comparison of matter and antimatter gravitation with ALPHA-g", Philosophical Transactions of the Royal Society of London A **376**, 0265 (2018) (cited on pp. 1, 70).

[13] J. Walz, and T. W. Hänsch, "A proposal to measure antimatter gravity using ultracold antihydrogen atoms", General Relativity and Gravitation **36**, 561 (2004) (cited on pp. 1, 3).

[14] P. Pérez, et al., "The GBAR antimatter gravity experiment", Hyperfine Interactions **233**, 21 (2015) (cited on pp. 1, 38, 70, 71, 88, 92, 95).

[15] B. Mansoulié, and on behalf of the GBAR Collaboration, "Status of the GBAR experiment at CERN", Hyperfine Interactions **240**, 11 (2019) (cited on p. 1).

[16] H. B. G. Casimir, "On the attraction between two perfectly conducting plates", Proc. K. Ned. Akad. Wet **51**, 793 (1948) (cited on p. 2).

[17] L. M. Woods, D. A. R. Dalvit, A. Tkatchenko, P. Rodriguez-Lopez, A. W. Rodriguez, and R. Podgornik, "Materials perspective on Casimir and van der Waals interactions", Reviews of Modern Physics **88** (2016) (cited on p. 2).

[18] V. A. Parsegian, Van der waals forces (Cambridge University Press, 2005) (cited on p. 2).

[19] K. A. Milton, "Resource Letter VWCPF-1: van der Waals and Casimir–Polder forces", American Journal of Physics **79**, 697 (2011) (cited on p. 2).

[20] J. E. Lennard-Jones, and A. F. Devonshire, "The interaction of atoms and molecules with solid surfaces. III. The Condensation and Evaporation of Atoms and Molecules", Proceedings of the Royal Society of London. Series A **156**, 6 (1936) (cited on pp. 2, 7).

[21] J. E. Lennard-Jones, and A. F. Devonshire, "The interaction of atoms and molecules with solid surfaces. IV. The condensation and evaporation of atoms and molecules", Proceedings of the Royal Society of London. Series A **156**, 29 (1936) (cited on pp. 2, 7).

[22] M. V. Berry, and K. E. Mount, "Semiclassical approximations in wave mechanics", Reports on Progress in Physics **35**, 315 (1972) (cited on pp. 2, 7, 10, 11, 70).

[23] I. A. Yu, J. M. Doyle, J. C. Sandberg, C. L. Cesar, D. Kleppner, and T. J. Greytak, "Evidence for universal quantum reflection of hydrogen from liquid He-4", Physical Review Letters **71**, 1589 (1993) (cited on pp. 2, 4, 7, 70).

[24] J. J. Berkhout, and J. T. M. Walraven, "Scattering of hydrogen atoms from liquid-helium surfaces", Physical Review B **47**, 8886 (1993) (cited on pp. 2, 26, 70).

[25] C. Carraro, and M. W. Cole, "Sticking coefficient at ultralow energy : Quantum reflection", Progress in Surface Science **57**, 61 (1998) (cited on pp. 2, 70).

[26] F. Shimizu, "Specular reflection of very slow metastable neon atoms from a solid surface", Physical Review Letters **86**, 987 (2001) (cited on pp. 2, 4, 7, 70).

[27] V. Druzhinina, and M. DeKieviet, "Experimental observation of quantum reflection far from threshold", Physical Review Letters **91**, 193202 (2003) (cited on pp. 2, 4, 7, 123).

[28] T. A. Pasquini, Y. Shin, C. Sanner, M. Saba, A. Schirotzek, D. E. Pritchard, and W. Ketterle, "Quantum reflection from a solid surface at normal incidence", Physical Review Letters **93**, 223201 (2004) (cited on pp. 2, 4, 7, 70).

[29] H. Friedrich, and J. Trost, "Working with WKB waves far from the semiclassical limit", Physics Reports **397**, 359 (2004) (cited on pp. 2, 11, 70).

[30] H. Oberst, Y. Tashiro, K. Shimizu, and F. Shimizu, "Quantum reflection of He-* on silicon", English, Physical Review A **71** (2005) (cited on pp. 2, 123).

[31] T. A. Pasquini, M. Saba, G.-B. Jo, Y. Shin, W. Ketterle, D. E. Pritchard, T. A. Savas, and N. Mulders, "Low velocity quantum reflection of Bose-Einstein condensates", Physical Review Letters **97**, 093201 (2006) (cited on pp. 2, 4, 7).

[32] B. S. Zhao, S. A. Schulz, S. A. Meek, G. Meijer, and W. Schöllkopf, "Quantum reflection of helium atom beams from a microstructured grating", Physical Review A **78**, 010902 (2008) (cited on pp. 2, 4).

[33] A. Y. Voronin, and P. Froelich, "Quantum reflection of ultracold antihydrogen from a solid surface", Journal of Physics B: Atomic, Molecular and Optical Physics **38**, L301 (2005) (cited on pp. 2, 38, 43, 64).

[34] P. Froelich, and A. Y. Voronin, "Interaction of antihydrogen with ordinary atoms and solid surfaces", Hyperfine Interactions **213**, 115 (2012) (cited on p. 2).

[35] G. Dufour, A. Gérardin, R. Guérout, A. Lambrecht, V. V. Nesvizhevsky, S. Reynaud, and A. Y. Voronin, "Quantum reflection of antihydrogen from the Casimir potential above matter slabs", Physical Review A **87**, 012901 (2013) (cited on p. 2).

[36] G. Dufour, "Quantum reflection from the Casimir-Polder potential", PhD thesis (Université Pierre et Marie Curie, 2015) (cited on pp. 2, 3, 9, 10, 14, 21, 42, 47, 73, 74, 80, 127).

[37] A. Jurisch, and H. Friedrich, "Realistic model for a quantum reflection trap", Physics Letters A **349**, 230 (2006) (cited on pp. 2, 5, 7, 37).

[38] J. Madroñero, and H. Friedrich, "Influence of realistic atom wall potentials in quantum reflection traps", Physical Review A **75**, 022902 (2007) (cited on pp. 2, 5, 7, 37).

[39] P.-P. Crépin, E. Kupriyanova, R. Guérout, A. Lambrecht, V. Nesvizhevsky, S. Reynaud, S. Vasilyev, and A. Voronin, "Quantum reflection of antihydrogen from a liquid helium film", EPL (Europhysics Letters) **119**, 33001 (2017) (cited on pp. 2, 16, 28, 30, 71, 93, 139).

[40] T. A. Wagner, S. Schlamminger, J. H. Gundlach, and E. G. Adelberger, "Torsion-balance tests of the weak equivalence principle", Classical and Quantum Gravity **29**, 184002 (2012) (cited on pp. 2, 80).

[41] S. Fray, C. A. Diez, T. W. Hänsch, and M. Weitz, “Atomic interferometer with amplitude gratings of light and its applications to atom based tests of the Equivalence Principle”, Physical Review Letters **93**, 240404 (2004) (cited on p. 2).

[42] D. Schlippert, J. Hartwig, H. Albers, L. L. Richardson, C. Schubert, A. Roura, W. P. Schleich, W. Ertmer, and E. M. Rasel, “Quantum test of the universality of free fall”, Physical Review Letters **112**, 203002 (2014) (cited on p. 2).

[43] P. Touboul, et al., “Microscope mission: first results of a space test of the equivalence principle”, English, Physical Review Letters **119** (2017) (cited on p. 2).

[44] G. Chardin, “Motivations for antigravity in General Relativity”, Hyperfine Interactions **109**, 83 (1997) (cited on p. 3).

[45] M. Villata, “CPT symmetry and antimatter gravity in general relativity”, EPL (Europhysics Letters) **94**, 20001 (2011) (cited on p. 3).

[46] V. A. Kostelecký, and J. D. Tasson, “Matter-gravity couplings and Lorentz violation”, Physical Review D **83**, 016013 (2011) (cited on p. 3).

[47] A. Benoit-Lévy, and G. Chardin, “Introducing the Dirac-Milne universe”, Astronomy & Astrophysics **537**, A78 (2012) (cited on p. 3).

[48] R. J. Hughes, and M. H. Holzscheiter, “Constraints on the gravitational properties of antiprotons and positrons from cyclotron-frequency measurements”, Physical Review Letters **66**, 854 (1991) (cited on p. 3).

[49] F. C. Witteborn, and W. M. Fairbank, “Experimental comparison of the gravitational force on freely falling electrons and metallic electrons”, Physical Review Letters **19**, 1049 (1967) (cited on p. 3).

[50] G. Baur, et al., “Production of antihydrogen”, Physics Letters B **368**, 251 (1996) (cited on p. 3).

[51] M. H. Holzscheiter, M. Charlton, and M. M. Nieto, “The route to ultra-low energy antihydrogen”, Physics Reports **402**, 1 (2004) (cited on p. 3).

[52] M. Hori, and J. Walz, “Physics at CERN’s Antiproton Decelerator”, Progress in Particle and Nuclear Physics **72**, 206 (2013) (cited on p. 3).

[53] S. Maury, W. Oelert, W. Bartmann, P. Belochitskii, H. Breuker, F. Butin, C. Carli, T. Eriksson, S. Pasinelli, and G. Tranquille, “ELENA: The extra low energy anti-proton facility at CERN”, Hyperfine Interactions **229**, 105 (2014) (cited on p. 3).

[54] AEGIS Collaboration, and M. G. Giammarchi, “AEGIS at CERN: Measuring antihydrogen fall”, Few-Body Systems **54**, 779 (2012) (cited on p. 3).

[55] P. Hamilton, A. Zhmoginov, F. Robicheaux, J. Fajans, J. S. Wurtele, and H. Müller, “Antimatter interferometry for gravity measurements”, Physical Review Letters **112**, 121102 (2014) (cited on p. 3).

[56] G. Chardin, et al., “Proposal to measure the Gravitational Behaviour of Antihydrogen at Rest”, CERN-SPSC-2011-029. SPSC-P-342 (2011) (cited on p. 3).

[57] P. Pérez, and Y. Sacquin, “The GBAR experiment: gravitational behaviour of antihydrogen at rest”, Classical and Quantum Gravity **29** (2012) (cited on p. 3).

[58] P. Crivelli, U. Gendotti, A. Rubbia, L. Liszkay, P. Pérez, and C. Corbel, “Measurement of the orthopositronium confinement energy in mesoporous thin films”, Physical Review A **81**, 052703 (2010) (cited on p. 3).

[59] P. Comini, and P.-A. Hervieux, “$\bar{\mathrm{H}}^+$ ion production from collisions between antiprotons and excited positronium: cross sections calculations in the framework of the GBAR experiment”, New Journal of Physics **15**, 095022 (2013) (cited on p. 4).

[60] L. Hilico, J.-P. Karr, A. Douillet, P. Indelicato, S. Wolf, and F. S. Kaler, “Preparing single ultra-cold antihydrogen atoms for free-fall in GBAR”, International Journal of Modern Physics: Conference Series **30**, 1460269 (2014) (cited on p. 4).

[61] Y. Giomataris, P. Rebourgeard, J. P. Robert, and G. Charpak, “MICROMEGAS: a high-granularity position-sensitive gaseous detector for high particle-flux environments”, Nuclear Instruments and Methods in Physics Research Section A: Accelerators, Spectrometers, Detectors and Associated Equipment **376**, 29 (1996) (cited on p. 4).

[62] V. V. Nesvizhevsky, et al., “Quantum states of neutrons in the Earth’s gravitational field”, Nature **415**, 297 (2002) (cited on pp. 4, 7, 37, 70).

[63] V. V. Nesvizhevsky, et al., “Measurement of quantum states of neutrons in the Earth’s gravitational field”, Physical Review D **67**, 102002 (2003) (cited on pp. 4, 37, 70).

[64] V. V. Nesvizhevsky, et al., “Study of the neutron quantum states in the gravity field”, European Physical Journal C **40**, 479 (2005) (cited on pp. 4, 37, 70).

[65] M. A. Kasevich, D. S. Weiss, and S. Chu, “Normal-incidence reflection of slow atoms from an optical evanescent wave”, Optics Letters **15**, 607 (1990) (cited on pp. 4, 37).

[66] C. G. Aminoff, A. M. Steane, P. Bouyer, P. Desbiolles, J. Dalibard, and C. Cohen-Tannoudji, “Cesium atoms bouncing in a stable gravitational cavity”, Physical Review Letters **71**, 3083 (1993) (cited on pp. 4, 37).

[67] T. M. Roach, H. Abele, M. G. Boshier, H. L. Grossman, K. P. Zetie, and E. A. Hinds, “Realization of a Magnetic Mirror for Cold Atoms”, Physical Review Letters **75**, 629 (1995) (cited on pp. 4, 37).

[68] A. Landragin, J.-Y. Courtois, G. Labeyrie, N. Vansteenkiste, C. I. Westbrook, and A. Aspect, “Measurement of the van der Waals force in an atomic mirror”, Physical Review Letters **77**, 1464 (1996) (cited on pp. 4, 37).

[69] C. Henkel, C. I. Westbrook, and A. Aspect, “Quantum reflection: Atomic matter-wave optics in an attractive exponential potential”, Journal of the Optical Society of America B **B13**, 233 (1996) (cited on pp. 4, 37).

[70] A. I. Sidorov, R. J. McLean, W. J. Rowlands, D. C. Lau, J. E. Murphy, M. Walkiewicz, G. I. Opat, and P. Hannaford, “Specular reflection of cold caesium atoms from a magnetostatic mirror”, Quantum and Semiclassical Optics: Journal of the European Optical Society Part B **8**, 713 (1996) (cited on pp. 4, 37).

[71] K. Bongs, S. Burger, G. Birkl, K. Sengstock, W. Ertmer, K. Rzazewski, A. Sanpera, and M. Lewenstein, “Coherent Evolution of Bouncing Bose-Einstein Condensates”, Physical Review Letters **83**, 3577 (1999) (cited on pp. 4, 37).

[72] S. Rosenblum, O. Bechler, I. Shomroni, R. Kaner, T. Arusi-Parpar, O. Raz, and B. Dayan, “Demonstration of Fold and Cusp Catastrophes in an Atomic Cloud Reflected from an Optical Barrier in the Presence of Gravity”, Physical Review Letters **112**, 120403 (2014) (cited on pp. 4, 37).

[73] V. U. Nayak, D. O. Edwards, and N. Masuhara, “Scattering of ^{4}He Atoms Grazing the Liquid-^{4}He Surface”, Physical Review Letters **50**, 990 (1983) (cited on pp. 4, 7).

[74] J. J. Berkhout, O. J. Luiten, I. D. Setija, T. W. Hijmans, T. Mizusaki, and J. T. M. Walraven, “Quantum reflection: Focusing of hydrogen atoms with a concave mirror”, Physical Review Letters **63**, 1689 (1989) (cited on pp. 4, 7).

[75] F. Shimizu, and J.-i. Fujita, “Reflection-type hologram for atoms”, Physical Review Letters **88**, 123201 (2002) (cited on p. 4).

[76] F. Shimizu, and J.-i. Fujita, “Giant quantum reflection of neon atoms from a ridged silicon surface”, Journal of the Physical Society of Japan **71**, 5 (2002) (cited on p. 4).

[77] H. Oberst, D. Kouznetsov, K. Shimizu, J.-i. Fujita, and F. Shimizu, “Fresnel diffraction mirror for an atomic wave”, Physical Review Letters **94**, 013203 (2005) (cited on p. 4).

[78] H. Oberst, Y. Tashiro, K. Shimizu, and F. Shimizu, “Quantum reflection of He* on silicon”, Physical Review A **71**, 052901 (2005) (cited on p. 4).

[79] B. S. Zhao, H. C. Schewe, G. Meijer, and W. Schoellkopf, “Coherent reflection of He atom beams from rough surfaces at grazing incidence”, Physical Review Letters **105**, 133203 (2010) (cited on p. 4).

[80] B. S. Zhao, W. Zhang, and W. Schöllkopf, “Non-destructive quantum reflection of helium dimers and trimers from a plane ruled grating”, Molecular Physics **111**, 1772 (2013) (cited on p. 4).

[81] R. Decca, E. Fischbach, G. Klimchitskaya, D. Krause, D. Lopez, and V. Mostepanenko, “Improved tests of extra-dimensional physics and thermal quantum field theory from new Casimir force measurements”, English, Physical Review D **68** (2003) (cited on pp. 5, 108).

[82] R. Decca, D. Lopez, E. Fischbach, G. Klimchitskaya, D. Krause, and V. Mostepanenko, "Precise comparison of theory and new experiment for the Casimir force leads to stronger constraints on thermal quantum effects and long-range interactions", English, Annals of Physics **318**, 37 (2005) (cited on pp. 5, 108).

[83] R. S. Decca, D. Lopez, E. Fischbach, G. L. Klimchitskaya, D. E. Krause, and V. M. Mostepanenko, "Tests of new physics from precise measurements of the Casimir pressure between two gold-coated plates", English, Physical Review D **75** (2007) (cited on pp. 5, 108).

[84] L. Brekhovskikh, Waves in layered media, 2nd (Elsevier, 2012) (cited on p. 5).

[85] A. Y. Voronin, P. Froelich, and V. V. Nesvizhevsky, "Gravitational quantum states of Antihydrogen", Physical Review A **83**, 032903 (2011) (cited on pp. 5, 7, 38, 43, 69).

[86] A. Y. Voronin, V. V. Nesvizhevsky, G. Dufour, P. Debu, A. Lambrecht, S. Reynaud, O. D. Dalkarov, E. A. Kupriyanova, and P. Froelich, "A spectroscopy approach to measure the gravitational mass of antihydrogen", International Journal of Modern Physics: Conference Series **30**, 1460266 (2014) (cited on pp. 5, 38, 43, 69).

[87] A. Y. Voronin, V. V. Nesvizhevsky, G. Dufour, and S. Reynaud, "Quantum ballistic experiment on antihydrogen fall", Journal of Physics B-Atomic Molecular and Optical Physics **49** (2016) (cited on pp. 5, 38, 43, 69).

[88] H. Friedrich, and J. Trost, "Working with WKB waves far from the semiclassical limit", Physics Reports **397**, 359 (2004) (cited on p. 7).

[89] A. Y. Voronin, P. Froelich, and B. Zygelman, "Interaction of ultracold antihydrogen with a conducting wall", Physical Review A **72**, 062903 (2005) (cited on pp. 7, 38, 43, 64).

[90] A. Y. Voronin, V. V. Nesvizhevsky, and S. Reynaud, "Whispering-gallery states of antihydrogen near a curved surface", Physical Review A **85**, 014902 (2012) (cited on p. 7).

[91] G. Dufour, A. Gérardin, R. Guérout, A. Lambrecht, V. V. Nesvizhevsky, S. Reynaud, and A. Y. Voronin, "Quantum reflection of antihydrogen from the Casimir potential above matter slabs", Physical Review A **87**, 012901 (2013) (cited on pp. 7, 15, 25, 26, 57, 100).

[92] G. Dufour, R. Guérout, A. Lambrecht, V. V. Nesvizhevsky, S. Reynaud, and A. Y. Voronin, "Quantum reflection of antihydrogen from nanoporous media", Physical Review A **87**, 022506 (2013) (cited on pp. 7, 30).

[93] G. Dufour, P. Debu, A. Lambrecht, V. V. Nesvizhevsky, S. Reynaud, and A. Y. Voronin, "Shaping the distribution of vertical velocities of antihydrogen in GBAR", European Physical Journal C **74**, 2731 (2014) (cited on pp. 7, 71, 80, 81, 87, 93).

[94] G. Breit, "The propagation of Schrödinger waves in a uniform field of force", Physical Review **32**, 273 (1928) (cited on p. 7).

[95] E. R. Pike, “On the related-equation method of asymptotic approximation (WKB or A-A Method) I. A proposed new existence theorem”, The Quarterly Journal of Mechanics and Applied Mathematics **17**, 105 (1964) (cited on p. 9).

[96] F. Olver, Asymptotics and special functions (Taylor & Francis, 1997) (cited on pp. 9, 16).

[97] G. Wentzel, “Eine verallgemeinerung der quantenbedingungen für die zwecke der wellenmechanik”, Zeitschrift für Physik **38**, 518 (1926) (cited on pp. 9, 10, 55).

[98] H. A. Kramers, “Wellenmechanik und halbzahlige quantisierung”, Zeitschrift für Physik **39**, 828 (1926) (cited on pp. 9, 55).

[99] L. Brillouin, “Remarques sur la mécanique ondulatoire”, Journal de Physique et le Radium **7**, 353 (1926) (cited on pp. 9, 55).

[100] H. Jeffreys, “On certain approximate solutions of linear differential equations of the second order”, Proceedings of the London Mathematical Society **s2-23**, 428 (1924) (cited on p. 9).

[101] S. Reynaud, “The casimir force and the quantum theory of optical networks”, in Lectures given at the ecole doctorale de physique (2002) (cited on pp. 11, 13, 14).

[102] C. Genet, A. Lambrecht, and S. Reynaud, “Casimir force and the quantum theory of lossy optical cavities”, Physical Review A **67** (2003) (cited on p. 11).

[103] L. Landau, and E. Lifshitz, Quantum mechanics: non-relativistic theory, Course of Theoretical Physics (Elsevier Science, 1981) (cited on pp. 14, 15).

[104] E. P. Wigner, “On the behavior of cross sections near thresholds”, Physical Review **73**, 1002 (1948) (cited on p. 15).

[105] F. Dalfovo, S. Giorgini, L. P. Pitaevskii, and S. Stringari, “Theory of Bose-Einstein condensation in trapped gases”, Reviews of Modern Physics **71**, 463 (1999) (cited on p. 15).

[106] J. Weiner, V. S. Bagnato, S. Zilio, and P. S. Julienne, “Experiments and theory in cold and ultracold collisions”, Reviews of Modern Physics **71**, 1 (1999) (cited on p. 15).

[107] J. Liouville, “Second mémoire sur le développement des fonctions ou parties de fonctions en séries dont les divers termes sont assujétis à satisfaire à une même équation différentielle du second ordre, contenant un paramètre variable”, Journal de Mathématiques Pures et Appliquées **2**, 16 (1837) (cited on p. 16).

[108] S. C. Miller, and R. H. Good, “A WKB-type approximation to the Schrödinger equation”, Physical Review **91**, 174 (1953) (cited on p. 16).

[109] H. Jeffreys, “On approximate solutions of linear differential equations”, Mathematical Proceedings of the Cambridge Philosophical Society **49**, 601 (1953) (cited on p. 16).

[110] R. B. Dingle, "The method of comparison equations in the solution of linear second-order differential equations (generalized W.K.B. method)", Applied Scientific Research, Section A **5**, 345 (1956) (cited on p. 16).

[111] C. E. Hecht, and J. E. Mayer, "Extension of the WKB Equation", Physical Review **106**, 1156 (1957) (cited on p. 16).

[112] P. Pechukas, "Analysis of the Miller–Good method for approximating bound states", The Journal of Chemical Physics **54**, 3864 (1971) (cited on p. 16).

[113] M. J. Richardson, "Approximate solutions to the one-dimensional Schrödinger equation by the method of comparison equations", Physical Review A **8**, 781 (1973) (cited on p. 16).

[114] J. Giraldo, R. G. Barrera, and G. A. Estévez, "An improvement to the comparison equation method for solving the Schrödinger equation", Chemical Physics Letters **113**, 37 (1985) (cited on p. 16).

[115] F. Robicheaux, U. Fano, M. Cavagnero, and D. A. Harmin, "Generalized WKB and Milne solutions to one-dimensional wave equations", Physical Review A **35**, 3619 (1987) (cited on p. 16).

[116] R. Milson, "Liouville transformation and exactly solvable schrodinger equations", International Journal of Theoretical Physics **37**, 1735 (1998) (cited on p. 16).

[117] J. Dereziński, and M. Wrochna, "Exactly solvable Schrödinger operators", Annales Henri Poincaré **12**, 397 (2011) (cited on p. 16).

[118] G. Dufour, R. Guérout, A. Lambrecht, and S. Reynaud, "Quantum reflection and Liouville transformations from wells to walls", EPL (Europhysics Letters) **110**, 30007 (2015) (cited on pp. 16, 19).

[119] G. Dufour., R. Guérout, A. Lambrecht, and S. Reynaud, "Liouville transformations and quantum reflection", Journal of Physics B **48**, 155002 (2015) (cited on pp. 16, 18, 19, 21).

[120] P.-P. Crépin, G. Dufour, R. Guérout, A. Lambrecht, and S. Reynaud, "Casimir-Polder shifts on quantum levitation states", Physical Review A **95**, 032501 (2017) (cited on pp. 16, 29, 30, 62, 100, 139).

[121] T. F. O'Malley, L. Spruch, and L. Rosenberg, "Modification of effective-range theory in the presence of a long-range r^{-4} potential", Journal of Mathematical Physics **2**, 491 (1961) (cited on pp. 18, 44, 45).

[122] B. Gao, "Quantum-defect theory for $-1/r^4$ type interactions", Physical Review A **88**, 022701 (2013) (cited on pp. 18, 45).

[123] N. a. W. Holzwarth, "Mathieu function solutions to the radial Schrödinger equation for the $-f/r^4$ interaction", Journal of Mathematical Physics **14**, 191 (1973) (cited on p. 18).

[124] N. W. Mac Lachlan, Theory and application of Mathieu functions (At the Clarendon Press, Oxford, Royaume-Uni, 1951) (cited on p. 18).

[125] F. W. J. Olver, D. W. Lozier, R. F. Boisvert, and C. W. Clark, “NIST Handbook of Mathematical Functions”, DLMF (2010) (cited on pp. 18, 39, 40, 61, 135).

[126] A. Lambrecht, P. A. M. Neto, and S. Reynaud, “The Casimir effect within scattering theory”, New Journal of Physics **8**, 243 (2006) (cited on pp. 23, 58, 59, 64).

[127] S. Reynaud, and A. Lambrecht, “Casimir forces”, in Proceedings of the 101th Les Houches summer school on "Quantum Optics and Nanophotonics", August 2013 (2013) (cited on pp. 23, 102, 117).

[128] M. Ahmadi, et al., “Characterization of the 1S-2S transition in antihydrogen”, English, Nature **557**, 71+ (2018) (cited on p. 24).

[129] M. Ahmadi, et al., “Observation of the 1S-2P Lyman-alpha transition in antihydrogen”, Nature **561**, 211+ (2018) (cited on p. 24).

[130] A. Derevianko, S. G. Porsev, and J. F. Babb, “Electric dipole polarizabilities at imaginary frequencies for hydrogen, the alkali-metal, alkaline-earth, and noble gas atoms”, Atomic Data and Nuclear Data Tables **96**, 323 (2010) (cited on p. 24).

[131] R. Messina, D. A. R. Dalvit, P. A. Maia Neto, A. Lambrecht, and S. Reynaud, “Dispersive interactions between atoms and nonplanar surfaces”, Physical Review A **80**, 022119 (2009) (cited on p. 25).

[132] H. B. G. Casimir, and D. Polder, “Influence of retardation on the London-van der Waals forces”, Nature **158**, 787 (1946) (cited on p. 25).

[133] H. B. G. Casimir, and D. Polder, “The Influence of Retardation on the London-van der Waals Forces”, Physical Review **73**, 360 (1948) (cited on p. 25).

[134] V. V. Goldman, “Kapitza conductance between gaseous atomic hydrogen and liquid helium”, Physical Review Letters **56**, 612 (1986) (cited on pp. 26, 27).

[135] B. Castaing, and M. Papoular, “Kapitza resistance at the H/liquid He interface”, Journal de Physique Lettres **44**, 537 (1983) (cited on p. 26).

[136] Y. Kagan, G. V. Shlyapnikov, and N. A. Glukhov, “Kapitsa jump in a gas of spin-polarized atomic hydrogen”, JETP Letters **40**, 1052 (1984) (cited on p. 26).

[137] S. Vasiliev, J. Ahokas, J. Jarvinen, V. Nesvizhevsky, A. Voronin, F. Nez, and S. Reynaud, “Gravitational and matter-wave spectroscopy of atomic hydrogen at ultra-low energies”, English, Hyperfine Interactions **240** (2019) (cited on pp. 26, 123).

[138] E. S. Sabisky, and C. H. Anderson, “Verification of the Lifschitz theory of the van der Waals potential using liquid helium films”, Physical Review A **7**, 790 (1972) (cited on p. 27).

[139] H. A. Kierstead, “Dielectric constant and molar volume of saturated liquid 3He and 4He”, Journal of Low Temparature Physics **23**, 791 (1976) (cited on p. 27).

[140] K. Sakimoto, “Systematics of shape resonances in reactive collisions”, Phys. Rev. A **94**, 042701 (2016) (cited on p. 36).

[141] P. Debu, "GBAR", Hyperfine Interactions **212**, 51 (2012) (cited on pp. 38, 71).

[142] G. Dufour, D. B. Cassidy, P. Crivelli, P. Debu, A. Lambrecht, V. V. Nesvizhevsky, S. Reynaud, A. Y. Voronin, and T. E. Wall, "Prospects for Studies of the Free Fall and Gravitational Quantum States of Antimatter", Advances in High Energy Physics (2015) (cited on p. 38).

[143] P.-P. Crépin, R. Guérout, and S. Reynaud, "Improved Effective Range Expansion for Casimir-Polder potential", submitted to European Physical Journal D (2019) (cited on pp. 38, 53, 139).

[144] A. I. Frank, "Modern optics of long-wavelength neutrons", Soviet Physics Uspekhi **34**, 980 (1991) (cited on p. 39).

[145] O. Vallée, and M. Soares, Airy functions and applications to physics (Imperial College Press, 2004) (cited on pp. 39, 40).

[146] J. Gea-Banacloche, "A quantum bouncing ball", American Journal of Physics **67**, 776 (1999) (cited on p. 40).

[147] B. Schwarzschild, "Ultracold neutrons exhibit quantum states in the Earth's gravitational field", Physics Today **55**, 20+ (2002) (cited on p. 40).

[148] V. Nesvizhevsky, and A. Voronin, Surprising quantum bounces (Imperial College Press, 2015) (cited on pp. 40, 70).

[149] G. Pignol, "Préparation de l'expérience granit et recherche de nouvelles interactions avec les neutrons.", PhD Thesis, PhD thesis (Université Joseph-Fourier - Grenoble I, 2009) (cited on p. 42).

[150] M. Kreuz, et al., "A method to measure the resonance transitions between the gravitationally bound quantum states of neutrons in the GRANIT spectrometer", Nuclear Instruments and Methods in Physics Research Section A **611**, 326 (2009) (cited on p. 43).

[151] T. Jenke, P. Geltenbort, H. Lemmel, and H. Abele, "Realization of a gravity-resonance-spectroscopy technique", Nature Physics **7**, 468 (2011) (cited on p. 43).

[152] S. Baeßler, V. V. Nesvizhevsky, G. Pignol, K. V. Protasov, D. Rebreyend, E. A. Kupriyanova, and A. Y. Voronin, "Frequency shifts in gravitational resonance spectroscopy", Physical Review D **91**, 042006 (2015) (cited on p. 43).

[153] J. Blatt, and J. Jackson, "On the interpretation of neutron-proton scattering data by the schwinger variational method", Physical Review **76**, 18 (1949) (cited on p. 44).

[154] H. Bethe, "Theory of the effective range in nuclear scattering", Physical Review **76**, 38 (1949) (cited on p. 44).

[155] F. Barker, and R. Peierls, "On the definition of the effective range of nuclear forces", Physical Review **75**, 312 (1949) (cited on p. 44).

[156] T. Teichmann, “On the interpretation of resonance levels and their widths in terms of the scattering length and the effective range”, Physical Review **83**, 141 (1951) (cited on p. 44).

[157] K. Brueckner, and F. Low, “Singular potentials and the theory of the effective range”, Physical Review **83**, 461 (1951) (cited on p. 44).

[158] E. Salpeter, “The effective range of nuclear forces - effect of the potential shape”, Physical Review **82**, 60 (1951) (cited on p. 44).

[159] F. Arnecke, H. Friedrich, and J. Madroñero, “Effective-range theory for quantum reflection amplitudes”, Physical Review A **74**, 062702 (2006) (cited on pp. 44, 45, 124, 125).

[160] J. Meixner, and F. Schafke, “Die grundlehren der mathematischen wissenschaften”, Springer-Verlag **71** (1954) (cited on pp. 44, 126).

[161] E. Vogt, and G. Wannier, “Scattering of ions by polarization forces”, Physical Review **95**, 1190 (1954) (cited on p. 45).

[162] L. Spruch, T. OMalley, and L. Rosenberg, “Modification of effective-range theory in the presence of a long-range potential”, Physical Review Letters **5**, 375 (1960) (cited on p. 45).

[163] P. Macri, and R. Barrachina, “Threshold behavior of the Jost function for the atomic polarization potential”, Physical Review A **65** (2002) (cited on pp. 45, 127).

[164] R. E. Langer, “On the asymptotic solutions of ordinary differential equations, with an application to the Bessel functions of large order”, Transactions of the American Mathematical Society **33**, 23 (1931) (cited on p. 56).

[165] R. E. Langer, “On the connection formulas and the solutions of the wave equation”, Physical Review **51**, 669 (1937) (cited on p. 56).

[166] G. Pignol, S. Ler, V. V. Nesvizhevsky, K. Protasov, D. Rebreyend, and A. Voronin, “Gravitational resonance spectroscopy with an oscillating magnetic field gradient in the GRANIT flow through arrangement”, Advances in High Energy Physics **2014**, e628125 (2014) (cited on p. 70).

[167] A. Y. Voronin, V. V. Nesvizhevsky, G. Dufour, P. Debu, A. Lambrecht, S. Reynaud, O. D. Dalkarov, E. A. Kupriyanova, and P. Froelich, “A spectroscopy approach to measure the gravitational mass of antihydrogen”, International Journal of Modern Physics: Conference Series **30**, 1460266 (2014) (cited on pp. 71, 87).

[168] P.-P. Crépin, C. Christen, R. Guérout, V. Nesvizhevsky, A. Voronin, and S. Reynaud, “Quantum interference test of the equivalence principle on antihydrogen”, Physical Review A (2019) (cited on pp. 71, 139).

[169] D. M. Greenberger, and A. W. Overhauser, “Coherence effects in neutron diffraction and gravity experiments”, Reviews of Modern Physics **51**, 43 (1979) (cited on p. 73).

[170] D. M. Greenberger, “The neutron interferometer as a device for illustrating the strange behavior of quantum systems”, Reviews of Modern Physics **55**, 875 (1983) (cited on p. 73).

[171] D. Greenberger, “Role of equivalence in quantum mechanics”, Annals of Physics **47**, 116+ (1968) (cited on p. 73).

[172] P. Langhoff, “Schrodinger particle in a gravitational well”, American Journal of Physics **39**, 954 (1971) (cited on p. 73).

[173] C. Lammerzahl, “On the equivalence principle in quantum theory”, General Relativity and Gravitation **28**, 1043 (1996) (cited on p. 73).

[174] C. Lammerzahl, “Minimal coupling and the equivalence principle in quantum mechanics”, Acta Physica Polonica B **29**, 1057 (1998) (cited on p. 73).

[175] M. Nauenberg, “Einstein’s equivalence principle in quantum mechanics revisited”, American Journal of Physics **84**, 879 (2016) (cited on p. 73).

[176] P. Storey, and C. Cohen-Tannoudji, “The Feynman path integral approach to atomic interferometry: A tutorial”, Journal de Physique II **4**, 29 (1994) (cited on p. 75).

[177] E. Wigner, “On the quantum correction for thermodynamic equilibrium”, Physical Review **40**, 749 (1932) (cited on p. 75).

[178] E. Kajari, N. L. Harshman, E. M. Rasel, S. Stenholm, G. Süßmann, and W. P. Schleich, “Inertial and gravitational mass in quantum mechanics”, Applied Physics B **100**, 43 (2010) (cited on p. 75).

[179] W. B. Case, “Wigner functions and Weyl transforms for pedestrians”, American Journal of Physics **76**, 937 (2008) (cited on p. 75).

[180] M. V. Berry, “Semi-classical mechanics in phase space: A study of Wigner’s function”, Philosophical Transactions of the Royal Society of London A **287**, 237 (1977) (cited on p. 75).

[181] G. Nogues, A. Rauschenbeutel, S. Osnaghi, P. Bertet, M. Brune, J. M. Raimond, S. Haroche, L. G. Lutterbach, and L. Davidovich, “Measurement of a negative value for the Wigner function of radiation”, Physical Review A **62**, 054101 (2000) (cited on p. 76).

[182] P. Bertet, A. Auffeves, P. Maioli, S. Osnaghi, T. Meunier, M. Brune, J. M. Raimond, and S. Haroche, “Direct Measurement of the Wigner Function of a One-Photon Fock State in a Cavity”, Physical Review Letters **89**, 200402 (2002) (cited on p. 76).

[183] R. v. Eötvös, D. Pekár, and E. Fekete, Annalen der Physik (Leipzig) **68**, 11 (1922) (cited on p. 80).

[184] H. Cramér, Mathematical methods of statistics, Princeton Landmarks in Mathematics PMS-9 (Princeton University Press, 1946) (cited on pp. 83, 86, 129).

[185] P. Réfrégier, Noise theory and application to physics, Advanced Texts in Physics (Springer, 2004) (cited on pp. 83, 86).

[186] V. V. Nesvizhevsky, A. Y. Voronin, R. Cubitt, and K. V. Protasov, "Neutron whispering gallery", Nature Physics **6**, 114 (2009) (cited on pp. 87, 94).

[187] V. Nesvizhevsky, A. Voronin, P.-P. Crépin, and S. Reynaud, "Interference of several gravitational quantum states of antihydrogen in GBAR experiment", Hyperfine Interactions **240** (2019) (cited on pp. 87, 139).

[188] V. Nesvizhevsky, A. Voronin, P.-P. Crépin, and S. Reynaud, "Interference of several gravitational quantum states of antihydrogen in GBAR experiment", Hyperfine Interactions **accepted** (2018) (cited on p. 94).

[189] J. Lussange, R. Guerout, and A. Lambrecht, "Casimir energy between nanostructured gratings of arbitrary periodic profile", English, Physical Review A **86** (2012) (cited on p. 101).

[190] N. Cherroret, R. Guérout, A. Lambrecht, and S. Reynaud, "Fluctuations of the Casimir potential above a disordered medium", The European Physical Journal D **69**, 1 (2015) (cited on pp. 101, 102, 108, 110, 112, 115).

[191] N. Cherroret, R. Guerout, A. Lambrecht, and S. Reynaud, "Statistical approach to Casimir-Polder potentials in heterogeneous media", Physical Review A **92** (2015) (cited on pp. 101, 102).

[192] A. Lambrecht, A. Canaguier-Durand, R. Guérout, and S. Reynaud, "Casimir Effect in the Scattering Approach: Correlations Between Material Properties, Temperature and Geometry", in Casimir Physics, edited by D. Dalvit, P. Milonni, D. Roberts, and F. da Rosa, Lecture Notes in Physics 834 (Springer Berlin Heidelberg, 2011), pp. 97–127 (cited on p. 101).

[193] R. S. Decca, D. Lopez, E. Fischbach, G. L. Klimchitskaya, D. E. Krause, and V. M. Mostepanenko, "Novel constraints on light elementary particles and extradimensional physics from the Casimir effect", European Physical Journal C **51**, 963 (2007) (cited on p. 102).

[194] C.-C. Chang, A. A. Banishev, R. Castillo-Garza, G. L. Klimchitskaya, V. M. Mostepanenko, and U. Mohideen, "Gradient of the Casimir force between Au surfaces of a sphere and a plate measured using an atomic force microscope in a frequency-shift technique", Physical Review B **85** (2012) (cited on p. 102).

[195] A. A. Banishev, G. L. Klimchitskaya, V. M. Mostepanenko, and U. Mohideen, "Demonstration of the Casimir Force between Ferromagnetic Surfaces of a Ni-Coated Sphere and a Ni-Coated Plate", Physical Review Letters **110** (2013) (cited on p. 102).

[196] G. Bimonte, D. Lopez, and R. S. Decca, "Isoelectronic determination of the thermal Casimir force", Physical Review B **93** (2016) (cited on p. 102).

[197] A. O. Sushkov, W. J. Kim, D. A. R. Dalvit, and S. K. Lamoreaux, “Observation of the thermal Casimir force”, English, Nature Physics **7**, 230 (2011) (cited on p. 102).

[198] D. Garcia-Sanchez, K. Y. Fong, H. Bhaskaran, S. Lamoreaux, and H. X. Tang, “Casimir Force and In Situ Surface Potential Measurements on Nanomembranes (vol 109, 027202, 2012)”, English, Physical Review Letters **109** (2012) (cited on p. 102).

[199] D. S. Dean, R. R. Horgan, A. Naji, and R. Podgornik, “Effects of dielectric disorder on van der Waals interactions in slab geometries”, Physical Review E **81** (2010) (cited on pp. 102, 115).

[200] P. J. van Zwol, V. B. Svetovoy, and G. Palasantzas, “Characterization of Optical Properties and Surface Roughness Profiles: The Casimir Force Between Real Materials”, in Casimir Physics, edited by D. Dalvit, P. Milonni, D. Roberts, and F. da Rosa, Lecture Notes in Physics 834 (Springer Berlin Heidelberg, 2011), pp. 311–343 (cited on p. 107).

[201] E. D. Palik, Handbook of Optical Constants of Solids (Academic Press: New York, 1985) (cited on p. 107).

[202] N. Cherroret, P.-P. Crepin, R. Guerout, A. Lambrecht, and S. Reynaud, “Casimir-Polder force fluctuations as spatial probes of dissipation in metals”, EPL (Europhysics Letters) **117**, 63001 (2017) (cited on pp. 110, 139).

[203] C. Kane, R. Serota, and P. Lee, “Long-range correlations in disordered metals”, English, Physical Review B **37**, 6701 (1988) (cited on p. 112).

[204] A. A. Allocca, J. H. Wilson, and V. M. Galitski, “Quantum interference phenomena in the Casimir effect”, Physical Review A **91** (2015) (cited on p. 112).

[205] N. W. Ashcroft, and N. D. Mermin, Solid state physics (Saunders college, Philadelphia, 1976) (cited on p. 116).

[206] D. Gall, “Electron mean free path in elemental metals”, Journal of Applied Physics **119** (2016) (cited on p. 116).

[207] J. L. Davidson, J. D. Gibson, S. A. Harris, and T. J. Rossiter, “Fusing mechanism of nichrome thin films”, International reliability physics symposium, 173 (1976) (cited on p. 117).

[208] P. Lee, and T. Ramakrishnan, “Disordered electronic systems”, English, Reviews of Modern Physics **57**, 287 (1985) (cited on p. 117).

[209] S. A. Ellingsen, S. Y. Buhmann, and S. Scheel, “Dynamics of thermal Casimir-Polder forces on polar molecules”, Physical Review A **79** (2009) (cited on p. 117).

[210] B. S. Zhao, G. Meijer, and W. Schoellkopf, “Quantum Reflection of He-2 Several Nanometers Above a Grating Surface”, English, Science **331**, 892 (2011) (cited on p. 123).

[211] B. S. Zhao, W. Zhang, and W. Schoellkopf, “Universal diffraction of atoms and molecules from a quantum reflection grating”, English, Science Advances **2** (2016) (cited on p. 123).

[212] W. Zhang, J. H. Lee, H. A. Kim, B. G. Jin, B. J. Kim, L. Y. Kim, B. S. Zhao, and W. Schoellkopf, “Universal Diffraction of Atomic and Molecular Matter-Waves: A Comparison of He and D-2 Quantum Reflected from a Grating”, English, ChemPhysChem **17**, 3670 (2016) (cited on p. 123).

[213] X. Halliwell, H. Friedrich, S. Gibson, and K. Baldwin, “Quantum reflection of metastable helium 2(3)S atoms in hollow optical fibres”, English, Optics Communications **224**, 89 (2003) (cited on p. 123).

[214] M. Stock, R. Davis, E. de Mirandes, and M. J. T. Milton, “The revision of the SI-the result of three decades of progress in metrology”, Metrologia **56** (2019) (cited on p. 134).

[215] P.-P. Crepin, E. A. Kupriyanova, R. Guerout, A. Lambrecht, V. V. Nesvizhevsky, S. Reynaud, S. Vasiliev, and A. Y. Voronin, “Quantum reflection of antihydrogen from a liquid helium bulk”, Hyperfine Interactions **240** (2019) (cited on p. 139).

Sujet : Réflexion quantique d'un paquet d'onde d'antihydrogène refroidi

---

Résumé : Le cadre de cette thèse est celui de la collaboration GBAR, au CERN, qui a pour objectif de mesurer l'accélération de pesanteur de l'antimatière. Dans cette thèse, nous étudions la réflexion quantique de l'antihydrogène sur le détecteur, provoquée par l'interaction Casimir-Polder que nous calculons pour différents matériaux. Nous trouvons une réflexion quantique particulièrement élevée pour un atome d'antihydrogène sur une surface d'hélium liquide. Nous présentons ensuite une description complète des états quantiques gravitationnels, mêlant la gravité et l'interaction de Casimir-Polder. Nous revisitons pour cela la théorie des collisions dans le cas du potentiel de Casimir-Polder à travers une nouvelle "effective range theory", obtenue après transformée de Liouville. La connaissance des états quantiques gravitationnels nous amène à proposer une nouvelle méthode de mesure de l'accélération de pesanteur, en créant des interférences quantiques entre ces états. Une analyse statistique de la figure d'interférence ainsi obtenue est réalisée, conduisant à une amélioration de la précision jusqu'à trois ordres de grandeurs par rapport à l'expérience initiale de chute libre classique. Enfin, nous étudions en détail l'influence du désordre au niveau de la plaque de détection, celle-ci n'étant en réalité pas une surface parfaite. Nous calculons l'effet de ce désordre sur les fluctuations du potentiel de Casimir-Polder lui-même, et observons un comportement en loi différent pour les modèles de conductivité que sont le modèle plasma et le modèle de Drude.

Subject : Quantum reflection of a cold antihydrogen wave packet

---

Abstract : The framework of this thesis is the GBAR collaboration at CERN, which aims to measure the free fall acceleration of antimatter . In this thesis, we study the quantum reflection of the antihydrogen on the detector, caused by the Casimir-Polder interaction that we calculate for different materials. We find a particularly high quantum reflection for an antihydrogen atom on a surface of liquid helium. We then present a complete description of the gravitational quantum states, mixing gravity and Casimir-Polder interaction. For this purpose, we revisit the theory of collisions in the case of the Casimir-Polder potential through a new "effective range theory", obtained after a Liouville transform. The knowledge of gravitational quantum states leads us to propose a new method of measuring free fall acceleration, by creating quantum interferences between these states. A statistical analysis of the interference pattern thus obtained is carried out, leading to an improvement in the accuracy until three orders of magnitude compared to the initial free-fall experiment. Finally, we study in detail the influence of the disorder at the level of the plate of detection, the latter being in fact not a perfect surface. We calculate the effect of this disorder on the fluctuations of the Casimir-Polder potential itself, and observe a different behavior in law for the conductivity models such as the plasma model and the Drude model.